Functional analysis of the phosphatase UIS2 in asexual blood stages of the human malaria parasite *Plasmodium falciparum*

DISSERTATION

With the aim of achieving a doctoral degree at the Faculty of Mathematics, Informatics and Natural Sciences

Department of Biology
University Hamburg

Submitted by

María Carolina Castro Peña

Hamburg, 2024

Ich versichere, dass dieses gebundene Exemplar der Dissertation und das in elektronischer Form eingereichte Dissertationsexemplar (über den Docata-Upload) und das bei der Fakultät (zuständiges Studienbüro bzw. Promotionsbüro Physik) zur Archivierung eingereichte gedruckte gebundene Exemplar der Dissertationsschrift identisch sind.

I, the undersigned, declare that this bound copy of the dissertation and the dissertation submitted in electronic form (via the Docata upload) and the printed bound copy of the dissertation submitted to the faculty (responsible Academic Office or the Doctoral Office Physics) for archiving are identical.

Hamburg, 08.05.2024

City, Date

Signature

Datum der Disputation: 03.05.2024
1.Gutachter der Dissertation: Dr. Tobias Spielmann
2.Gutachter der Dissertation: Prof. Dr. Tim-Wolf Gilberger
Vorsitz der Prüfungskommission: Prof. Dr. Julia Kehr

Eidesstattliche Versicherung

Hiermit erkläre ich an Eides statt, dass ich die vorliegende Dissertationsschrift selbst verfasst und keine anderen als die angegebenen Quellen und Hilfsmittel benutzt habe.

Declaration of academic honesty

I hereby declare, on oath, that I have written the present dissertation by my own and have not used other than the acknowledged resources and aids.

Hamburg, den 08.03.2024	
Ort, Datum	**Unterschrift**

Language certificate

I am a native speaker, have read the present PhD thesis and hereby confirm that it complies with the rules of the English language.

Hamburg, 08.03.2024	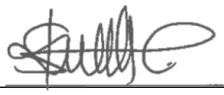
Ort, Datum	**Sheila Mainye**

Acknowledgments

First, I would like to express my profound gratitude to my supervisor Dr. Tobias Spielmann for allowing me to pursue my doctoral thesis within his research team. His exemplary dedication and fervor for scientific inquiry have been a great inspiration in so many ways. I am deeply appreciative of his trust, and support, and for providing me with the opportunity to advance my expertise in this area of study.

I would like to express my gratitude to Prof. Dr. Tim-Wolf Gilberger for his invaluable suggestions and encouraging words. I also appreciate his willingness to evaluate my doctoral thesis. Furthermore, I am thankful to Dr. Richárd-Bártfai for providing the necessary facilities for conducting mass spectrometry analyses, particularly to Pascal Wilhelmus Theodorus and Gala Ramón-Zamorano.

I want to thank Dr. Paolo Mesén Ramírez for his invaluable advice, unwavering support, and expert guidance in the laboratory. His confidence in my abilities and constant encouragement to push my limits have been instrumental in my success. Additionally, I owe a great debt to Dr. Melissa Khosh-Naucke whose prior work has been indispensable to the completion of my doctoral project. Without her crucial contribution, my project would not have reached its current stage of completion. To Dr. Stephan Wichers-Misterek, thank you for sharing your scientific knowledge and providing valuable advice, as well as assisting with experiments for my thesis. I would also like to thank Dr. Hannah Behrens for dedicating her valuable time to read, evaluate, and provide feedback on my doctoral work.

I would like to express my gratitude to all the members of the AG Spielmann team, and extend special thanks to Ricarda, Sarah, Sabine, Jan, Lea, Sheila, Lea and José. Their coffee breaks and valuable advice made the workplace enjoyable. I appreciate their unconditional support during challenging times, and am grateful for their friendship.

I also want to thank Prof. Dr. Esteban Chaves-Olarte for being the first person to believe in me and for providing me with the opportunity to grow both personally and

professionally in the field of science. To my beloved parents, who have always been my role models of perseverance and determination, I am immensely grateful for your constant support, guidance, and unwavering belief in my abilities. Despite the distance between us, you have always been present in my life, inspiring me to pursue my dreams and achieve great things. To my wonderful sisters, you have been the pillars of strength in my life, providing me with unconditional love, support, and valuable advice whenever I needed it the most. I am truly blessed to have you in my life and cannot thank you enough for everything you have done for me. And to Jakob, thank you for being my rock through the ups and downs during this journey, for your comforting words of wisdom, and for always believing in me. Your encouragement and unwavering faith in my abilities have helped me become the best version of myself.

Lastly, I would like to express my gratitude to the German Academic Exchange Service (DAAD) for providing me with the opportunity to pursue my doctoral studies and for always showing concern for my well-being and the progress of my project. This thesis was printed with the support of the DAAD.

Summary

Malaria, a deadly disease caused by unicellular parasites from the *Plasmodium* genus, continues to be a significant health threat in tropical and subtropical regions. Among the various species of *Plasmodium*, *P. falciparum* is the most lethal, accounting for the majority of malaria-related fatalities. The life cycle of these parasites includes a phase of asexual proliferation within human red blood cells (RBCs) that is the reason for the disease manifestation in the host. In the RBC, the parasites reside inside a specialized compartment known as the parasitophorous vacuole (PV). This vacuole is enveloped by the parasitophorous vacuole membrane (PVM), a barrier that parasite-derived proteins must cross to reach the host cell where they induce host cell modifications crucial for the parasite's survival. To be exported into the host cell, these proteins are first secreted into the PV followed by translocation across the PVM to reach the host cell. This translocation is facilitated by a specialized protein complex known as the *Plasmodium* Translocon of Exported proteins (PTEX). A protein located in the PV that in preliminary results was found to be essential for the parasite´s survival and possibly protein export is the phosphatase upregulated in infected sporozoites 2 (UIS2, PF3D7_1464600). UIS2 had previously been believed to be involved in the regulation of translation by dephosphorylating eukaryotic initiation factor 2α (eIF2α-P) during the liver stages of *P. berghei*. However, the determined location of UIS2 in the PV renders such function unlikely.

This thesis presents a detailed study of the function of UIS2 (PF3D7_1464600) and its role in protein export. In order to do this, a conditional UIS2 knockout (condΔUIS2) cell line using diCre based conditional gene elimination was used to study the effect of UIS2 loss on *P. falciparum* blood stages. The loss of UIS2 resulted in a severe growth defect with an arrest of the parasite at the early ring stage of the asexual blood stage. Export of the Maurer's clefts (membranous parasite-derived structures in the host cell) protein SBP1 and the host cell membrane protein KAHRP, was significantly impaired in ΔUIS2 parasites, causing an accumulation of these proteins within the parasite or at its periphery. This observed phenotype supports the hypothesis that UIS2 could be involved in a dephosphorylation-dependent sorting step in the PV, essential for the progression of the parasite's life cycle. However, as the ring stages missing UIS2 appeared to arrest immediately after invasion, it was unclear whether

the disruption in protein export was a specific defect or a result from a general loss of viability of ring stage parasites. Delaying the timing of *uis2* excision in the parasite life cycle revealed that UIS2 loss later during ring stage allowed the parasites to progress to the trophozoite stage when again a defect in protein export was evident. Characterization of different markers in ΔUIS2 parasites showed that the exported proteins SBP1, KAHRP and GBP$^{1-108}$ were retained in the PV. In addition, a soluble PV reporter showed an altered distribution, potentially indicating architectural alterations of the PV compartment. In contrast, an integral plasma membrane protein was not affected, reinforcing that the effect of UIS2 loss on protein export was specific and affected transport processes beyond the boundary of the parasite. These findings highlight the critical role of UIS2 in protein export.

Structural analysis revealed that despite the initial classification of UIS2 as a protein phosphatase 2C (PP2C), UIS2 lacks the canonical PP2C catalytic domain. Instead, its phosphatase domain shares significant structural similarities and ligand-binding sites (LBs) with those of purple acid phosphatases (PAPs). Using predictive model like AlphaFold and Swiss model protein templates, the study demonstrated a high degree of structural congruity between UIS2 and human PAPs. These observations allowed to design phosphatase catalytic site mutants constructs of UIS2. These were used in a complementation assay to explore the significance of the phosphatase activity for the function of UIS2. Mutations at conserved residues crucial for metal ion binding and catalysis were replaced, resulting in a presumably catalytically dead domain. Complementation with constructs carrying single-point mutations (D542N or D591N) in the UIS2 phosphatase domain induced moderate growth defects, indicating a partial reduction of UIS2 function and suggested that the phosphatase activity plays a role in the function of UIS2, while a double mutant (D542N-D591N) showed severe phenotype, including reduced parasite size, suggesting a more profound loss of phosphatase activity compared to single mutations. As the work in this thesis found that UIS2 is needed for protein export in *P. falciparum* parasites, the research investigated the functional conservation of UIS2. A potential UIS2 ortholog from *T. gondii,* GRA44 which is involved in protein export in that parasite, was also tested for its capacity to complement UIS2 loss in *P. falciparum*. However, *Tg*GRA44 did not complement, suggesting a limited functional conservation between *Pf*UIS2 and *Tg*GRA44, which might be due to the different translocon complexes used for

export in these two parasites, although incorrect folding or lowered expression levels as the reason for this finding remain a possibility.

In this work, dimerization induced quantitative (DiQ)-BioID was used to investigate the UIS2 interactome within the PV. DiQ-BioID, a proximity labeling method using an inducible heterodimerization system and the promiscuous biotin ligase BirA*, enabled the biotinylation and subsequent mass spectrometry-based identification of proteins proximal to UIS2. The experimental results confirmed the recruitment of BirA* to UIS2, with mass spectrometry identifying UIS2 as the most significantly enriched protein, alongside the surface protein P113, which previously has been shown not to impair parasite growth or protein export. The lack of significant enrichment of PTEX components suggested that UIS2, despite its established role in protein export, may not be in direct physical contact with the PTEX complex. Instead, UIS2 might function upstream of PTEX translocation. Two additional potential interactors from the DiQ-BioID PF3D7_1133800 (RNA (uracil-5-) methyltransferase) and PF3D7_0922100 (ubiquitin-like protein, putative) were identified. Conditional knockouts and localization studies for these candidates indicated that these proteins are import for parasite growth. These proteins were localized in the parasite cytosol (PF3D7_1133800) and at the parasite periphery (PF3D7_0922100). However, despite being enriched in the UIS2 interactome, their loss did not impact protein export, indicating these proteins are unlikely to function in the same process as UIS2 and their precise roles in relation to UIS2 remained unclear.

The data in this thesis provides a comprehensive analysis of the UIS2 phosphatase and its indispensable role in the biology of *P. falciparum* parasites and highlights it as the so far only protein beside Plasmepsin V (a protease processing exported proteins) involved in protein export that is present in different apicomplexan parasites. By combining genetic, biochemical, and bioinformatic approaches, this thesis reveals UIS2 as a parasite-specific phosphatase with an important function in protein export and parasite survival.

.

Zusammenfassung

Malaria ist eine tödliche Krankheit die von einzelligen Parasiten aus dem Genus *Plasmodium* verursacht wird. Malaria bleibt eine erheblich Gesundheitsbedrohung in tropischen und subtropischen Regionen. Von den verschiedenen *Plasmodium*-Arten ist *P. falciparum* die tödlichste und verantwortlich für die Mehrheit der Malaria-bedingten Todesfälle. Der Lebenszyklus dieser Parasiten beinhaltet eine asexuelle Proliferation innerhalb menschlicher roter Blutkörperchen (RBCs). Ausschließlich diese Phase des Lebenszyklus ist verantwortlich für die Symptome der Krankheit. In den RBCs befinden sich die Parasiten in einem spezialisierten Kompartiment, das parasitophore Vakuole (PV) genannt wird. Diese Vakuole ist von der parasitophoren Vakuolenmembran (PVM) umgeben. Diese Barriere muss von den Proteinen der Parasiten überwunden werden, um in die Wirtszelle zu gelangen, wo diese für den Parasiten essentielle Modifizierungen der Wirtszelle induzieren. Um in die Wirtszelle exportiert zu werden, müssen diese Proteine zunächst in die PV sekretiert und anschließend durch Translokation über die PVM in die Wirtszelle transportiert werden. Diese Translokation wird durch einen spezialisierten Proteinkomplex ermöglicht, der als Plasmodium Translocon of Exported proteins (PTEX) bekannt ist. Upregulated in Infected Sporozoiten Phosphatase 2 (UIS2, PF3D7_1464600) ist ein Protein in der PV. Erste vorläufige Ergebnisse aus unserem Labor zeigten, dass UIS2 essenziell für das Überleben des Parasiten und möglicherweise auch für den Proteinexport ist. Frühere Arbeiten lieferten Hinweise, dass UIS2 den eukaryotischer Initiationsfaktor 2α (eIF2α-P) während der Leberstadien von *P. berghei* dephosphoryliert und so an der Regulierung der Translation beteiligt ist soll. Die Lokalisation von UIS2 in der PV macht eine solche Funktion jedoch sehr unwahrscheinlich.

Diese Dissertation präsentiert eine detaillierte Studie über die Funktion von UIS2 (PF3D7_1464600) und dessen Rolle beim Proteinexport. Um dies zu tun, wurde eine konditionale UIS2-Knockout-Zelllinie (condΔUIS2) unter Verwendung einer diCre-basierten Genedeletion verwendet, um die Auswirkungen eines *uis2* Knockouts auf die Blutstadien von *P. falciparum* zu untersuchen. Der Verlust von UIS2 führte zu einem erheblichen Wachstumsdefekt mit einer Stagnation des Parasiten im frühen Ringstadium des asexuellen Blutstadiums. Der Export der Proteine SBP1, welches

in den Maurer'schen Spalten (membranöse, von Parasiten induzierten Strukturen in der Wirtszelle) und KAHRP, ein Parasitenprotein in der Wirtzellmembran, waren in ΔUIS2-Parasiten erheblich beeinträchtigt und führte zu einer Ansammlung dieser Proteine innerhalb des Parasiten oder an dessen Peripherie. Dieser Phänotyp stützt die Hypothese, dass UIS2 an einem überlebensnotwendigen phosphorylierungsabhängigen Sortierungsschritt innerhalb der PVM beteiligt sein könnte. Da jedoch die Ringstadien ohne UIS2 unmittelbar nach der Invasion ihr Wachstum einstellten, war unklar, ob die Beeinträchtigung im Proteinexport ein spezifischer Defekt war oder aus einem allgemeinen Verlust der Lebensfähigkeit der Ringstadienparasiten resultierte. Die Induktion der *uis2*-deletion später im Lebenszyklus des Parasiten und der Verlust von UIS2 während des späten Ringstadiums führte dazu, dass die Parasiten das Trophzoitenstadium erreichten, wo erneut ein Defekt im Proteinexport ersichtlich war. Die Charakterisierung verschiedener Marker in ΔUIS2-Parasiten zeigte, dass die exportierten Proteine SBP1, KAHRP und GBP1-108 in der PV verbleiben. Außerdem zeigte ein löslicher PV-Reporter ein verändertes Lokalisationsmuster in der PV, was auf strukturelle Veränderungen des PV-Kompartiments hindeuten könnte. Im Gegensatz dazu wurde ein integrales Plasmamembranprotein in ΔUIS2-Parasiten nicht beeinträchtigt, was den spezifischen Effekt des UIS2-Verlusts auf den Proteinexport und auf Prozesse jenseits der Grenze des Parasiten verstärkte. Diese Ergebnisse heben die essenzielle Rolle von UIS2 im Proteinexports hervor.

Strukturanalysen zeigten, dass UIS2 trotz der ursprünglichen Einordnung als eine Proteinphosphatase 2C (PP2C) nicht über eine kanonische PP2C-Katalysedomäne verfügt. Stattdessen weist seine Phosphatasedomäne bedeutende strukturelle Ähnlichkeiten und Ligandenbindungsstellen (LBs) mit denen der Purple Acid Phosphatasen (PAPs) auf. Mithilfe von AlphaFold und Swiss-Modell generierten Strukturmodellen wurde in dieser Arbeit ein hoher Grad an struktureller Übereinstimmung zwischen UIS2 und menschlichen PAPs festgestellt. Diese Beobachtungen ermöglichten die Herstellung von Konstrukten für die Mutation der Phosphatase-Katalyse Domänen von UIS2. Diese wurden in Komplementierungsexperimenten verwendet, um die Bedeutung der Phosphataseaktivität für die Funktion von UIS2 zu untersuchen. Mutationen konservierter Metallionenbindungsstellen die für die Katalyse entscheidend sind,

wurden entworfen. Dies sollte zu einer Inaktivierung der katalytischen Domäne führen. Komplementation mit Konstrukten die Einzelmutationen (D542N oder D591N) in der Phosphatasedomäne von UIS2 trugen, führten zu einem moderate Wachstumsdefekte, was auf eine teilweise Reduktion der UIS2-Funktion hinweist und vermuten lässt, dass die Phosphataseaktivität eine Rolle in der Funktion von UIS2 spielt. Eine Doppelmutation (D542N-D591N) führte zu einem schwerwiegenden Phänotyp, einschließlich reduzierter Parasitengröße, was auf einen umfänglicheren Verlust der Phosphataseaktivität im Vergleich zu Einzelmutationen hindeutet. Auf Grund der Ergebnisse, dass UIS2 für den Proteinexport in *P. falciparum*-Parasiten benötigt wird, wurde in dieser Arbeit die funktionelle Konservierung von UIS2 untersuchen. Ein potenzielles Ortholog von UIS2 in *T. gondii*, GRA44, welches am Proteinexport in diesem Parasiten beteiligt ist, wurde ebenfalls auf seine Fähigkeit getestet, den Verlust von UIS2 in *P. falciparum* zu komplementieren. Allerdings führte die Komplementierte mit TgGRA44 nicht zu einer Umkehr des Phänotyps, was auf eine eingeschränkte funktionelle Konservierung zwischen PfUIS2 und TgGRA44 hinweist. Dies könnte darauf zurückzuführen sein, dass diese beiden Organismen unterschiedliche Translokon-Komplexe für den Protein export nutzen. Jedoch ist es nicht auszuschließen, dass eine falsche Faltung oder niedrigere Expressionslevels die Gründe für die unzureichende funktionelle Komplementierung sind.

Zusätzlich wurde in dieser Arbeit DiQ-BioID (dimerization induced quantitative BioID) verwendet, um das Interaktom von UIS2 innerhalb der PV zu untersuchen. DiQ-BioID verwendet ein induzierbares Heterodimerisierungssystem und die promiskuitive Biotin-Ligase BirA*, wodurch Proteine in der Nähe eines Zielproteins biotinyliert werden können und nachfolgend durch Massenspektrometrische Analysen identifiziert werden können. Die Ergebnisse der Experimente bestätigten die Rekrutierung von BirA* zu UIS2, wobei die Massenspektrometrie UIS2 als das am stärksten angereicherte Protein identifizierte. Daneben wurde auch das Oberflächenprotein P113 angereichert, von dem zuvor gezeigt wurde, dass es für das Parasitenwachstum oder den Proteinexport nicht benötigt wird. Das Fehlen einer signifikanten Anreicherung von PTEX-Komponenten deutete darauf hin, dass UIS2 trotz seiner Rolle im Proteinexport möglicherweise nicht in direktem physischem Kontakt mit dem PTEX-Komplex steht. Stattdessen könnte UIS2 an einem Prozess vor der PTEX-Translokation fungieren. Zwei weitere potenzielle Interaktoren aus der

DiQ-BioID, PF3D7_1133800 (RNA (Uracil-5-) Methyltransferase) und PF3D7_0922100 (putatives ubiquitinähnliches Protein) wurden ebenfalls analysiert. Induzierbare Knockouts dieser Kandidaten zeigten, dass diese Proteine wichtig für das Parasitenwachstum sind. Diese Proteine waren im Parasitenzytosol (PF3D7_1133800) und an der Parasitenperipherie (PF3D7_0922100) lokalisiert. Trotz der Anreicherung im Interaktom von UIS2 hatte ihr Verlust keinen Einfluss auf den Proteinexport, was darauf hinweist, dass diese Proteine vermutlich nicht am selben Prozess wie UIS2 beteiligt sind. Damit bleibt ihre genauen Rollen in Bezug auf UIS2 unklar.

Die Daten in dieser Doktorarbeit liefern eine umfassende Analyse der UIS2-Phosphatase und ihrer essenziellen Rolle in der Biologie der *P. falciparum*-Parasiten. Außerdem hebt dies UIS2 als bisher einziges Protein neben Plasmepsin V (einem Protein, das exportierte Proteine prozessiert) hervor, dass am Proteinexport beteiligt ist und in verschiedenen Parasiten des Genus *Apicomplexa* vorhanden ist. Durch die Kombination von genetischen, biochemischen und bioinformatischen Ansätzen enthüllt diese Doktorarbeit UIS2 als parasitenspezifische Phosphatase mit einer wichtigen Funktion im Proteinexport und im Überleben des Parasiten.

Table of contents

Abbreviations

ACTs	ART Combination Therapies
ACP5	5 Acid Phosphatases
ACß	Adenylate Cyclase Beta
AMA1	Apical Membrane Antigen 1
ARO	Armadillo Repeats Only- Protein
ART	Artemisinin Derivatives
BSVs	Blood-Stage Vaccines
CHMI	Controlled Human Malaria Infection
CLAG3	Cytoadherence-Linked Asexual Protein 3
CNB	Calcineurin B
CNA	Calcineurin A
CPS	Circumsporozoite Protein
CyRPA	Cysteine-Rich Protective Antigen
D	Aspartic Acid
DAPI	4',6-Diamidino-2-Phenylindole
DIQ-BioID	Dimerization Induced Quantitative BioID
DV	Digestive Vacuole
EBA175	Erythrocyte Binding Antigen 175
EBAs	Erythrocyte Binding Antigens
EMP1	Erythrocyte Membrane Protein 1
END	Endogenous
eIF2α	Eukaryotic Initiation Factor 2 Alpha
EPIC	Exported Protein-Interacting Complex
EXP1	Exported Protein 1
EXP2	Exported Protein 2
FIKK 4.1	Serine/Threonine Protein Kinase 4
FV	Food Vacuole

FNT	Formate-Nitrite Transporter
GBP	Glycophorin-Binding Protein
GAS	Genetically Attenuated Sporozoites
GFP	Green Fluorescent Protein
GSK	Glaxosmithkline
HAD	Haloacid Dehydrogenase
HA	Hemagglutinin
HBsAg	Hepatitis B Surface Antigen
HSP101	Heat Shock Protein 101
HSPGs	Heparin-Sulfate Proteoglycans
Hz	Hemozoin
IFAs	Immunofluorescence Assays
IMC	Inner Membrane Complex
IPTp	Chemoprevention In Pregnancy
IRS	Indoor Residual Spraying
ITNs	Insecticide-Treated Nets
KAHRP	Knob-Associated Histidine-Rich Protein
KO	Knockout
LCAT	Lecithin:Cholesterol Acyltransferase
LBs	Ligand-Binding Sites
MAHRP1	Membrane-Associated Histidine-Rich Protein 1
MAHRP2	Membrane-Associated Histidine-Rich Protein 2
MCs	Maurer's Clefts
MPP/ACP5	Metallophosphatase-Acid Phosphatase 5
MSP1	Merozoites Surface Protein 1
MSRP6	The Merozoite Surface-Related Protein-6
NPC	Nutrient Permeable Channel
NIF	NLI-Interacting Factor-Like Phosphatase
PAP	Purple Acid Phosphatase

Pf	*Plasmodium falciparum*
SPZ	Sporozoites
PDB	Protein Data Bank
PEXEL	*Plasmodium* Export Element
PFK9	6-phospho-1-fructokinase on chromosome 9
PIESP2	*Plasmodium*-Infected Erythrocyte Surface Protein 2
PMC	Perennial Malaria
PMV	Plasmepsin V
PNEPs	PEXEL-Negative Exported Proteins
PPP	Phospho-Protein Phosphatase
PPM/PP2C	Mn2+/Mg2+ Metal Dependent Protein Phosphatase
PPM	Parasite Plasma Membrane
TEXEL	*Toxoplasma* Export Elements
PV	Parasitophorous Vacuole
RAS	Sporozoites Attenuated Through Radiation
RBCs	Red Blood Cells
REX1	Ring Exported Protein 1
REX2	Ring Exported Protein 2
RIPR	Rh5-Interacting Protein
Rhs	Reticulocyte-Binding Protein Homologs
RISP	Rhoptry Apical Surface Protein
SBP1	Skeleton Binding Protein-1
SERA	Serine-Rich Antigen
SMC	Seasonal Malaria
SP	Signal Peptide
TBVs	Transmission-Blocking Vaccines
TEXEL	Toxoplasma Export Elements
Thr	Threonine
TM	Transmembrane Domain

TRAP	Thrombospondin-Related Anonymous Protein
TRC	Transmembrane Domain Recognition Complex
TRP	Triplet Artemisinin-Based Combination Therapies
TVN	Tubovesicular Network
Tyr	Tyrosine
UIS	Upregulated Genes In Infected Sporozoites
UIS2	Serine/Threonine Phosphatase UIS2
ULD	Ubiquitin-Like Domain
WHO	World Health Organization
WSV	Whole Sporozoites Vaccines
yDHODH	Yeast Dihydroorotate Dehydrogenase

List of figures

List of tables

1 Introduction

1.1 Malaria

In 1880, Charles Louis Alphonse Laveran's identified a parasitic protozoan within the red blood cells (RBCs) of patients suffering from malaria, suggesting it as the likely primary etiological agent of that disease (Laveran, 1880). Malaria is a mosquito-borne infectious disease transmitted through the bite of infected female *Anopheles* mosquitoes (Garrido-Cardenas *et al.*, 2019), caused by Apicomplexan parasites belonging to the genus *Plasmodium* (Müller, 2011). While there are over 200 species of *Plasmodium* known, only five have the potential to infect human hosts: *P. vivax*, *P. malariae*, *P. ovale*, *P. knowlesi* and *P. falciparum*. Among these, *P. falciparum* is responsible for the majority of malaria cases (WHO, 2022). The higher virulence of *P. falciparum*, compared to the other four human-infecting species, is at least in part attributed to its ability to bind to the endothelium of the host during the blood stage of the infection (Greenwood *et al.*, 2008).

1.1.1 Epidemiology

The World Health Organization (WHO) reported approximately 247 million cases of malaria worldwide for 2021, an increase of 2 million cases over the previous year, resulting in 619 000 malaria deaths (WHO, 2022). During the 2 years of COVID-19 pandemic, the number of malaria cases increased by 14 million, leading to approximately 63,000 more deaths from the disease (WHO, 2021). African regions accounted for the majority of cases, with children under 5 years of age representing about 80% of all malaria deaths in the region. To date, malaria cases are predominantly concentrated in tropical and subtropical areas (Figure 1) (WHO, 2022). However, extensive eradication programs have successfully eliminated malaria in some of these regions. These programs typically involved a combination of strategies, including vector control measures such as the use of insecticide-treated nets (ITNs) and indoor residual spraying (IRS). The WHO also recommends the mitigation of mosquito breeding grounds through the regulation of water levels and the use of chemoprevention in pregnancy (IPTp), perennial malaria (PMC) and seasonal malaria (SMC) (WHO, 2022).

The overarching aim of the WHO is to prevent the re-establishment of malaria in all those countries that have been declared malaria-free and reduce the global malaria burden by 90% by 2030 (Figure 1) (WHO, 2022).

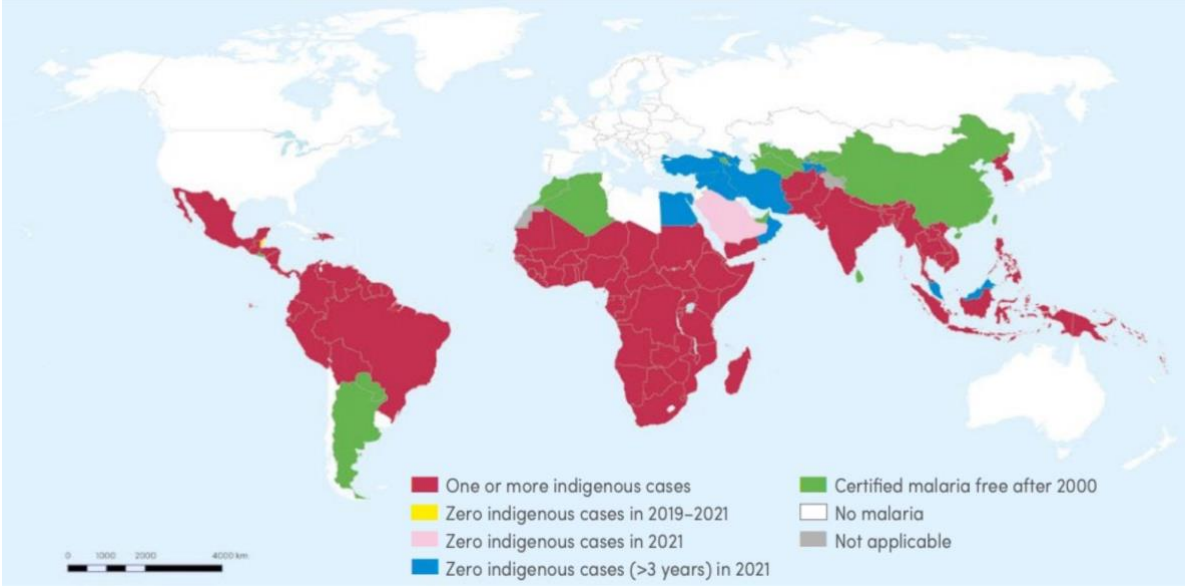

Figure 1. Global distribution of the indigenous cases of malaria. Countries with indigenous cases in 2000 and their status by 2021 (WHO, 2022).

1.1.2 Malaria Treatment

Despite the existence of parasites that currently display partial resistance to antimalarial drugs in Southeast Asia (Dondorp *et al.*, 2009; Ashley *et al.*, 2014) and some regions of East Africa (Uwimana *et al*., 2020; Balikagala *et al.*, 2021), a key component of the current malaria therapies are artemisinin derivatives (ART) in combination with other drugs, known as ART combination therapies (ACTs). These ACTs continue to be the most crucial first-line therapy for treating uncomplicated and severe malaria (Hanboonkunupakarn *et al*., 2022). Artemisinin possesses a potent antimalarial effect; however, it has a short half-life (<1h) (Tarning *et al*., 2012; Kloprogge *et al*., 2015). To overcome this limitation, ACTs are employed, which involve the use of a short half-life ART drug along with a longer half-life partner drug. This approach likely improves efficacy by eliminating parasite after the effect of ART drug has diminished. It also enhances clinical and parasitological cure rates while reducing selection for antimalarial resistance (Eastman & Fidock, 2009). Typically, these combinations involve artemisinin derivatives such as artemether, artesunate, and dihydroartemisinin (DHA), combined with piperaquine, mefloquine, or lumefantrine (Davis *et al.,* 2005). Currently, triple artemisinin-based combination

therapies (TACTs) are being tested in clinical trials. TACTs include a second slowly eliminated partner drug in addition to the standard ACT, and they have been found to be safe and well-tolerated (Hanboonkunupakarn *et al*., 2019).

Currently, there are strategies that have been implemented to address antimalarial drug resistance in Africa, consisting of four key pillars: (1) enhancing antimalarial drug surveillance for effectiveness and resistance, (2) optimizing diagnostic and therapeutic practices to reduce drug pressure proactively, (3) restricting the spread of antimalarial drug-resistant parasites in response to resistance and (4) promoting research and innovation to bolster existing tools and develop new solutions against resistance (WHO, 2022).

1.1.3 Vaccine Development

A notable challenge in the development of malaria vaccines is the limited commercial interest. This is primarily because the countries where malaria is most prevalent are among the poorest in the world, lacking in economic resources for vaccine acquisition (Carter *et al*., 2000). Some programs have proposed a strategy that combines prolonged artemisinin-based combination therapy (ACT) by mass drug administration (MDA) combined with a malaria vaccine to accelerate the elimination of the disease (Hanboonkunupakarn *et al*., 2022). Currently, some promising malaria vaccines are under development. They are categorized based on the developmental stages of the parasite they target (pre-erythrocyte and asexual stages in the human host and mosquito sexual stage (section 1.2.1)) (Duffy & Gorres, 2020).

1.1.3.1 Pre-erythrocyte vaccines

1.1.3.1.1 RTS, S and R21/Matrix-M vaccines

The only vaccine that has successfully passed a phase 3 trial is RTS,S/AS01, known as Mosquirix and developed by GlaxoSmithKline (GSK). This vaccine targets the pre-erythrocyte stage and has demonstrated approximately 46% of protection against malaria in children aged 5 to 17 months and 27% in infants aged 6 to 12-weeks (Moris *et al.*, 2018; RTS, S. Clinical Trials Partnership, 2015). RTS,S/AS01 is based on the presentation of epitopes of the major sporozoite surface protein, the circumsporozoite protein (CSP) to the immune system (Casares *et al*., 2010; Collins *et al.*, 2017; Draper *et al.*, 2018; Kurtovic *et al*., 2020). The next generation of this

vaccine, the R21/Matrix-M, has shown high efficacy and safety in phase II trials. It shares similarities with the RTS vaccine since both are based on a CSP-Hepatitis B surface antigen (HBsAg) fusion protein. While R21 contains only the CSP-HBsAg fusion protein, presenting CSP at a higher proportion on its particle surface (Collins *et al.*, 2021), RTS presents also unfused HBsAg at a rate 4-times higher than R21. As a result, a significant portion of the antibody response targets HBsAg and could potentially hinder the development of CSP-specific immunity (Collins *et al.*, 2017).

1.1.3.1.2 Whole sporozoite vaccines (WSV)-PfSPZ vaccines

The initial vaccine developed using *P. falciparum* sporozoites *(Pf*SPZ) technology was the Sanaria® PfSPZ. This involves the attenuation of *Pf*SPZ through radiation which early work had shown to be able to confer sterile protection (Nussenzweig *et al.,* 1967). These PfSPZ are extracted from the salivary glands of infected mosquitoes, purified, and cryopreserved in liquid nitrogen (Hoffman *et al*., 2010, Richie *et al.*, 2015). The PfSPZ vaccine has demonstrated a protection rate of over 90% against a homologous controlled human malaria infection (CHMI) delivered by mosquito bite or by injection (Seder *et al.*, 2013; Epstein *et al.*, 2017; Jongo *et al.*, 2020). Currently, three general classes of whole sporozoites vaccines (WSV) are under development: (i) Genetically attenuated sporozoites (GAS), (ii) sporozoite infection under chemoprophylaxis to remove blood stages (CPS), and (iii) sporozoites attenuated through radiation (RAS). These approaches do not result in an established blood stage infection: either they are arrested in the liver stage of development (GAS and RAS) or at the initial steps of the blood stage (CPS), which are eliminated by an antimalarial drug (Itsara *et al.*, 2018).

1.1.3.1.3 Blood-Stage Vaccines (BSVs)

Blood-Stage Vaccines (BSVs) can be divided into two categories: those that target the intracellular parasite stages and those that target the merozoite, preventing its invasion of new red blood cells (RBC) (Draper *et al*., 2018). Many of the candidate antigens targeted for blood stage vaccines are proteins present on merozoites, including merozoite surface proteins 1, 2, and 3 (MSP1, MSP2, and MSP3), the apical membrane antigen 1 (AMA1), and the erythrocyte binding antigen 175 (EBA175) (Cai *et al*., 2021). So far, clinical trials targeting these antigens (MSP1,

MSP2, MSP3, AMA1, and EBA 175) have demonstrated low efficiency (Sagara *et al*., 2009; Chitnis *et al.,* 2015; Payne *et al*., 2016; Salamanca *et al*., 2019). A recently unpublished study using MSP2 knockout lines revealed that antibodies against MSP2 had minimal impact for the direct inhibition of *P. falciparum* by serum from individuals immune to malaria (Henshall, 2021), highlighting some of the challenges of using merozoite surface proteins as vaccines. Recent preclinical studies based on the reticulocyte-binding protein homolog 5 (pfRH5) have shown to confer immunity and restrict parasitemia (Payne *et al*., 2017; Ndwiga *et al*., 2021). However, the new combined vaccine containing the antigens RH5.1-PfCyRPA-PfRipr does not show significant neutralizing activity or improvement in protective immunity compared to the RH5.1 antigen alone. (Healer *et al*., 2022). The prospects for obtaining an efficacious blood stage vaccine are therefore at present unclear.

1.1.3.1.4 Transmission-Blocking Vaccines

Malaria Transmission-Blocking Vaccines (TBVs) target surface antigens of infecting parasite stages, such as gametes (*Pf*s230, *Pfs*48/45) (van Dijk *et al*, 2001; Marin-Mogollon *et al.*, 2018; Singh *et al.*, 2019) or zygotes (*Pf*s25, *Pf*s28) (Sala *et al.*, 2018), to induce an immune response that produces antibodies. This response aims to disrupt parasite development in the midgut and halt the transmission of the parasite through the vector. TBVs are not designed to offer protection against contracting malaria but rather have the potential to prevent the spread of malaria within the community (Carter *et al*., 2000). During the subsequent blood meal, the parasite absorbs both the malaria parasite and the antibodies. This process effectively prevents the development of the parasites inside the mosquito. In this way, TBVs can effectively prevent the transmission and further dissemination of malaria (Carter & Chen, 1976; Duffy & Gorres, 2020).

1.2 The Life Cycle of Plasmodium falciparum

Parasites undergo a cyclical process, alternating between sexual development within the female *Anopheles* mosquito (referred to as the mosquito sexual stage (section 1.2.1)) and asexual replication within the human host. In the human host they initially replicate asexually in the liver (known as the liver stage/pre-erythrocyte stage (section 1.2.2)) and later in red blood cells (termed the asexual blood stage/erythrocyte stage (section 1.2.4)) (Figure 2).

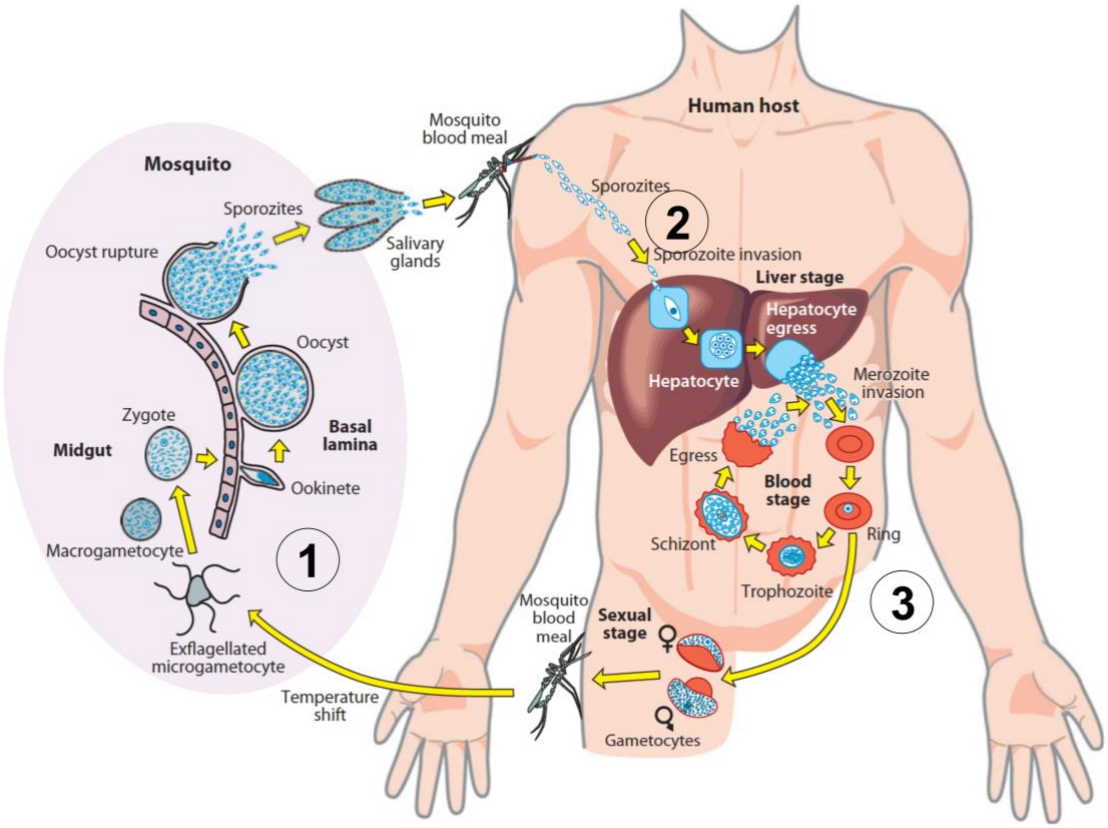

Figure 2. Overview of *Plasmodium* life cycle. The life cycle of *P. falciparum* consists of different development phases that can be classified into three main stages: (1) Sexual development in the *Anopheles* mosquito (mosquito stage) and two different phases of asexual development in the human host: (2) the liver stage and (3) the asexual blood stage (modified Boddey & Conwan, 2013).

1.2.1 Mosquito Sexual Stage

The female *Anopheles* mosquito acquires the transmissible sexual stage of the parasite when it ingests gametocytes during a blood meal of an infected human host (Figure 2). Inside the midgut of the mosquito, gametogenesis occurs, transforming the gametoyctes into macrogametes and microgametes. This is triggered by changes

in temperature, xanthurenic acid level, and an increase in pH (Billker *et al.,* 2004; Aly *et al*., 2009). Thereafter, the microgametes exflagellate and fuse with the macrogamete, leading to the formation of a diploid zygote (Billker *et al.,* 1997; Billker *et al.*, 1998). The fertilized female gametes develop to form a diploid zygote that undergoes structural changes in a meiotic division, transforming into an elongated motile ookinete capable of penetrating the mosquitoe's midgut epithelium and settling between the epithelial cells and the basal lamina (Kojin & Adelman*,* 2019). The ookinete matures into an immobile oocyst, initiating a process called sporogony, during which thousands of sporozoites are generated (Aly *et al*., 2009). Upon rupture of the oocyst wall, the sporozoites are released and can reach the acinar cells of the salivary glands of the mosquito where they undergo adaptations for long-term survival (Boyd *et al.*, 1936; Porter *et al.,* 1954*;* Sherman*,* 1998*;* Zhang *et al.*, 2008). Upon the next blood meal of the mosquito, the sporozoites can be transmitted to the next host (Frischknecht & Matuschewski, 2017*;* Vennugopal *et al.,* 2020; Briquet *et al.*, 2021) (Figure 2).

1.2.2 Liver/Pre-erythrocyte Stage

After the injection of fewer than a hundred sporozoites under the skin of the human host, some of these motile sporozoites reach a blood vessel, allowing them to travel through the blood to reach the liver. However, some sporozoites remain in the skin, while others migrate to the lymph nodes, where they are subsequently eliminated (de Niz *et al.*, 2017).

Once a sporozoite reaches the liver, it moves along the sinusoid and traverses resident Kupffer cells and stellate cells to arrive at its final destination, the hepatocytes (Prundêncio *et al.*, 2006). The attachment of sporozoites to hepatocytes is initiated by the interaction between the major sporozoite surface protein, the circumsporozoite protein (CSP), the thrombospondin-related anonymous protein (TRAP), and highly sulphated heparin-sulfate proteoglycans (HSPGs) (Matuschewski *et al.*, 2002a; Pinzon-Ortiz *et al*., 2001). These components play a central role in the activation of the sporozoite, transitioning them from a migratory state to an invasive one (Blackman & Bannister, 2001; Pinzon-Ortiz *et al*., 2001; Coppi *et al*., 2007). A putative phospholipase (PL), the UIS-encoded protein UIS10, present on the sporozoite surface, plays a role in tissue traversal by sporozoite before

hepatocyte invasion (Bhanot *et al.*, 2005). Upon invasion of the parasite into the hepatocyte, a vacuolar compartment is formed through the invagination of the host cell membrane. This compartment is known as the parasitophorous vacuole (PV) and is defined by the parasitophorous vacuole membrane (PVM) (section 1.3.5) (Mota *et al.,* 2001). The establishment of the PV involves the participation of the hepatocyte receptor EphA2 and sporozoite proteins *Pf*36 and *Pf*52 from the 6-cys family (Kaushansky *et al*., 2015). Within the liver cell, the parasites turn into trophozoites and start a process known as exoerythrocytic schizogony, during which daughter merozoites are generated (Striepen *et al.,* 2007; Francia & Stripen, 2014; Gubbels *et al.,* 2021). The liver-stage concludes when merozoites egress the host cell by the rupture of the PVM, enclosed in membranous sacs known as merosomes (Sturm *et al*., 2006). After the rupture of these merosomes in the lung capillaries, merozoites are released into the bloodstream, which marks the beginning of the asexual blood stage of the infection (Baer *et al.*, 2007).

1.2.3 Invasion

Free merozoites invade erythrocytes through a dynamic, fast, and coordinated process, that includes multiples steps: pre-invasion, reorientation, tight junction formation, active invasion, and formation of the PVM (Figure 3) (Cowman *et al.*, 2016). The pre-invasion process involves initial affinity interactions between proteins present on the surface of the merozoite and erythrocyte receptors (Weiss *et al.*, 2015). Merozoites surface protein 1 (MSP1) is required for the reversible attachment to the RBC (Holder *et al.*, 1994; Sanders *et al.*, 2005). Subsequently, the merozoite reorients its apical tip toward the RBC membrane, bringing into position the secretory organelles (micronemes, rhoptries and dense granules) required for invasion (section 1.3.1) (Figure 3A). During this process, the interaction between the merozoite and erythrocyte leads to erythrocyte deformation, driven by the actin motor of the parasite (Weiss *et al.*, 2015). This interaction involves two adhesin-ligand protein families: the erythrocyte binding antigens (EBAs), located in the micronemes, and reticulocyte-binding protein homologs (Rhs) in the rhoptries (Figure 3B) (O`Donnell *et al.*, 2000; Triglia *et al.*, 2001; Cowman *et al.,* 2012; Tham *et al.*, 2012). EBAs bind to erythrocyte glycophorin receptors in a sialic acid-dependent invasion pathway, with EBA-175 binding glycophorin A and triggering the release of proteins from the rhoptries. Calcineurin of the parasite is also involved in attachment of the merozoite, enhancing

the dimerization of EBAs and Rhs proteins. This dimerization is crucial for host-receptor interaction and the subsequent signal transduction required for the invasion process (Paul *et al.*, 2015; Cowman *et al.,* 2017).

Following deformation of the erythrocyte, Rh proteins initiate the irreversible downstream invasion event through the formation of a tight junction. This process involves the binding of Rh5 to the host cell receptor basigin, which is associated with a calcium spike within the RBC, in a sialic acid-independent pathway (Crosnier *et al.*, 2011; Tham *et al.*, 2012, Cowman *et al.,* 2016; Volz *et al.*, 2016; Wong *et al.,* 2018). Rh5 interacts with Rh5-interacting protein (RIPR) and cysteine-rich protective antigen (CyRPA) (Figure 3B) (Chen *et al.*, 2011; Scally *et al.*, 2022). The formation of a tight junction is primarily finalized when AMA1 interacts with the RON complex on the surface of the merozoite (Figure 3B). This parasite-derived complex consists of the proteins RON2, 4 and 5 and is deposited into the RBC, with RON2 extending across the host membrane and interacting with AMA1 on the surface of the merozoite (Besteiro *et al.*, 2011, Srinivasan *et al.,* 2011*; Tonkin et al.,* 2011*;* Srinivasan *et al.,* 2013). The entire active invasion process is driven by an action-myosin motor, during which the discharge of lipids from the rhoptries occurs concurrently, contributing to the formation of the PVM (Baum *et al.,* 2006; Riglar *et al.,* 2011; Weiss *et al,* 2016). Invasion concludes when membrane fusion takes places at the rear end of the merozoite, sealing the parasite within the PVM (section 1.3.5) (Figure 3B). (Weiss *et al*, 2015).

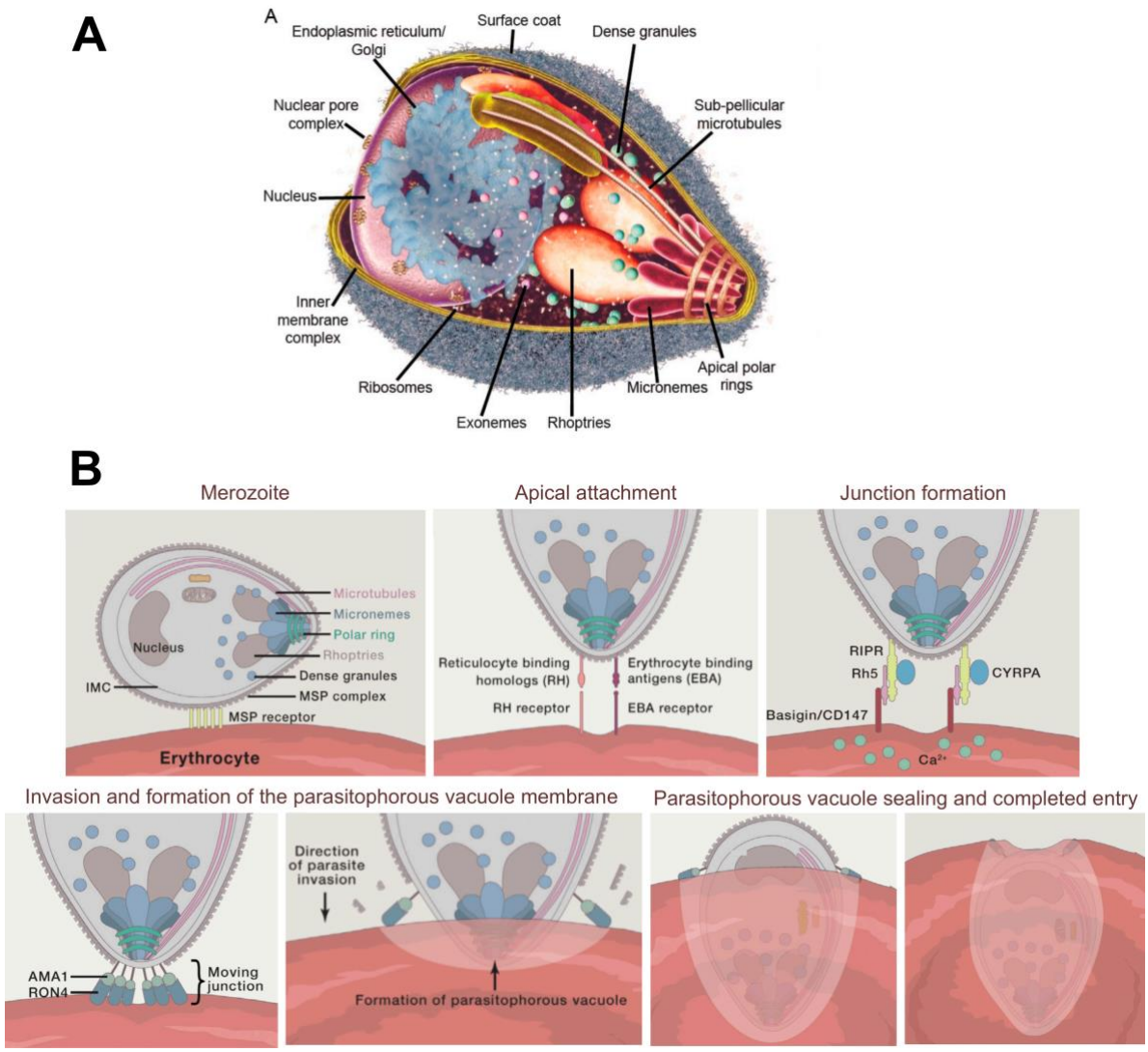

Figure 3. Merozoite Invasion of Erythrocytes. (A) Schematic representation of a *Plasmodium* merozoite highlighting secretory organelles and cellular structures vital for the invasion process (modified from Cowman *et al.*, 2012) (B) Series of schematic images showing the sequential stages of merozoite invasion into a red blood cell and formation and sealing of the PVM (modified from Cowman *et al.*, 2016).

1.2.4 Asexual Blood Stage

Within the RBC, the parasites undergo repetitive cycles of asexual replication (Figure 4). This process involves differentiation through three successive morphological stages (Bannister *et al.*, 2000). The initial stage of development, the ring stage (~0-18 hours post infection (hpi)) is characterized by the biconcave disc or cup shaped morphology of the parasite cell (Aikawa *et al.*, 1967; Langreth *et al.*, 1978; Grüring *et al*., 2011). In this stage, the highest peak of expression occurs for parasite proteins that are exported into the host cell (Marti *et al*., 2004). Subsequently, the parasite

develops into the second phase, the trophozoite stage (20-36 hpi), characterized by rapid parasite growth and the presence of hemozoin– a residual product from digested hemoglobin– in the food vacuole (FV) (section 1.3.4) (Grüring *et al.*, 2010). Finally, the parasite progresses into the schizont stage (36-48 hpi), initiating the process of schizogony, which involves repeated nuclear divisions, followed by cytokinesis, resulting in the formation of approximately 16-32 daughter cells, the merozoites. Following this process, the merozoites are released from the infected RBCs to invade new host RBCs. As a result of successive cycles of parasite invasion, replication, and growth, there is an exponential increase of parasite numbers, leading to the manifestation of various malaria-related pathologies in the infected patient (Figure 4) (Cowman *et al.*, 2016; White *et al*., 2014; Mattews *et al.*, 2018).

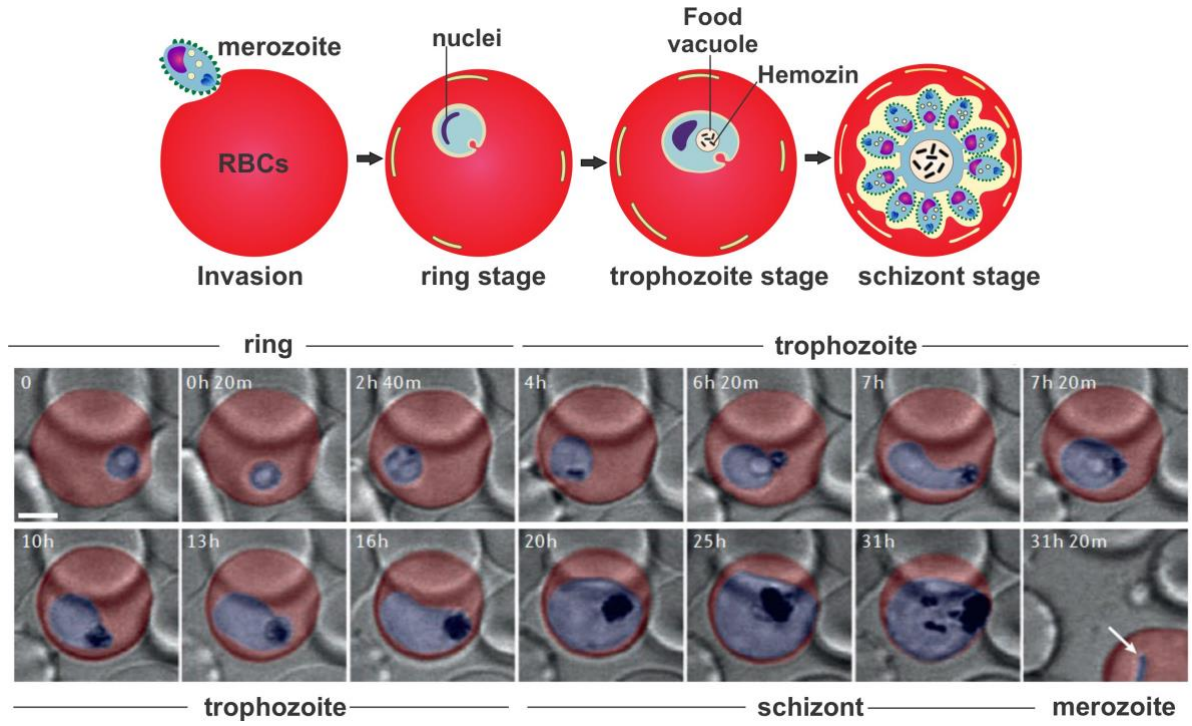

Figure 4. Asexual development of *P. falciparum* parasites in RBCs. (Upper panel): A graphic representation of the three main blood stages of development of the *P. falciparum* parasite; rings, trophozoites and schizonts. (Lower panel): Time-lapse imaging of the full erythrocytic cycle (note that the start is towards the end of the ring stage; time indicated is time in the experiment, not parasite age) of the *P. falciparum* parasite (blue) inside of red blood cells (red). In the final picture, the arrow points out a ring stage resulting from the reinvasion of a released merozoite (modified from De Niz *et al.*, 2017).

1.3 Fundamental Cell Biology of Malaria Parasites

Like most eukaryotes, *P. falciparum* parasites possess a nucleus, endoplasmic reticulum (ER), an unstacked Golgi apparatus and mitochondria (Van Dooren *et al.,* 2005; Struck *et al.*, 2005; Hallée *et al.*, 2018). Notably, peroxisomes, crucial for lipid metabolism and detoxification of reactive oxygen species in eukaryotes, are absent in *P. falciparum* (Gabaldón, 2010; Schlüter *et al*., 2006; Žárský & Tachezy, 2015). The challenges these parasites face during transmission between different hosts have driven the evolution of unique, specialized organelles, most of which are shared only with other apicomplexan parasites. This group of specialized organelles includes rhoptries, micronemes, dense granules (section 1.3.1), the inner membrane complex (IMC) (section 1.3.2), the apicoplast (section 1.3.3) and the food vacuole (section 1.3.4).

1.3.1 Apical Complex

Each merozoite is equipped with two rhoptries (Figure 3A), which play a crucial role for invasion, the formation of the PV, and modifications to the host cell. Rhoptries have a distinctive club-shaped structure (Figure 3A), divided into a bulb and a neck (François *et al*., 2017). The neck is located at the apical end of the merozoite (Hanssen *et al*., 2013), and during the invasion process fuses with the parasitic plasma membrane (PPM) to release numerous proteins that facilitate host cell entry (Weiss *et al*., 2015; Riglar *et al.,* 2011). Groups of proteins, such as armadillo repeats only (ARO) (Cabrera *et al*., 2012), ARO interacting protein (AIP) (Geiger *et al*., 2020), adenylate cyclase beta (ACß) (Patel *et al*., 2019), and rhoptry apical surface protein (RASP) (Liffner *et al*., 2020; Suarez *et al*., 2019), are known to be located on the cytoplasmic side of the rhoptry membrane. Rhoptries contain a repertoire of proteins ranging from soluble, transmembrane to GPI-anchored proteins.

A second class of specialised secretory organelles are the micronemes (Figure 3A). They are small, rod-shaped vesicles located at the apical pole of the parasite and are involved in the invasion of *P. falciparum* parasites into RBCs and for egress (Carruthers & Tomley, 2008). In sporozoites, characterized micronemal proteins include the circumsporozoite protein (CSP) and thrombospondin-related protein (TRAP), which are important for establishing attachment to the hepatocytes (section 1.2.2) (Blackman & Bannister, 2001; Pinzon-Ortiz *et al*., 2001; Matuschewski *et al*.,

2002a). Another crucial protein found in micronemes is AMA1, which is essential for the formation of a tight junction in the invasion process (section 1.2.3) (Besteiro *et al.*, 2011; Tonkin *et al.,* 2011; Srinivasan *et al.,* 2011*;* Srinivasan *et al.,* 2013).

Dense granules (Figure 3A) are small microspheres distributed throughout the cell and are involved in the maturation of the PV, rather than its initial formation (Lingelbach & Joiner, 1998; Iriko *et al*., 2018; Morita *et al*., 2018). Only a limited number of proteins have been identified within the dense granules such as the ring-infected erythrocyte surface antigen (RESA). During invasion RESA is delivered to the membrane of newly infected erythrocyte where it is positioned beneath the host cell membrane and contributes to stabilizing the infected cell by altering its membrane properties through interactions with its cytoskeleton (Brown *et al*., 1985; Pei *et al.,* 2007).

1.3.2 The Inner Membrane Complex

The inner membrane complex (IMC) is located beneath the parasite plasma membrane and is interconnected with the cytoskeleton (Figure 3A). This complex consists of a double lipid bilayer formed from a mosaic of flattened membranous vesicles (Morissette & Sibley, 2002; Dearnley *et al*., 2012; Kono *et al*., 2012). The IMC plays an essential role in several parasite-specific functions, primarily acting as an anchor for numerous glideosome proteins essential for actin-myosin motility. In this context, two gliding-associated proteins, GAP50 and GAP45, are responsible for anchoring MyoA to the IMC (Gaskins *et al*., 2004; Pazicky *et al*., 2020). In merozoites, this actin-myosin complex plays a crucial role in erythrocyte invasion (Harding & Meissner, 2014). Moreover, the IMC also acts as a scaffold during cytoplasm division, providing stability and shape to the cell and rigidity to new merozoites (Bergman *et al*., 2003; Keeley & Soldati, 2004; Baum *et al.,* 2006; Frénal *et al*., 2010; Kono *et al*., 2012; Ferreira *et al*., 2021; Elaagip *et al.,* 2022)

1.3.3 The Apicoplast

The apicoplast is surrounded by four membranes, and its origin can be traced back to the result of a secondary endosymbiosis (Köhler *et al.*, 1997). In the primary endosymbiotic event, the incorporation of a cyanobacterium into a eukaryotic cell gave rise to the modern chloroplast. In a subsequent secondary endosymbiotic episode, a photosynthetic red algal entity was engulfed by a protist, culminating in

the formation of a secondary plastid (Janouškovec *et al.*, 2010; Van Dooren & Striepen, 2013). Despite losing its photosynthetic function, the apicoplast plays a central role in cellular functions, such as the synthesis of fatty acids, iron-sulfur clusters, isoprenoids and heme (Ralph *et al*., 2004; Yeh & DeRisi, 2011; Van Dooren & Striepen, 2013; Swift *et al.*, 2021; Verhoef *et al.*, 2021; Elaagip *et al.,* 2022). The apicoplast cannot not be synthesized de novo and must be inherited. Consequently, the precise division of the apicoplast into multiple organelles, as well as their accurate segregation into the merozoites' daughter cells, are essential processes to ensure that each emerging parasite contains a single apicoplast (Elaagip *et al.,* 2022).

1.3.4 The Food Vacuole

The food vacuole (FV), also known as the digestive vacuole (DV), is a specialized lysosome-like compartment (Figure 4). It serves as the primary site for the degradation of hemoglobin taken up from the host RBC, which blood stage parasites consume in substantial quantities during their development (Francis *et al*., 1997; Vander Jagt *et al*., 1986). While host cell cytosol uptake commences already in early ring stages (Birnbaum *et al*., 2020), the food vacuole only becomes visible in the late ring phase of the parasite (Dluzewski *et al*., 2008; Abu Bakar *et al*., 2010). This organelle, which maintains an acidic environment, processes approximately 60-80% of the hemoglobin of the infected erythrocyte in the DV. This digestion process is organized and involves a series of proteolytic events. Plasmepsins (aspartic proteases) and falcipains (cysteine proteases) cleave the large subunits of hemoglobin, resulting in smaller polypeptides that are more easily digested by other enzymes within the food vacuole (Wunderlich *et al.*, 2012). The uptake and digestion of hemoglobin regulates osmotic pressure, provides a pool of amino acids and physical space for the growth of the parasite in the RBC (Liu *et al.,* 2006*;* Hanssen *et al*., 2012). During the digestion process, significant quantities of toxic free heme are generated. Without proper detoxification, this could lead to the death of the parasite. To counteract this toxicity, through mechanisms that are still poor understood, the parasite transforms heme into inert crystals known as hemozoin (Hz), which accumulate within the food vacuole and appear as brown crystals also known as “malaria pigment” (Figure 4) (Egan, 2008; Chugh *et al.*, 2013; de Villiers & Egan, 2021; Kapishnikov *et al.*, 2021).

1.3.5 The parasitophorous vacuole (PV) and its membrane (PVM)

Once the merozoite has fully entered the RBC, the PVM seals at the apical end, forming a new intraerythrocytic compartment known as the parasitophorous vacuole (PV). Thus, the parasite resides in the PV lumen (Figure 5). This compartment constitutes the principal barrier between the parasite and the host cell (Lingelbach & Joiner, 1998) and is surrounded by two membranes –the parasite plasma membrane (PPM) and the PVM– which are an estimated 50 nm apart (Trelka *et al*., 2000; Koch & Baum, 2016). The intracellular parasite develops in the PV throughout the entire blood cycle until it generated progeny that egress into the bloodstream following the destruction of the host cell (Matz *et al*., 2020). The PV mediates critical functions for parasite survival, including the facilitation of nutrient uptake from the host cell plasma and the management of waste product disposal (Spielmann *et al*., 2012; Sherling & van Ooji, 2016; Goldberg & Zimmerberg, 2020). Additionally, to enable the survival, growth, and replication of the parasite within the host RBC, many parasite proteins are transported into the PV before being translocated into the host cytoplasm via the PVM (Kirk & Lehane, 2014; Cowman *et al*., 2017). The PVM establishes a complex and interconnected system. Membranous extensions from the PVM give rise to the tubovesicular network (TVN) (Figure 5) (Behari & Haldar, 1994; Elmendorf & Haldar, 1994; Haldar, 1998). This network extends into the host cell, and was proposed to support the uptake of nutrients, lipids and raft proteins from the host cell membrane. This process has been observed in RBCs during the transition from the ring to trophozoite stage (Lauer *et al.,* 1997; Lauer *et al.,* 2000; Tamez *et al.*, 2008).It has been suggested that TVN could contribute to the formation of extended parasite-derived membranous structures known as Maurer's clefts (MCs) (section 1.3.7) (Wickert *et al*., 2004; Spycher *et al*., 2006; Goldberg & Cowman, 2010), although later work showed that the full number of MCs is present as soon as markers render them detectable shortly after invasion, indicating that this idea of MC formation is unlikely or it occurs within the first 90 minutes after invasion (Grüring *et al*., 2011). An origin of the MC from the PVM would, however, be congruent with the observations that saponin, a reagent known for permeabilizing the PVM, can also disrupt the MCs (Spielmann *et al*., 2006b). The MCs, along with the TVN, constitute the exomembranous system established by the parasite during RBC infection (Figure 5).

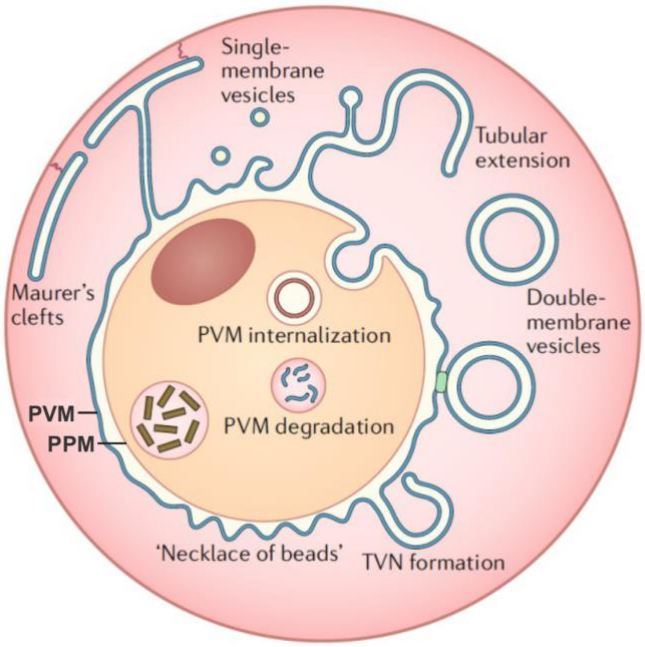

Figure 5. The parasitophorous vacuole and its membrane. (A). Schematic representation highlighting structures that have been reported in the host cell that may be connected to the PVM, including the TVN, as well as single and double membrane vesicles. A hypothetical model for the generation of the MCs from the PVM is also shown. Brown rectangles represent hemozoin formation resulting from the degradation of the PVM during hemoglobin digestion (modified from Matz *et al*, 2020).

1.3.5.1 PVM proteins in asexual blood stages

To date, only a limited number of proteins associated with the PVM have been identified (Spielmann *et al.*, 2012; Nyboer *et al.*, 2017). These include: the Exported Protein 1 (EXP1) (section 1.3.5.1.1) (Simmons & Woollett, 1987; Ansorge *et al*., 1997; Sanchez *et al*., 1994), the Early-Transcribed Membrane Proteins (ETRAMPs) (section 1.3.5.1.2) (Spielmann *et al*., 2003), and the components of the *Plasmodium* Translocon of Exported Proteins (PTEX) (section 1.3.6.1.2) (de Koning-Ward *et al*., 2009). Recent study identified new PVM proteins in asexual blood stages of *P. falciparum* (Khosh-Naucke *et al*., 2018) and *P. berghei* blood and liver stages (Schnider *et al*., 2018). However, the function of most of these remain elusive. The newly discovered proteins in *P. falciparum* include a putative alkaline phosphatase (PF3D7_0912400), a conserved *Plasmodium* protein of unknown function (PF3D7_1024800) that both contain a single transmembrane domain, and a protein

named UIS2 (PF3D7_1464600), named UIS2, a unique serine/threonine phosphatase (Khosh-Naucke *et al*., 2018) and is the topic of this thesis (section 1.6).

1.3.5.1.1 Exported protein 1 (EXP1)

EXP1, a protein with a single transmembrane domain, was identified as the first PVM proteins (Simmons & Woollett, 1987; Kara *et al*., 1988). EXP1 forms oligomeric arrays in the PVM with the C-terminus facing the RBC cytosol and the N-terminus oriented towards the PV lumen (Simmons & Woollett, 1987; Ansorge *et al*., 1997; Spielmann *et al*., 2006; Spielmann *et al*., 2012). The insertion of EXP1 into the PVM occurs independently of protein folding and PTEX (section 1.3.6.1.2) (Tribensky *et al*., 2017). EXP1 is essential for parasite development in RBCs (Maier *et al.*, 2008; Mésen-Ramírez *et al*., 2019). Patch clamp experiments showed that parasites lacking EXP1 are devoid of the PVM nutrient permeable channel (NPC) function and parasites with reduced EXP1 levels exhibit heightened sensitivity to nutrient deprivation, indicating that EXP1 is needed for nutrient uptake (Mésen-Ramírez *et al*., 2019). A recent study, using mutants of EXP1 demonstrated the function of the NPCs in the acquisition of small molecules across the PVM in ART-resistant parasites. The resistants are hyper-sensitive to growth under low amino acids and had increased EXP1 expression levels, presumably to compensate for the fitness cost of resistance (due to the reduced supply of hemoglobin-derived amino acids, Birnbaum *et al.*, 2020) (Mésen-Ramírez *et al*., 2021). These findings indicate that the reduction of hemoglobin uptake in these parasites triggers compensatory adaptations for their survival and supports that EXP1 plays a crucial role in nutrient uptake (Mésen-Ramírez *et al*., 2021).

EXP1 depletion disrupts the proper distribution of exported protein 2 (EXP2), a further protein of the PVM (Nessel *et al.,* 2020). EXP2 serves a dual role, acting as both a pore-forming protein essential for NPCA and facilitating protein export from the PV lumen to the cytoplasm of the host cell via PTEX (Mésen-Ramírez *et al*, 2016; Mésen-Ramírez *et al*., 2019). The EXP2 pore permits the diffusion of solutes up to 1.400 kD between the PV lumen and the host cell cytoplasm (Desai *et al*., 1993; Desai & Rosenberg, 1997; Garten *et al*., 2018). Interestingly, EXP1 loss affects only the NPC activity but not protein export through PTEX, whereas EXP2-loss affects both (Mésen-Ramírez *et al*., 2019; Nessel *et al.*, 2020; Garten *et al*., 2018).

1.3.5.1.2 Early-transcribed membrane proteins (ETRAMPs)

Early-transcribed membrane proteins (ETRAMPs) constitute a family of small, highly charged integral membrane proteins located at the PVM that in *P. falciparum* comprise 14 proteins. They share a similar organization with EXP1 and constitute a group of genes with high expression during the blood stage of *P. falciparum* parasites, with domains extending into the PV (Spielmann *et al*., 2000; Spielmann *et al*., 2003; Spielmann *et al.*, 2006a; Mackellar *et al.*, 2011). Several ETRAMPs exhibit distinct stage-specific expression patterns. During the ring stage, an initial group of six ETRAMPs is expressed, including ETRAMPs 2, 10.1, 11.1, 11.2, 12, and 14. These are subsequently replaced by different ETRAMPs during the transition from the ring to the trophozoite stage, such as ETRAMPs 4 and 10.2. ETRAMP 4 is also expressed during the transition from the trophozoite to schizont stage (Spielmann *et al*., 2003). To date, there is a lack of concrete functional data to determine the exact role of ETRAMPs in *P. falciparum*. Nevertheless, ETRAMPs might contribute to PVM organization or transport (Spielmann *et al*., 2006a; Currà *et al*., 2012; Spielmann *et al*., 2012; Beck *et al.*, 2021). In rodent malaria species, P*. yoelli and P. berghei*, proteins upregulated in infective sporozoites 3 and 4 (UIS3, UIS4) which are orthologues of ETRAMP13 and 10.3 in *P. falciparum,* respectively, were identified as crucial members of the ETRAMP family. UIS3 and UIS4 localize to the secretory organelles of sporozoites and the PVM during the liver stage where they have an essential function and knock outs were used to generate the first experimental GAS (Kaiser *et al*., 2004; Matuschewski *et al*., 2002b; Mueller *et al*., 2005).

1.3.6 Protein Export

Protein export is a crucial mechanism for trafficking proteins beyond the PV compartment, facilitating essential modifications in the host erythrocyte to ensure parasite survival and virulence (Boddey *et al.*, 2013; Spillman *et al.*, 2015). Proteins destined for the PV and beyond follow a canonical secretory pathway via an N-terminal signal peptide (SP) or transmembrane domain (TM). This process involves several steps, including protein synthesis, translocation into the parasite endoplasmic reticulum (ER), cleavage of the SP, transport through the Golgi apparatus and trafficking to the PPM (transmembrane proteins) or delivery into the PV (soluble proteins) (Marti & Spielmann, 2013). Trafficking across the PVM to reach their final destination in the erythrocyte cytosol is then mediated by the plasmodium translocon

of exported protein PTEX (de Koning-Ward *et al*., 2009; Beck *et al.*, 2014; Elsworth *et al.*, 2014; Spillman *et al*., 2015; Mésen-Ramírez *et al.*, 2016; Ho *et al*., 2018).

1.3.6.1.1 PEXEL proteins and PNEPs

Most exported proteins contain a *Plasmodium* Export Element (PEXEL) with the consensus sequence RxLxE/Q/D, which is located 20-30 amino acids downstream of the signal peptide (Martin *et al.*, 2004; Hiller *et al.*, 2004). PEXEL containing proteins enter the ER through a translocation complex composed of SEC61 and SPC25 (Marapana *et al.*, 2018). The PEXEL motif is proteolytically cleaved between the third and fourth residues by the aspartyl protease, plasmepsin V (PMV), presumably co-translationally (Chang *et al.*, 2008; Russo *et al.*, 2010; Boddey *et al.*, 2010; Boddey *et al*., 2016) and the newly exposed N-terminal residue undergoes acetylation (Chang *et al*., 2008; Boddey *et al*., 2009; Marapana *et al*, 2018).

Furthermore, PEXEL processing is not an absolute prerequisite for translocation into the host cell, as evidenced by several PEXEL-negative exported proteins (PNEPs) such as the skeleton binding protein-1 (SBP1), the membrane-associated histidine-rich protein 1 (MAHRP1), the membrane-associated histidine-rich protein 2 (MAHRP2), the ring exported protein 1 (REX1), and the ring exported protein 2 (REX2) (Spielmann & Gilberger, 2010). These proteins have an SP or a TM domain either of which can mediate entry into the ER (Heiber *et al*, 2013; Spielmann & Gilberger, 2010) independently of SPC25 (Marapana *et al.*, 2018). Despite these differences, both PEXEL-positive and PEXEL-negative proteins carry the necessary functional information for export in their mature N-terminal ends (Grüring *et al*., 2012) and pass through PTEX to reach their destination in the host cell (Beck *et al*., 2014; Elsworth *et al*., 2014; Mesen-Ramirez *et al*., 2016; Boddey *et al*., 2009; Boddey & Cowman, 2013). In contrast, proteins lacking other trafficking signals are secreted into the PV lumen by default but not transported across the PVM. Interestingly, recent studies have revealed a non-exported protein, with a PEXEL motif, attached to the inner face of the PVM (van Ooji *et al*., 2013; Hi *et al.,* 2016; Khosh-Naucke *et al.*, 2018; Schnider *et al.*, 2018; Fierro *et al.*, 2023).

1.3.6.1.2 PVM translocation

PTEX is an essential protein complex of the PVM responsible for transporting effector proteins across the PVM into the host cell cytoplasm (de Koning-Ward *et al*., 2009; Beck *et al*., 2014; Elsworth *et al.,* 2014). PTEX consists of three main components: a hexamer of heat shock protein 101 (HSP101), a heptamer of exported protein 2 (EXP2) and the heptamer of PTEX150 (de Koning-Ward *et al*., 2009, Ho *et al*., 2018) (Figure 6). HSP101, an AAA+ ATPase chaperone, functions as the PTEX motor, utilizing energy derived from ATP hydrolysis to unfold exported cargo and facilitate their translocation through an oligomeric transmembrane pore formed by EXP2 (de Koning-Ward *et al*., 2009; Bullen *et al*., 2012; Beck *et al.*, 2014; Ho *et al.*, 2018). The unfolded cargo is protected by a flange-shaped structure formed by PTEX150, which serves a structural role in connecting HSP101 to EXP2 (de Koning-Ward *et al*., 2009; El Bakkouri *et al*., 2010; Beck *et al.*, 2014; Elsworth *et al.*, 2014; Bullen *et al.*, 2012; Ho *et al.*, 2018). Conditional inactivation of any of these core components, HSP101, EXP2, or PTEX150, leads in the inhibition of protein export across the PVM (Beck *et al.*, 2014; Elsworth *et al.*, 2014; Garten *et al.*, 2018). The inactivation of HSP101 did not impair nutrient uptake, supporting the idea that the dual function in NPC and PTEX is restricted to EXP2 (Garten *et al.*, 2018). In the Apicomplexan *T. gondii*, the orthologs of EXP2, the dense granule proteins GRA17 and GRA23, serve as pores for the transport of small molecules between the host cell and the PV. In a complementation assay, EXP2 from *P. falciparum* was able to rescue the function of GRA17, suggesting conservation of the NPC function between these two parasites (Gold *et al.*, 2015).

In addition to the 3 core PTEX components, two accessory proteins were also identified (de Koning-Ward *et al*., 2009). One of these is thioredoxin 2 (TRX2), which likely assists in disulfide bond dependent folding (Figure 6) to facilitate the unfolding of exported cargo, enabling their passage through PTEX (Sharma *et al.,* 2011; Matthews *et al.*, 2013; Elsworth *et al.*, 2014; Peng *et al.*, 2015). For the other accessory protein, PTEXT88, recent studies indicated highly dynamic interactions with chaperones, potentially contributing to the delivery of specific cargo to HSP101 (Figure 6) (Chisholm *et al.,* 2018; Matthews *et al.*, 2019).

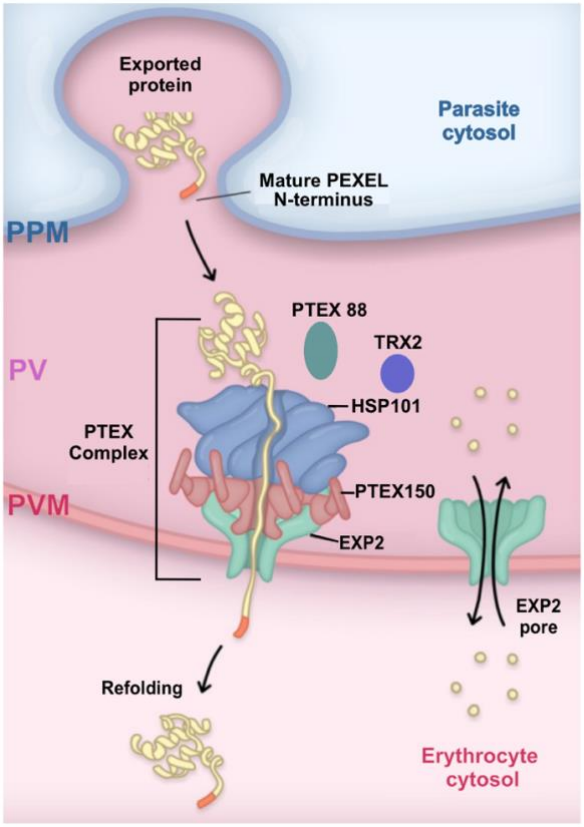

Figure 6. Plasmodium Translocon of Exported Proteins (PTEX). Scheme illustrating the structural organization of the PVM translocon. The core PTEX complex comprises three key components: an AAA+ ATPase heat shock protein 101 (HSP101), the exported protein 2 (EXP2), and PTEX150 and, two accessory proteins, PTEX88 and thioredoxin 2 (TRX2). EXP2 serves a dual function by acting as part of PTEX and as nutrient pore. Exported proteins are released into the PV lumen through vesicles and undergo translocation via PTEX complex and subsequent refolding in the erythrocyte cytosol (modified from Beck & Ho, 2021).

1.3.7 Remodeling of the infected red blood cell

Most exported proteins are synthesized shortly after invasion into erythrocytes during the ring stage of parasite development (Marti *et al*., 2004). These proteins modify the RBC to assist the parasite in obtaining nutrients and avoiding splenic clearance and the immune response of the host (Jonsdottir *et al.*, 2021). Once these proteins are inside the host cell cytoplasm, many reach membranous structures located beneath the RBC membrane, known as Maurer's clefts (MCs) (Maurer, 1902; Maier *et al.*, 2009; Grüning *et al.*, 2011). These structures are mobile during the ring stage, but their mobility diminishes during the transition to the trophozoite stage (Grüring *et al*., 2011), and they become tethered to the cytoskeleton of the host cell by so called

tethers (Pachlatko *et al*., 2010; Hanssen *et al*., 2010) or via host cell actin (Cyrklaff et *al.,* 2011; Kilian *et al.,* 2013). MCs are believed to serve as an intermediate platform, facilitating the transport and sorting of exported effector proteins between the parasite and the plasma membrane of the erythrocyte (Lanzer *et al.*, 2006; Mundwiler-Pachlatko & Beck, 2013). There are many known MC resident proteins (Takano *et al.,* 2019), examples of include REX1 (Hawthorne *et al.*, 2004), REX2 (Spielmann *et al.*, 2006a), MAHRP1 (Spycher *et al.*, 2003), the *Pf*EMP1-trafficking protein 1 (PTP1) (Maier *et al.,* 2008; Rug *et al.,* 2016), the *Plasmodium*-infected erythrocyte surface protein 2 (PIESP2) (Vincensini *et al.,* 2005), the merozoite surface-related protein-6 (MSRP6) (Heiber *et al.*, 2013), the *P*. *falciparum* EMP1 trafficking protein-7 (PTP7) (Carmo *et al.,* 2022) and the serine/threonine protein kinase 4 (FIKK 4.1) (Davies *et al*., 2020). Many of these are important for the transport of the major virulence factor erythrocyte membrane protein 1 (*Pf*EMP1). *Pf*EMP1 is pivotal for cytoadherence and serves as the primary parasite virulence protein in *P. falciparum* (Knuepfer *et al*., 2005; McHugh *et al.*, 2015).

Another crucial exported protein is the knob-associated histidine-rich protein (KAHRP), which plays a significant role in one of the most prominent host modifications: the formation of protrusions on the surface of the host erythrocyte membrane known as 'knobs' which are present in the trophozoite stage (Wickham *et al*., 2001; Rug *et al*., 2016). These protrusions are needed for *Pf*EMP1 to mediate its cytoadherence under flow conditions and hence likely serves a function in mediating proper display of the surface antigen *Pf*EMP1 (Crabb *et al*., 1997). Another critical host cell modification is the establishment of new permeability pathways (NPP) at the RBC membrane to facilitate acquisition of metabolites such as for instance purines and amino acids from the blood plasma (Ginsburg *et al*., 1987; Baumeister *et al*., 2006). One of these pathways is the Plasmodium Surface Anion Channel (PSAC) on the RBC membrane, serving as a passive conduit for nutrient import and contributing to waste disposal. This function depends on the cytoadherence-linked asexual protein 3 (CLAG3) (Nguitragool *et al*., 2011; Desai, 2012; Gupta *et al*., 2018; Desai, 2022). CLAG3 is packaged into the rhoptries and secreted into the host erythrocyte upon invasion (Vincensini *et al*., 2008). It is currently disputed whether its trafficking to the host cell depends on PTEX or not (Beck *et al.*, 2014; Ito *et al*., 2017). The conserved rhoptry proteins RhopH2 and RhopH3 are also essential for PSAC activity

(Kaneko *et al.*, 2005; Ito *et al.*, 2017; Sherling *et al.*, 2017; Counihan *et al.*, 2017) and a complex involving these proteins has recently been solved (Schureck *et al.,* 2021; Ho *et al*., 2018).

While both the RBC membrane NPP and the PVM NPC are thought to play a role in facilitating waste secretion, this has not been thoroughly explored (Kirk & Saliba, 2007; Garten *et al*, 2020). The *P. falciparum* Formate-Nitrite Transporter (*Pf*FNT) located at the PPM with domains extending into the PV, plays a vital role in the energy metabolism of the parasite. FNT facilitates the release of formate and lactate across the PPM, which are byproducts of glucose uptake by the parasite from the host cell cytoplasm (Marchetti *et al*., 2015; Wu *et al*., 2015; Rajendran *et al.,* 2017).

1.3.8 Egress of asexual blood stage parasites

The asexual development in the RBC culminates in the generation of new daughter merozoites which are released in a highly coordinated process known as host cell egress. Egress is independent of the actin-myosin motor complex (Das *et al.*, 2017; Perrin *et al.*, 2018) and involves changes in membrane permeability, cytoskeletal alterations, and rupture of the RBC membrane (Figure 7A), leading up to the actual release of the merozoites in a very rapid event (Abkarian *et al*., 2011). The cGMP-dependent protein kinase (PKG) plays a crucial role in activating proteases and other effector proteins to prepare the infected cell for merozoite release. PKG acts together with calcium-dependent parasite kinase 5 (CDPK5), which facilitates apical organelle secretion (Dvorin *et al*., 2010; Absalon *et al*., 2018). The permeabilization of the PVM occurs before PKG triggers the rupture of the PVM (Hale *et al*., 2017). The use of PKG inhibitors prevent the release of a serine protease known as SUB1 into the PV lumen (Taylor *et al.*, 2010; Collins *et al.*, 2013; Thomas *et al.,* 2018). SUB1 is secreted from a subset of secretory organelles termed exonemes into the PV, initiating a proteolytic signaling pathway by activating and cleaving effector components that are crucial for parasite egress (Yeoh *et al.,* 2007; Koussis *et al*., 2009; Silmon de Monerri *et al.,* 2011; Das *et al.,* 2015). SUB1 substrates include members of the serine-rich antigen family (SERA) family as well as merozoites surface protein 1 (MSP1), which lead to the subsequent disruption of the PVM and the RBC membrane. SERA 6 is involved in the disassembly of the RBC cytoskeleton by cleaving β-spectrin (Ruecker *et al.,* 2012; Thomas *et al*., 2018), while MSP1 binds to spectrin, enabling the egress

of merozoites from the RBC membrane (Koussis *et al*., 2009; Das *et al.,* 2015). Recent research has revealed that perforin-like proteins, specifically lecithin:cholesterol acyltransferase (LCAT), play a role in facilitating efficient parasite egress. A conditional deletion of LCAT resulted in abnormal egress of the parasite from RBCs and a reduction in parasite multiplication rate (Ramaprasad *et al*., 2023) (Figure 7).

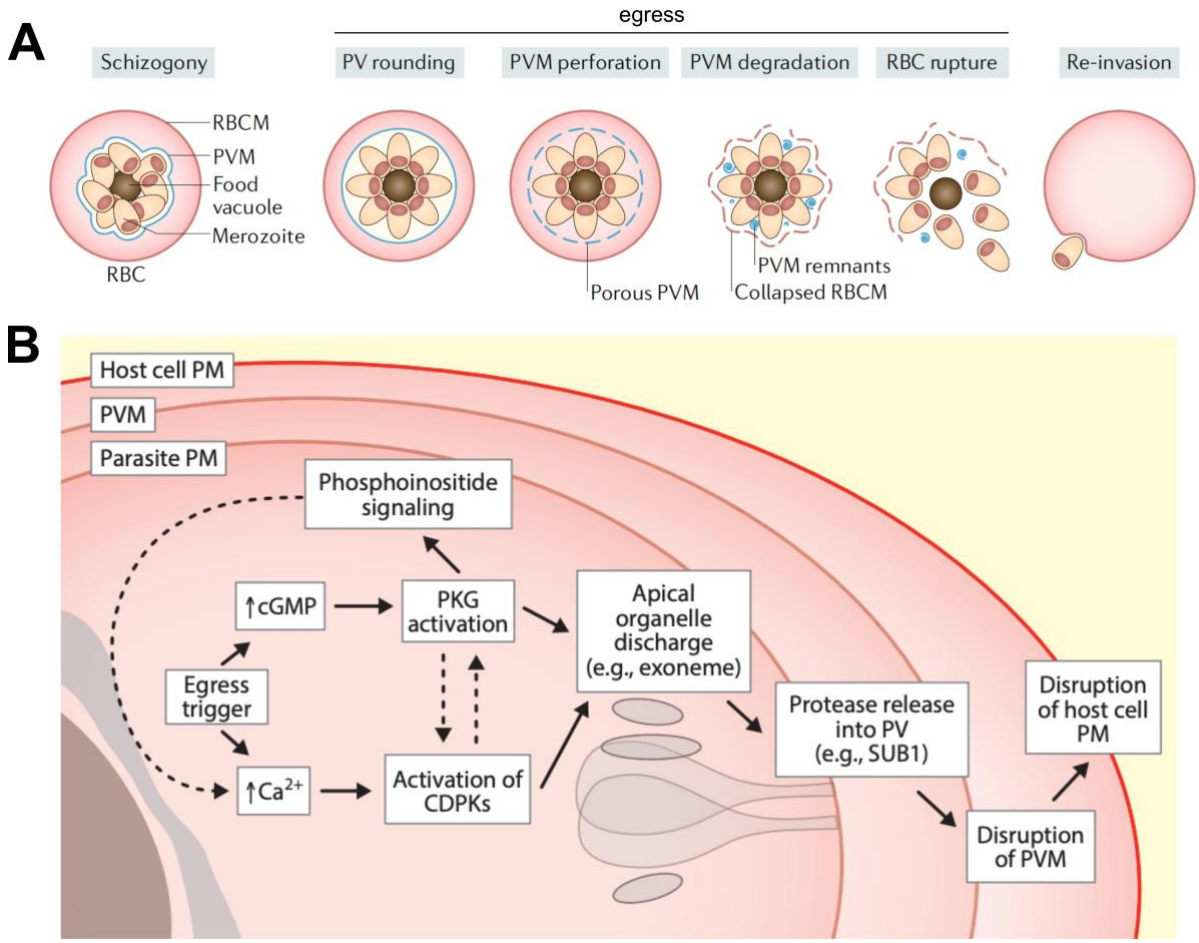

Figure 7. Egress of the Asexual Blood Stage in *P. falciparum*. (A) Morphological changes in the infected RBC during egress. Specific morphological changes of the PVM during parasite egress. The mature segmented schizont permeabilizes the PVM, causing it to divide into multilamellar vesicles. The cytoskeleton disassembles, increasing the porosity of the RBC membrane, resulting in its rupture, the release of merozoites, and the initiation of the re-invasion process (modified from Matz *et al.*, 2020). (B) Schematic representation showing the cascade of signal activation required for the parasite to egress the host RBC (modified from Dvorin & Goldberg, 2022).

1.4 Proteome of the PV/PVM

Despite the available information on PV proteins, the identification of novel PVM proteins beyond the established EXP1, ETRAMPs, and PTEX components has proven to be challenging and continues to be an intriguing field in parasite cell biology (Spielmann *et al.*, 2012; Nyboer *et al.*, 2017). This limitation arises from difficulties in isolating the PVM from other membranes, such as the PPM (Schnider *et al.*, 2018). Nevertheless, several studies have provided valuable insights into the proteins associated with the PV/PVM. In an initial proteomic investigation aimed at identifying PV proteins, infected erythrocytes were differentially permeabilized and the soluble proteins released from the PV labelled with sulfo NHS-LC-biotin (Nyalwidhe & Lingelbach, 2006). Through mass spectrometry, this approach successfully identified a range of proteins categorized into classes such as chaperones, proteins involved in nutrient acquisition and parasite egress proteins. Nevertheless, this method failed to detect highly expressed well-known PV proteins (Nyalwidhe & Lingelbach, 2006). Recent studies in both *P. falciparum* and *P. berghei* adopted the proximity-dependent biotinylation method called BioID to find PV proteins. This approach involves the use of the promiscuous biotin ligase BirA*, which can be fused to a protein of interest and, upon addition of biotin, leads to the biotinylation of proximal and potentially interacting proteins (Roux *et al*., 2012; Kimmel *et al*., 2022. In these studies, the PF3D7_0830400 signal peptide (SP) (Khosh-Naucke *et al*., 2018) and EXP1 (Schneider *et al*., 2018) were N-terminally fused to BirA*. Subsequent purification and mass spectrometry analysis using this approach identified novel PV and PVM proteins. Notably, among these proteins, the serine/threonine phosphatase UIS2, the topic of this thesis, was discovered to be a protein associated with the PVM (section 1.6) (Khosh-Naucke, 2018; Khosh-Naucke *et al*., 2018). Moreover, another study, employing an *in-silico* approach and subsequent experimental validation, lead to the discovery of additional PV proteins (Matz *et al*., 2018). All these findings contributed to an improve understanding of the proteomic composition of the PV and PVM in *P. falciparum* but the function of many of the identified proteins remain unknown.

1.5 Characterization of the Serine/Threonine phosphatases in *Plasmodium falciparum*

Based on current knowledge, the *P. falciparum* genome encodes approximately 85 protein kinases and 27 protein phosphatases, presenting one of the smallest kinome/phosphatome among eukaryotes (Wilkes & Doerig, 2008). In a recent study, 6 new phosphatases were identified using bioinformatic algorithms and protein structure comparison (similarities in domains) (Behrens & Spielman, 2023). Protein kinases are responsible for phosphorylation which involves the formation of a covalent bond between a protein substrate and a phosphate group (Krebs *et al.,* 1983; Skamnaki *et al.*, 1999). These proteins can catalyze the phosphorylation of serine (Ser), threonine (Thr), tyrosine (Tyr) and histidine (His) residues (Huang *et al*., 2018). This modification can rapidly alter protein activity through one of two primary mechanisms: (1) allostery, where phosphorylation within the activation loop of the catalytic domain - or in regions flanking the phosphorylated domain - causes conformational changes or (2) inducible binding of interaction domains to phosphorylated residues, resulting in a phosphorylation-dependent phospho-protein-protein interaction (Huse & Kuriyan, 2002; Hubbard, 2004; Jin *et al.*, 2012). Phosphatases are responsible for reversing the reaction catalyzed by protein kinases through dephosphorylation (Krebs *et al,* 1983; Barford, 1998). Protein kinases and phosphatases act as molecular switches, playing a crucial role in regulating essential cellular pathways and processes (Zhang, 2002). Phosphatases and kinases can undergo transient modifications, enabling them to transition between two conformations, one associated with an active state (on) and another with an inactive state (off) (Hunter, 1995). The catalytic domain of protein kinases derives from a single structural fold (Manning *et al.,* 2002), whereas the catalytic domain of protein phosphatases differ in structural fold and catalytic mechanism (Andersen *et al,* 2001; Shi *et al.,* 2009). *P. falciparum* possess 13 serine/threonine phosphatases, which can be categorized into three superfamilies, the PPP-like group (phospho-protein phosphatase) (section 1.5.1.1), PPM/PP2C (Mn2+/Mg2+ metal dependent protein phosphatase) (section 1.5.1.2) and HAD (haloacid dehydrogenase) (section 1.5.1.3) (Kutuzov & Andreeva, 2008; Moorhead *et al.*, 2009; Wilkes & Doering, 2008).

1.5.1.1 The PPP-like superfamily

The members of the PPPL family constitute one of the most conserved groups of phosphatases in eukaryotes in general and Apicomplexa specifically. This superfamily can be classified into two families: (1) phospho-protein phosphatase (PPP) (section 1.5.2.1.1) and (2) purple acid phosphatase (PAP) (section 1.5.2.1.2) (Cohen, 1997). The catalytic subunits of these phosphatases have the potential to interact with numerous protein partners, thereby regulating their localization and activity (Yang *et al.*, 2017; Fréville *et al.*, 2022). The PPP family comprises seven subfamilies: PP1, PP2A, PP2B or PP3, PP4, PP5, PP6, and PP7 (Barton *et al.*, 1994; Andreeva & Kutuzov, 2001; Gallego & Virshup, 2005) and protein phosphatase containing Kelch-like domains (PPKL) and Shewanella-like protein phosphatase (SHLP), of which the apicomplexan parasites *P. falciparum* and *T. gondii* possess at least one representative member in each of the latter groups (Kutuzov & Andreeva, 2002; Yang *et al.*, 2017). These phosphatases are characterized not only by their shared sequence motif which is highly conserved among the families but also by their similar fold, active-site metal coordination (indicated here by bold letters) and conserved non-ligand residues in the catalytic site (indicated here by underlined). The PPP family exhibits the motif **D**I**H** $(X)_{23}$G**D**YVDR$(X)_{27}$G**N**HE, while the PAP family exhibits the motif **D**XG$(X)_n$G**D**XX**Y**XD$(X)_m$G**N**HD/E (Rusnack & Mertz, 2000).

1.5.1.2 PPM/PP2C-metal dependent superfamily

The activity of these metallo-dependent protein phosphatases, as indicated by their name, depends on the binding of Mg^{2+} or Mn^{2+} ions. Unlike PPPL they do not share a conserved sequence, but they share a similar three-dimensional structure of the catalytic site and the approach how substrates are dephosphorylated (Das *et al.,* 1996; Moorhead *et al.*, 2009). *P. falciparum* possesses 13 PPM members; however, 77% of these members do not have any human ortholog (Fréville *et al.,* 2022).

1.5.1.3 The HAD superfamily

The HAD superfamily phosphatases can be subdivided into two families: (1) TFIIF-associating C-terminal domain phosphatase (FCP) and (2) NLI-interacting factor-like phosphatase (NIF) (Wilkes & Doering *et al.,* 2008). HAD phosphatases are involved in the dephosphorylation of a wide range of substrates (Seifried *et al.,* 2013). Although they do not share sequence similarity with the PPPL family, they exhibit a

congruent nucleotide-binding fold within the active site and they also possess a conserved sequence motif DxDx[V/T] (Seifried *et al*., 2013).

1.5.2 Functional analysis of *Plasmodium* protein phosphatases

1.5.2.1 Protein Phosphatases (PPP)

1.5.2.1.1 Protein phosphatase type 1 (PP1)

Members of the PP1 family exhibit an exceptional level of sequence conservation across phylogeny, signifying their fundamental importance as regulatory entities within diverse cellular pathways (Bollen & Stalmans, 1992). In *P. falciparum*, PP1 is among the most abundant serine/threonine phosphatases. The indispensability of PP1 in the parasite's physiology has been corroborated through phenotypic gene knockdown experiments employing synthetic short interfering RNA (siRNA) (Kumar *et al*., 2022). A recent study, using a reverse genetic approach (*pfpp1*-inducible knockout), it was identified that PP1 is critical for parasite egress (Paul *et al.*, 2020).

1.5.2.1.2 Calcineurin

Calcineurin-like metallophosphoesterase, also known as protein phosphatase PP2B, is a heterodimeric protein composed of two units: a catalytic subunit called calcineurin A (CNA) and a regulatory subunit known as calcineurin B (CNB) (Klee *et al*., 1998; Rusnak & Mertz, 2000). This phosphatase exhibits a multi-functional profile at specific stages in both the human host cell and mosquito vector (Bhattacharyya *et al.,* 2002; Otto *et al.*, 2014; Paul *et al.,* 2015). PP2B is essential for parasite development during the asexual blood stage in *P. falciparum* and is also associated with the merozoite attachment and invasion process in *P. berghei.* In the mosquito stage, PP2B has been found to regulate male gametogenesis, the fertilization process, life cycle transitions in ookinetes, and sporozoite invasion (Philip & Waters *et al.,* 2015).

1.5.2.1.3 Protein Phosphatase Containing Kelch-like Domains (PPKL)

This phosphatase consists of an N-terminal kelch repeat domain and a C-terminal PP1-like phosphatase domain. Initially, it was identified in *P. falciparum* (previously known as *Pf*PPα) with a known role in sexual stage development (Li & Baker, 1998; Kutuzov & Andreeva, 2002). Further work found that this protein is involved in

ookinete maturation, preservation of the architecture of the ookinete, and it is essential for mosquito invasion (Guterry *et al.*, 2012; Philip *et al.,* 2012).

1.5.2.1.4 Phosphatase Shewanella-like (SHLP)

In *P. falciparum*, two distinct SHLP isoforms, SHLP1 and SHLP2, are found in late schizonts and merozoites (Hu *et al*., 2010). SHLP1 plays a pivotal role in the invasion process and is essential for parasite survival during asexual blood stage development (Zhang *et al.*, 2018). In *P. berghei*, SHLP1 is localised in the membrane of the ER and is needed for microneme formation in ookinetes and parasite transmission (Patzewitz *et al*., 2013).

1.5.2.2 Purple acid phosphatase (PAP)

In eukaryotes, PAPs are characterized by the presence of a coordinated Fe (III) and a divalent metal such as Mn (II), Zn (II), or Fe (II) in their catalytic site. Each metal forms coordination bonds with three amino acids and connects through a linking aspartic acid bridge. In the case of Fe (III), the coordination typically involves a histidine (His), an asparagine (Asn), and a tyrosine (Tyr), while the divalent metal is bound by two His and an Asn (Clark *et al.*, 1989; Meng & Lin, 1998). In mammals, these enzymes are also referred to as tartrate-resistant acid phosphatases (TRAPs) or type 5 acid phosphatases (ACP5) (Vincent & Averill, 1990). All known PAPs encompass an Fe^{3+} ion in the catalytic site, which coordinates with an invariant tyrosine ligand. This interaction produced a ligand-to metal charge transfer (CT) transition, giving rise to the characteristic purple colour of the enzyme (Bosch *et al.,* 2012; Schenk *et al.,* 2013). In *P. falciparum,* two phosphates belong to this group based on a structure resembling the PAP family. These members include: (1) the Glideosome associated protein 50 (GAP50) (section 1.5.2.2.1) (Bosch *et al.*, 2011) and (2) the serine/threonine phosphatase UIS2 (section 1.6) (Kaida *et al*., 2010).

1.5.2.2.1 Glideosome associated protein 50 (GAP50)

GAP50 is part of a multi-protein complex called glideosome, a molecular machine required for host cell invasion and parasite motility (Gaskins *et al*., 2004; Baum *et al*., 2006; Jones *et al.*, 2006;). GAP50 is anchored to the IMC and is essential in all apicomplexan parasites (Keeley & Soldati, 2004). Its principal role is to act as a scaffolding protein that anchors the MyoA-MLC-GAP45 complex to the IMC (Gaskins *et al.*, 2004; Baum *et al.*, 2006; Soldati-Favre, 2008; Yeoman *et al.*, 2011). Recently,

potential binding pockets of GAP50 were identified that could serve as potential drug interaction sites and to screen for antimalarial compounds (Agrawal *et al.,* 2023).

1.6 The Serine/threonine phosphatase UIS2

1.6.1 Classification of UIS2

Using suppression subtractive cDNA hybridization, several developmentally upregulated genes in infected sporozoites (UIS) were identified, with UIS2 being the only one among the 30 *uis* genes encoding a phosphatase (Matuschewski *et al*., 2002b). UIS2 comprises a phosphatase domain, a predicted N-terminal signal peptide, and a PEXEL motif (Figure 8) (Pandey *et al.,* 2014; Fierro *et al.,* 2023). In a genome-wide *in silico* analysis of the *P. falciparum* phosphatome, UIS2 was initially categorized alongside GAP50 in the Metallophosphatase-Acid Phosphatase 5 (MPP/ACP5) family (Pandey *et al*., 2014). This enzyme family is characterized by a conserved domain containing a catalytic site composed of two metal ions, typically Mn (II), Fe (II), or Zn (II). These ions are coordinated within an octahedral geometry by a cage formed by His, Asn, and aspartate (Asp) residues (Pandey *et al*., 2014). However, a recent study reclassified UIS2 as a member of the PP2C/PPM family. This reclassification was based on its observed activity enhancement with Mn^{2+} and Mg^{2+} and its susceptibility to inhibition by EDTA and Cd^{2+}. UIS2's activity remained unaffected by a PP1/PP2A phosphatase inhibitor, okadaic acid (Zhang *et al*., 2016). Despite this reclassification, UIS2 lacks a canonical PP2C catalytic domain. Instead, UIS2 shows a high structural similarity to PAPs, which are known for their phosphoserine phosphatase activity (Kaida *et al*., 2010).

Figure 8. Serine/threonine phosphatase UIS2. Schematic of full length UIS2. Black bar indicates signal peptide (SP); dotted box indicates location of the PEXEL motif.

1.6.2 Functional analysis of UIS2 – Current Insights

In the liver stage of *P. berghei,* UIS2 was suggested to play a role in translational regulation by dephosphorylating the parasite's eukaryotic initiation factor 2 alpha (eIF2α-P, Zhang *et al*., 2016). UIS2 is highly transcribed in the mosquito salivary gland (Le Roch *et al*., 2003; Zhang *et al.,* 2010; Matuschewski *et al.,* 2002b). The translation of *uis2* is suggested to be controlled by the Pumilio protein Puf2 (Zhang *et al.*, 2016), which is essential to maintain the infectivity of sporozoites (Wharton *et al.*, 1998; Cui *et al.*, 2002; Le Roch *et al.*, 2003). According to Zhang *et al.*, 2016, Puf2 binds to *uis2* mRNA, suggesting the likely repression of *uis2* phosphatase translation, while the kinase UIS1 phosphorylates eIF2α-P inside the sporozoites. Once sporozoites developed into the liver stage, the suppression of UIS2 translation is likely relieved, resulting in the dephosphorylation of eIF2α (Zhang *et al.,* 2016). However, a recent study found that UIS2 is associated with the luminal face of the PVM in asexual blood stages (Khosh-Naucke *et al*., 2018) and in liver stages (Schnider *et al.,* 2018). The location of UIS2 in the PV is congruent with the presence of an N-terminal signal peptide and challenge the previously assumed function of UIS2 of being involved in the dephosphorylation of cytosolic eIF2a-P. A previous PhD thesis found that UIS2 is important for the survival of *P. falciparum* blood stages and preliminary data indicated a potential role for ring stage development and protein transport (Khosh-Naucke *et al.,* 2018). Furthermore, a recent preprint in *P. falciparum* reaffirms that UIS2, despite its PEXEL motif is a not exported but located in the PVM during blood stages (Figure 8) (Fierro *et al*., 2023).

Interestingly, two orthologs of this phosphatase are found in *T. gondii* (TGGT1_228160 and TGGT1_228170), arranged in tandem on chromosome X, suggesting a duplication event (Tonkin *et al.,* 2014). TGGT1_228170, now renamed GRA44, exhibits homology with the UIS2 phosphatase of *P. falciparum*, showing a 28% identity over 21% of the protein (Cygan *et al*., 2020). GRA44 has been identified as a secreted acid phosphatase, containing a predicted phosphatase domain, signal peptide, and two predicted Toxoplasma Export Elements (TEXEL) motif (Tonkin *et al.,* 2014; Cygan *et al*., 2020). Recent study has revealed the specific localization of this phosphatase within the PV lumen at the PVM and have suggested that GRA44 interacts with members of the putative translocon complex MYR1/2/3 at the PVM in *T. gondii* (Blakely *et al*., 2020).

1.7 Aims of this work

The phosphatase UIS2 has recently been identified as a protein of the inner face of the PVM using BioID (Khosh-Naucke *et al*., 2018). In recent unpublished work, it was found to be essential for parasite survival and progression through the asexual cycle. It was previously proposed that UIS2 functions by dephosphorylating eIF2α. However, the location of UIS2 at the PVM renders such a function improbable but rather it indicates that there may be indispensable dephosphorylation events in the PV that are needed for parasite survival. To understand this important and potentially regulatory function, the present project aims to characterize the phenotypical outcomes of *P. falciparum* parasites lacking UIS2 to identify the function of UIS2 in asexual blood stages. Additionally, the project seeks to identify the role of the phosphatase activity in UIS2 function. The identification of the specific function of UIS2 will contribute to a better understanding of the critical functions at the parasite-host cell interface.

2 Material and Methods

2.1 Materials

2.1.1 *Plasmodium* and Bacterial strains

***Plasmodium* and Bacterial strains**	**Genetic background, origin**
Plasmodium falciparum 3D7	Clone of NF54 isolate (MRA-1000) from a malaria patient near the Amsterdam airport (Walliker *et al*., 1987)
Escherichia coli XL10-Gold	Tet^rΔ(mcrA)183 Δ(mcrCB-hsdSMR-mrr) 173 endA1 supE44 thi-1 recA1 gyrA96 relA1 lac Hte [F'proAB $lacI^qZ$ΔM15 Tn10 (Tet^r) Amy Cam^r]

2.1.2 Chemicals

Reagent	**Company**	**Location**
Acetic acid	Roth	Karlsruhe
Acetone	Roth	Karlsruhe
Acrylamide/Bisacrylamide solution (40%)	Roth	Karlsruhe
Agar Lysogeny-broth (LB) (Lennox)	Roth	Karlsruhe
Agarose	Invitrogen	USA
Albumax II	Gibco, Life Technologies	USA
Albumin bovine Fraction V (BSA)	Biomol	Hamburg
Ammonium persulfate (APS)	Applichem	Darmstadt
Ampicillin	Roche	Mannheim
Blasticidin S	Life Technologies	USA
Bromophenol blue	Roth	Karlsruhe
Calcium chloride (CaCl2)	Sigma Aldrich	Steinheim
Chloramphenicol	Sigma Aldrich	Steinheim

10x Cutsmart buffer	Neb	Ipswich/USA
Desoxynucelotides (dNTPs)	Thermo Scientific	Lithuania
Dihydroethidium (DHE)	Cayman Chemical	Ann Arbor/USA
4‘,6-diamidino-2-phenylindole (DAPI)	Roche	Mannheim
Dimethyl sulfoxide (DMSO)	Sigma Aldrich	USA
1,4-dithiothreitol (DTT)	Biomol	Hamburg
6x DNA-loading dye TriTrack	Thermo Scientific	Schwerte
4x DNA-loading dye purple	Neb	Ipswich/USA
DSM1	BEI Resources	
Ethanol	Roth	Karlsruhe
Ethidium bromide (EtBr)	Sigma Aldrich	Steinheim
Ethylenediaminetetraacetic acid (EDTA)	Biomol	Hamburg
Ethyleneglycoltetraacetic acid (EGTA)	Biomol	Hamburg
10x Fire-polymerase buffer	Solis Biodyne	
Formaldehyde (methanol free), 10%	Polysciences	Warrington/USA
G418 disulfate salt	Sigma Aldrich	Steinheim
Gentamycin	Ratiopharm	Ulm
Giemsa’s azure, eosin, methylene blue solution	Merck	Darmstadt
D-Glucose	Merck	Darmstadt
Glutaraldehyde (25%)	Roth	Karlsruhe
Glycerol	Merck	Darmstadt
Glycine	Biomol	Hamburg
Hoechst 33342	Chemodex	Switzerland
4-(2-hydoxyethyl)-1-piperazineethanesulfonicacid (HEPES)	Roche	Mannheim
Hydrochloric acid (HCl)	Merck	Darmstadt
Hypoxanthine	Sigma Aldrich	Steinheim

Isopropanol	Roth	Karlsruhe
Magnesium chloride (MgCl2)	Merck	Darmstadt
Manganese(II) chloride (MnCl2)	Merck	Darmstadt
Methanol Ethanol (EtOH)	Roth	Karlsruhe
Milk powder	Roth	Karlsruhe
2-[N-(7-nitrobenz-2-oxa-1,3-diazol-4-yl)amino]-2-deoxy-D-glucose (2-NBDG)	Invitrogen	USA
N, N, N, N-tetramethylethylenediamin (TEMED)	Merck	Darmstadt
β-Nicotinamide adenine dinucleotide hydrate (NAD)	Sigma Aldrich	Steinheim
Percoll	Ge Healthcare	Sweden
Piperazine-N,N'-bis(2-ethanesulphonic acid) (PIPES)	Sigma Aldrich	Steinheim
Potassium chloride (KCl)	Merck	Darmstadt
Potassium di-hydrogen phosphate (KH2PO4)	Merck	Darmstadt
Potassium hydroxide (KOH)	Roth	Karlsruhe
Protease inhibitor cocktail tablets “Complete Mini” (EDTA-free)	Roche	Mannheim
Rapalog (A/C Heterodimerizer AP21967)	Clontech	Mountain View/USA
Roswell Park Memorial Institute (RPMI) 1640 medium	Applichem	Darmstadt
Saponin	Sigma Aldrich	Steinheim
Sodium acetate (NaOAc)	Merck	Darmstadt
di-Sodium hydrogen phosphate (Na2HPO4)	Roth	Karlsruhe
Sodium di-hydrogen phosphate (NaH2PO4)	Roth	Karlsruhe
Sodium hydroxide (NaOH)	Merck	Darmstadt

Sodium chloride (NaCl)	Gerbu	Gaiberg
Sodium dodecyl sulfate (SDS)	Applichem	Darmstadt
Sorbitol	Sigma Aldrich	Steinheim
Soybean trypsin inhibitor (STI)	Sigma Aldrich	Steinheim
10x T4 DNA ligase buffer	Neb	Ipswich/USA
Tris base	Roth	Karlsruhe
Tris-EDTA (TE)	Invitrogen	Karlsruhe
Triton X-100	Biomol	Hamburg
Tryptone	Sigma Aldrich	Steinheim
Water for molecular biology (Ampuwa)	Fresenius Kabi	Bad Homburg
WR99210 (WR)	Jacobus Pharmaceuticals	Washington/USA
Yeast extract	Sigma Aldrich	Steinheim
Agar-Agar	Bectondickinson	Heidelberg
Aceton	Roth	Karlsruhe
Developer solution G150 (Western Blot)	Agfa	Leverkusen
Dextran, Alexa Fluor 647 labelled (10,000 MW)	Invitrogen	Karlsruhe
Dulbecco`s Phosphate Buffered Saline (DPBS)	Pan, Biotech	Aidenbach
Milk powder	Roth	Karlsruhe

2.1.3 Kits

Product	**Company**	**Location**
NucleoSpin® Plasmid Kit	Macherey-Nagel	Düren
NucleoSpin® Gel and PCR Clean-up Kit	Macherey-Nagel	Düren
QIAamp DNA Mini Kit	Qiagen	Hilden
QIAGEN® Plasmid Midi Kit	Qiagen	Hilden
Western Blot ECL – SuperSignal West Pico	Thermo Scientific	Schwerte

Western Blot ECL – Clarity Detection Kit	Bio-Rad	USA

2.1.4 DNA and protein ladders

Product	Company	Location
GeneRulerTM 1 kb DNA ladder	Thermo Scientific	Schwerte
PageRulerTM prestained protein ladder	Thermo Scientific	Schwerte
PageRulerTM plus prestained protein ladder	Thermo Scientific	Schwerte

2.1.5 Solutions, buffers and media

2.1.5.1 Media, solutions and buffers for bacterial culture

Media, solutions and buffers	Composition
10x Lysogeny broth (LB) medium stock solution	10% NaCl, 5% peptone, 10% yeast extract, in dH_2O
1x LB medium working solution	1 %(w/v) NaCl2m 0.5% (m/v) peptone, 1% (w/v) yeast extract, in dH_2O
Ampicillin stock solution	100 mg/ml in 70% ethanol
LB-Amp working solution	0.1% ampicillin in 1x LB medium working solution
LB Agar plate solution	1.5% Agar-Agar 1x LB medium
Glycerol freezing solution	50% Glycerol (v/v) in 1x LB medium
Transformation buffer for ultra-competent cells	10 mM PIPES 15 mM $CaCl_2$ 250 mM KCl pH 6.7 (with 10 N KOH) 55 mM $MnCl_2$
SOB medium for ultra-competent cells	0.05% NaCl (w/v) 2% tryptone (w/v)

	0.5% yeast extract (w/v) deionized H_2O, to 950 ml 1% 250 mM KCl (v/v) pH 7.0 (with 5 N NaOH) add dH_2O to 1000 ml, autoclaved 0.5% 2 M $MgCl_2$ (v/v) (sterile)

2.1.5.2 Solutions and buffers for molecular biology analyses

DNA gel electrophoresis buffers	Composition
1x TAE buffer	40 mM Tris base 20 mM pure acetic acid 1 mM EDTA pH 8.5, in dH_2O
50x TAE buffer	2 M Tris base 1 M pure acetic acid 50 mM EDTA pH 8.5, in dH_2O
6x Loading buffer	40 % Glycerol (v/v) 2.5% (w/v) Xylene cyanol 2.5% (w/v) Bromophenol blue, in dH2O

DNA precipitation	Composition
Sodium acetate	3 M NaOAc, pH 5.2
Tris-EDTA (TE) buffer	10 mM Tris-HCl pH 8,0 1 mM EDTA pH 8,0

Etanol (EtOH)	70 % and 100 %

Gibson assembly buffers	**Composition**
5x isothermal reaction buffer (6 ml)	3 ml 1 M Tris-HCl pH 7.5 150 µl 2 M $MgCl_2$ 60 µl each of 100 mM dGTP/dATP/dTTP/ dCTP 300 µl 1 M DTT 1.5 g PEG-8000 300 µl 100 nM NAD add 6 ml dH_2O
Assembly master mixture (1.2 ml)	320 µl 5x isothermal reaction buffer 0.64 µl 10 U/µl T5 exonuclease 20 µl 2 U/µl Phusion DNA polymerase 160 µl 40 U/µl Taq DNA ligase add 1.2 ml dH_2O

2.1.5.3 Solutions and buffers for protein analyses

SDS-PAGE solutions and buffers	**Composition**
10x Running buffer	250 mM Tris base 1.92 M Glycine 1% SDS (w/v), in dH_2O
Ammonium persulfate (APS)	10% in dH_2O (w/v)
Stacking gel buffer	1 M Tris-HCl, pH 6.8 in dH_2O
Separating gel buffer	1.5 M Tris-HCl, pH 8.8 in dH_2O
Stacking gel (for two gels, 5%)	0.75 ml stacking gel buffer

	4.35 ml dH_2O 0.75 ml Acryl amide (40%) 60 µl SDS (10%) 60 µl APS (10%) 6 µl TEMED
Separating gel (for two gels, 12%)	2.5 ml running gel buffer 4.2 ml dH_2O (4.7 ml for 10%) 3 ml Acryl amide (40%) (2.5 ml for 10%) 100 µl SDS (10%) 100 µl APS (10%) 4 µl TEMED
4x SDS sample buffer	375 mM Tris-HCl, pH 6.8 12% SDS (w/v) 60% Glycerol (v/v) 0.6 M DTT 0.06% Bromophenol blue (w/v)

Western blot solutions and buffers	**Composition**
10x Western blot transfer buffer	250 mM Tris base 1.92 M Glycerol 0.1% SDS (w/v), in dH_2O
1x Western blot transfer buffer	10% 10x Western blot transfer buffer 20% Methanol in dH_2O
Blocking solution	5% milk powder (w/v) in 1x PBS

2.1.5.4 Media, solutions and buffers for cell biology experiments

Media, solutions and buffers	Composition
RPMI complete medium	1.587% (w/v) RMPI 1640 12 mM $NaHCO_3$ 20 mM D-Glucose 0.5% (w/v) Albumax II 0.2 mM Hypoxanthine 0.4 mM Gentamycin in dH_2O, sterile filtered, pH 7.2
10% Giemsa solution	10 ml Giemsa's azure, eosin, methylene blue solution 90 ml dH_2O
Synchronisation solution	5% D-Sorbitol (w/v) in dH_2O, sterile filtered
Amaxa transfection buffer	90 mM Na_2HPO4 5 mM KCl 0.15 mM $CaCl_2$ 50 mM HEPES in dH_2O, sterile filtered, pH 7.3
Transfection buffer (Cytomix)	120 mM KCl 150 µM $CaCl_2$ 2 mM EGTA 5 mM $MgCl_2$ 10 mM KH_2PO_4 25 mM HEPES pH 7.6
Malaria freezing solution (MFS)	4.2% D-Sorbitol

	0.9% NaCl 28% Glycerol in dH_2O, sterile filtered
Malaria thawing solution (MTS)	3.5% NaCl in dH_2O, sterile filtered
Rapalog (AP21967) stock solution	500 mM in ethanol
Rapalog (AP21967) working solution	1:20 dilution of stock solution in RPMI complete medium
Human red blood cells (RBCs)	sterile concentrate, blood group 0+,
DSM1 stock solution (50x)	187.5 mM DSM1 in DMSO
DSM1 working solution	100 µl DSM1 stock solution ad 5 ml in 95% DMSO/5% 1x PBS
WR99210 (WR) stock solution	20 µM WR99210 (in DMSO) in RPMI complete medium, sterile filtered
Blasticidin S (BS) working solution	5 mg/mL BS in RPMI complete medium, sterile filtered
DHE stock solution (10x)	5 mg DHE in 1 ml DMSO
DHE working solution (1x)	0.5 mg DHE in 1 ml DMSO
Hoechst 33342 stock solution (10x)	4.5 mg Hoechst 33342 in 1 ml DMSO
Hoechst 33342 working solution (1x)	0.45 mg Hoechst 33342 in 1 ml DMSO
Flow cytometry stop solution	0.5 µl Glutaraldehyde (25%) in 40 ml RPMI complete medium

2.1.5.5 Solutions and buffers for cell biology and biochemical assays

Solutions and buffers	Composition
Parasite lysis buffer	4% SDS 0.5% Triton X-100 0.5x PBS

	in dH_2O
Percoll stock solution	90% Percoll (v/v) 10% 10x PBS (v/v)
80% Percoll solution	89% (v/v) Percoll stock solution 11% (v/v) RPMI complete medium 4% (w/v) sorbitol, sterile filtered
60% Percoll solution	67% (v/v) Percoll stock solution 33% (v/v) RPMI complete medium 4% (w/v) sorbitol, sterile filtered
40% Percoll solution	44% (v/v) Percoll stock solution 56% (v/v) RPMI complete medium 4% (w/v) sorbitol, sterile filtered
Saponin solution	0.03% Saponin (w/v) in 1x PBS

2.1.6 Technical devices

Equipment	**Manufacturer**	**Location**
Agarose gel chamber "Sub Cell GT basic"	Bio-Rad	Munich
Analytical balance "870"	Kern	Balingen
Autoclave "V120"	Systec	Wettenberg
Bacterial incubator "Thermo function line"	Heraeus	Hanover
Centrifuge "Megafuge 1.0R"	Heraeus	Hanover
Centrifuge "5415D"	Eppendorf Ag	Hamburg
Centrifuge "J2-HS"	Beckman Coulter	Krefeld
Centrifuge "Avanti J-26S XP"	Beckman Coulter	Krefeld
Confocal microscope "Olympus FV3000"	Olympus	Hamburg
Cooling Unit Centrifuge "Rotor JA-12"	Beckman Coulter	Krefeld
Gel holder cassette	Bio-Rad	Munich
Microcentrifuge "Butterfly"	Thermo Scientific	Schwerte
Electroporator "Gene Pulser X- Cel"	Bio-Rad	Munich
Electroporator "Nucleofector II AAD-	Amaxa	Germany

1001N"	Biosystems	
Electroporator "Nucleofector II AAD-1001N"	Amaxa Biosystems	Germany
Flow cytometry cell analyser "LSR II"	Becton Dickinson	USA
Fluorescence Microscope "Axioscope A1"	Zeiss	Jena
Light Microscope "Axio Lab A1"	Zeiss	Jena
Microscope digital camera "Orca C4742-95"	Hamamatsu Phototonics K. K.	Japan
Microwave "Micro 750W"	Whirlpool	China
Gel imager "ChemiDocTM XRS+"	Bio-Rad	Munich
PCR Mastercycler "epgradient"	Eppendorf Ag	Hamburg
PCR Thermal cycler "C1000 Touch"	Bio-Rad	Munich
pH-meter "SevenEasy"	Mettler-Toledo	Giessen
Photometer "BioPhotometer Plus"	Eppendorf Ag	Hamburg
Photometer "Nano Drop"	Eppendorf Ag	Hamburg
Pipettes: 0.2-2, 1-10, 100, 200, 1000 µl	Gilson	Middleton, USA
Pipettor "Cell Mate II"	Thermo Scientific	Langenselbold
Pipettor "Pipetboy acu 2"	Integra Biosciences	USA
Power supply "Power Source 300 V"	VWR	Taiwan
Power supply "E835 300 V"	Consort	Belgium
Power supply "EV231"	Consort	Belgium
Roller mixer "STR6"	Stuart	Staffordshire, UK
Roller mixer "SU1400"	Sun Lab	Germany
Sterile laminar flow bench "Sterilguard III Advance"	Baker	Stanford, USA
Sterile laminar flow bench "Safe 2020"	Thermo Scientific	Pinneberg
Thermoblock "Thermomixer compact"	Eppendorf Ag	Hamburg
Vacuum pump "BVC Control"	Vacuubrand	Germany
Vortexer "Genie 2"	Scientific Industries	USA

Water bath "1083"	Gfl	Burgwedel
Ultrapure water purification	Milli Q	Merck, Darmstadt
UV transluminator "PHEROlum 289"	Biotec Fischer	Reiskirchen

2.1.7 Labware and disposables

Product	**Company**	**Location**
Chromatography paper	Whatman	United Kingdom
Conical falcon tubes: 15 ml, 50 ml	Sarstedt	Nümbrecht
Cryotubes: 1.6 ml	Sarstedt	Nümbrecht
Culture bottles: 50 ml	Sarstedt	Nümbrecht
Diagnostic microscope slides: 10 wells, 6.7 mm	Thermo Scientific	Portsmouth/USA
Flow cytometry tubes 55.1579: 5 ml, 75x 12 mm	Sarstedt	Nümbrecht
Glass cover slips: 24x65 mm, thickness 0.13-0.16 mm	R. Langenbrinck	Emmendingen
Glass cover slips: 24x55 mm, thickness 0.13-0.17 mm	Engelbrecht	Edermünde
Glass slides	Engelbrecht	Edermünde
Gloves, purple nitrile	Kimtech Science	
Gloves, blue nitrile “35PLUS”	Bingold	Hamburg
Leukosilk tape	BSN	
Nitrocellulose blotting membrane: Amersham 0.45 µm	Ge Healthcare	Germany
One way cannula	Braun	Melsungen
One way injection	Braun	Melsungen
Parafilm	Bemis	USA
Pasteur pipettes	Brand	Wertheim
Petri dishes: 2 ml, 10x35 mm	Thermo Scientific	Denmark

Petri dishes: 5 ml, 15x60 mm; 10 ml, 14x90 mm	Sarstedt	Nümbrecht
Pipette tips: 1-10, 20-200, 100-1000 µl	Eppendorf	Hamburg
Filter tips: 1-10, 20-200, 100-1000 µl	Sarstedt	Nümbrecht
Plastic pipettes: 5 ml, 10 ml, 25 ml	Sarstedt	Nümbrecht
Reaction tubes: 1.5 ml, 2 ml	Eppendorf	Hamburg
PCR reaction tubes: Multiply-µStrip Pro 8-Strip	Sarstedt	Nümbrecht
Scalpel	Braun	Melsungen
Sterile filter: 0.22 µm	Sarstedt	Nümbrecht
Transfection cuvettes: 0.2 cm	Bio-Rad	München
TC-6-well plates (standard): 2-4 ml, 85.2x 127.8 mm	Sarstedt	Nümbrecht
TC-12-well plates (standard): 2-4 ml, 85.2x 127.8 mm	Sarstedt	Nümbrecht

2.1.8 Enzymes

2.1.8.1 Polymerases

Enzyme	**Manufacturer**	**Location**
FirePol DNA Polymerase [5 U/µl]	Solis Biodyne	Taipei, Taiwan
Phusion High-Fidelity DNA Polymerase [2U/µl]	NEB	Ipswich, Usa
KAPA HiFi HotStart	Roche	USA

2.1.8.2 Restriction enzymes

Enzyme	**Manufacturer**	**Location**
AvrII	NEB	Ipswich, USA
BamHI-HF®	NEB	Ipswich, USA
BglII	NEB	Ipswich, USA
BsiWI	NEB	Ipswich, USA
DpnI	NEB	Ipswich, USA
HindIII-HF®	NEB	Ipswich, USA
KpnI-HF®	NEB	Ipswich, USA

MfeI-HF®	NEB	Ipswich, USA
MluI-HF®	NEB	Ipswich, USA
NotI-HF®	NEB	Ipswich, USA
NheI-HF®	NEB	Ipswich, USA
PmeI	NEB	Ipswich, USA
PstI-HF®	NEB	Ipswich, USA
SalI-HF®	NEB	Ipswich, USA
SmaI	NEB	Ipswich, USA
SpeI-HF®	NEB	Ipswich, USA
StuI-HF®	NEB	Ipswich, USA
XhoI	NEB	Ipswich, USA
XmaI	NEB	Ipswich, USA

2.1.9 Antibodies

2.1.9.1 Primary antibodies

Antigen	Origin	IFA	WB	Source
Aldolase	rabbit		1.4000	Nyalwidhe & Lingelbach, 2006
ETRAMP4	rabbit	1:500	-	Spielmann *et al*., 2006a
ETRAMP5	mouse	1:400	-	Spielmann *et al*., 2006a
GFP	mouse	-	1:1000	Roche, Mannheim
HA	rat	1:500	1:1000	Roche, Mannheim
RFP	rat	1:500	1:200	Chromotek, Germany
SBP1C	rabbit	1:2000	1:2000	Mesén-Ramírez *et al.,* 2016
KAHRP	rabbit	1:500	-	Prof.Dr. Brian Cooke
BIP	rabbit	-	1:2000	Struck *et al*., 2005

2.1.9.2 Secondary antibodies for IFA

Antigen	Conjugate	Origin	Dilution	Source
Mouse	Alexa488	Goat	1:2000	Life Technologies, USA
	Alexa594	Goat	1:2000	Life Technologies, USA
Rabbit	Alexa488	Donkey	1:2000	Invitrogen, Molecular Probes
	Alexa594	Donkey	-	Invitrogen, Molecular Probes
Rat	Alexa594	Goat	1:2000	Invitrogen, Molecular Probes

2.1.9.3 Secondary antibodies for WB

Antigen	Conjugate	Origin	Dilution	Source
Mouse	HRP	Goat	1:3000	Dianova, Hamburg
Rabbit	HRP	Donkey	1:2500	Dianova, Hamburg
Rat	HRP	Goat	1:3000	Dianova, Hamburg

2.1.9.4 Streptavidin conjugates

Conjugate	Application	Dilution	Source
Alexa594	IFA	1:1000	Invitrogen, Molecular Probes
HRP	WB	1:5000	Thermo Scientific
Streptavidin Sepharose™	Purification	50 µl/1 ml lysate	Cytiva

2.1.10 General Plasmids

Plasmids	Source
pSLI-3xHA-T2A-Neo	Mésen-Ramírez
pSLI-GFP-T2A-Neo	Mésen-Ramírez
pSLI-2xFKBP-GFP-T2A-Neo	Birnbaum *et al.,* 2017
pSLI-2xFKBP-GFP-2xFKBP-T2A-Neo	Birnbaum *et al.,* 2017
pSkip-Flox	Birnbaum *et al.,* 2017
pBirA N-terminal	Birnbaum *et al.,* 2017

2.1.11 Online Sources

Online sources	Source
COACH	https://zhanggroup.org/COACH/
COFACTOR	https://zhanggroup.org/COFACTOR/
ImageJ 64 1.43u	http://rsbweb.nih.gov/ij/
HHpred	https://toolkit.tuebingen.mpg.de/#/tools/hhpred
MotifScan	http://myhits.isb-sib.ch/cgi-bin/motif_scan
PlasmoDB	Plasmodb.org

PlasmoGem	https://plasmogem.sanger.ac.uk/
UbPred	http://www.ubpred.org/cgi-bin/ubpred/ubpred.cgi
NCBI databases	https://www.ncbi.nlm.nih.gov/
ClustalOmega	https://www.ebi.ac.uk/Tools/msa/clustalo/
BLAST	http://blast.ncbi.nlm.nih.gov/Blast.cgi
Reverse complement	https://www.bioinformatics.org/sms/rev_comp.html
ToxoDB	https://toxodb.org/
AlphaFold	https://alphafold.ebi.ac.uk/
SWISS-Model	https://swissmodel.expasy.org/

2.1.12 Computer Software /Program

Program	**Source**
ApE (A plasmid Editor)	Open Source
Axio Vision 40 v4.7.0.0	Zeiss, Jena
Corel Draw 2022	Corel Corporation, Ottawa
Corel Photo Paint 2022	Corel Corporation, Ottawa
GraphPad Prism 8	GraphPad Software, La Jolla, USA
Microsoft Office 2021 v.16.47	Microsoft Corporations, Redmond, USA
Image Lab software (v 5.2.1)	Bio Rad
ImageJ	https://imagej.nih.gov/ij/
Fiji	https://imagej.net/software/fiji
Pymol	Schrödinger, USA

2.2 Methods

2.2.1 Microbiological Methods

2.2.1.1 Production of competent *E. coli*

To prepare DNA-plasmid transformations, competent *E. coli* XL10 Gold bacterial cells were generated following the procedure established by Inoue *et al*., 1990. Bacteria from a freshly thawed glycerol stock stored at -80°C were inoculated into 10 ml of SOB medium supplemented with 34 µg/ml chloramphenicol and cultured overnight with constant agitation (120-150 rpm) at 37°C. The following day, 200 ml of SOB medium were inoculated with 5 mL of the overnight culture and incubated at 18°C with continuous shaking at 160 rpm. Regular monitoring of the optical density at 600 nm (OD600) was conducted after 24 h, and cultures were harvested when the OD600 reached 0.45-0.6. The bacterial cultures were centrifuged at 3900 rpm and 4°C for 15 minutes. The supernatant was discarded, and the pellet was gently resuspended in ice-cold transformation buffer (10 mM PIPES, 15 nM $CaCl_2$, 250 nM KCl, 55 nM $MnCl_2$ in H_2O). Next, the suspension was centrifuged again at 3900 rpm and 4°C for 15 minutes. The resulting pellet was resuspended in 16 ml of ice-cold transformation buffer, and 1.2 ml of dimethyl sulfoxide (DMSO) was slowly added to the cell suspension. The bacterial suspension was divided into 100 µl aliquots and stored at -80°C.

2.2.1.2 Transformation of *E.coli* chemically competent cells

To facilitate the transfer of plasmid DNA into *E. coli* XL10 Gold bacterial cells, a 100 µl aliquot of chemically competent cells was thawed on ice. 10 µl of a ligation mixture (section 2.2.2.4) or 1 µL of purified plasmid was added to the cells and incubated on ice for 15-30 minutes. The mixture was heat shocked at 42°C for precisely 30 seconds to promote cell permeability and facilitate DNA uptake. Following the heat shock, the cell suspension was maintained on ice for an additional 5 minutes to stabilize cellular conditions. The treated cells were inoculated onto pre-warmed Lysogeny Broth (LB) agar plates supplemented with 0.1 mg/ml ampicillin to select for transformed cells. The inoculated plates were then incubated overnight at 37°C.

2.2.1.3 Cultivation and storage of *E. coli* transgenics cells

After successfully transforming plasmid DNA into *E. coli*, the resulting bacterial colonies were selectively cultured on LB agar plates containing ampicillin (0.1 mg/ml). This selective medium ensured the survival and proliferation of only those cells that had acquired the plasmid and, consequently, the ampicillin resistance gene. Individual transformed colonies were then transferred into fresh LB medium supplemented with ampicillin and incubated overnight at 37°C with agitation at 150 rpm. To ensure the long-term viability and availability of the new transgenic cells, they were preserved using a 50% glycerol solution. These treated cultures were aliquoted into cryovials and stored at -80°C.

2.2.2 Molecular biology methods

2.2.2.1 Polymerase chain reaction (PCR)

The polymerase chain reaction (PCR) was employed to amplify DNA fragments originating from various sources, including *P. falciparum* 3D7 genomic DNA (gDNA), *T. gondii* gDNA, plasmid DNA, or synthesized genes acquired from BioCat, Germany. Two distinct types of high-fidelity DNA polymerases were employed in preparative PCR: Phusion High Fidelity DNA polymerase (NEB) or KAPA High Fidelity Hotstart (Roche) (Table 1, Table 2). These polymerases were selected due to their proofreading activity, which significantly reduces the likelihood of introducing unintended mutations during DNA amplification. For validation purposes, the non-proofreading FIREPol® DNA polymerase (Solis Biodyne) was utilized to confirm the accurate integration of plasmids into the genome, gene excision (section 2.2.3.11) (Table 1), and colony-PCR screening (section 2.2.2.6). The use of a non-proofreading polymerase in these validation steps ensured accurate detection of any potential mutations or alterations in the DNA sequence. PCR conditions, including annealing and elongation temperatures, were meticulously adjusted based on the length of the DNA sequences targeted for amplification. After PCR amplification, visualization of the resulting DNA products was achieved through agarose gel electrophoresis (section 2.2.2.2). Oligonucleotides were ordered from Sigma-Aldrich (Steinheim) and are listed in Appendix 1.

Table 1. PCR master mix for Phusion, FirePol and KAPA DNA polymerase

Phusion PCR (50 µl final volume)	
Reagents	Volume
5x Phusion HF reaction buffer	10 µl
dNTPS (10mM)	5 µl
Primer fw (10µM)	1 µl
Primer rv (10µM)	1 µl
Phusion DNA polymerase [2 U/µl]	0.5 µl
DNA Template	0.5 µl
H2O	32 µl

FIREPol PCR (40 µl final volume)	
Reagents	Volume
10x FIREPol reaction buffer	4 µl
dNTPS (10mM)	4 µl
MgCl2 (25mM)	2.4 µl
Primer fw (10µM)	1.6 µl
Primer rv (10µM)	1.6 µl
Polymerase [5 U/µl]	0.4 µl
DNA Template	0.5 µl
H2O	25.5 µl

KAPA PCR (40 µl final volume)	
Reagents	Volume
5 x HiFi-Buffer	4 µl
dNTPS (200µM)	4 µl
Primer fw (0,50µM)	1.6 µl
Primer rv (0,50µM)	1.6 µl
KAPA Hot Start [1U/rxn]	0.4 µl
DNA Template	0.5 µl
H2O	33.50 µl

Table 2. Conditions for analytic PCRs

Phusion PCR program			
Phase		**Temperature**	**Time**
Initial denaturation		95 °C	2 min
	Denaturation	95 °C	30 s
25-30 cycles	Annealing	42-72 °C	30 s
	Elongation	72 °C	6 min
Final hold		4 °C	

Firepol PCR program			
Phase		**Temperature**	**Time**
Initial denaturation		95 °C	4 min
	Denaturation	95 °C	30 s
25-30 cycles	Annealing	42-60 °C	30 s
	Elongation	72 °C	6 min
Final hold		4 °C	

KAPA PCR program			
Phase		**Temperature**	**Time**
Initial denaturation		94 °C	2 min
	Denaturation	95 °C	20 s
25-30 cycles	Annealing	45-60 °C	1 min
	Elongation	72 °C	5 min
Final hold		4 °C	

2.2.2.2 Agarose gel electrophoresis

Agarose gel electrophoresis was employed for molecular weight-based separation of double-stranded DNA. Under an electric field, DNA molecules, with their negative charge stemming from phosphate groups, migrate towards the anode. 1% Agarose

gels derived from seaweed with a melting temperature of approximately 95°C were prepared by dissolving the powder in buffer through microwave heating, followed by cooling to a moderate temperature (30-35°C). Ethidium bromide (1 µg/mL) was added, and the solution was cast into a plastic carrier, forming a gel structure within 30 minutes. The gel, loaded with PCR samples treated with 6x DNA-loading buffer (250 nM Tris, 4% SDS (10%), 40% Glycerine, 400 mN DTT, 0.1% Bromophenol blue), along with a 1kb DNA size ladder (Thermo Scientific, #10787018), was subjected to electrophoresis at 150 V for 30 minutes. The migration distance of DNA fragments correlates with their size. Fragment visualization was achieved through UV radiation, and gel analysis was performed using ChemiDoc™ XRS (Bio Rad). Images were analyzed with Image J and Fiji.

2.2.2.3 Purification of PCR-products and digested DNA

PCR products and DNA digested with restriction enzymes were purified with the NucleoSpin Gel and PCR Clean-up Kit (Macherey-Nagel), following the manufacturer's instructions. This procedure effectively removed polymerases, restriction enzymes, oligonucleotides, salts, and other additives. The resulting purified PCR products and digested DNA were then eluted in 40-50 µl of the provided elution buffer.

2.2.2.4 Restriction digest of PCR-products and vectors

Purified PCR products and vectors were digested using different NEB restriction enzymes to generate sticky ends for subsequent ligation. DpnI was utilized to eliminate methylated plasmid DNA. (Table 3). Analytical digestions of mini and midi DNA preparations (section 2.2.2.7) were conducted to verify correct insertion of PCR products into the plasmid and to exclude recombination events. Digestions were carried out at 37°C for 2h.

Table 3. Standard mix for preparative DNA restriction digest

Restriction digest (100 µl final volume)	
CutSmart® buffer (10x)	10 µl
PCR product	45 µl
DpnI	1 µl
H_2O	44 µl

Restriction digest (100 µl final volume)	
CutSmart® buffer (10x)	10 µl
Plasmid DNA	3 µl
Enzyme 1	1 µl
Enzyme 2	2 µl
H_2O	85 µl

2.2.2.5 Gibson assembly

Digested DNA, previously purified (section 2.2.2.3), was ligated into the target vector using. Gibson DNA assembly (Gibson et al., 2009) (Table 4). Gibson assembly eliminates the need for insert digestion and can simultaneously ligate multiple inserts – up to six –into the target vector. This versatility is made possible by the design of primers used during PCR, which introduce specific complementary overhangs at the ends of each DNA fragment. These overhangs facilitate the precise assembly of the DNA fragments into the vector. The Gibson DNA assembly reaction was then carried out by incubating the reaction mixture at 50°C for 1 hour. During this incubation period, the DNA fragments and the target vector undergo annealing and ligation mediated by the complementary overhangs, resulting in the formation of the final construct. After the incubation time the reaction mixture was transformed into competent *E. coli* bacteria by heat shock for 30 seconds at 42 °C.

Table 4. Standard mix for preparative Gibson assembly

Gibson assembly (10 µl final volume)	
Gibson Assembly Master Mix	8 µl
Vector	1 µl
Insert	0.5 µl

2.2.2.6 Colony-PCR-screen

After transforming competent *E. coli* cells with the DNA plasmid resulting from ligation, colony-PCR screening was performed using Firepol DNA polymerase in order to identify bacterial clones carrying the correct plasmid with the desired insert. Individual bacterial colonies were selected from the LB-agar plate using a small pipette tip and transferred into separate PCR reaction tubes. Each PCR reaction contained a primer specific to the vector (backbone) and the other specific to the DNA insert that was ligated into the vector. The resulting PCR products were then analyzed via agarose gel electrophoresis (section 2.2.2) to confirm the presence of clones with the expected product size.

2.2.2.7 Purification of bacterial plasmids

To achieve the necessary DNA concentrations for sequencing (section 2.2.2.7) a correct clone was selected from either a master plate or its corresponding glycerol stock. The selected clone was cultured in 1 ml of LB-Amp medium, with continuous agitation at 120-150 rpm, and incubated overnight at 37°C. The culture was then centrifuged at 6000 rpm for 15 minutes at 4°C to pellet the bacteria. Plasmid DNA was isolated from the resulting pellet using the QIAGEN Plasmid Mini Kit, following the manufacturer's instructions. The purified DNA was resuspended in 40 µl of TE buffer for mini-preps. For larger-scale preparations for transfection of *P. falciparum* parasites (section 2.2.3.7), the QIAGEN Plasmid Midi Kit was employed with 200 ml of LB-Amp medium, and the extracted DNA was resuspended in 200 µl of TE buffer. All purified plasmid DNA samples were stored at -20°C for further use.

2.2.2.8 Sequencing of plasmid DNA

To analyze DNA sequences (insert and restriction sites) for potential mutations and confirm the accurate insertion of DNA sequences into vectors, sequencing was conducted. Samples containing 200–800 ng of plasmid DNA and 3 µl of a 10 mM sequencing primer were diluted in 15 µl of Ampuwa® H2O and sent to Sequence Laboratories, Göttingen (Seqlab).

2.2.2.9 DNA precipitation

For the transfection of *P. falciparum* parasites (section 2.2.3.7), purified plasmid DNA obtained using the QIAGEN Plasmid Midi Kit was utilized. A volume containing 50-100 µg of DNA was mixed with a 1/10 volume of 3 M sodium acetate, followed by

precipitation with three volumes of absolute ethanol. The resulting DNA precipitate was centrifuged for 15 minutes at 14 000 rpm and was washed with 70% ethanol. The sterile DNA pellet obtained was air-dried before being dissolved in 40 µl of sterile TE buffer.

2.2.2.10 Genomic DNA isolation

Genomic DNA (gDNA) extracted from transgenic and wild-type *P. falciparum* 3D7 cell lines served as the basis for PCR analysis, aiming to verify the accurate integration of knock-in constructs into the parasite genome and to provide templates for preparative PCRs. 1 ml of a parasite culture was centrifuged at 1800 x g for 3 minutes. Purification of gDNA from the blood pellet was carried out using the QIAamp DNA Mini Kit (QIAGEN) following the manufacturer's protocol. The purified gDNA was eluted with 200 µl of dH_2O and stored at -20°C.

2.2.3 2.2.3 Cell biological Methods

2.2.3.1 *In vitro* cell culture of *P. falciparum* parasites

The blood stages of the parasite were cultivated in 5 ml or 10 ml petri dishes with RPMI complete medium (Applichem, No. A1538,9010) supplemented with human erythrocytes (blood group O+) at a 5% hematocrit. They were maintained at 37°C under controlled low-oxygen conditions (5% CO_2, 1% O_2, and 94% N_2) to simulate human bloodstream conditions, in accordance with established methodologies (Trager & Jensen, 2005). For the selection of transgenic parasites, different drugs were added according to the particular selection marker. These included 4 nM WR99210 (Jacobus Pharmaceuticals), 2 µg/ml Blasticidin S (Life Technologies), 400 µg/ml G418 (Sigma Aldrich), or 0.9 µM DSM1 (BEI Resources). The intraerythrocytic asexual life cycle of the parasite lasts about 48 hours. As a result, parasitemia can increase by a factor of 4 to 10 after approximately 2 days. Parasite populations were meticulously maintained within the range of 0.1-10% parasitemia and subjected to dilution every two days to prevent overgrowth. Parasitemia, the percentage infection of erythrocytes by the parasite, was determined by cell counting of Giemsa - stained thin blood smears (section 2.2.3.2).

2.2.3.2 Blood smears and Giemsa staining

To assess parasitemia and observe parasite development, a measured volume ranging from 0.5 to 0.8 µl of cultured blood was carefully spread on a glass slide using another slide angled at 45 degrees, forming a monolayer of red blood cells (RBCs). The prepared smear was air-dried and then fixed with 99.8% methanol for a duration of 10 to 20 seconds. For cellular differentiation, the smear was stained using a 10% Giemsa stain – a blend of azure, eosin, and methylene blue solutions – for a period ranging from 15 to 30 minutes. After staining, the slide was washed with water and the remaining solution was removed with a tissue before allowing it to dry completely. An optical light microscope was employed to count the number of infected versus uninfected erythrocytes, thereby determining the level of parasitemia.

2.2.3.3 Cryo-stabilates of *P. falciparum*

P. falciparum parasites, including transgenic cell lines, can be preserved long-term by cryopreservation. For this process, 5-10 ml of parasite culture with a parasitemia of 0.1-10% rings was centrifuged at 1800 - 3000 x g for 3 minutes. Following centrifugation, the supernatant was discarded and the resulting cell pellet was resuspended in 1 ml of malaria freezing solution (MFS). This suspension was then transferred into a sterile cryotube of 2 ml in capacity. For storage, the cryotubes were immediately placed at -80 °C in a standard freezer or at -196 °C in liquid nitrogen.

2.2.3.4 Thawing of *P. falciparum* cryo-stabilates

To re-culture frozen *P. falciparum* parasites, the cryotube was placed in a 37°C water bath for approximately 1 minute. The thawed cell suspension was then transferred into a 15 ml Falcon tube and centrifuged at 1800 x g for 3 minutes at room temperature. After discarding the supernatant, the cell pellet was resuspended in 1 ml of malaria thawing solution (MTS). The suspension underwent another round of centrifugation under the same conditions to completely remove the MTS. The pellet was washed twice with pre-warmed RPMI medium to eliminate any remaining MTS. The washed cells were then transferred to a 5 ml petri dish, adjusting the hematocrit to 5%. The culture was incubated at 37°C, with the medium being replaced the next day.

2.2.3.5 Synchronization of parasite cultures with sorbitol

To synchronize *P. falciparum* cultures starting from the ring stage, a volume of 5 - 10 ml from an asynchronous culture containing rings, trophozoites, and schizonts was centrifuged in a 15 ml Falcon tube at 1800 - 3000 x g for 3 minutes. The supernatant was discarded, and the pellet was resuspended in 1 - 2 ml of pre-warmed 5% D-sorbitol solution, then incubated at 37°C for 10 - 15 minutes. This incubation step led to the lysis of the mature parasite stages, with D-sorbitol selectively lysing trophozoites and schizonts, as described by Lambros & Vanderberg (1979), while the ring-stage parasites remained unaffected. Following this incubation, the culture was centrifuged again at 1800 - 2000 x g for 3 minutes. The resulting pellet was washed once with 5 ml of RPMI complete medium to remove residual sorbitol, and then transferred to a new petri dish containing fresh RPMI medium. This resulted in a culture that contained predominantly parasites that were 0-18 hours post-invasion (hpi). For a tighter timeframe of parasite development, this procedure was repeated after 10 hours to obtain parasite of 0 - 8 hpi. The effectiveness of the synchronization was confirmed by examining a Giemsa - stained thin blood smear.

2.2.3.6 Percoll gradient of *P. falciparum* infected erythrocytes

A Percoll gradient was utilized to isolate trophozoites and schizonts from uninfected erythrocytes and ring-stage parasites. In this process, 5 - 10 ml of parasite culture containing the desired parasite stages was centrifuged in a 15 ml Falcon tube at 2000 - 3000 rpm for 2 minutes. A 2 ml reaction tube was prepared with 400 - 500 µl of 80% Percoll (GE Healthcare), onto which 400 - 500 µl of 60% Percoll was carefully layered, followed by 400 µl of 40% Percoll, creating a tiered gradient. After centrifugation, the supernatant was discarded, and the cell pellet was resuspended and slowly layered onto the top of the gradient. Owing to their differential permeability to sorbitol (Aley *et al*., 1986), denser cells, namely rings and uninfected RBCs, settled at the bottom, while trophozoites and schizonts gathered in the percoll layers. After centrifugation at 2000 x g for 5 minutes, the layers containing the desired parasite stages were carefully transferred to a new tube and washed with RPMI complete medium and put back into culture.

2.2.3.7 Transfection of *P. falciparum* schizonts

Electroporation facilitated the transfection of *P. falciparum* parasites. Initially, 50 µg of plasmid DNA was precipitated using 1/10 volume of 3 M sodium acetate (pH 5.2)

and 2.5 volumes of absolute ethanol. The mixture was then centrifuged at 20000 x g for 15 minutes to pellet the DNA, which was subsequently washed with 70% ethanol, centrifuged, and air-dried in sterile conditions. The dry pellet was resolubilized in 10 µl of Tris-EDTA (TE) buffer and mixed with 90 µl of Amaxa transfection solution (90 mM Na_2HPO_4, 5 mM KCl, 0.15 mM $CaCl_2$, 50 mM HEPES in distilled H_2O, pH 7.3). For the isolation of schizont-stage parasites, a culture volume containing at least 2% schizonts (5 - 10 ml) was overlaid onto 4 ml of 60% Percoll in a 15 ml Falcon tube and centrifuged at 2000 rpm for 8 minutes without break. Post-centrifugation, the schizont layer was carefully collected and transferred to a clean 15 ml tube and washed with RPMI medium. A volume of 10-15 µl from the schizont pellet was then added to the DNA solution. This mixture was placed into a 2 mm electroporation cuvette (BioRad) and transfected using the Nucleofector II device (Bio-Rad) set to the U-033 program. The transfected parasites were transferred to a 2 ml reaction tube containing 500 µl RPMI and 250 µl of uninfected RBCs. The sample was incubated at 37°C with constant shaking at 800 rpm for a minimum of 30 minutes. Following incubation, the parasites were transferred to a culture dish containing 5 ml of RPMI medium. After 24 hours, the medium was changed, and the selection drug was added. To support growth, 50 µl of fresh blood was added weekly. Parasite development was controlled with Giemsa-stained thin blood smears at least once or twice per week.

2.2.3.8 Saponin lysis of P. falciparum infected erythrocytes

The isolation of parasites from RBCs is a critical step for the analysis of the proteins of the parasite. Saponin, a detergent, is utilized for its ability to lyse erythrocyte membranes and the PVM while preserving the integrity of the PPM. For this, 10 ml culture with a parasitemia of 5 - 10% was collected and centrifuged at 11 000 x g for 5 minutes. The supernatant was discarded, and the pellet was then washed with 10 ml of 1x PBS to remove any residual medium components. After second centrifugation, the supernatant was again discarded, and the pellet was carefully resuspended. The pellet was treated with ten volumes of ice-cold, freshly prepared 0.03% saponin in PBS. This mixture was incubated on ice for 10 minutes to ensure gentle lysis. The suspension was centrifuged at 11 000 x g for 5 minutes at 4°C, and the supernatant was discarded. The lysed cells were transferred to a 2 ml tube and centrifuged for 3 minutes at 1800 x g. The pellet was washed with ice-cold 1x PBS in successive steps until the supernatant appeared clear of hemoglobin. After the final

wash, the pellet was treated with 5 µl of 25x protease inhibitor cocktail and 1 mM PMSF was added and mixed with the pellet. The pellet was resuspended in 50 -100 µl of SDS lysis buffer, adjusted based on pellet size, and incubated for 5 minutes to lyse the PVM, Next, it was centrifuged for 3 minutes at 1800 x g. This supernatant was then gently transferred to a new tube and stored at -20°C for subsequent analyses. To prevent protein degradation, the lysate was immediately mixed with 4x SDS sample buffer preheated to 85 - 90°C in a ratio of 15 µl of dye per 50 µl of supernatant. The prepared samples were then promptly processed for SDS-PAGE (section 2.2.4.1).

2.2.3.9 Selection for transgenic parasite cell lines using SLI

The Selection-Linked Integration system (SLI) (Birnbaum *et al*., 2017), provides a robust method for achieving genomic integrations. To achieve this, the SLI plasmid, or its modified variant, was transfected into parasites with a culture adjusted to 4 - 10% parasitemia in 10 ml RPMI complete medium. Selection was initiated by adding the episomal selection marker WR99210, followed by G418 at a final concentration of 400 µg/ml (Figure 8), or 1.5 µM DSM1 if parasites carried a plasmid with yDHODH as the SLI resistance marker, instead of G418. The SLI plasmid contains a promoter less, C-terminal homologous targeting region (500 - 1000 bp) of the gene of interest, linked to the desired protein tag and a selection marker (neomycin or yDHODH resistance), separated by a skip peptide. This configuration ensures that transcription occurs under the endogenous promoter only after single crossover integration into the target locus. Due to the skip peptide, the tagged protein and the resistance marker are produced as two separate translation products, allowing for the selection of parasites with the integration using the corresponding resistance marker (Figure 8). After the addition of the selection drugs, the culture medium was changed daily for five days and then every other day until parasites were obtained. Upcoming parasites during the selection process were monitored by Giemsa-stained thin blood smears. In cases of parasite growth, genomic DNA was extracted using the QIAamp DNA Mini Kit and subjected to PCR to verify the correct plasmid integration into the genomic locus of the target gene. If the original wild-type locus was detected, WR99210 treatment was continued for an additional two weeks before reevaluating for correct integration (Figure 8).

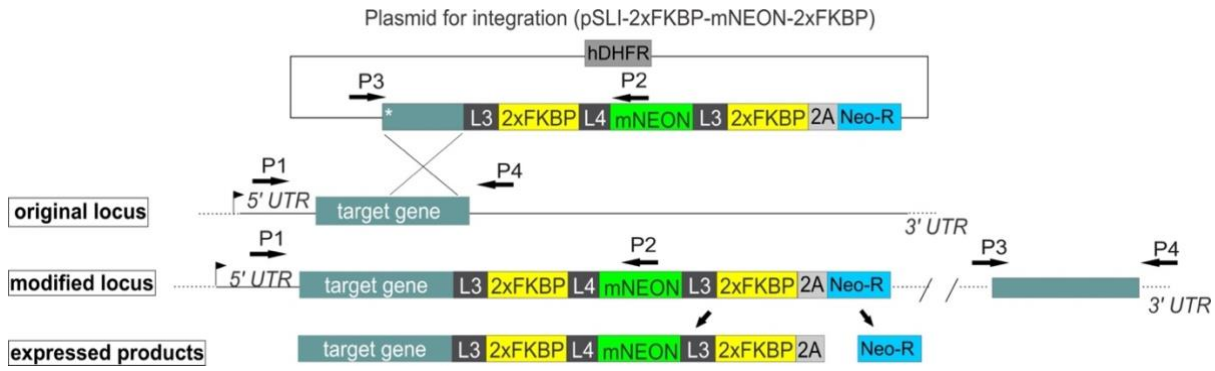

Figure 8. Scheme of selection linked integration strategy. A homologous targeting region (500-1000 bp) corresponding to the protein of interest is cloned into the pSLI sandwich vector. This facilitates single crossover integration, resulting in the expression of a 2xFKBP-GFP-2xFKBP-tagged version of the protein under its native promoter. The inclusion of a 2A skip peptide ensures that the resistance marker, neomycin, is translated independently from the tagged protein, although they are part of the same transcriptional unit. hDHFR: WR99210 resistance marker; L3 and L4: linkers; mNeon Green: green fluorescent protein; 2A: T2A skip peptide; Neo-R: neomycin resistance gene; asterisk: stop codon; arrowheads: promoters; numbered arrows 1-4: primers used to verify the correct plasmid integration into the genomic locus of the target gene.

2.2.3.10 SLI-based conditional deletion using diCre-mediated gene excision

The integration of the SLI system with the dimerizable Cre recombinase (diCre) system has been utilized to create inducible knockout parasites (Birnbaum *et al*., 2017; Mesén-Ramírez *et al*., 2019). This technique involves disrupting the gene of interest while providing a floxed functional copy at the same genomic locus to ensure parasite viability. The plasmid pSkip-Flox facilitates the expression of diCre in two separate fragments (Figure 9). The introduction of a dimerizing ligand, rapalog, triggers the assembly of these diCre fragments, thereby reconstituting the active recombinase. This reactivation enables the inducible excision of the recodonized target gene, which is situated between loxP sites (Figure 9). The SLI-based conditional deletion using diCre was used to perform conditional knockout of PF3D7_1464600, PF3D7_1133800 and PF3D7_0922100.

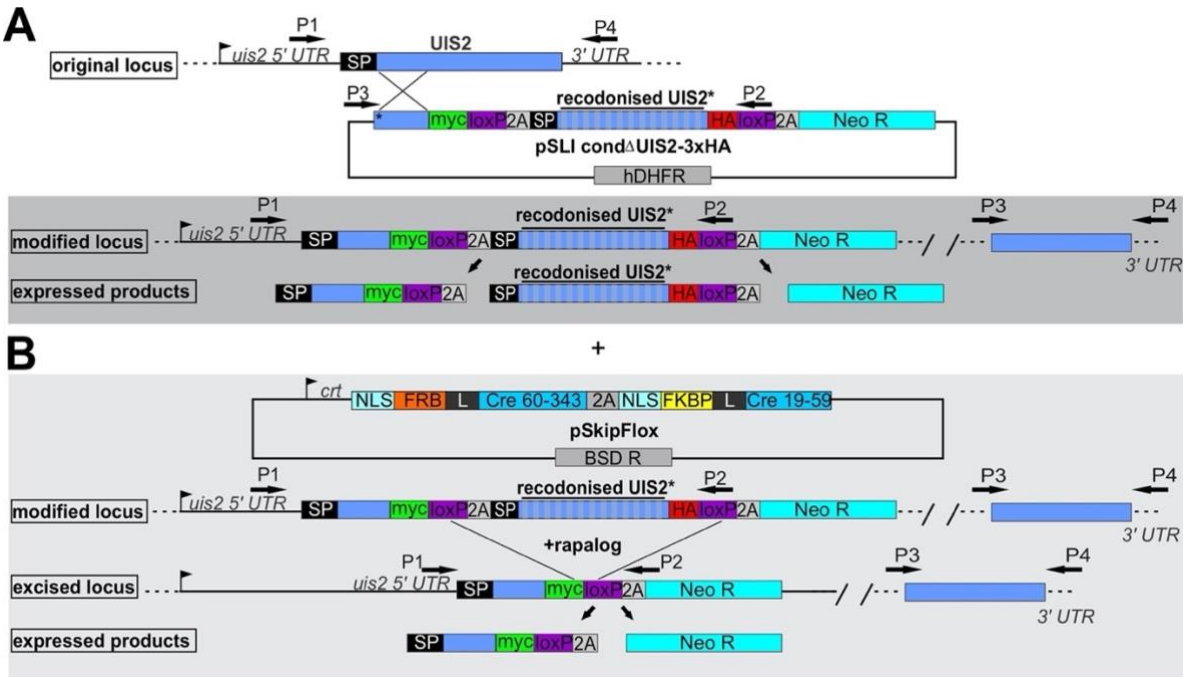

Figure 9. Conditional deletion of a target gene using the diCre-based excision system. (A) The *uis2* gene was disrupted using the Selection-Linked Integration (SLI) system, which was combined with the insertion of a recodonized copy of the gene flanked by loxP sites. The truncated gene segment was conjugated with a myc-tag, and the recodonized version was linked to a 3x hemagglutinin (HA) tag. For episomal selection, human dihydrofolate reductase (hDHFR) was employed and Neomycin facilitates the selection of parasites that have incorporated the SLI plasmid into their genome. Two skip peptides lead to three expressed products. (B) The diCre-recombinase was expressed episomally in two parts. Upon rapalog-addition, the recodonized gene copy was excised, forcing the parasites to rely on the truncated target gene. Black arrows labeled with P1-P4 indicate primer binding sites of primers used to verify the correct plasmid integration into the genomic locus of the target gene and excision of the gene; black boxes indicate the N-terminal SP; UIS2* indicates the recodonized gene. BSD, Blasticidin S deaminase; FKBP, FK506 binding protein; FRB, FKBP rapamycin binding domain; HA, 3x hemagglutinin; hDHFR, human dihydrofolate reductase; L, Linker; Neo, neomycin phosphotransferase II; NLS, nuclear localisation signal; SLI, selection-linked integration; UTR, untranslated region; 2A, T2A skip peptide. Schematic modified from Mésen-Ramírez *et al*., 2019.

2.2.3.11 PCRs to check integration of the plasmid into the genome and the excision of the gene

For assessing the correct integration of the plasmid into the genome and the excision of the gene, genomic DNA (gDNA) was isolated from the transgenic parasite cell lines, followed by PCR analysis. To confirm the proper integration of the SLI-plasmid, two distinct primer pairs were employed (Figure 9). The first set, designed for the 5' end, included a forward primer (P1) targeting just upstream of the gene of interest (or the homology region for genes with extended lengths) and a reverse primer (P2) that

annealed to the selected tag (or to the SLI-resistance gene for shorter tags). The second set, aimed at the 3' end, consisted of a forward primer (P3) that attached to the SLI-plasmid slightly upstream of the homology region and a reverse primer (P4) that bound just downstream of the gene of interest. To demonstrate the elimination of the original, unaltered genomic locus in the analyzed cell lines, primers P1 and P4 were utilized together, with gDNA from 3D7 used as a control. For the examination of gene excision in conditional knock-out cell lines, the same primer pairing approach was used on genomic DNA (gDNA) isolated from parasites cultured in both the presence and absence of rapalog. The forward primer (P1) was designed to bind upstream of the UIS2, PF3D7_1133800 or PF3D7_0922100 gene, whereas the reverse primer (P2) targeted the SLI-resistance gene.

2.2.3.12 Flow cytometry growth assays

Flow cytometry was employed to evaluate parasite growth. Cultures were standardized to a 0.1% parasitemia, and growth was monitored over five consecutive days (excision cycle, 1st cycle, and 2nd cycle). The cultures were divided into two groups: one treated with rapalog and a control without rapalog. The second growth curve commenced on the third day of the first curve, starting again at 0.1% parasitemia and parasitemia levels were measured every 24 hours for another five consecutive days (1st cycle, 2nd cycle, and 3rd cycle). For flow cytometry analysis, 20 µl of the resuspended culture was mixed with 80 µl of RPMI medium containing 1 µl of dihydroethidium (DHE, 4.5 µg/ml, Cayman Chemical) and 1 µl of Hoechst 33342 (5 µg/ml, Chemodex) and incubated for 20 minutes at room temperature, protected from light. To terminate the staining process, 400 µl of FACS staining stop solution (0.003% glutaraldehyde) was added. Using an LSR II flow cytometer (Becton Dickinson), 100,000 events were recorded per sample. Parasitemia was quantified with FACS Diva software version 6.1.3 (Becton Dickinson) (Birnbaum *et al.,* 2017). Growth curves were generated with Graph Pad Prism 8. Version 8.2.0.

2.2.3.13 Shifting the time of UIS2 loss and classification of protein export

The timing of UIS2 excision was adjusted so that the loss of UIS2 impacted the parasites later during ring stage. A 10 ml parasite culture with 2% rings was synchronized with sorbitol (section 2.3.3.5). The cells were washed once with RPMI complete medium and divided into two groups, control and rapalog. The cells were transferred to a 2.5 ml petri dish with 100 µl fresh erythrocytes. Rapalog at 250 nM

was added at various time points to the synchronized ring and early trophozoite stages parasites: (1) Immediately after ring synchronization, referred to as "standard induction" (0 - 8 hours post-induction (hpi)), (2) Later in the ring stage, referred to as "mid-induction" (12 - 16 hpi), or (3) later in the early trophozoite stages, referred to as "late-induction" (20 - 26 hpi) (Figure 10). The cells with standard induction were recultivated for 8 hours using standard culture conditions and were then synchronized with 1 ml prewarmed 5% sorbitol at 37 °C for 10 minutes to obtain 0 - 8 hour old rings. The young rings were washed three times with RPMI, resuspended in RPMI, and split again into two culture dishes. To one dish, 250 nM rapalog was added to induce excision of the *uis2* gene in ring stages; the other dish served as a control. The culture medium was changed daily, and new rapalog (250 nM) was added each time to the cells cultivated in the presence of rapalog. If the parasitemia was too high, the culture was diluted to prevent overgrowth. Parasite development was meticulously monitored with Giemsa-stained blood smears every 24 hours until harvest times A (4 - 12 hpi) or B (26 - 32 hpi) at the 1st cycle (Figure 10). After selecting the right time point, samples from parasites under both conditions, control and rapalog, were taken to perform analyses using immunofluorescence assays (IFAs) (section 2.2.3.15**)**, Western blot (section 2.2.4.2), or live imaging with fluorescence microscopy (section 2.2.5.1).

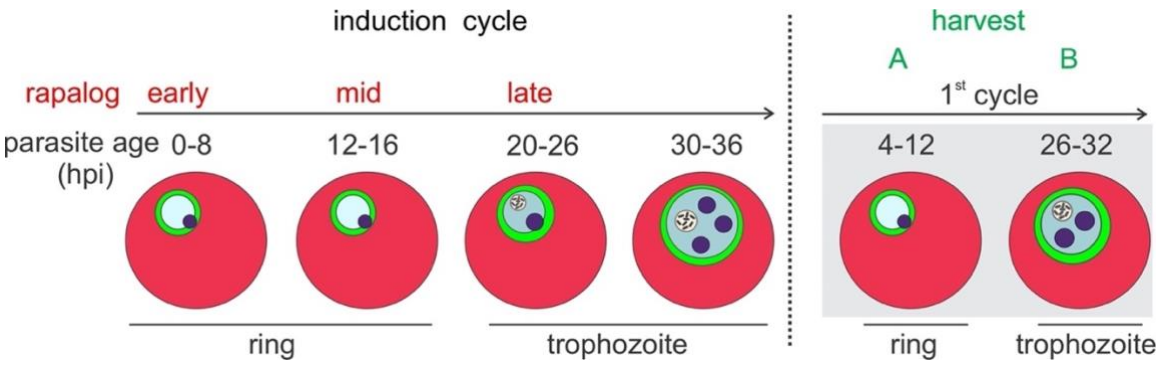

Figure 10. Schematic diagram of the experimental setup for the conditional knockout of UIS2. Induction of the excision of the *uis2* gene at various time points: 0 - 8 hours hpi for 'early induction,' 12 - 16 hpi for 'mid-induction,' or 20 - 26 hpi for 'late induction' in the parasites. The parasites were harvested at point A or B during the first cycle.

To evaluate protein export in parasites lacking UIS2, cells were categorized based on the location of the mScarlet signal within the parasite, host cell cytosol or at the parasite periphery. Full export was characterized by the presence of signal at the

Maurer's clefts (SBP1), at the erythrocyte membrane (KAHRP), or within the erythrocyte cytosol with the glycophorin-binding protein ($GBP^{1-108\ aa}$). Partial export was indicated by signal within the host cell and confined areas inside the parasite. No export was identified by foci inside the parasite with no dispersion of the signal. For the FNT-mScarlet marker, cells were further categorized based on signal presence at the parasite plasma membrane (PPM) or absence thereof. For the soluble marker at the parasitophorous vacuole (PV), cells were assessed for the presence of signal as foci or no signal, confined signal at the PV, or signal present throughout the PV and internally. Parasites were harvested at designated time points during the first cycle, referred to as A or B, depending on the marker being evaluated. The exact timing of harvest was chosen to coincide with the peak expression of the markers of interest to ensure optimal detection and analysis. Live cells were evaluated under fluorescence microscopy (section 2.2.5.1). Image analysis was conducted blindly with respect to the control and rapalog-treated samples.

2.2.3.14 IFAs with formaldehyde- and glutaraldehyde-fixed cells performed in suspension

Immunofluorescence assays (IFAs) in suspension were performed according to established protocols (Tonkin *et al*., 2004; Mesén-Ramírez *et al*., 2019). A 1 ml sample of parasite culture was centrifuged at 10 000 rpm for 1 minute. The pellet was then washed once with 1x PBS (Phosphate-Buffered Saline) and subsequently fixed with 750 µl of a fixation solution (composed of 4% formaldehyde and 0.0075% glutaraldehyde in 1x PBS) for 30 minutes at room temperature. Post-fixation, cells were centrifuged at 10 000 rpm for 1 minute and then washed three times with 1x PBS. Next, the cells were permeabilized with 2-3 pellet volumes of 0.1% Triton X-100 in 1x PBS for 10 minutes at room temperature, followed by another three 1x PBS washes. For blocking, cells were incubated with 100 µl of 3% BSA (Bovine Serum Albumin) in 1x PBS for 1 hour at room temperature and then washed three times with 1x PBS. Cells were then incubated with the primary antibody, diluted in 3% BSA in 1x PBS, for 1 hour at room temperature or overnight at 4°C with gentle agitation to ensure uniform exposure. After incubation, cells were washed three times with 1x PBS. Next, 100 µl of the secondary antibody also diluted in 3% BSA in 1x PBS (1:2000), was added. Nuclear staining was performed by adding DAPI (4',6-diamidino-2-phenylindole) at a final concentration of 1 µg/ml or Hoechst 33342 at a

final concentration of 5 µg/ml to the control and rapalog-cultured cells, which were then incubated for 1 hour at room temperature in the dark. Upon completion of three final washing steps, 5 µl of the cell suspension was placed on a microscope slide, covered with a coverslip, and imaged using an "Axioscope A1" fluorescence microscope by Zeiss. The imaging settings were kept identical for both parasite cultures. The remaining cell pellet was stored at 4°C in 100 µl 1x PBS supplemented with 0.1 mg/ml ampicillin.

2.2.3.15 Immunofluorescence assays (IFAs) with acetone

Acetone-IFAs were conducted in accordance with the protocols established by Spielmann *et al*, (2003). A volume of 500 µl of parasite culture was collected and washed once with 1x PBS. The culture was adjusted to a 2-3% haematocrit level, and a thin layer was applied onto a 10-well microscopy slide (manufactured by Thermo Scientific). The slide was then left to dry at room temperature and subsequently fixed using 100% acetone for 30 minutes at the same temperature. After fixation, the slide was placed in a humid chamber, and 50 µl of 1x PBS were added to each well to rehydrate the cells for 10-15 minutes. Next, the cells were washed three times 1x PBS. The antigen-specific primary antibody was diluted in 3% BSA in 1x PBS and incubated for one hour. After the incubation time, cells were washed five times with 1x PBS. Then the organism-specific secondary antibody conjugated with a fluorophore was added and incubated for 1 hour protected from light. DAPI staining was carried out to a final concentration of 1 µg/ml. After the incubation period, the slide was washed five times with 1x PBS and dried at 37°C in the incubator. The slide was covered with a coverslip using 4 drops of Dako fluorescent mounting medium (DAKO, Inc), applied meticulously to prevent the formation of air bubbles. To secure the coverslip, nail polish was applied at the outer area of the slide and allowed to dry at room temperature. The IFA was analyzed using fluorescence microscopy (section 2.2.5.1).

2.2.3.16 DiQ-BioID: Proximity-induced dimerization facilitates *In vitro* biotinylation of interacting proteins

To conduct DiQ-BioID, 150 ml of asynchronous cultures of parasite cell line, with endogenously FKBP-tagged targets, UIS2-2xFKBP-GFP and expressing episomal biotinylizer (SP-BirA*-FRB-mCherry), were divided into two identical cultures with a starting parasitemia of 1-2%. Both cultures were grown in RPMI complete medium

supplemented with 50 µM biotin (Sigma-Aldrich) and 2 µg/mL blasticidin S (Invitrogen), with rapalog added to one of the cultures to achieve a final concentration of 250 nM. After 12 - 14 hours, the medium and supplements were changed. The mixed-stage parasite cultures were then incubated for 24 hours in the presence of biotin and rapalog, resulting in parasitemia levels reaching approximately 10% after this period. Cultures were then centrifuged at 6000 x g for 20 minutes at room temperature and the supernatant was discarded. Parasites were lysed using 0.03% saponin in 1x PBS on ice for 10 min, followed by five washes in 1x PBS. Lysis for mass spectrometry analysis was carried out using 2 ml of lysis buffer (50 mM Tris-HCL pH 7.5, 500 mM NaCl, 1% Triton-X-100) per condition, with subsequent washing steps to remove unbound material. DTT (final concentration of 1 mM), 160 µl of 25x protein inhibitor cocktail (Roche), and PMSF (final concentration of 1 mM) were added, and the lysate was frozen at -80 °C, subjected to two freeze-thaw cycles and centrifuged at 16 000 g for 10 min. The supernatant was then diluted 1:2 in 50 mM Tris-HCl pH 7.5. For the purification of biotinylated proteins, 50 µl of Streptavidin-Sepharose beads (equilibrated in 50 mM TrisHCL pH 7.5) were added to the lysate and incubated overnight at 4 °C with rotation. The beads were washed twice with lysis buffer, dH_2O (Ampuwa), TrisHCl pH 7.5, and 100 mM Triethylammonium bicarbonate buffer pH 8.5 (TEAB, Sigma-Aldrich), with centrifugation after each step at 1600 x g for 2 minutes at room temperature. After the final washing step, the sepharose beads were resuspended in 50 µl 100 mM TEAB and shipped on ice for mass spectrometry analysis. The mass spectrometry analysis was performed by Pascal Wilhelmus Theodorus Christianus Jansen (Radboud Institute, Nijmegen, Netherlands) using dimethyl labeling for quantification (Boersema et al., 2009).

2.2.4 Biochemical Methods

2.2.4.1 Sodium dodecyl sulphate- polyacrylamide gel electrophoresis (SDS PAGE)

Proteins were separated based on their molecular weight using sodium dodecyl sulphate-polyacrylamide gel electrophoresis (SDS-PAGE) under denaturing conditions (Laemmli, 1970). This method employs discontinuous gel electrophoresis, where the proteins' intrinsic charge is neutralized by SDS, causing them to unfold into linear molecules with a uniform negative charge. The amount of SDS bound to each polypeptide chain is proportional to its molecular mass, ensuring separation is

primarily based on differences in molecular weight. DTT (dithiothreitol) present in the SDS sample buffer leads to the reduction of disulfide bonds, contributing to an unfolded conformation. Gels were prepared with concentrations of either 10% or 12% acrylamide, polymerized using ammonium persulfate (APS) and TEMED as a catalyst. The separating gel was overlaid with isopropanol to achieve a smooth surface, which was then replaced by a stacking gel with a 5% concentration to form wells using 10 - 15-wells combs (Bio-Rad). Protein samples, after heat denaturation and centrifugation at 13 200 rpm for 5 minutes, were mixed with reducing 4x SDS sample buffer and heated at 85° - 90°C for 5 minutes. Equivalent volumes of these samples were loaded into the gel alongside a pre-stained protein ladder (PageRulerTM prestained or plus prestained protein ladder, Thermo Scientific) as molecular weight markers. Electrophoresis was run at 150 V for approximately 90 minutes in an electrophoresis chamber (Bio-Rad) filled with 1x SDS running buffer (250 mM Tris-Base, 1.92 M Glycine, 1% SDS). After electrophoresis, the gels containing the separated proteins were subjected to Western blot analysis (section 2.2.4.2).

2.2.4.2 Western blot

Proteins separated by SDS-PAGE (section 2.2.4.1) were transferred onto nitrocellulose membranes to prepare for subsequent immunodetection, employing a wet transfer method. The transfer stack was assembled by aligning the SDS-PAGE gel directly against the nitrocellulose membrane, with three layers of Whatman filter paper on each side and a supportive metal sponge placed within a specialized blotting cassette. The entire assembly was then placed in a tank blotting system, ensuring the membrane was adjacent to the anode and the gel to the cathode. This configuration ensured that the negatively charged proteins migrated toward the membrane under the influence of the electric field. The blotting chamber was filled with re-cooled 1x transfer buffer (10 x SDS-electrophoresis buffer, 20% methanol in distilled H_20), which was maintained at 4°C to preserve protein integrity and prevent overheating throughout the transfer process. The protein transfer was initiated by applying a steady voltage. For rapid transfer, a voltage of 100 V was applied for 90 minutes, or for a gentler transfer, a voltage of 15 V was applied overnight.

2.2.4.3 Protein immuno-detection

After Western blotting, immunodetection was carried out to visualize the proteins. To prevent non-specific binding of antibodies, the membrane was blocked with 5% milk powder in 1x PBS for 1 hour at room temperature. Next, the membrane was incubated with a primary antibody specific to the antigen of interest. This antibody was diluted in the blocking solution and applied to the membrane for 2 hours at room temperature or, alternatively, left overnight at 4°C with gentle agitation. After the incubation with the primary antibody, the membrane was washed three times with 1x PBS for 5 minutes each to remove unbound antibodies. A secondary antibody, which is organism-specific and conjugated to horseradish peroxidase (HRP), was prepared in the same blocking solution and then applied to the membrane. The membrane was incubated for 1 hour at room temperature, with protection from light. After binding of the secondary antibody, the membrane was washed three times with 1x PBS for 5 minutes each to eliminate non-specifically bound secondary antibodies. For chemiluminescence detection, the membrane was incubated with a mixture of 1 ml luminol/enhancer solution and 1 ml peroxide solution, sourced from either the ECL Clarity Detection Kit (Bio-Rad) or the ECL SuperSignal West Pico (Thermo Scientific), and agitated gently for 1 minute at room temperature and the signal were recorded with a ChemiDoc XRS imaging system (Bio-Rad) equipped with Image Lab software 5.2 (Bio-Rad).

2.2.5 Microscopy

2.2.5.1 Live cell and fluorescence microscope

Microscopy of live parasite-infected erythrocytes was performed as previously described (Grüring & Spielmann, 2012). To analyze the proteins of *P. falciparum*, the target genes were genetically modified and tagged with different fluorochromes such as GFP (green fluorescent protein), mCherry, or mNeonGreen (green fluorescent protein). This tagging allowed for detection after expression in the cells, and the proteins were visualized by fluorescence microscopy. Nuclear staining was performed by adding DAPI (4',6-diamidino-2-phenylindole) at a final concentration of 1 µg/ml or Hoechst 33342 at a final concentration of 5 µg/ml, followed by incubation for 10 minutes at room temperature. The cells were then centrifuged for 1 minute at 1800 x g, and the pellet was resuspended in one-third of the supernatant. A 5 µl sample was transferred to a glass slide and covered with a coverslip. Cells were

imaged using an Axioscope A1 microscope equipped with a 100X/1.4 numerical aperture oil immersion objective. An Orca C4742-95 digital camera and the Axiovision software 4.7 (Zeiss) were used to collect images. GFP and mNeonGreen-labeled proteins both have absorption maxima wavelengths of 395/475 and emit at 509/540 nm. The fluorochrome mCherry has an absorption/emission spectrum with peaks at 587 nm and 610 nm, respectively. For co-localization studies, images were taken with identical microscope acquisition settings. Parasite size measurement was based on the DIC channel, and was measured using Fiji software (Schindelin *et al.*, 2012). Images were processed using Corel PHOTO-PAINT version X8.

2.2.5.2 Confocal microscope

Laser scanning confocal microscopy of live cells was performed at 37 °C using an Olympus FluoView FV3000 system equipped with a Universal Plan Apochromat objective (60×, 1.5 NA, oil) and a cell Vivo incubation system.

2.2.6 Analysis of *Pf*UIS2 phosphatase domain structure and prediction of binding sites

Multiple Sequence Alignments were performed with Clustal Omega (Sievers *et al*., 2011) (https://www.ebi.ac.uk/Tools/msa/clustalo/). The complete three-dimensional structure (3D) of *Pf*UIS2 (AF-Q8IKJ1-F1) was obtained from the AlphaFold database, (https://alphafold.ebi.ac.uk/). This structure underwent structural analysis using SWISS-Model (Waterhouse *et al*., 2018) (https://swissmodel.expasy.org/). The analysis aimed to identify similar phosphatases, leveraging the extensive database of crystal structures of metallophosphoesterases. Based on the USI2 model, the meta-server COACH (Jianyi *et al.*, 2013a; Jianyi *et al.*, 2013b) (https://zhanggroup.org/COACH/) and COFACTOR (Roy *et al.*, 2012; Zhang *et al.*, 2017) (https://zhanggroup.org/COFACTOR/) were used to predict protein-ligand binding sites. Comparative studies were conducted with crystal structures of human (PDB ID: 2BQ8), rat (PDB ID: 1QHW), and pig (PDB ID: 1UTE) purple acid phosphoesterases from the protein data bank, focusing on their catalytic cores in relation to *Pf*UIS2. Visualization and alignment of the protein structures were accomplished using PyMOL, Version 2.5 by Schrödinger, LLC (https://pymol.org/2/).

2.2.7 Software

Statistical analysis was conducted using GraphPad Prism version 8 (GraphPad Software, USA). Microscopy images were processed with Corel Photo-Paint X8 (htpps://www.coreldraw.com) and Fiji (Schindelin *et al*., 2012). Plasmid and oligonucleotide designs were facilitated by ApE software (Davis & Jorgensen, 2022), while protein structures were analyzed and visualized with PyMol (Schrödinger, USA). All figures were compiled using CorelDraw X8.

3 Results

To understand the function of the PV-resident phosphatase UIS2 (PF3D7_1464600), it is necessary to obtain a detailed characterization of the phenotype of *P. falciparum* parasites lacking UIS2. Therefore, the conditional *uis2* KO (cond∆UIS2) cell line previously generated (Khosh-Naucke, 2018) was verified and characterized in detail followed by experiments for the functional analysis of UIS2.

3.1 Validation and kinetics of the conditional deletion of *uis2*

The previously designed conditional *uis2* KO (cond∆UIS2) cell line, obtained from Khosh-Naucke, 2018, was generated using genome editing with the selection-linked integration system (SLI) (Birnbaum *et al* 2017; Mesén-Ramírez *et al.*, 2019). With this approach the gene encoding UIS2 was disrupted and a floxed functional copy of *uis2* was provided at the same genomic locus that was tagged with 3xHA (Figure 11A, modified locus). The parasites with the corresponding integration of the plasmid into the genome were transfected with pSkipFlox (Birnbaum *et al*., 2017). This plasmid encodes split Cre recombinase (diCre), which can be induced to dimerize by the addition of the small ligand rapalog. This dimerization activates the recombinase, and this leads to the excision of *uis2* (Jullien *et al.*, 2007; Andenmatten *et al.*, 2013; Collins *et al.*, 2013). The correct integration of the plasmid into the genome was re-confirmed by PCR in this study (Figure 11B).

To analyse the effect of *uis2* deletion, the kinetics of protein loss was first assessed. For this, different analyses were conducted to test for gene loss and protein loss. For the former, diCre activation for *uis2* excision was initiated by adding rapalog to synchronized ring stage parasites. This led to gene excision while the previously expressed UIS2 was still in the PV and maintaining parasite viability during the first cycle of induction (“excision cycle") (Figure 11C-E, 24 hours post induction rapalog (hpi)). When this cycle was complete, the infected RBC ruptured, leaving behind all previously expressed UIS2 with the PVM that is shed in this process. Hence, when the parasites invaded fresh RBCs to initiate the next cycle ("1st cycle"), they began without UIS2 in their PV (Figure 11C-E, 48 hpi). To confirm in detail that the cell line behaved as expected, the excision of the active *uis2* gene was demonstrated by PCR at 24 h and 48 h post addition of rapalog. The bands observed demonstrate efficient

excision of the functional copy of *uis2* (Figure 11C). The control cells maintained the original genomic locus (intact *uis2* locus) at both time points (Figure 11C). Taken together, these PCR results confirmed that complete excision of the functional *uis2* gene is achievable within a single asexual growth cycle.

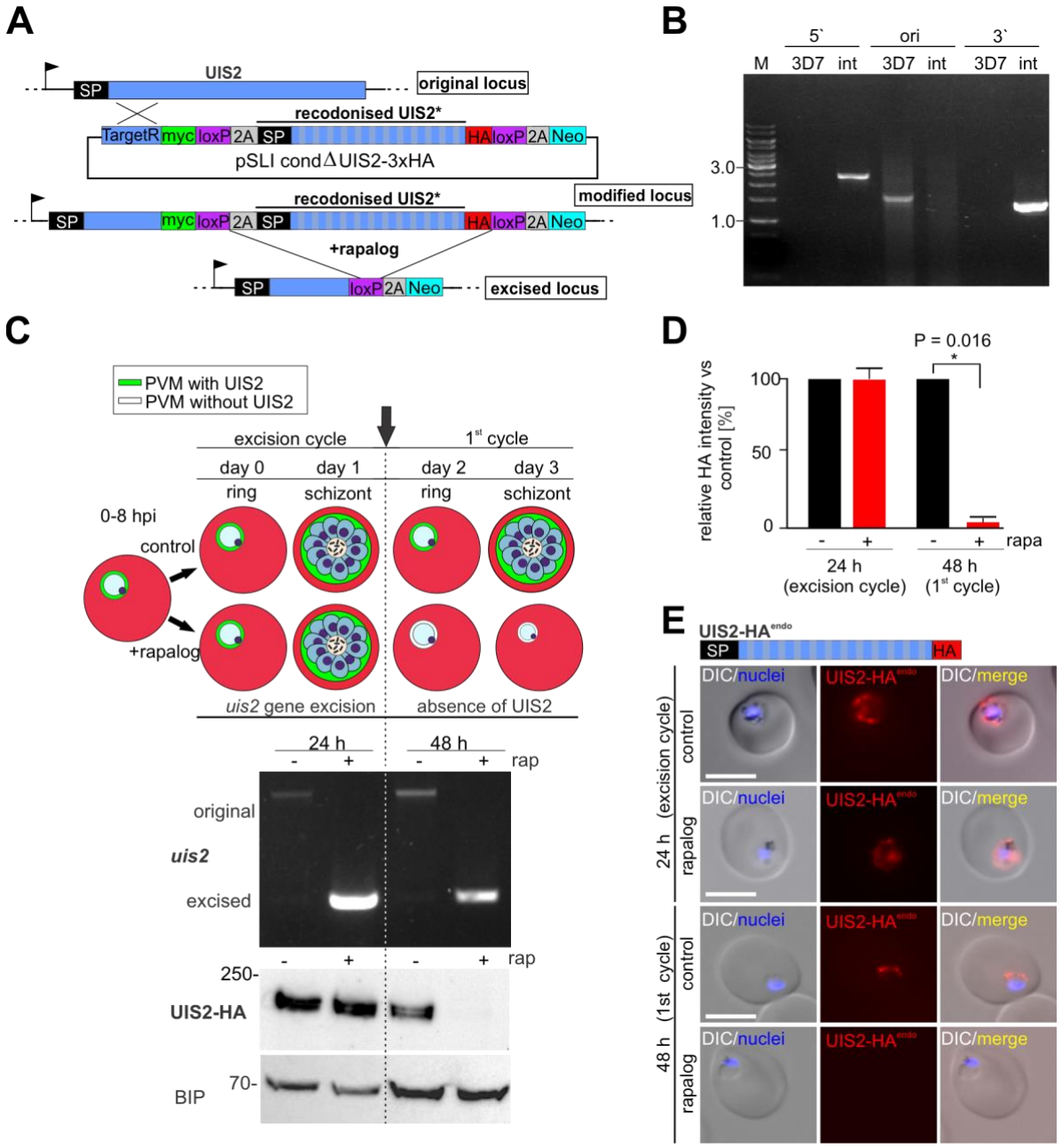

Figure 11. Validation of conditional uis2 knock out cell line. (A) Simplified schematic of the generation of the diCre-based condΔUIS2 knockout cell line using SLI and subsequent excision upon the addition of rapalog (modified from Mesén-Ramírez *et al*, 2019). Black arrows, native *uis2* promotor; blue box, target region (TargetR) for homologous recombination; blue/gray striped box, recodonized UIS2; cond, conditional; HA, 3x human influenza hemagglutinin; 2A, T2A skip peptide. Full condΔUIS2-SLI schematic is shown in Appendix 2. (B) Agarose gel showing PCR-products to assess

correct integration of the SLI-plasmid into the genome to obtain the indicated cell line. For *Pf*3D7_1464600-HA^{endo}, primers (Appendix 1) were “1464600-Int-fw” + 3`UTR-rv” to demonstrate 5’ integration (5’ int, 2449 bp) and “pARL55-fw” + “1464600-Int-rv” to demonstrate 3’ integration (3’ int, 1439 bp). Primers “1464600-Int-fw” + “1464600-Int-rv” were used to show absence of unmodified original locus in the respective cell line (ori int) and 3D7 gDNA was used as a control (ori 3D7, 1707 bp). M, marker (GeneRuler^{TM} 1kb, Thermo Scientific); DNA fragment size standard is indicated in kbp. (C) Top: schematic representation of experimental setup for condΔUIS2 by inducing excision of *uis2* in 0 - 8 hpi ring stage parasites divided in two cultures, one with rapalog and one without rapalog (control). Top image: agarose gels showing PCR-products to test for excision of the floxed functional *uis2* in ΔUIS2 knockout (+rapalog) and control (without rapalog) condΔUIS2 parasites at 24 h and 48 h post-rapalog addition. Bottom image: Western blot using anti-HA (from rat) confirmed knockout of UIS2 on the protein level 24 and 48 h post-rapalog addition. The expected molecular weight of UIS2-3xHA is 170 kDa. Anti-BIP (from rabbit) served as loading control. Molecular weight standard is indicated in kDa. One representative experiment of three biological replicas; full blots and replica in Appendix 3. (D) Quantification of UIS2-3xHA levels based on densitometric analysis of anti-HA immunoblots at the indicated time points (mean of n = 3 independent experiments) (immunoblots used for quantification are shown in Appendix 3). HA signal was normalized to BIP. P value is indicated (unpaired two-tailed t-test). Error bars indicate standard deviation (SD). (E) IFA of formaldehyde/glutaraldehyde fixed ΔUIS2 (+rapalog) and control (without rapalog) condΔUIS2 parasites at 24 h and 48 h post addition of rapalog showing localization of UIS2-3xHA^{endo}. Anti-HA (from rat) was used to detect UIS2-3xHA^{endo}. Representative cells from one of three independent experiments with at least 20 image series per experiment and condition. DIC: differential interference contrast. Nuclei were stained with Hoechst. Size bar = 5µm. BIP, binding immunoglobulin protein.

Next, the protein level of UIS2 in ΔUIS2 parasites was assessed by Western blot analysis at 24 h and 48 h post addition of rapalog. In α-HA Western blot analysis (Figure 11C), it was observed that the UIS2 protein derived from previous expression (and possible left-over mRNA) remained in comparable amounts to the control (Figure 11C,D, 24 h after induction). In contrast, during the next replication cycle (1st cycle), Western blot analysis indicated the loss of UIS2 (approximately 5% residual protein) observed 48 h after induction (Figure 11C,D). This was in comparison to a prominent band observed in the control, which had the expected molecular weight of 170 kDa (Figure 11C). Confirming the Western blot results, the HA-tagged UIS2 arising from the floxed functional *uis2* was detected around the parasite by immunofluorescence assays (IFAs) at 24 h (control and condΔUIS2 parasites) but was absent in the ΔUIS2 parasites 48 h after addition of rapalog (Figure 11E). Overall, these findings indicated that the UIS2 present during the excision cycle was lost when the parasites egressed from the host cell, resulting in ΔUIS2 parasites in

the 1st cycle. This validated that this cell line can be used to achieve a conditional knock out of *uis2* and that no major effects are expected during the excision cycle.

3.2 Lack of UIS2 severely impairs the viability of the parasites

After demonstrating the effective excision of the functional *uis2* and the absence of UIS2 in the 1st cycle post-rapalog addition (see section 3.1), the importance of UIS2 for parasite survival was assessed. The growth of cond∆UIS2 parasites was monitored over five consecutive days, using the same culture split into one with rapalog and a control without rapalog (Figure 12A). The growth curves showed similar parasitemia until day 3 post-rapalog addition, but there was a failure of the ∆UIS2 parasites to expand on day 4, while the control parasites continued to multiply (Figure 12A). This indicates that – in agreement with the finding that UIS2 protein levels do not change in the excision cycle (Figure 12B,C) – the *uis2* gene can be removed during the excision cycle by rapalog induction without impact on growth, resulting in parasites that start the first cycle without UIS2, leading to a growth defect (Figure 12A). Tracking growth of ∆UIS2 ring stage parasites showed that this growth defect was severe, and the loss of UIS2 almost entirely abolished parasite multiplication (Figure 12B).

The growth defect was examined in further detail through an analysis of the parasite stages present in ∆UIS2 and control parasites at different time points (provided by Melissa Khosh-Naucke) (Figure 12C). Flow cytometric analysis of DHE-stained parasites showed that while the parasitaemia on day 2 (1st cycle rings) was identical, the parasites lacking UIS2 remained as rings also on day 3 (1st cycle trophozoites and schizonts), whereas the control cells had already developed to the trophozoite stage (Figure 12C). This was corroborated by an analysis of Giemsa smears to monitor the growth and morphology changes in ∆UIS2 ring stage, starting with rings from the first cycle compared to the control. While the control progressed through the cycle, the ∆UIS2 rings did not develop into trophozoites (Figure 12D). Instead, these parasites arrest as rings of small diameter ("phenotype rings", Figure 12D, black arrows), and over time either remained in this state or appeared as pyknotic cells (Figure 12D, grey arrow). These results indicate that UIS2 is needed for blood stage growth and that parasites starting a new cycle without UIS2 arrest in early ring stage.

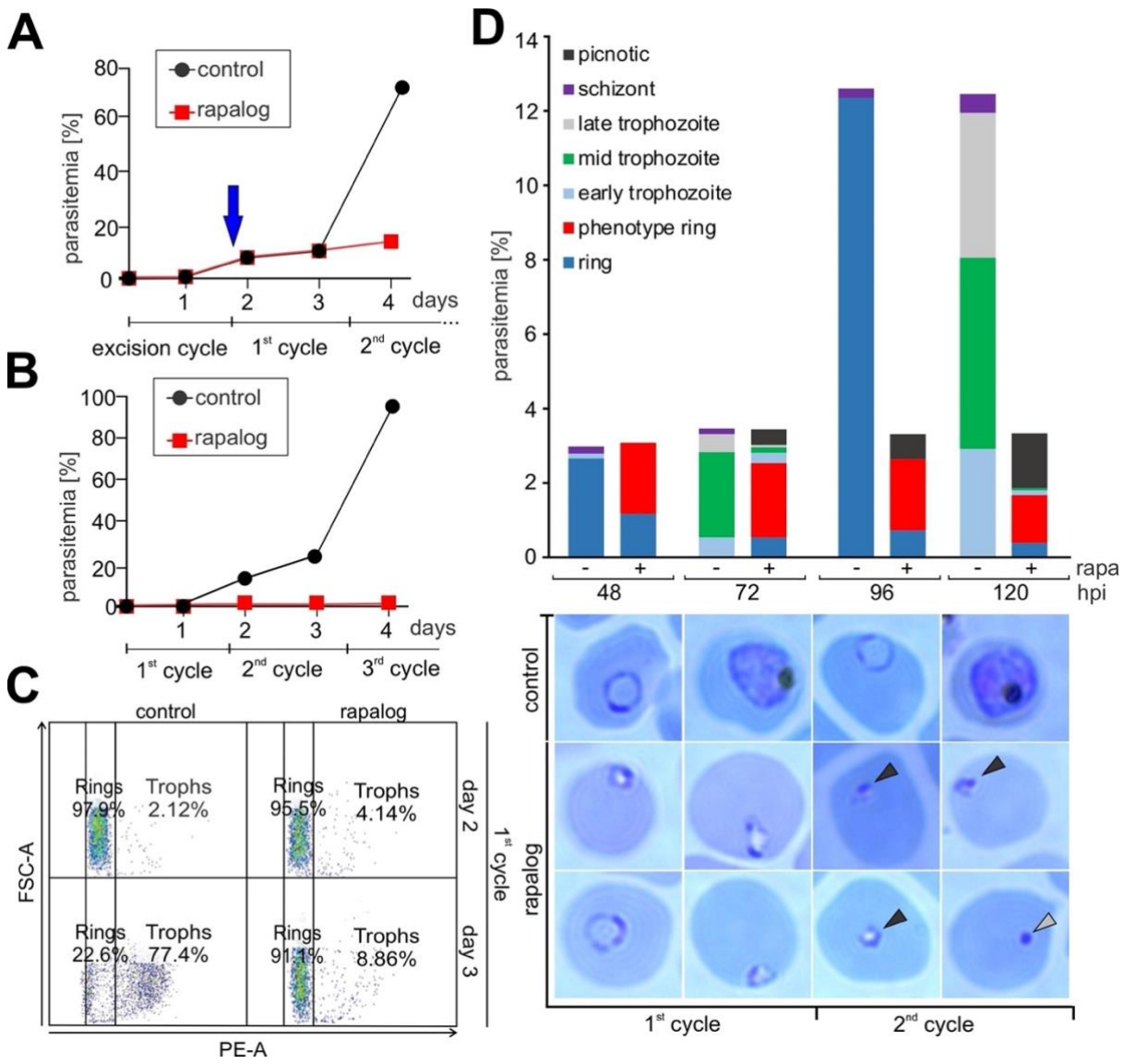

Figure 12. UIS2 is essential for asexual blood stage development. Flow cytometry growth curves of synchronous ring stage condΔUIS2 parasites starting either at the excision cycle (A) or cycle 1 (B) on 5 consecutive days. Blue arrow indicates invasion into the first cycle and loss of UIS2. One representative of n = 4 independent experiments (replicas are shown in Appendix 4). (C) Flow cytometry-based quantification of ring and trophozoite stage parasitaemia of condΔUIS2 parasites in the excision (24 h) and first (48 h) cycle after addition of rapalog; x - axis: PE-A represents DHE staining; y-axis: FSC-A = forward scatter. One representative experiment with a sample size of n= 100 000 cells per condition at each evaluated time. (D) Stage distribution of condΔUIS2 parasites in Giemsa-stained smears of synchronous parasites grown with (+) or without (−) rapalog at 48 h, 72 h, 96 h or 120 h after adding rapalog (hpi). Stage classification of parasites is indicated. Representative microscopy images of Giemsa-stained thin smears of the experiment shown in the graph are shown below the graph. Images are representatives of one microscopy session with at least 15 image series per time point. One experiment in total (n = 1). Black arrow indicates phenotype rings and grey arrow indicates pyknotic or dead parasites. hpi: hours post induction rapalog.

3.3 Lack of UIS2 impairs trafficking of exported proteins

The small ring phenotype observed in ΔUIS2 parasites showed similarity to either plasmepsin V knockout (Boonyalai *et al.*, 2018) or knockdown (Polino *et al.*, 2020) and in *T. gondii* parasites, the likely putative orthologue of UIS2 is needed for the export of effectors into the host cell (Blakely *et al*, 2020; Cygan *et al*, 2020). Therefore, to determine the cause of the loss of viability in those parasites, protein export was analysed. For this the location of the exported protein skeleton binding protein 1 (SBP1), an integral membrane protein of the Maurer´s clefts (MCs) (Blisnick *et al*., 2000), and the knob-associated histidine-rich protein (KAHRP), which assembles at the cytoplasmic face of the host cell membrane (Culvenor *et al.,* 1987; Pologne *et al.,* 1987) was assessed in ΔUIS2 rings using immunofluorescence assays (IFAs) (Figure 13A,B).

SBP1 and KAHRP exhibited noticeable differences in their locations between cells with and without UIS2. In the control group, SBP1 was correctly trafficked to the Maurer's clefts, whereas in the ΔUIS2 parasites, SBP1 failed to undergo proper trafficking, resulting in its concentration in a focal area within the parasite (Figure 13A). Similarly, the trafficking of KAHRP was adversely affected; while the control cells correctly trafficked KAHRP to the erythrocyte membrane, cells lacking UIS2 were unable to transport into the host cell (Figure 13B). These results could indicate a specific trafficking defect in proteins transported beyond the parasite PPM. However, since the parasites arrested in development, it could also indicate that this was an unspecific effect resulting from a growth arrest with an indirect halting of trafficking processes due to viability loss.

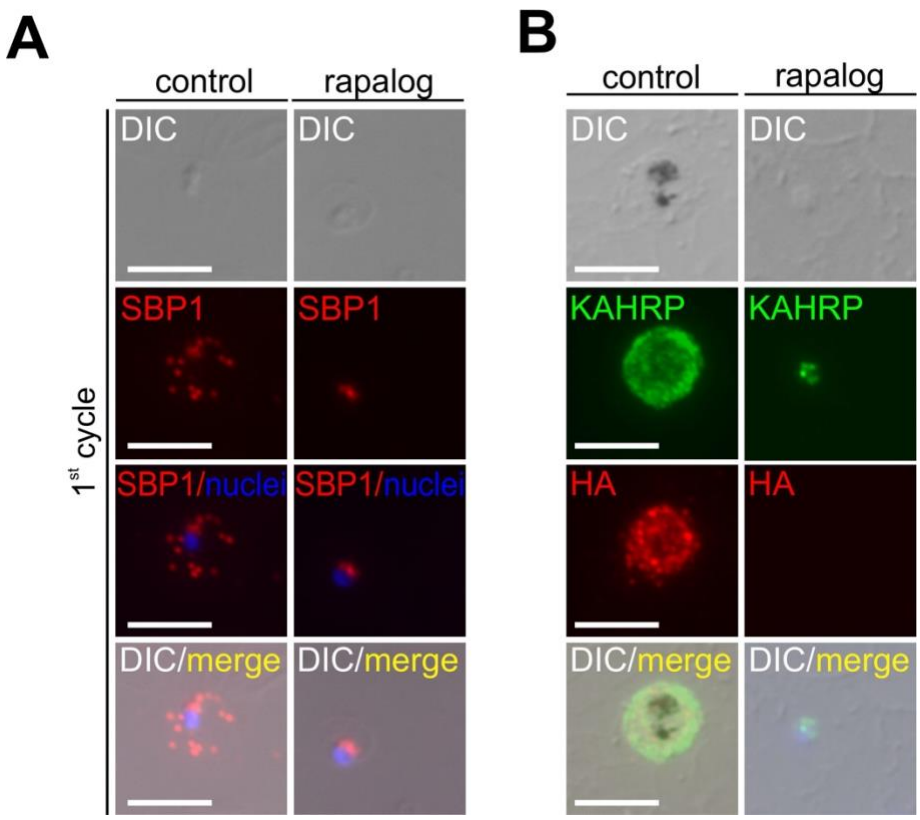

Figure 13. Conditional knock out of UIS2 result in SBP1 and KAHRP export defect. Microscopy images of IFAs using acetone-fixed cells of ΔUIS2 parasites (+rapalog) and control (without rapalog) condΔUIS2 parasites at the 1st cycle, showing failure to export SBP1 (A) and KAHRP (B). Anti-SBP1 and KAHRP (both from rabbit) were, anti-HA (from rat) to detect UIS2-HA (in B only). Images are representatives of 3 independent experiments. DIC: differential interference contrast; nuclei were stained with DAPI; merge indicates overlay of all fluorescent channels. Size bar = 5µm.

3.4 UIS2-KO results in a defect in protein export

To differentiate whether the observed disturbance of protein trafficking in the UIS2-KO was attributable to a specific effect on proteins export or if it arose from a general loss of viability of the observed small ring stage parasites, a series of pilot experiments were carried out. In these experiments, the timing of *uis2* excision was shifted in a way that the UIS2 loss affected the parasites after the ring stage (Figure 14A and Figure 15A). An initial test of induction regimes revealed that when rapalog was added later in the ring stage of the excision cycle (12 - 16 hpi), referred to as 'mid induction' or even later (20 - 26 hpi), referred to as 'late-induction', the parasites had sufficient UIS2 to move further into the first cycle (Figure 14A, Figure 15A). The mid and late-induction strategy resulted in a significant number of parasites progressing to the trophozoite stage (Figure 14B,C; 1st cycle). This was evident

through the analysis of Giemsa smears, which were used to monitor the growth and morphological changes in ΔUIS2 rings under these induction regimes compared to the control. While the synchronized parasites in the control progressed through the cycle, the majority of ΔUIS2 rings in ‘mid induction’ showed various stages, including "phenotype rings," young to mid trophozoites, and few parasites that showed a growth rate comparable to the control (Figure 14B). The ΔUIS2 rings from the first cycle under the ‘late-induction’ regimen showed a growth rate similar to the control but with a development delay and a stage and phenotype distribution resembling that of the mid induction at 120 hpi (Figure 14C).

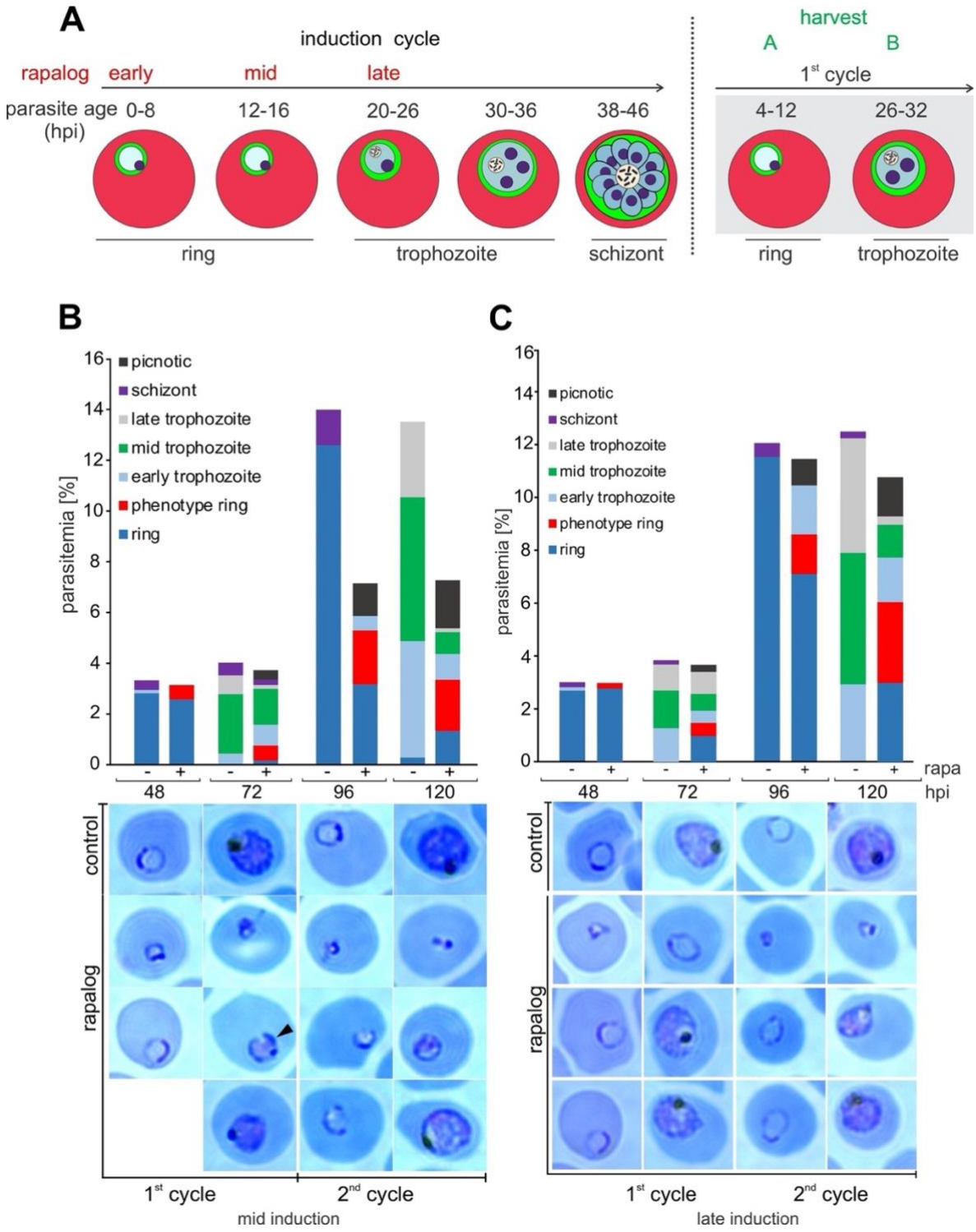

Figure 14. Shifting the time of UIS2 loss results in parasites progressing beyond the ring stage. (A) Schematic representation of experimental setup for conditional knockout of UIS2 by inducing excision of *uis2* in 0 - 8 hpi ('early induction'), 12 - 16 hpi ('mid induction') or 20 - 26 hpi ('late-induction') parasites. Parasites were harvested at point A for the analysis of SBP1 and at point B for the analysis of KAHRP. (B, C) Stage distribution of condΔUIS2 parasites ('mid induction') (B) and ('late-induction') (C) in Giemsa-stained smears of synchronous parasites grown with (+) or without (−) rapalog at 48 h, 72 h, 96 h or 120 h after adding rapalog (hpi). Stage classification of parasites is indicated. Representative images of 1st cycle (48, 72 hpi) and 2nd cycle (96 and 120 hpi) are shown below the

graph. Images are representatives of one microscopy session with at least 15 image series per time point. One experiment in total (n = 1). Black arrow indicates a UIS2 knockout trophozoite of the stage used for the experiments shown in Figure 15B,C.

The ΔUIS2 parasites under the two induction regimes were examined by IFAs using antibodies detecting SBP1 and KAHRP (Figure 15B,C). Following mid-rapalog induction (12 - 16 hpi), rings from the first cycle (Harvest A) were used to evaluated SBP1 (marker to evaluate early protein export) and young-mid trophozoites (Harvest B) to evaluated KAHRP (marker to evaluate later protein export as it is not expressed in rings). IFAs showed that these parasites exhibited a complete absence of detectable UIS2 and showed variable export defects in both exported proteins SBP1 and KAHRP, with some cells showing no export (SBP1: 42.4% ± 7.5%, KAHRP: 6.8% ± 2.6%), some showing partial export (SBP1: 41.3% ± 4.0%, KAHRP: 86.7% ± 4.7%), with a portion of the protein population located within the host cell and another portion being arrested in confined areas inside the parasite (white arrows), and others showing full export (SBP1: 16.3 ± 3.5%, KAHRP: 6.5 ± 2.1%) (Figure 15B-E).

In the case of the later rapalog induction (22 - 26 hpi), a larger percentage of cells showed full export of SBP1 and KAHRP (SBP1: 77.8% ± 6.5%, KAHRP: 66.5% ± 5.1%), while fewer cells with partial (SBP1: 7.1% ± 2.6%, KAHRP: 22.1% ± 2.9%) or no export (SBP1: 14.9% ± 5.0%, KAHRP: 11.2% ± 2.3%) were observed, behaving nearly similar to the control wherein SBP1 was correctly trafficked to the MCs, and KAHRP to the erythrocyte membrane (Figure 15B-E). These results indicated that the export defect also occurred in trophozoites, speaking against a general growth defect that would indirectly lead to the export defect in ΔUIS2 rings obtained with the early induction regime. The observed variation in export levels between individual cells likely originated from different times when individual cells lost sufficient UIS2 to result in a phenotype. Shifting the induction time point also demonstrated the significance of UIS2 for growth in parasites that had developed beyond the ring stage.

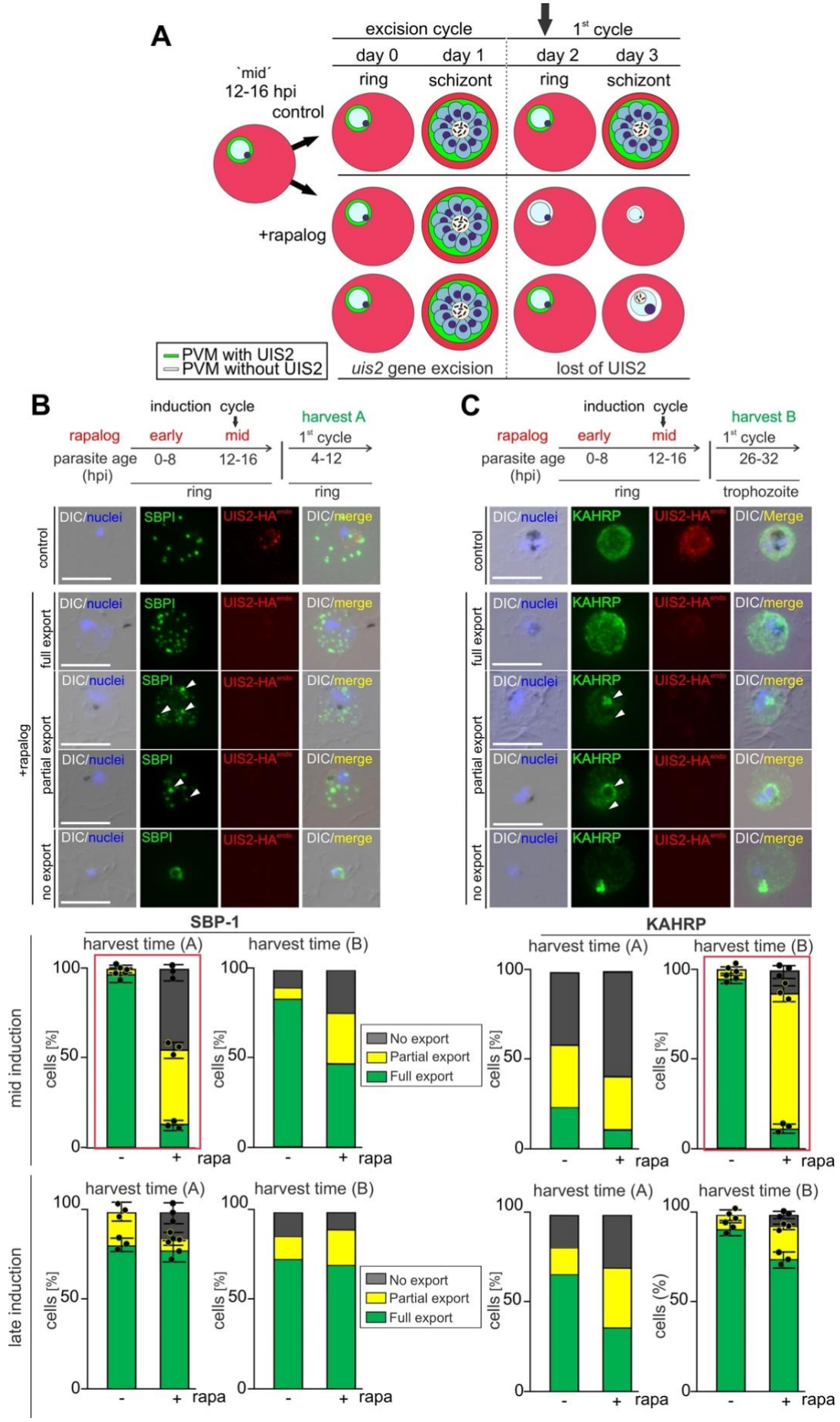
A
excision cycle
1st cycle
day 0
day 1
day 2
day 3
ring
schizont
ring
schizont
`mid´
12-16 hpi
control
+rapalog
PVM with UIS2
PVM without UIS2
uis2 gene excision
lost of UIS2
B
induction cycle
rapalog
early
mid
harvest A
1st cycle
parasite age (hpi)
0-8
12-16
4-12
ring
ring
control
+rapalog
full export
partial export
no export
DIC/nuclei
SBPI
UIS2-HAendo
DIC/merge
C
induction cycle
rapalog
early
mid
harvest B
1st cycle
parasite age (hpi)
0-8
12-16
26-32
ring
trophozoite
KAHRP
DIC/Merge
SBP-1
KAHRP
harvest time (A)
harvest time (B)
mid induction
late induction
cells [%]
100
50
0
- + rapa
No export
Partial export
Full export

Figure 15. UIS2-KO results in a protein export defect. (A) Schematic representation of experimental setup for conditional UIS2 knockout by inducing excision of *uis2* at 12 - 16 hpi ring stage parasites ('mid- induction'). (B) IFA using acetone-fixed cells of condΔUIS2 parasites (control) and ΔUIS2 parasites (+ rapalog) at the 1st cycle (72 h post addition of rapalog). Anti-SBP1C (from rabbit) was used to show SBP1 localization in 4 - 12 h ring stages (Harvest time A). (C) IFA using acetone-fixed cells of condΔUIS2 parasites (control) and ΔUIS2 parasites (+ rapalog) at the 1st cycle (96 h post addition of rapalog). Anti-KAHRP (from rabbit) used to showed KAHRP localization in 26 - 32 h trophozoite stages (Harvest time B). DIC: differential interference contrast; nuclei were stained with DAPI; merge indicates overlay of all presented channels. Size bar = 5µm. Cells were categorized based on the GFP signal into full export (observed at the Maurer's clefts (SBP1) (D) and erythrocyte membrane (KAHRP) (E)), partial export (observed within the host cell and in confined areas inside the parasite, white arrows), and no export (observed as foci inside the parasite) phenotype. Representative images of three independent experiments with at least 20 image series per experiment and condition. Red box indicates the chosen harvest time for assessing the effect of UIS2 loss on the exported protein SBP1 and KAHRP (section 3.5). Error bars indicate SD.

3.5 Loss of UIS2 specifically affects protein export

The disruption of protein export in the absence of UIS2 raised the question of whether the loss of UIS2 affects all secretory proteins or if it is specific to exported proteins. In order to obtain a detailed picture of the protein transport pathways affected, episomal plasmids, each encoding a different trafficking marker fused to the red fluorescent protein mScarlet, were transfected into the condΔUIS2-3xHA cell line previously generated (Khosh-Naucke, 2018) (Figure 16A,B, Figure 17A-C). This allowed the analysis of the transport of these markers after UIS2-loss in live cells using fluorescence microscopy. All markers encoded on the episomal plasmids were expressed under the *crt*-promotor to induce their expression at the trophozoite stage.

First, the export of the SBP1-mScarlet and KAHRP-mScarlet fusion proteins was assessed under both induction regimes. In the control, SBP1 was correctly trafficked to the MCs and KAHRP to the erythrocyte membrane (Figure 16A,B). The removal of UIS2 in these parasites (using early induction) confirmed the export phenotype observed in IFAs resulted in arrested small rings, with 95.6% of cells showing no export of SBP1 (Figure 16A,C), and parasites arrested in development, with 94.5% of cells showing no KAHRP export (Figure 16B,C). Under mid-induction, cells demonstrated different levels of export of these markers, ranging from no export to full export (Figure 16A,B). Trophozoites exhibiting an export-arrest as foci at the PV

were observed in 37% of the cells for SBP1-mScarlet and 14% of the cells for KAHRP-mScarlet (Figure 16C). The phenotype was defined as mixed when the assessed marker was observed both within the host cell and arrested in confined areas inside the parasite. This mixed phenotype was identified in 49% of the cells for SBP1-mScarlet and in 76% of the cells for KAHRP-mScarlet (Figure 16A-C).

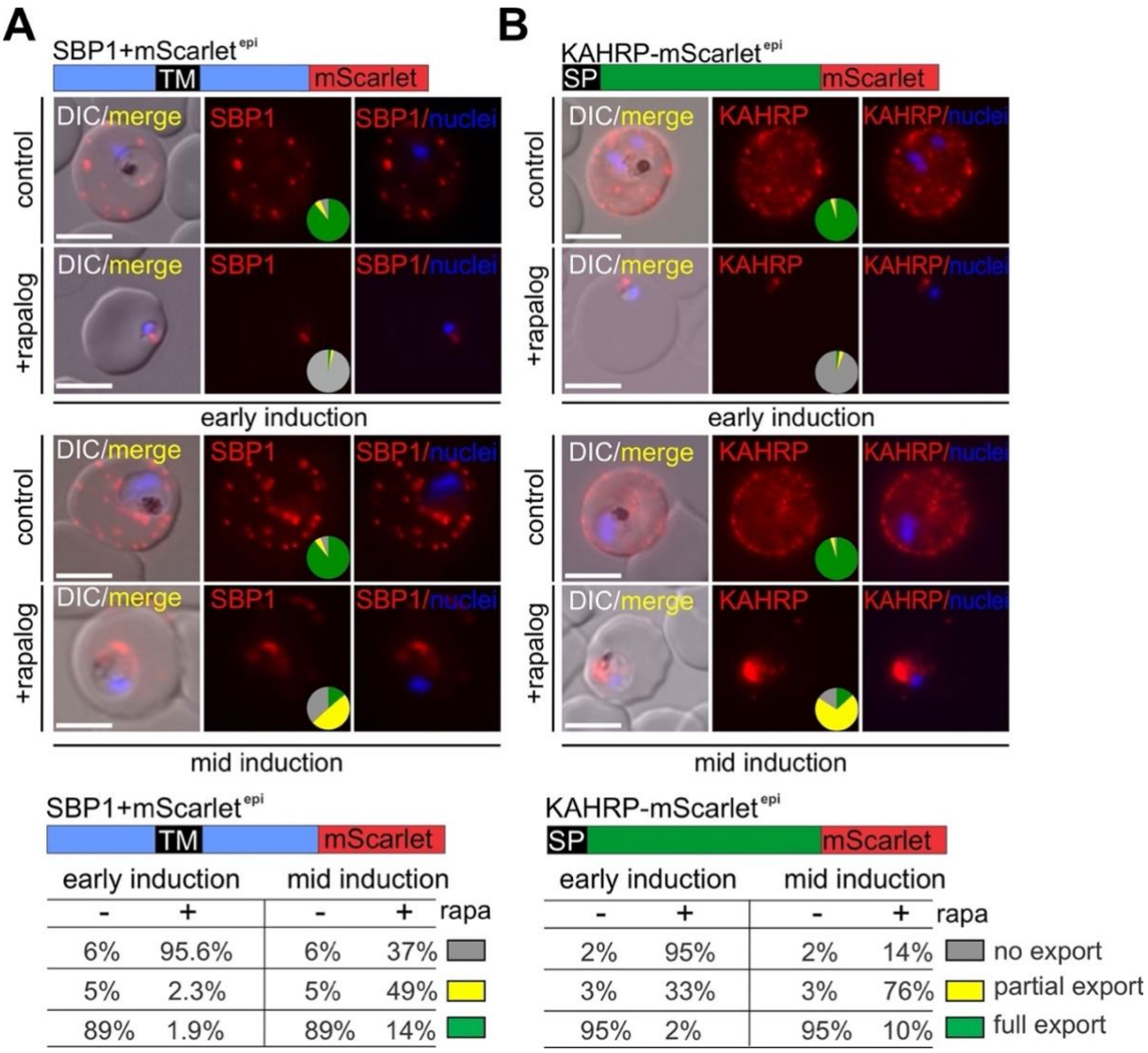

Figure 16. UIS2 knockout affects exported proteins. (A-B) Live cell microscopy images (representative images of three independent experiments with at least 15 image series per experiment and condition) of control (without rapalog) condΔUIS2 parasites and ΔUIS2 parasites (+ rapalog) inducing excision of *uis2* in 0 - 8 hpi ('early induction', upper panel) or 12 - 16 hpi ('mid-induction', lower panel) and co-expressing the markers indicated: (A) SBP1-mScarlet (Maurer's clefts) (B) KAHRP-mScarlet (knobs at erythrocyte membrane). (C) Pie charts show quantification from three independent experiments with exact values of pies in A and B (-rapa n = 20, +rapa n= 20 per experiment). DIC: differential interference contrast; nuclei were stained with Hoechst; merge indicates overlay of all presented channels. Size bar = 5µm.

Subsequently, mScarlet fusions of a number of markers were expressed in the cond∆UIS2 parasites, namely a soluble PEXEL export reporter, the glycophorin-binding protein (GBP) (1-108 aa of GBP, Grüring *et al*., 2012) (Figure 17A) as a further exported protein, a multi-transmembrane protein of the PPM, the formate-nitrite transporter (FNT) (Wu *et al*., 2015; Marchetti *et al*, 2015) (Figure 17B), and a soluble PV reporter, no exported protein, the SP of PF3D7_0830400 fused to mScarlet (PlasmoDB) (the SP mediates entry into the secretory pathway and default transport to the PV) (Figure 17C) (Birnbaum *et al*, 2020). The control cells showed proper trafficking of the soluble PEXEL reporter to the erythrocyte cytosol, the multi-transmembrane protein FNT to the PPM and secretion of the SP-mScarlet into the PV (Figure 17A-C). In contrast, after loss of *uis2* (using early induction), the GBP reporter was no longer exported in 96% of the cells, confirming the export phenotype and lead to the arrest of these parasites as small rings (Figure 17A,D). The PPM protein FNT remained unaffected (Figure 17B,D). For the SP marker, a faint signal or no signal was present in 96% of the cells. Although the exact location of the signal remained unclear, blurry foci were observed in the PV and within the parasite (Figure 17C). Only 3% of the cases showed a signal surrounding the PV; notably, this signal was observed specifically in parasites that had developed beyond the ring stage (Figure 17D).

The removal of UIS2 under the mid-induction regime resulted in an export defect of GBP, with an altered distribution of this marker in 48% of the parasites, as evident by the concentration of GBP in small regions at the parasite periphery (Figure 17A,D). The PPM protein FNT remained unaffected after excision of UIS2 (Figure 17B,D), indicating that the transport to the parasite plasma membrane is not affected in ∆UIS2 parasites. In contrast, an effect on the soluble PV reporter was observed, leading to an aberrant distribution of this marker in 34% of the ∆UIS2 parasites (Figure 17C,D). As the PV reporter was still in the periphery but appeared more confined to a smaller region (observed in 45% of the cells), this indicating that it did not constitute a loss of transport phenotype (Figure 17C,D). Instead, it is possible that UIS2 loss impacts the integrity or architecture of the PV, indirectly influencing the correct distribution of SP-mScarlet in the PV.

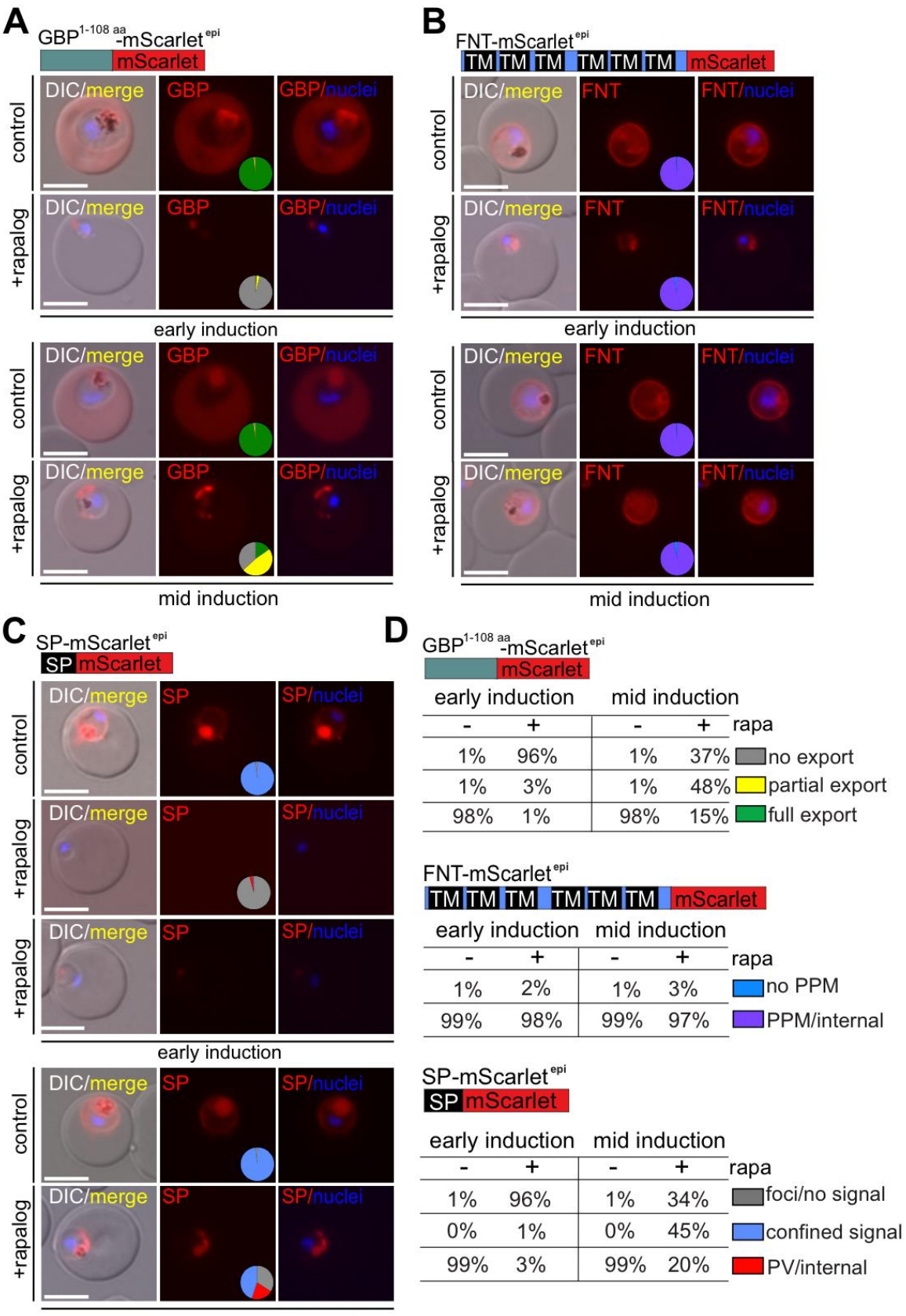

GBP$^{1-108\ aa}$-mScarlet^{epi}				
early induction		mid induction		
-	+	-	+	rapa
1%	96%	1%	37%	no export
1%	3%	1%	48%	partial export
98%	1%	98%	15%	full export

FNT-mScarlet^{epi}				
early induction		mid induction		
-	+	-	+	rapa
1%	2%	1%	3%	no PPM
99%	98%	99%	97%	PPM/internal

SP-mScarlet^{epi}				
early induction		mid induction		
-	+	-	+	rapa
1%	96%	1%	34%	foci/no signal
0%	1%	0%	45%	confined signal
99%	3%	99%	20%	PV/internal

Figure 17. UIS2 knockout affects proteins transported beyond the parasite plasma membrane. (A-C) Live cell microscopy images (representative images of three independent experiments with at least 15 image series per experiment and condition) of control (without rapalog) condΔUIS2 parasites

and ΔUIS2 parasites (+ rapalog) inducing excision of *uis2* in 0 - 8 hpi ('early induction', upper panel) or 12 - 16 hpi ('mid-induction', lower panel) and co-expressing the markers indicated: (A) GBP^{1-108}-mScarlet (soluble PEXEL export reporter), (B) FNT-mScarlet (PPM), (C) SP-mScarlet, (PV lumen). (D) Pie charts show quantification from three independent experiments with exact values of pies in A, B and C (-rapa n = 20, +rapa n= 20 per experiment). DIC: differential interference contrast; nuclei were stained with Hoechst; merge indicates overlay of all presented channels. Size bar = 5µm.

To demonstrate at the individual live cell level that the trophozoites with an export defect indeed had lost UIS2, a new *uis2* cKO line was generated. In this line, the floxed functional *uis2* was fused to the sequence encoding green fluorescence protein (GFP). It was previously shown that GFP-fusion did not impair UIS2 function, as such a fusion was readily obtained by modification of the endogenous *uis2* locus (Khosh-Naucke *et al.,* 2018) instead of using the HA-tag in the condΔUIS2 parasites used up to now (Figure 18A). Correct integration of the plasmid into the genome was confirmed by PCR (Figure 18B). Fluorescence microscopy images of condΔUIS2-GFP demonstrated the presence of UIS2-GFP surrounding the parasite in all asexual blood stages in the control (Figure 18C). This observation supports the documented location of UIS2-GFP in the PV compartment which was concluded from UIS2-GFP fluorescence still being observed in late schizonts surrounding the bulk of the remaining merozoites, with no fluorescence observed in released merozoites (Khosh-Naucke *et al*, 2018). During the next replication cycle (1^{st} cycle), loss of UIS2 was observed (a few ring stage parasites showed small amounts of remaining UIS2-GFP) (Figure 18C, harvest time A). In the subsequent parasite stages (trophozoites and schizonts), no GFP signal was detected in ΔUIS2 parasites, indicating the effective excision of the functional *uis2* gene and loss of the protein (Figure 18C, harvest time B).

It was next tested, whether the loss of UIS2 affected the viability of the parasites. The newly established condΔUIS2-GFP cell line showed identical growth kinetics to the previously generated condΔUIS2-HA (Figure 18D,E). During the excision cycle there was no impact on growth, and only in the first cycle without UIS2-GFP present, a severe multiplication-defect was detectable (Figure 18D,E). Overall, these results indicated the successful generation of a cell line for achieving an efficient conditional knock out of *uis2,* that at the same time allowed for the tracking of UIS2 loss in live cells.

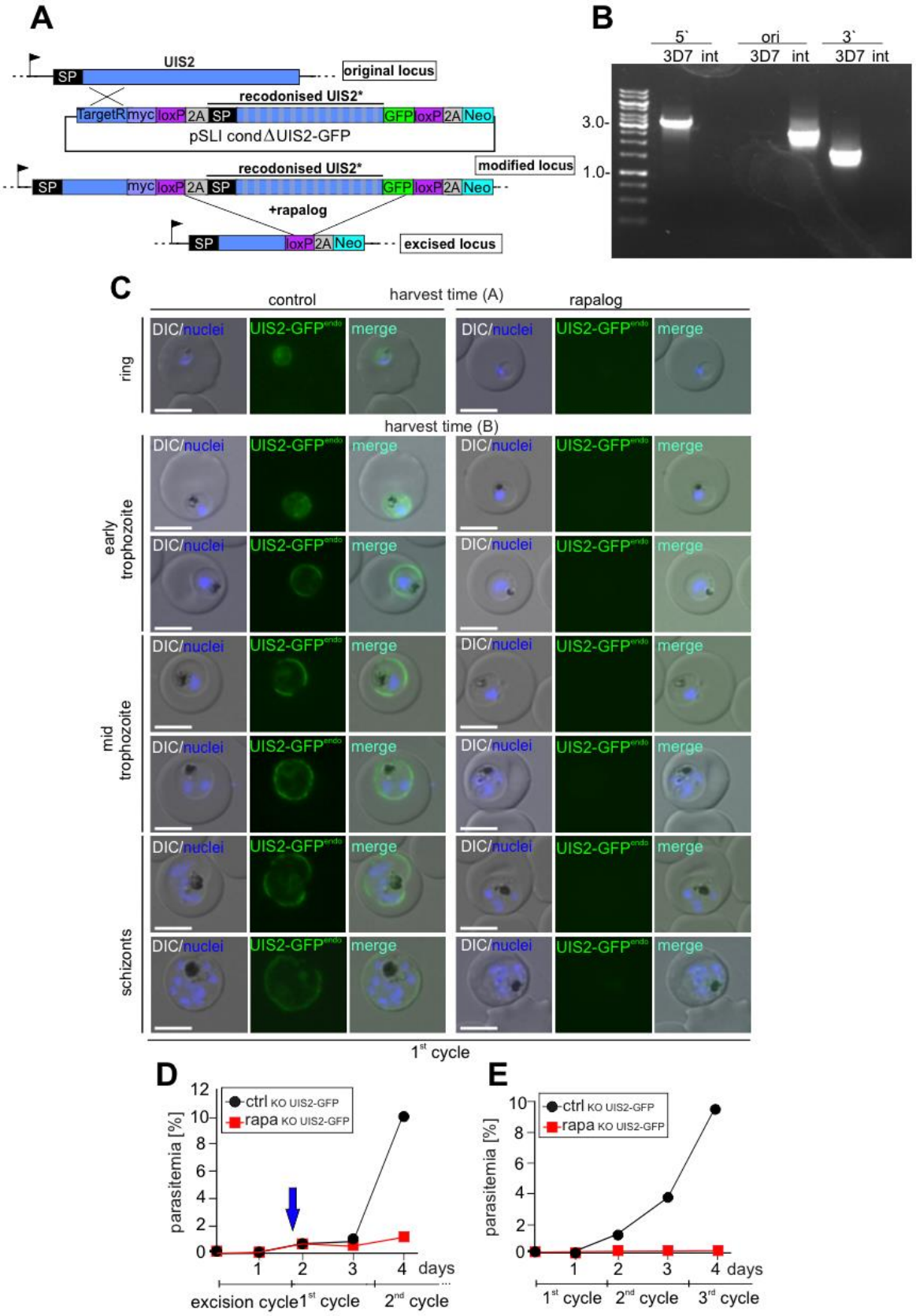

Figure 18. Conditional UIS2-GFP knock out cell line permits tracking of UIS2 loss. A) Simplified schematic of the generation of the diCre-based condΔUIS2-GFP knockout cell line using SLI and <subsequent excision upon the addition of rapalog (modified from Mesén-Ramírez *et al*, 2019). Black

arrows, native *uis2* promotor; blue box, target region (TargetR) for homologous recombination; 2A, T2A skip peptide. Full condΔUIS2-GFP-SLI schematic is shown in Appendix 2. (B) Agarose gel showing PCR-products to assess correct integration of the SLI-plasmid into the genome to obtain the indicate cell line. For *Pf*3D7_1464600-GFP^{endo}, primers (Appendix 1) were "1464600-GFP-Int-fw" + 3`UTR-rv" to demonstrate 5' integration (5' int, 3221 bp) and "pARL55-fw" + "1464600-GFP-Int-rv" to demonstrate 3' integration (3' int, 1570 bp). Primers "1464600-GFP-Int-fw" + "1464600-GFP-Int-rv" were used to show absence of unmodified original locus in the respective cell line (ori int) and 3D7 gDNA was used as a control (ori 3D7, 2320 bp). M, marker (GeneRuler^{TM} 1kb, Thermo Scientific); DNA fragment size standard is indicated in kbp. (C) Live cell microscopy images (representative images of 2 independent experiments with at least 20 image series per experiment) of the condΔUIS2-GFP parasites (control) and ΔUIS2-GFP parasites (+ rapalog) showing a ring (top) (harvest time A as indicated in Figure 15), early and mid-trophozoite stages (middle) and a schizont stage parasite (bottom) (harvest time B as indicated in Figure 15). DIC: differential interference contrast; nuclei were stained with Hoechst; the merge indicates overlay of all presented channels. Size bar = 5µm. Growth curves of synchronous ring stage condΔUIS2-GFP parasites starting in excision cycle (D) or cycle 1 (E) on 5 consecutive days, blue arrow indicates invasion into the first cycle and loss of UIS2. One representative of n = 3 independent experiments (replicas are shown in Appendix 5).

Next, the conditional *uis2* KO-GFP (condΔUIS2-GFP) was used to permit tracking of UIS2 loss and the markers KAHRP-mScarlet, SBP1-mScarlet and SP- mScarlet in live cells (Figure 19A-D). These parasites were examined by fluorescence microscopy. In the control parasites, the exported proteins SBP1 was correctly trafficked to the MCs, whereas KAHRP to the erythrocyte membrane, and SP secreted into the PV lumen (Figure 19A-C). The removal of UIS2 in these parasites (using early induction) confirmed the exported phenotype observed in *uis2* KO-HA (condΔUIS2-HA). In this condition, parasites resulted in arrested small rings, where SBP1-mScarlet was no longer exported in 96.5% of the cells (Figure 19A,D) and in the parasites arrested in development, KAHRP-mScarlet was no longer exported in 96% of the cells (Figure 19B,D). For the SP marker, prominent focus at the PV or no signal were observed in 99% of the cells (Figure 19C,D). In these ΔUIS2 parasites, the GFP signal was no longer observed, indicating that the effective excision of the functional *uis2* gene and the observed effect on protein transport was indeed specific to UIS2 loss.

The removal of UIS2 in these parasites (using mid-induction), demonstrated cells with different levels of exported of these markers, ranging from no export to full export (Figure 19A-D), probably reflecting the loss of UIS2 at different times during the cycle.

This confirmed the previous results observed in this study using the *uis2* KO-HA (cond∆UIS2-HA) cell line (Figure 15). For SBP1-mScarlet, trophozoites exhibited an export-arrest, resulting in a prominent SBP1-mScarlet focus in 20% of the cells (no export) and a mixed export with blurred signal around the PV and within the host cell in 62% of the parasites (Figure 19A,D). For KAHRP-mScarlet, a prominent ring-shape pattern of foci around the parasite was observed in 10% of the cells. A mixed phenotype (a similar confined signal as foci around the PV with an additional faint signal inside the host cell), was observed in 82% of the parasites (Figure 19B,D). This demonstrated loss of UIS2 in cells with an export phenotype at the individual cell level.

The cell line to track UIS2 loss on the individual cell level was also used to assess the effect of UIS2 loss on the soluble PV (SP-mScarlet) marker. After UIS2 loss using mid-induction the soluble marker, was still found in the periphery of the parasite but appeared confined in smaller areas in 64% of the parasites (Figure 19C,D). The inspected cells all lacked UIS2-GFP, confirming that the cells had lost UIS2 and that this likely was the reason for the altered distribution of this marker in the PV, possible indicating an impact on the architecture of the PV. Further experiments are necessary to assess the impact of UIS2 loss on PV integrity.

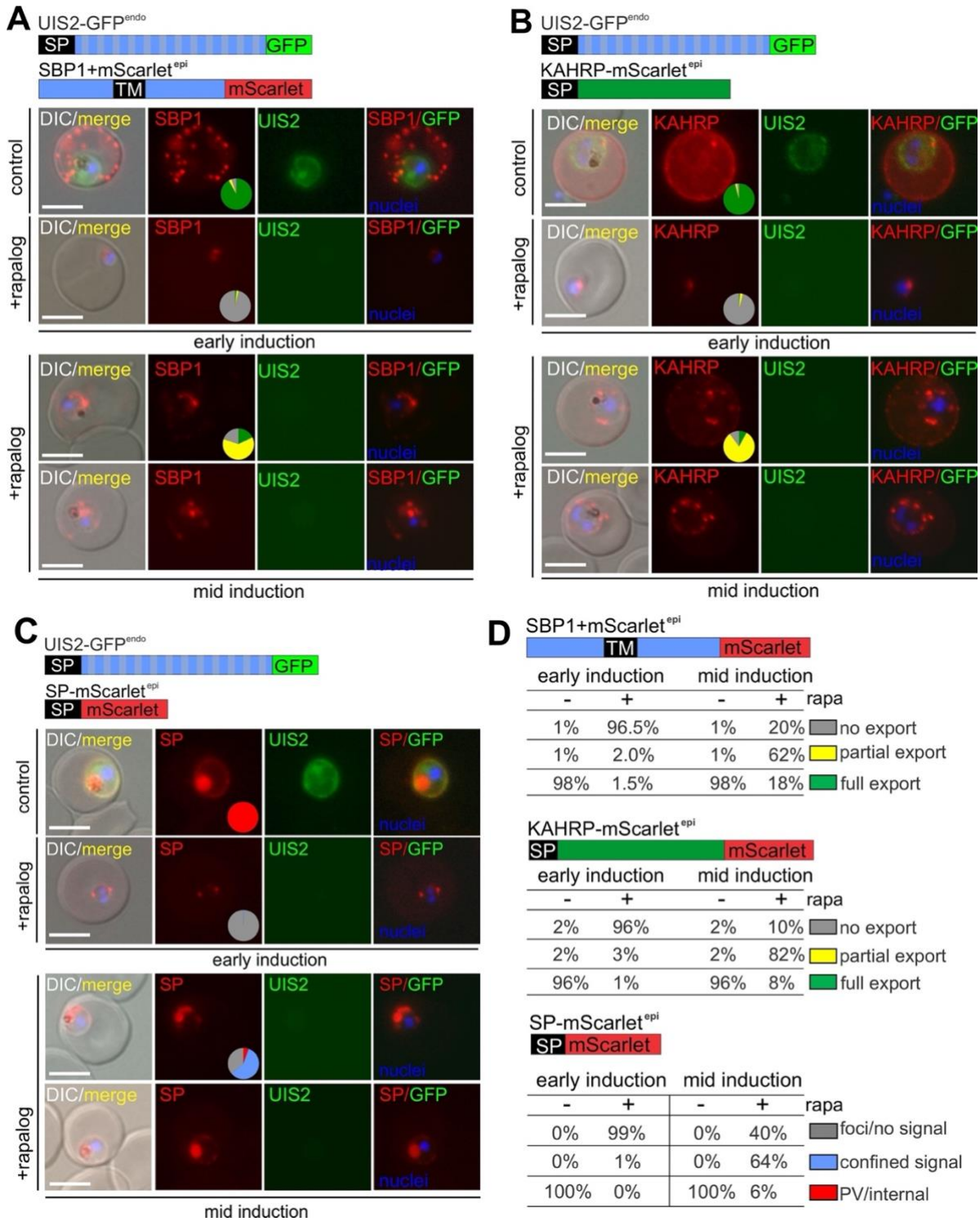

Figure 19. Protein export defect observed in ΔUIS2-GFP parasites is indeed due to UIS2 loss. (A-C) Live cell microscopy images (representative images of 3 independent experiments with at least 15 image series per experiment and condition) of control (without rapalog) condΔUIS2-GFP parasites and ΔUIS2-GFP parasites (+ rapalog) inducing excision of *uis2* in 0 - 8 hpi ('early induction', upper panel) or 12 - 16 hpi ('mid-induction', lower panel) and co-expressing the markers indicated: (A) SBP1-mScarlet (Maurer´s clefts), (B) KAHRP-mScarlet (knobs at erythrocyte membrane), (C) SP-mScarlet (PV lumen). (D) Pie charts show quantification from three independent experiments with exact values

of pies in A, B and C (-rapa n = 30, 25, 15, +rapa n= 30, 25, 15). DIC: differential interference contrast; nuclei were stained with Hoechst; merge indicates overlay of all presented channels. Size bar = 5µm.

3.6 Assessment of the transport of further marker of the PVM

The failure of the ΔUIS2 parasites to export proteins into the host cell during the first cycle of replication was examined in further detail by IFAs, where the distribution of integral PVM proteins was evaluated (Figure 20). This evaluation included the early transcribed membrane proteins, ETRAMP4 and ETRAMP5 (Spielmann *et al.,* 2003) as well as EXP2, one of the core components of the *Plasmodium* translocon of exported protein (PTEX), (Fischer *et al,* 1998; de Koning-Ward *et al*., 2009). SBP1 was used as a positive control for phenotype (Figure 20). In the control, SBP1 was correctly trafficked to the MCs, and ETRAMP4, 5 and EXP2 were found in the parasite periphery, in agreement with a location at the PVM. Upon addition of rapalog and the evaluation of ΔUIS2-GFP parasites at the trophozoites stage in the first cycle (72 hpi), the parasites showed an altered distribution of all tested markers with accumulation in a confined area of the PVM (Figure 20A-C). All PVM markers were confined to the same area where the arrested SBP1 signal was found (Figure 20A-C). Overall, these results indicated that the loss of UIS2 negatively impacts the organization of proteins of the PVM.

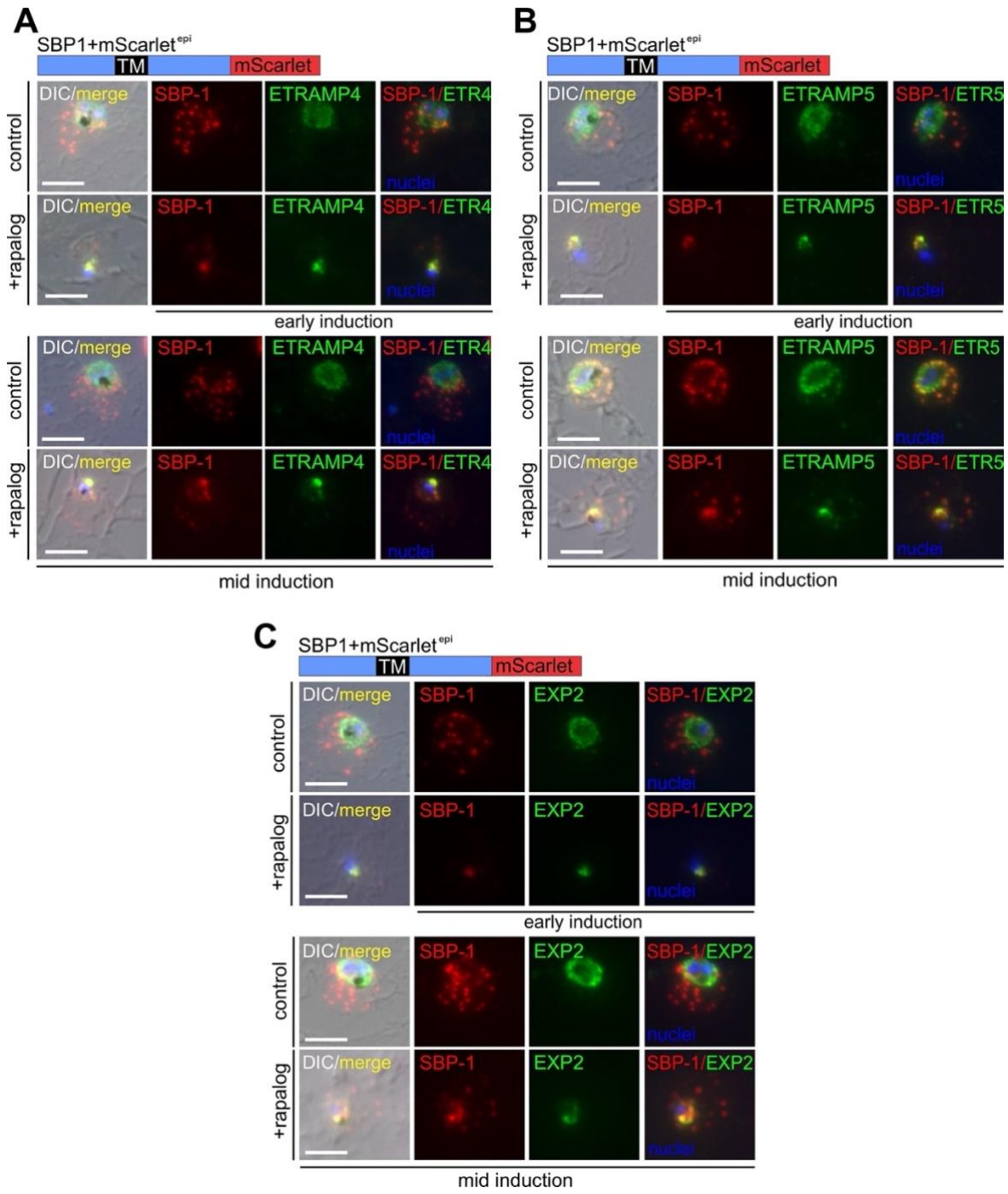

Figure 20. Loss of UIS2 negatively impact the location of integral PVM proteins. IFA using acetone-fixed cells of the condΔUIS2-GFP parasites (control) and ΔUIS2-GFP parasites (+rapalog) at the 1st cycle (96 h post addition of rapalog), showing the integral PVM proteins ETRAMP4 (A), ETRAMP5 (B) and EXP2 (C) in both induction regimes (early and mid-induction). Anti-SBP1C and anti-ETRAMP4 (both from rabbit) was used to detect Maurer´s clefts and ETRAMP4 at the PVM, respectively. Anti-ETRAMP5 and anti-EXP2 (both from mouse) were used to detect ETRAMP5 and EXP2 at the PVM, respectively. Representative cells from one of two independent experiments with at least 20 image series per experiment and condition. DIC: differential interference contrast. Nuclei were stained with Hoechst. Size bar = 5µm.

3.7 UIS2 phosphatase shares architecture with purple acids phosphatases

To classify the UIS2 phosphatase domain, gain insights into its potential phosphatase function and design phosphatase dead complementation constructs (see section 3.8), the similarity of the phosphatase domain of UIS2 to other phosphatases was analysed. For this, primary amino acid sequence comparisons of the UIS2 phosphatase domain with well-characterised phosphatase domains were carried out. In addition, structural alignments of phosphatase domain of the AlphaFold predicted UIS2 structure (AF-Q8IKJ1-F1) with other metallophosphoesterase domains was performed (Figure 21-Figure 23). These metallophosphoesterase domains have a unique active site containing two metal ions (typically manganese, iron, or zinc) with an octahedral geometry coordinated by histidine (H), aspartate (D), and asparagine (N) side chains (Pandey *et al*., 2014). These residues are located in five different blocks of conserved residues (Figure 21). Residues in blocks I and V coordinate metal ion α (MI), whereas those in blocks III, IV, and V coordinate metal ion β (MII). A conserved aspartate in block II coordinates both metal ions α and β (Matange *et al.*, 2015).

A prototypical member of binuclear metallophosphoesterases (with two metal ions in the active site) is bacteriophage λ phosphatase (λ-Pase), which has been extensively characterized. λ-Pase catalyzes the hydrolysis of phosphoesters in the presence of Mn^{2+} (Barik, 1993; Voegtli *et al.,* 2000; Matange *et al.*, 2015). Similar to λ-Pase, UIS2 of *P. berghei* has a strong preference for Mn^{2+} for its phosphoserine phosphatase activity (Zhang *et al,* 2016). However, although UIS2 was classified as a protein phosphatase 2C (PP2C) due to its preference for Mn^{2+} over Mg^{2+} (Zhang *et al.*, 2016), this enzyme notably lacks a canonical PP2C catalytic domain but shows high similarity to purple acids phosphatases (PAPs) (Figure 21) (Kaida *et al.,* 2010). Sequence alignment analysis of the UIS2 phosphatase with other metallophosphoesterases showed a conserved sequence motif, confirming its similarity to PAPs (Figure 21). For instance, it has a conserved glycine residue in block I (DI**G**) that is present only in PAPs (Figure 21). Curiously, UIS2 also has the tyrosine residue in block II that is part of the GDNFY motif in PAPs, but the motif was split into two right after the GDN residues by an insertion of 49 amino acids (Figure 21B). For this reason, the tyrosine in the structure of UIS2 is close but not exactly in

the same position as where most purple acid phosphatases (PAPs) have it (Figure 21C), making it unlikely to contribute to Fe (II) and Mn^{2+} ions binding.

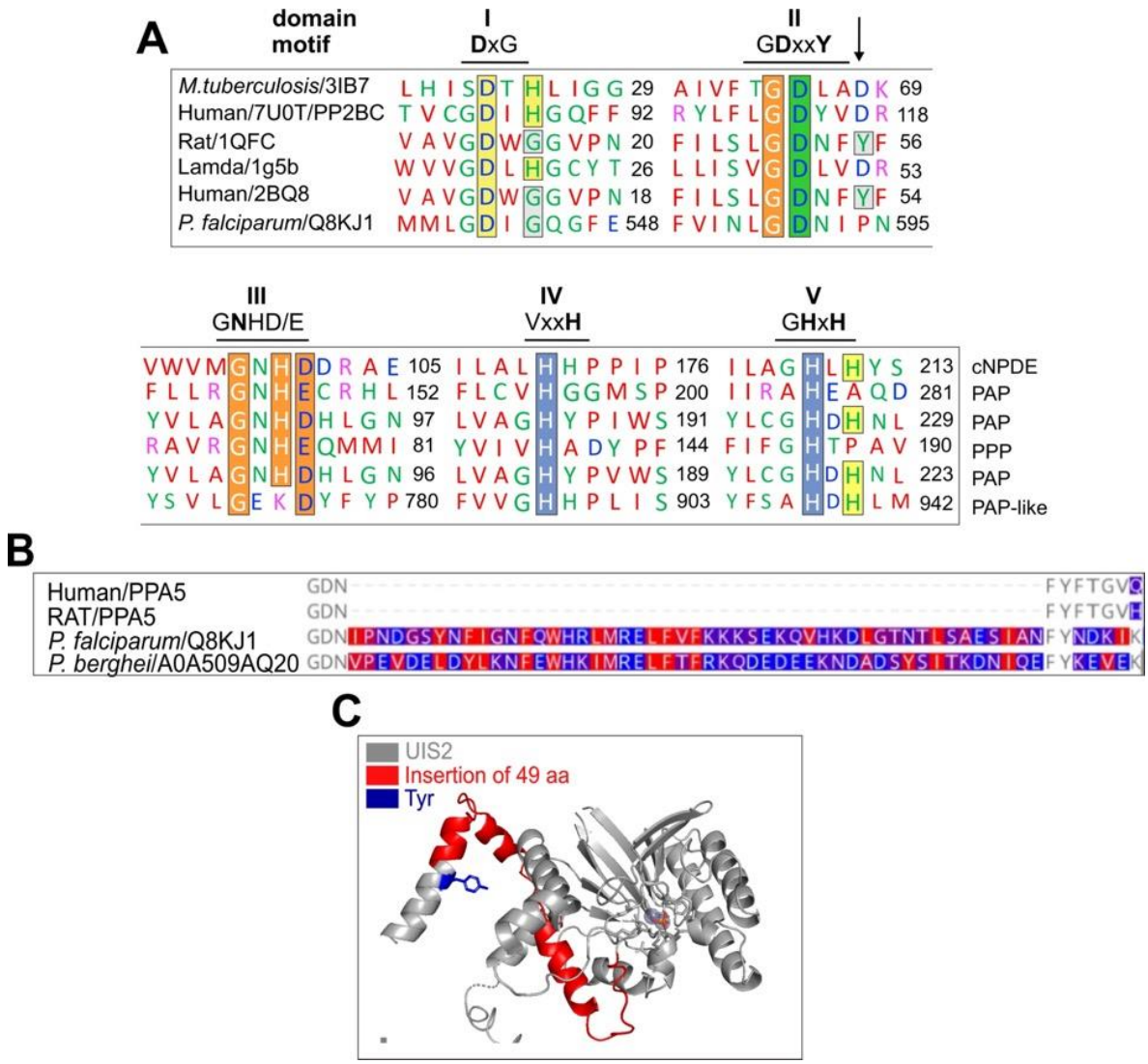

Figure 21. Conserved catalytic domains between metallophosphoesterases. (A) Sequence alignment of the different catalytic blocks (marked I-V) of archetypical metallophosphoesterases (M. tuberculosis (PDB ID: 3IB7); Human (PDB ID: 7U0T); Rat (PDB ID: 1QFC); Lambda (PDB ID: 1G5B); Human (PDB ID: 2BQ8); P. falciparum (UniProt: Q8KJ1). PDB, Protein Data Bank. Conserved residues are boxed. Residues in yellow coordinate metal ion α (MI), in blue metal ion β (MII), in green both metal ions. In grey are conserved residues found only in purple acids phosphatases (PAPs). Other conserved residues are highlighted in orange. cNPDE, cyclic nucleotide phosphodiesterase; PPP, phospho-protein phosphatase. (B) Sequence alignment showing the insertion of 49 amino acids that disrupts the GDNFY motif in block II in *P. falciparum* (UniProt: Q8JK1) and *P. berghei* (UniProt: A0A509AQ20), which is absent in human and rat purple acid phosphatases type 5 (PPA5). UniProt, Universal Protein Resource. (C) 3D structure of the UIS2 phosphatase domain predicted by AlphaFold

(AF-Q8IKJ1-F1) (grey), showing insertion of 49 aa downstream (red) and position of the tyrosine 643 (blue). Protein structure was visualized using PyMOL, Version 2.5, LLC.

Structural alignment analysis of the UIS2 phosphatase domain, as predicted by AlphaFold (AF-Q8IKJ-F1), with the experimentally determined structure of human purple acid phosphatases (PDB ID: 2BQ8) (Figure 22), revealed a root-mean-square deviation (RMSD, a measure for the average distance between the alpha carbon atoms in superimposed structures (Laskowski & de Beer, 2014)) of 1.1 Å for 152 aligned amino acids (Figure 22C), indicative of a high level of structural similarity. However, AlphaFold's prediction of the UIS2 phosphatase domain does not include ions at the catalytic site. Therefore, the positions of metal ions (Fe (II) and Zn) within the active site of human PAP—which exhibits a high level of structural similarity—were used as reference points for the 3D structure of the UIS2 phosphatase domain. The predicted positions of the ions were used to guide the selection of potential candidate residues to generate catalytically inactive versions of UIS2 for the complementation assay (see section 3.8).

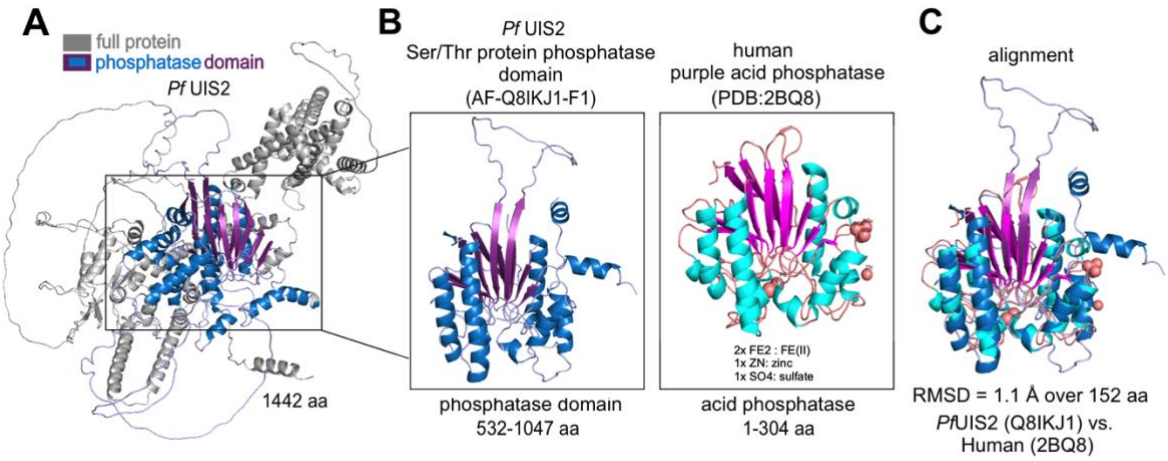

Figure 22. Alignment of 3D structures of the phosphatase domain of AlphaFold-predicted UIS2 with human PAP reveals similar architecture. (A) 3D structure of the full length of *Pf*UIS2, as predicted by AlphaFold (AF-Q8IKJ1-F1) in grey, highlighting the phosphatase domain alone (depicted in blue (α-helical regions) with purple (β-sheet regions)). (B) Individual 3D protein structure of the phosphate domain (aa 532-1047) of *Pf*UIS2 in detail (blue with purple, AlphaFold: AF-Q8IKJ1-F1) and the phosphatase domain of human PAP (aa 1-304, PDB ID: 2BQ8) including ions (depicted in cyan (α-helical regions) with magenta (β-sheet regions). (C) Structural alignment of the structures shown in B. RMSD, 1.1 Å. Protein structures were visualized and aligned using PyMOL, Version 2.5, LLC.

To identify the ligand-binding sites (LBs), a comparison was made between the structure of the AlphaFold-predicted UIS2 phosphatase domain and the experimentally determined structures of some purple acid phosphoesterases determined by X-ray diffraction (Figure 23). This comparison encompassed PAPs from human (PDB ID: 2BQ8, 2.2 Å resolution (Strater *et al*, 2005)), rat (PDB ID: 1QHW, 2.2 Å resolution (Lindqvist *et al*, 1999)), and pig (PDB ID: 1UTE, 1.5 Å resolution (Guddat *et al.*, 1999)) (Figure 22A). Among these phosphatases, the human (PDB ID: 2BQ8) and rat (PDB ID: 1QHW) PAPs were the closest structural analogs to *Pf*UIS2 with an RMSD of 1.31 Å and 1.18 Å, respectively, indicating a high degree of structural conservation (Figure 23B). The LBs were found to be conserved across the compared phosphatases (Figure 23A,C). The residues D542 and D591 in UIS2 – used for inserting mutations in the UIS2 catalytic domain (Section 3.8) – are highlighted in underlined letters in the UIS2 phosphatase (Figure 23C).

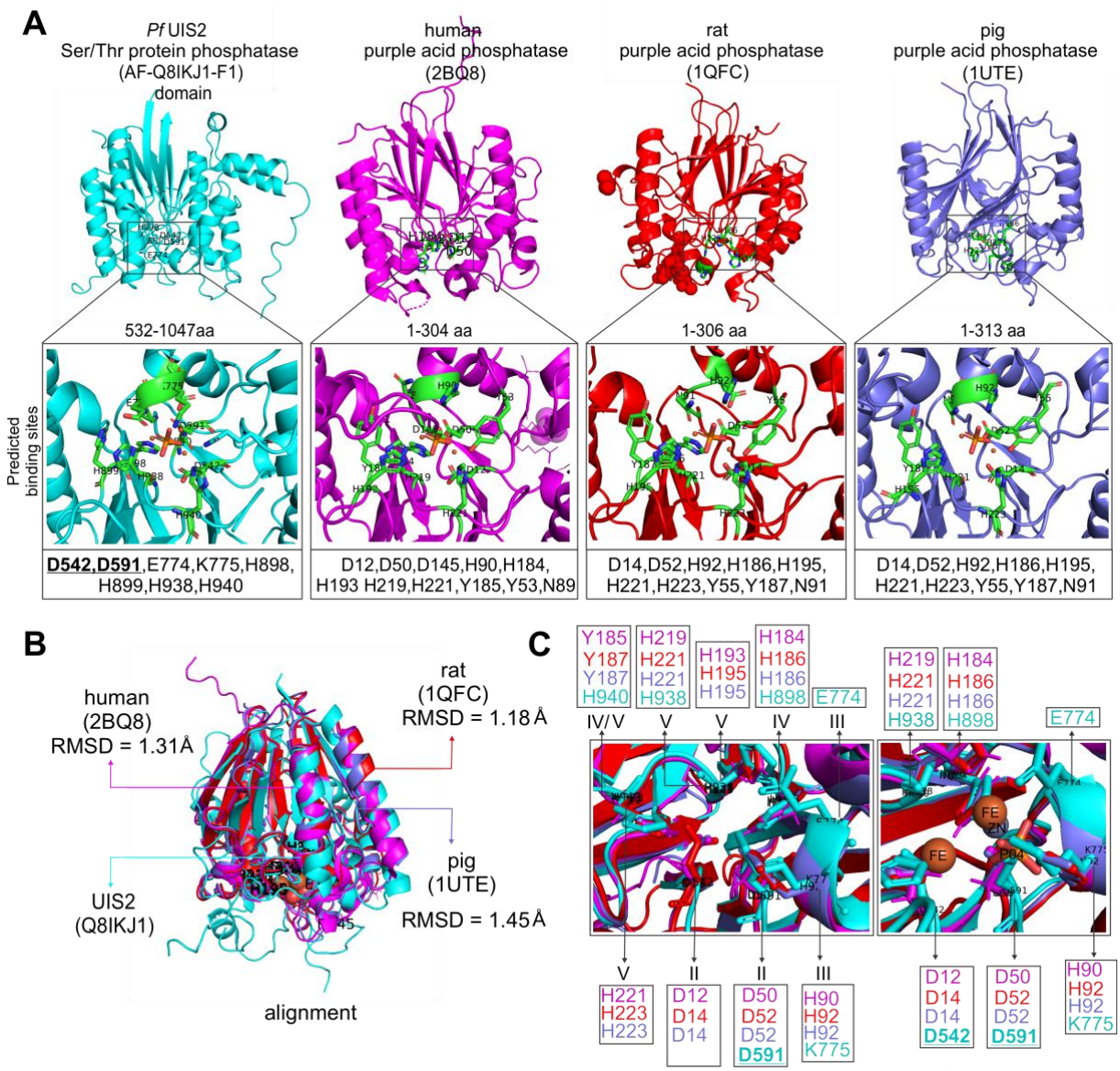

Figure 23. Comparison of UIS2 phosphatase domain with multiple PAPs confirms architectural and ligand-binding site similarities. (A) The core catalytic domain of AlphaFold-predicted *Pf*UIS2 (AF-Q81KJ1-F1) resembles that of purple acid phosphatases (PAPs) from human (PDB ID: 2BQ8), rat (PDB ID:1QFC) and pig (PDB ID: 1UTE). Conserved ligand binding sites (LBs) in the catalytic site of each PAP are indicated beneath the protein structure. PDB: Protein Data Bank. (B) Structural alignment of the *Pf*UIS2 catalytic domain with those of human, rat, and pig PAPs shown in panel A. (C) Aspartates from blocks I and II, along with histidines from blocks III, IV, and V are conserved across all the phosphatases examined in this study. Residues D542, D591 in UIS2 (mutated in the complementation constructs, see section 3.8) are highlighted in underlined letters. Ligand biding sites of PfUIS2 were predicted with the bioinformatics tools COACH (Jianyi *et al.*, 2013a; Jianyi *et al.*, 2013b) and COFACTOR (Roy *et al.*, 2012; Zhang *et al.*, 2017). Residues in blocks I and V coordinate metal α (MI), whereas those in blocks III, IV, and V coordinate metal β (MII). Protein structures were visualized and aligned using PyMOL, Version 2.5, LLC.

3.8 Complementation assay of UIS2 phosphatase domain

To elucidate the role of the phosphatase domain for UIS2 function, a complementation assay with potential catalytic site mutants was performed. The position of the mutations was based on the analysis in 3.7 and aimed at mutating residues analogous to those that have been shown to be essential for the phosphatase activity in other metallophosphoesterases (Figure 24). Previous work determined that λ-Pase aspartates and histidines from sequence blocks I (DLH), II (GD), and III (GNH) were relevant for metal ion binding and mutations in the two aspartates residues from blocks I (D20) and II (D49) were reported to heavily affect catalysis (Zhuo *et al*., 1994) (Figure 24A). Subsequent sequence (Figure 21) and structural alignments (Figure 23) were carried out to identify the equivalents of the mutated residues in the *Pf*UIS2 and human phosphatase domains, revealing D542 and D12 to be the equivalents in block I and D591 and D50 to be the equivalents in block II, respectively (Figure 23A; Figure 24B,C). These residues were identified as aligning with two of the ligand binding sites (LBs) previously predicted in the phosphatase domain of UIS2, as well as in those of human, pig and rat phosphatase domains – corresponding to D14 (block I) and D52 (block II) in both rat and pig PAPs – indicating a conservation of these residues across species (Figure 23A,C). The residues D542, D591 in UIS2 and D12, D50 in human phosphatase domains were located in the same position to their counterparts in the λ-Pase, suggesting a conserved role in interacting with metal ions at the catalytic site (Figure 24). This conservation implies that these aspartates are likely involvement in the catalytic activity in *Pf*UIS2 and human phosphatases. Therefore, these residues were selected for the complementation assay.

Next, the complementation assay in UIS2 was performed. This assay involved the episomal expression of mCherry-tagged UIS2 catalytic site mutants in the UIS2 knock out. The complementation constructs were generated contained either a single-point mutation at the catalytic site D542N (block I) or D591N (block II), or a combination of both single-point mutations (D542N-D591N) (Figure 24B). These mutations resulted in the amino acid switch from the negatively charged aspartic acid (D) to the structurally similar but uncharged asparagine (N) in an attempt to decrease the likelihood of negatively affecting the general folding of the protein. All complementation constructs were expressed under the control of the *nmd3* promoter,

which shows a similar expression profile to the *uis2* gene promoter (Otto *et al*, 2010; Birnbaum *et al.*, 2017). To enable tracking the loss of endogenous UIS2, the constructs were transfected into the cond∆UIS2-GFP parasites cell line (generated in 3.5).

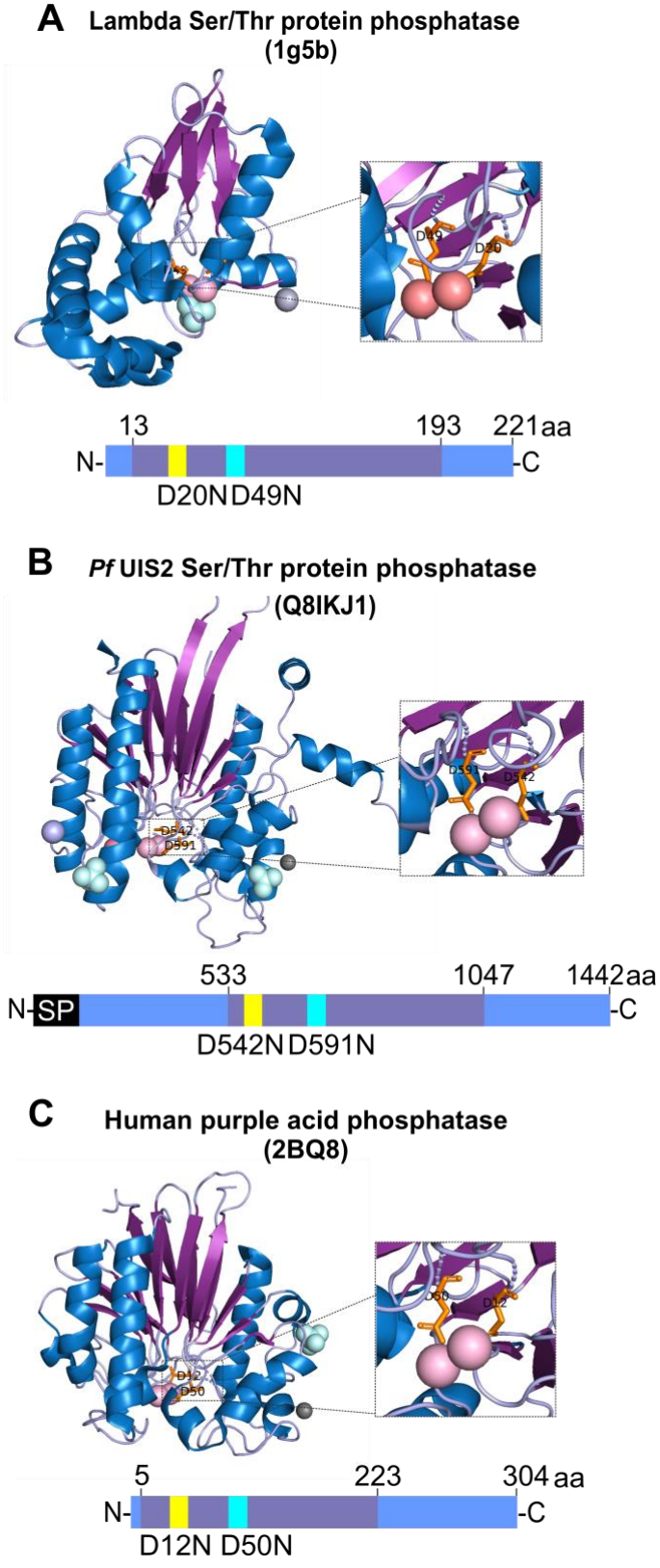

Figure 24. Mutations in UIS2 corresponding to catalytically relevant residues in lambda and human phosphatase domains. (A) Structural model of λ-phosphatase (PDB ID: 1G5B), highlighting the aspartate residues D20 and D49 in sequence blocks I and II. UIS2 phosphatase domain (aa 532-1047 from AF-Q8IKJ1-F1) (B) and human phosphatase domain (aa 1-304, PDB ID: 2BQ8) (C) showing structural conservation in the aspartate residues corresponding to those of the catalytic site in λ-phosphatase. Protein scheme: the phosphatase domain is represented as purple box; blue box, full protein sequence. Protein structures were visualized and aligned using PyMOL, Version 2.5, LLC.

To assess the functional impact of mutations in the phosphatase domain, a control complementation construct expressing a wild-type copy of UIS2 (UIS2-WT^{epi}-m-Cherry), was initially generated. To verify the expression of the episomal construct in the cond∆UIS2-GFP integrant cell line, the parasites were examined by fluorescence microscopy (Figure 25B). The complementation construct was localized around the parasite and co-localized with the endogenously expressed UIS2-GFP fusion protein (Figure 25B, control). Upon addition of rapalog using 'early induction' (Figure 25A), the endogenous UIS2 became undetectable in the ∆UIS2-GFP parasites during the first cycle, and this absence persisted into the subsequent replication cycle (2nd cycle) (Figure 25B). In contrast, the episomally expressed UIS2-WT^{epi}-m-Cherry exhibited consistent localization in the periphery of the parasite throughout the second replication cycle (Figure 25B). This result indicates the successful episomal expression of UIS2-WT^{epi} in ∆UIS2 parasites following the excision of the *uis2* gene.

To evaluate the functional complementation capacity of the UIS2-WT^{epi} construct, the endogenous floxed *uis2* locus was excised by adding rapalog ('early induction'), and parasite growth was quantitatively assessed using flow cytometry (Figure 25A,C). The growth curves of the cond∆UIS2-WT^{epi} parasites showed no significant difference in parasite development between rapalog-treated and control cells (Figure 25C). These observations indicated that UIS2-WT^{epi} fully reverted the functional impairment caused by the loss of UIS2 and shows the suitability of the complementation approach to test modified UIS2 versions.

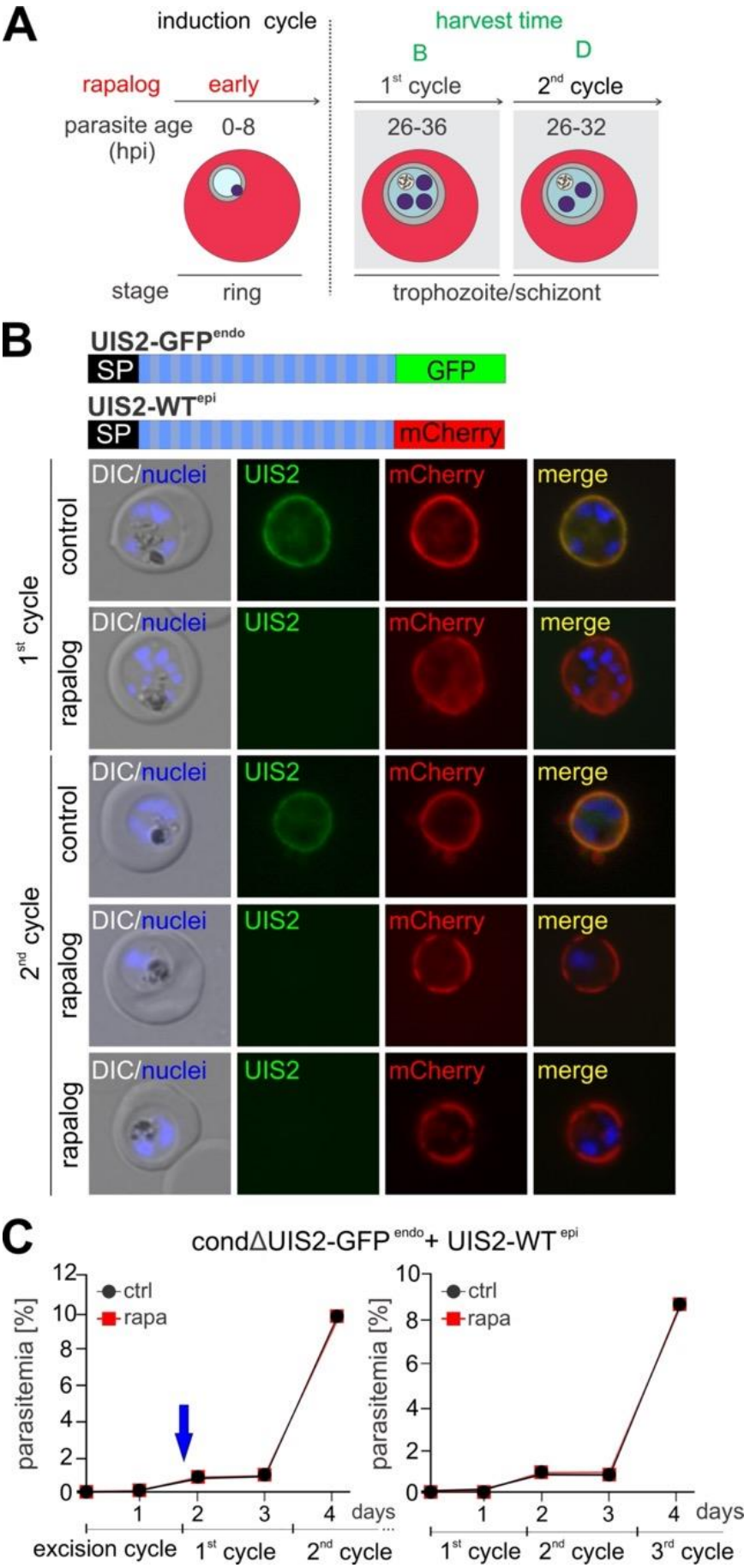
A
induction cycle
harvest time
B
D
rapalog
early
1st cycle
2nd cycle
parasite age (hpi)
0-8
26-36
26-32
stage
ring
trophozoite/schizont
B
UIS2-GFPendo
SP
GFP
UIS2-WTepi
SP
mCherry
1st cycle
2nd cycle
control
rapalog
DIC/nuclei
UIS2
mCherry
merge
C
condΔUIS2-GFPendo + UIS2-WTepi
parasitemia [%]
ctrl
rapa
days
excision cycle
1st cycle
2nd cycle
3rd cycle

Figure 25. Functional characterization of UIS2-GFPendo parasites with episomal UIS2-WTepi expression. (A) Schematic representation of the experimental setup for the conditional knockout of UIS2-GFP^{endo} expressing UIS2-WT^{epi} by inducing excision of the *uis2 gene* in 0 - 8 hpi ('early induction') ring stage parasites during the excision cycle. Parasites were harvested at point B at mid trophozoite-early schizont stage (1st cycle) and point D at trophozoite stage (2nd cycle). (B) Live cells microscopy images of ΔUIS2-GFP (+ rapalog) and control (without rapalog) condΔUIS2-GFP parasites expressing the episomal construct UIS2-WT^{epi}. Parasites were analysed at the 1st cycle in time point B (top panel) and 2nd cycle in time point D (bottom panel). Representative images of three independent experiments (+ rapa n = 30, 32, 30, - rapa 24, 32, 30). DIC: differential interference contrast; nuclei were stained with Hoechst; the merge indicates overlay of blue, red and green channels. Size bar = 5µm. (C) Flow cytometry growth curves of synchronous ring stage of condΔUIS2-GFP parasites episomally expressing UIS2-WT^{epi} starting either in excision cycle (left) or cycle 1 (right) over 5 consecutive days. Blue arrow indicates invasion into the first cycle and loss of *uis2*. One representative of n = 3 independent experiments (replicas are shown in Appendix 6).

Subsequently, the complementation capacity of the single-mutant versions of UIS2, UIS2-D542Nepi (Figure 26) and UIS2-D591N^{epi} (Figure 27) in ΔUIS2-GFP parasites was assessed. The localization and expression of the UIS2-D542N^{epi} construct was evident from its location in the periphery of the parasite and its co-localization with UIS2-GFP (Figure 26B, control). All parasites were positive for expression of the complementation construct. Upon the addition of rapalog using 'early induction' (Figure 26A), the parasites lost the endogenous UIS2-GFP signal (Figure 26B).In contrast, UIS2-D542N^{epi}-mCherry was still observed surrounding the parasite during the first and subsequent replication cycles, indicating the successful expression of UIS2-D542N^{epi} in ΔUIS2 parasites (Figure 26B). Functional analysis of UIS2-D542N^{epi} revealed that during the first cycle, while control parasites progressed to mid-late trophozoite and schizonts stages, the rapalog-treated parasites lacking the endogenous *uis2* gene exhibited a general delay in development (Figure 26B,C). This delayed phenotype became more pronounced in the subsequent parasite cycle, where ring and young trophozoite stages were observed in rapalog-treated parasites in contrast to the development to trophozoite and schizont stages observed in the control (Figure 26B,C). Next, to evaluate the functional complementation capacity of the UIS2-D542N^{epi} construct, the endogenous floxed *uis2* locus was excised by adding rapalog ('early induction'), and parasite growth was quantitatively assessed using flow cytometry (Figure 26D). The growth analysis indicated a moderate growth reduction at the second cycle and subsequent replication cycle (3rd cycle) post-

rapalog addition, suggesting partial complementation of UIS2-D542N^{epi} construct (Figure 26D).

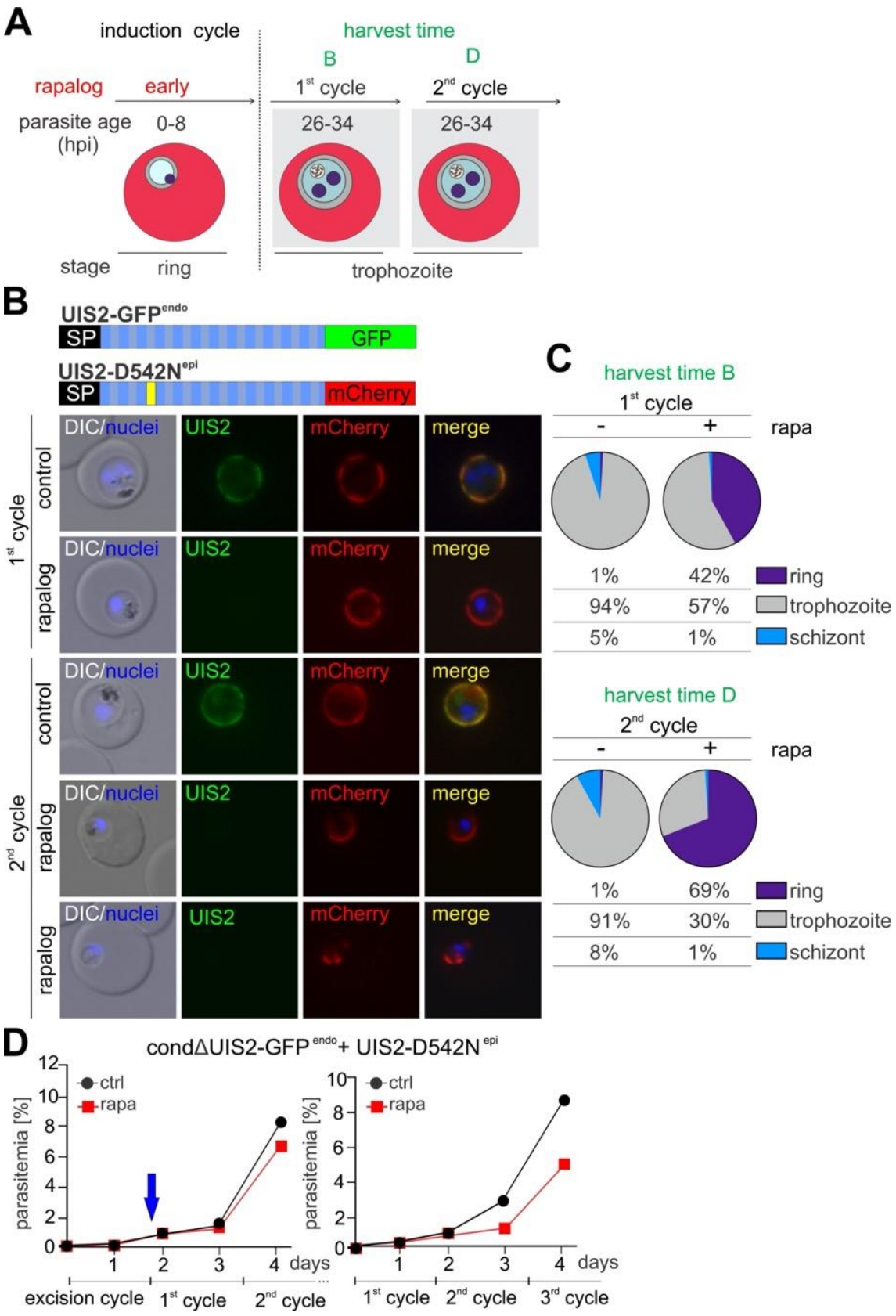

Figure 26. Functional characterization of UIS2-GFP^{endo} parasites with episomal UIS2-D542N^{epi} expression. (A) Schematic representation of the experimental setup for the conditional knockout of UIS2-GFP^{endo} expressing UIS2-D542N^{epi} by inducing excision of the *uis2 gene* in 0 - 8 hpi ('early induction') ring stage parasites during the excision cycle. Parasites were harvested at points B (1st cycle) and D (2nd cycle) at trophozoite stage. (B) Live cells microscope images of ΔUIS2-GFP (+ rapalog) and control (without rapalog) condΔUIS2-GFP parasites expressing the episomal construct UIS2-D542^{epi}. Parasite were analysed at the 1st cycle in time point B (top panel) and 2nd cycle in time point D (bottom panel). Representative images of three independent experiments (+ rapa n = 21, 16, 30, - rapa 17, 18, 33). DIC: differential interference contrast; nuclei were stained with Hoechst; the merge indicates overlay of blue, red and green channels. Size bar = 5µm. (C) Pie charts show parasite stage distribution from three independent experiments with exact values of pie in the table, based on the DIC images (+ rapa n = 17, 16, 30, - rapa 17, 16, 30). (D) Flow cytometry growth curves of synchronous ring stage condΔUIS2-GFP parasites episomally expressing UIS2-D542N^{epi} starting in excision cycle (left) or cycle 1 (right) on 5 consecutive days. Blue arrow indicates invasion into the first cycle and loss of *uis2*. One representative of n = 3 independent experiments (replicas are shown in Appendix 7).

Next, UIS2-GFP parasites expressing UIS2-D591Nepi were analysed (Figure 27A). The UIS2-D591N construct showed a complementation capacity that was comparable to the UIS2-D542N^{epi} construct. The localization and expression of the UIS2-D591N^{epi} construct was evident from its location in the periphery of the parasite and its co-localization with UIS2-GFP (Figure 27B, control). All parasites were positive for expression of the complementation construct. Upon the addition of rapalog using 'early induction' (Figure 27A), the parasites lost the endogenous UIS2-GFP signal (Figure 27B). In contrast, UIS2-D591N^{epi}-mCherry was still observed surrounding the parasite during the first and subsequent replication cycles, indicating the successful expression of UIS2-D542N^{epi} in ΔUIS2 parasites (Figure 27B).

Functional analysis of UIS2-D591N^{epi} revealed that during the first cycle, while control parasites progressed to mid-late trophozoite and schizonts stages, the rapalog-treated parasites lacking the endogenous *uis2* gene exhibited a general delay in development (Figure 27B,C). This delayed phenotype became more pronounced in the subsequent parasite cycle, where ring and young trophozoite stages were observed in rapalog-treated parasites in contrast to the development to trophozoite and schizont stages observed in the control parasites (Figure 27B,C). Next, to evaluate the functional complementation capacity of the UIS2-D591N^{epi} construct, the endogenous floxed *uis2* locus was excised by adding rapalog ('early induction'), and

parasite growth was quantitatively assessed using flow cytometry (Figure 27D). The growth analysis indicated a moderate growth reduction at the second cycle and subsequent replication cycle (3rd cycle) post-rapalog addition, suggesting partial complementation of UIS2-D591N^{epi} construct (Figure 27D). These findings agree with the results obtained with the UIS2-D542N^{epi} complementation construct, indicating that a single-point mutation at the catalytic site of the phosphatase domain reduces UIS2 function and suggests that the phosphatase activity plays a role in the function of UIS2. However, it remains unclear whether the moderate growth reduction in parasites relying on these single point mutation UIS2 versions is attributable to a partial requirement for phosphatase activity or whether it is the result of only a partial inactivation of the phosphatase activity with these mutations.

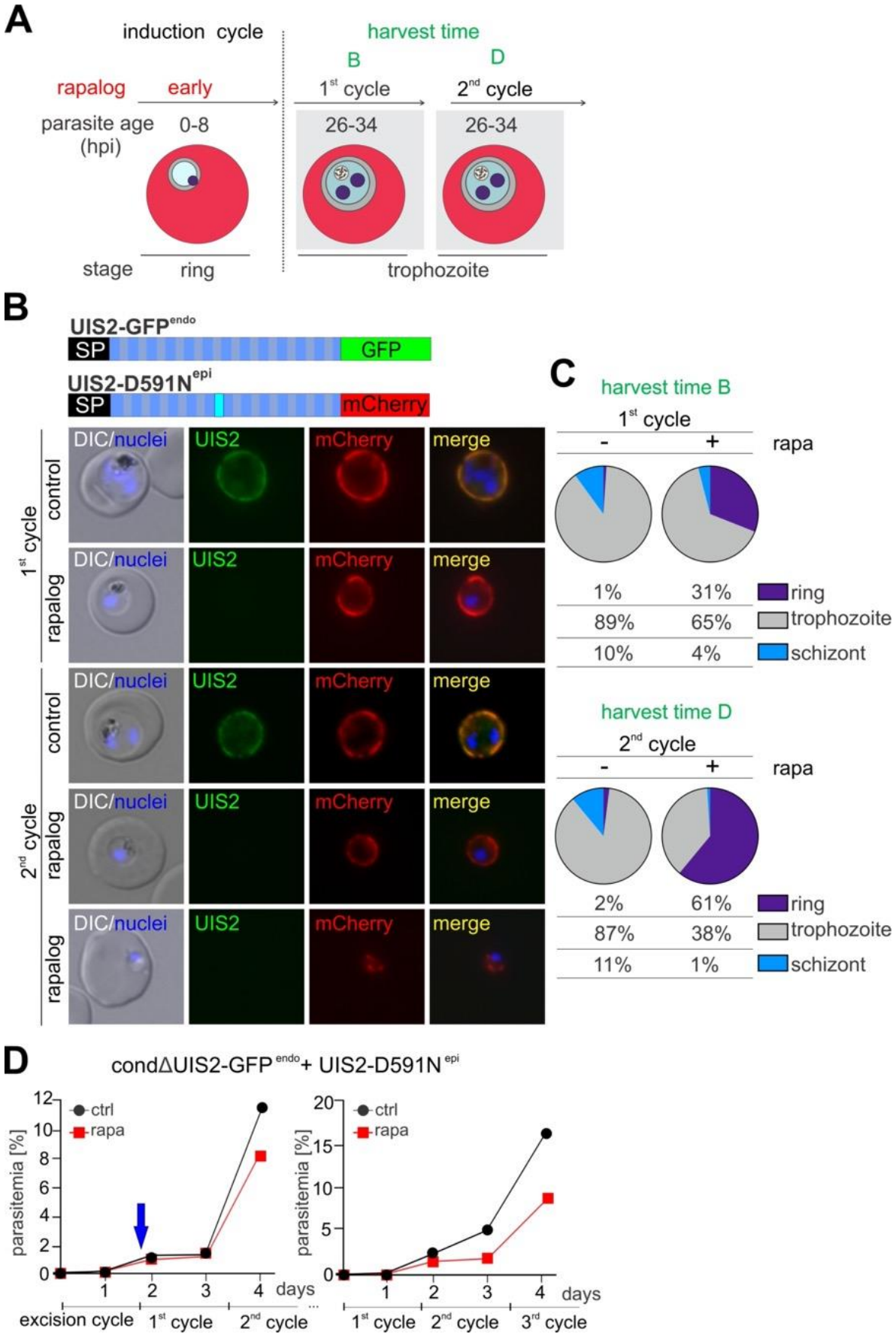
A
induction cycle
harvest time
B
D
rapalog
early
1st cycle
2nd cycle
parasite age (hpi)
0-8
26-34
26-34
stage
ring
trophozoite
B
UIS2-GFPendo
SP
GFP
UIS2-D591Nepi
SP
mCherry
1st cycle
2nd cycle
control
rapalog
DIC/nuclei
UIS2
mCherry
merge
C
harvest time B
1st cycle
-
+
rapa
1%
31%
ring
89%
65%
trophozoite
10%
4%
schizont
harvest time D
2nd cycle
2%
61%
87%
38%
11%
1%
D
condΔUIS2-GFPendo+ UIS2-D591Nepi
ctrl
rapa
parasitemia [%]
days
excision cycle
1st cycle
2nd cycle
3rd cycle

Figure 27. Functional characterization of UIS2-GFP^{endo} parasites with episomal UIS2-D591N^{epi} expression. (A) Schematic representation of the experimental setup for the conditional knockout of UIS2-GFP^{endo} expressing UIS2-D591N^{epi} by inducing excision of the *uis2 gene* in 0 - 8 hpi ('early induction') ring stage parasites during the excision cycle. Parasites were harvested at points B (1st cycle) and D (2nd cycle) at trophozoite stage. (B) Live cells microscope images of ΔUIS2-GFP (+ rapalog) and control (without rapalog) condΔUIS2-GFP parasites expressing the episomal construct UIS2-D591N^{epi}. Parasite were analysed at the 1st cycle in time point B (top panel) and 2nd cycle in time point D (bottom panel). Representative images of three independent experiments (+ rapa n = 19, 10, 30, - rapa 18, 7, 30). DIC: differential interference contrast; nuclei were stained with Hoechst; the merge indicates overlay of blue, red and green channels. Size bar = 5µm. (C) Pie charts show parasite stage distribution from three independent experiments with exact values of pie in the table, based on the DIC images (+ rapa n = 18, 7, 30, - rapa 18, 7, 30). (D) Flow cytometry growth curves of synchronous ring stage condΔUIS2-GFP parasites episomally expressing UIS2-D591N^{epi} starting in excision cycle (left) or cycle 1 (right) on 5 consecutive days. Blue arrow indicates invasion into the first cycle and loss of *uis2*. One representative of n = 3 independent experiments (replicas are shown in Appendix 7).

In order to clarify the question whether the only partial phenotype in the single point mutations was due to only a partial inactivation of the phosphatase function or due only a partial reliance of UIS2 on the phosphatase activity, a construct harboring both point mutations was generated, designated as UIS2-D542-591N^{epi} (Figure 28). In line with the other two single-point mutations constructs, the UIS2-D542-591N^{epi}-mCherry was detected around the periphery of the parasite, showing co-localization with the endogenously expressed UIS2-GFP (Figure 28B, control).

Upon the addition of rapalog using 'early induction' (Figure 28A), it was observed that only a few of the parasites expressing the UIS2-D542-D591N^{epi}-mCherry construct showed a mCherry signal–based on presence of red fluorescence around the parasite– and a decline in the number of m-Cherry positive parasites was observed over time from approximately 15% to less than 1% in the course of two weeks (Figure 28B). Two repeated transfections showed a similar decline of expression of the complementation construct. This result indicated either a generally poor expression of the complementation construct or a potential dominant negative effect. Consequently, due to these observations, the complementation capacity of these parasites was not assessed.

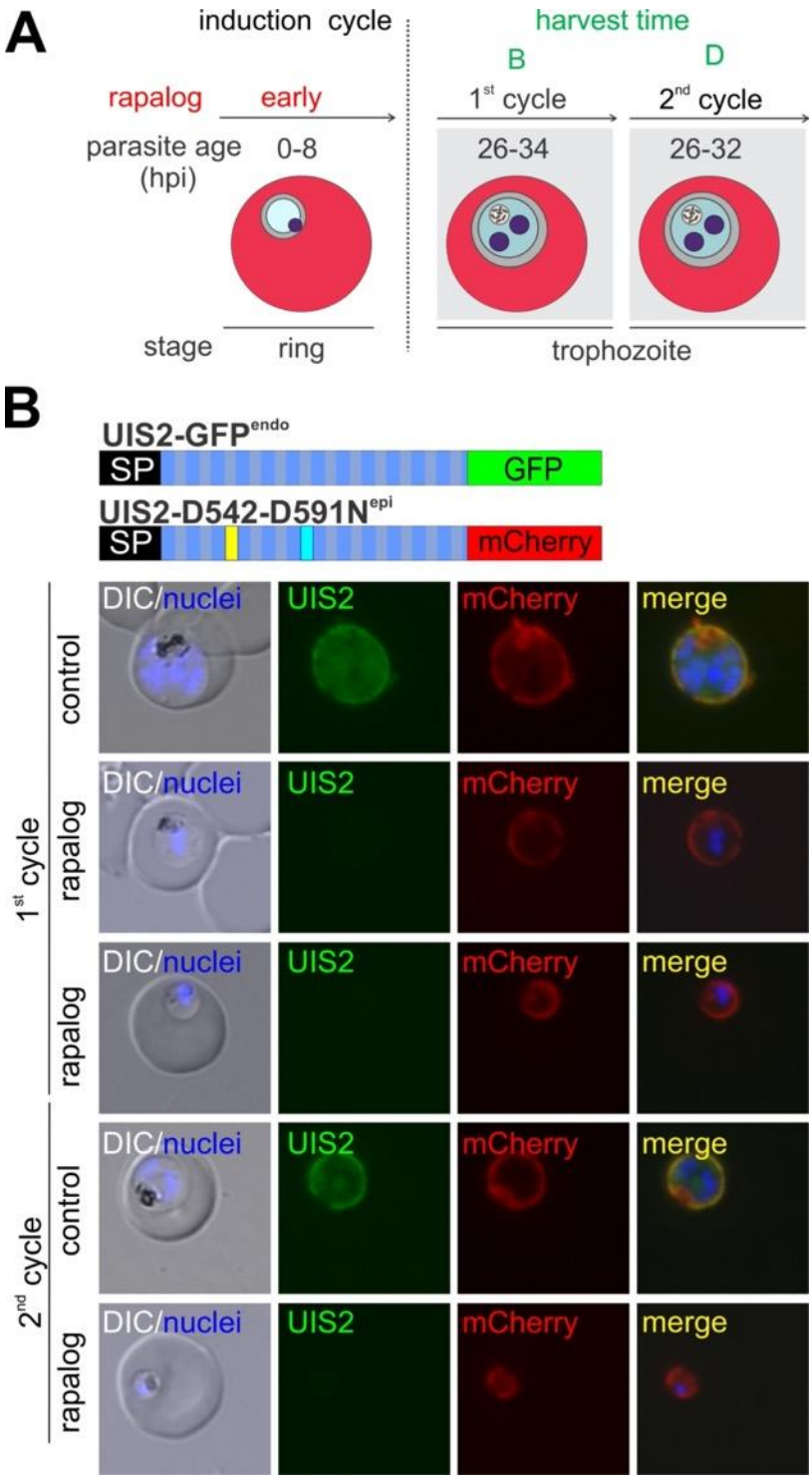

Figure 28. Generation of UIS2-GFP^{endo} parasites with episomal UIS2-D542-D591N^{epi} expression. (A) Schematic representation of the experimental setup for the conditional knockout of UIS2-GFP^{endo} expressing UIS2-D542-D591N^{epi} by inducing excision of the *uis2 gene* in 0 - 8 hpi ('early induction') ring stage parasites during the excision cycle. Parasites were harvested at points B (1st cycle) and D (2nd cycle) at trophozoite stage. (B) Live cells microscope images of ΔUIS2-GFP (+ rapalog) and control (without rapalog) condΔUIS2-GFP parasites expressing the episomal construct UIS2-D542-D591N^{epi}. Parasite were analysed at the 1st cycle in time point B (top panel) and 2nd cycle in time point D (bottom panel). Representative images of three independent experiments (+ rapa n = 30, 10, 26, -

rapa 30, 11, 26). DIC: differential interference contrast; nuclei were stained with Hoechst; the merge indicates overlay of blue, red and green channels. Size bar = 5µm.

As only few parasites were positive for the UIS2-D542N-D591N^{epi}-mCherry complementation construct, parasite size was used as a surrogate to assess the complementation activity of this construct. For this, the size of the remaining UIS2-D542N-D591N^{epi}-mCherry parasites in the second replication cycle after the loss of endogenous UIS2-GFP was assessed (Figure 29A). These parasites – as evident from the red fluorescence of mCherry around the parasite (Figure 28B) – were significantly smaller in terms of area (29.7% ± 3.07%) compared to UIS2-WT^{epi} complemented parasites than the parasites relying on the single mutation complementation constructs (Figure 29B). The complementations with the single mutation constructs (UIS2-D591N and UIS2-D542N), the parasites remaining after excision of the endogenous *uis2* were smaller in size (Figure 29A) compared to the control (Figure 29B). These results suggest that the UIS2 double-mutant exhibits a reduced functional complementation capability in comparison to the single-mutation counterparts. The observed reduction in UIS2-D542N-D591N^{epi} parasites size may be attributed to a more profound reduction in the phosphatase activity. This observation supports the hypothesis that the single point mutations only partially inactivated the phosphatase activity of UIS2.

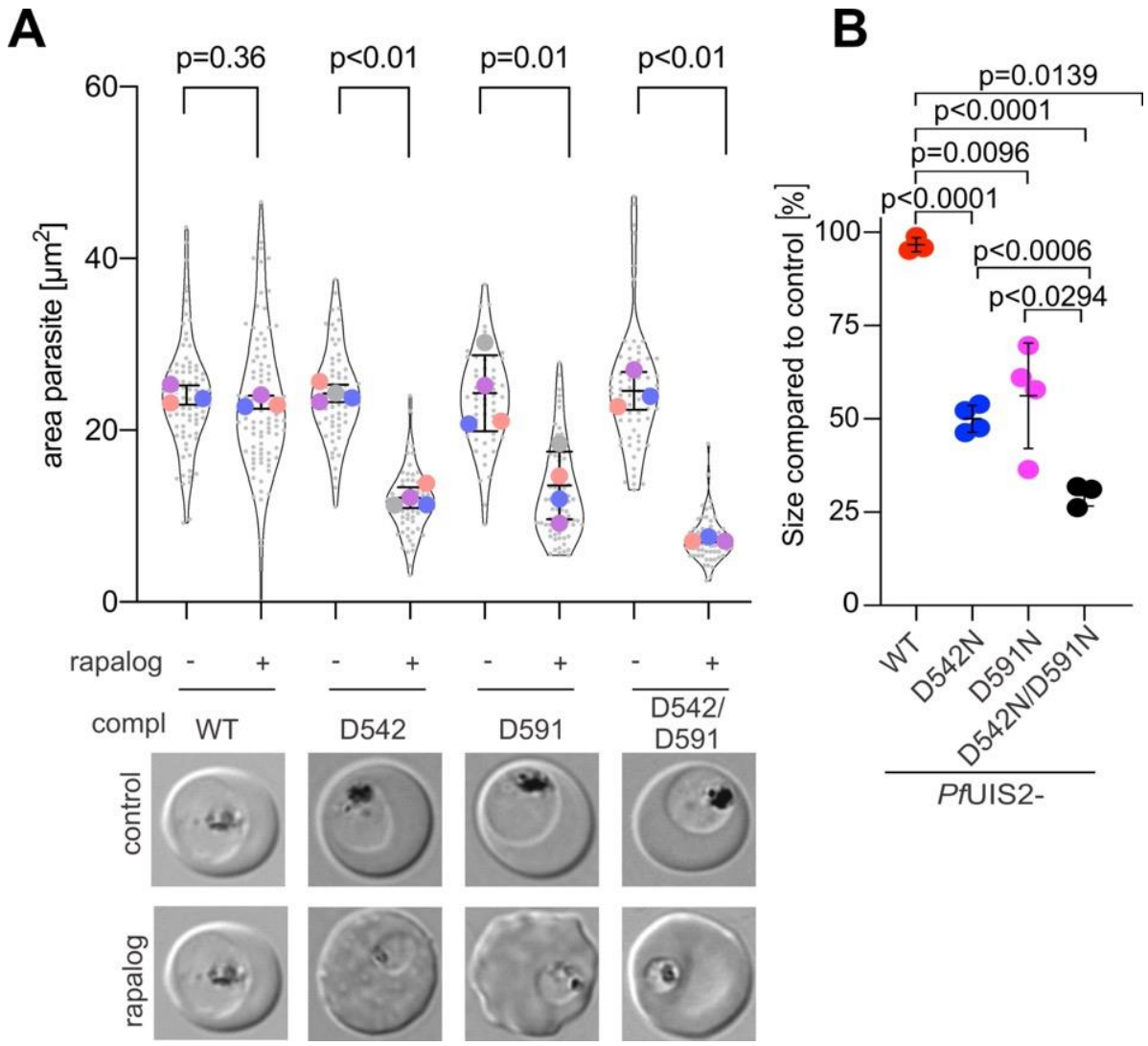

Figure 29. Impact of the UIS2 phosphatase domain mutations on parasite size and diameter. Measurement of area (µm^2) (A) and compared to the control (B) of ΔUIS2-GFP (+ rapalog), expressing a wild-type UIS2 complementation construct (UIS2-WT^{epi}), single-point mutations (UIS2-D542N^{epi}, UIS2-D591N^{epi}) or double-mutations (UIS2-D542N-D591N^{epi}). Parasites were harvested at point D (2nd cycle, see Figure 25). Only parasites expressing the mCherry signal after excision of the endogenous *uis2* were measured and the parasite area was calculated based on the DIC images. Data from three independent experiments, UIS2-WT^{epi} (+ rapa n = 30, 32, 30, - rapa 24, 32, 30), UIS2-D542N^{epi} (+ rapa n = 21, 16, 30, - rapa 17, 18, 33), UIS2-D591N^{epi} (+ rapa n = 19, 10, 30, - rapa 18, 7, 30) and UIS2-D542N-D591N^{epi} (+ rapa n = 30, 10, 26, - rapa 30, 11, 26). Mean values of each independent experiment indicated by colored dots, with individual measurements of each cell by grey dots. Data presented according to SuperPlot guidelines (Lord *et al,* 2020). P values are indicated (Unpaired two-tailed t-test with Welch´s correction); Error bars represent mean ± SD; DIC: differential interference contrast; Size bar = 5µm.

3.8.1 Complementation assay with UIS2 ortholog

In a recent study, it was reported that the phosphatase GRA44 from *Toxoplasma gondii*, designated TGGT1_228170, exhibited a 28% sequence identity over 21% of the amino acid sequence of *P. falciparum* UIS2 (Cygan *et al.,* 2020). Notably, *Tg*GRA44 has been found to be associated with the protein translocon complex MYR within *T. gondii* (Cygan *et al*., 2020). As it here was found that *Pf*UIS2 is needed for protein export in malaria parasites, the sequence similarity between *Tg*GRA44 and UIS2 could indicate homologous functions. Therefore, *Tg*GRA44 was tested for its capacity to complement UIS2 loss in the to test for an evolutionary conservation of the function of these two phosphatases.

To assess the complementation capacity of this potential UIS2 ortholog in *P. falciparum,* an additional episomal complementation construct expressing full length GRA44 was used (Figure 30B). To enable tracking the loss of the endogenous *Pf*UIS2-GFP, the *Tg*GRA44 construct was transfected into the cond∆UIS2-GFP parasites. To confirm the expression of the episomally expressed *Tg*UIS2-mCherry in the cond∆UIS2-GFP integrant cell line, the parasites were examined by fluorescence microscopy (Figure 30B). The m-Cherry signal of *Tg*GRA44 was detected surrounding the periphery of the parasite; however, a significant proportion was localized internally within the parasite, in the food vacuole (Figure 30B). Upon rapalog addition during 'early induction' in the excision cycle –90% of the parasite population was positive for the mCherry signal– (Figure 30B), *Tg*GRA44-mCherry remained in the parasite periphery in both replication cycles, indicating the correct episomal expression of *Tg*GRA44 in ∆UIS2 parasites following the excision of the *uis2* gene (Figure 30B).

To evaluate the functional complementation capacity of the *Tg*GRA44 construct, the endogenous floxed *uis2* locus was excised by adding rapalog (‘early induction’) (Figure 30A), and parasite growth was quantitatively assessed using flow cytometry (Figure 30E). The growth of *Tg*GRA44 parasites was monitored over five consecutive days, using the same culture split into one with rapalog and a control without rapalog (Figure 30E). The growth curves showed similar parasitemia until day 3 post-rapalog addition, but there was a failure of the ∆UIS2 parasites to expand on day 4, while the control parasites continued to multiply. This complementation assay did not indicate

a significant level of complementation (6.7% ± 0.7% growth of control), suggesting a limited functional conservation between *Pf*UIS2 and *Tg*GRA44 (Figure 31). After obtaining this complementation cell line, the positive *Tg*GRA44-mCherry cells (based on presence of red fluorescence around the parasite) (Figure 30B) were used to perform a comparative analysis in terms of parasite size. This analysis revealed that these *Tg*GRA44-mCherry parasites after the excision of the *uis2* gene were smaller than the control but larger than those harboring two phosphatase domain mutations (UIS2-D542N-D591N^{epi}) (Figure 29A, Figure 30C,D).

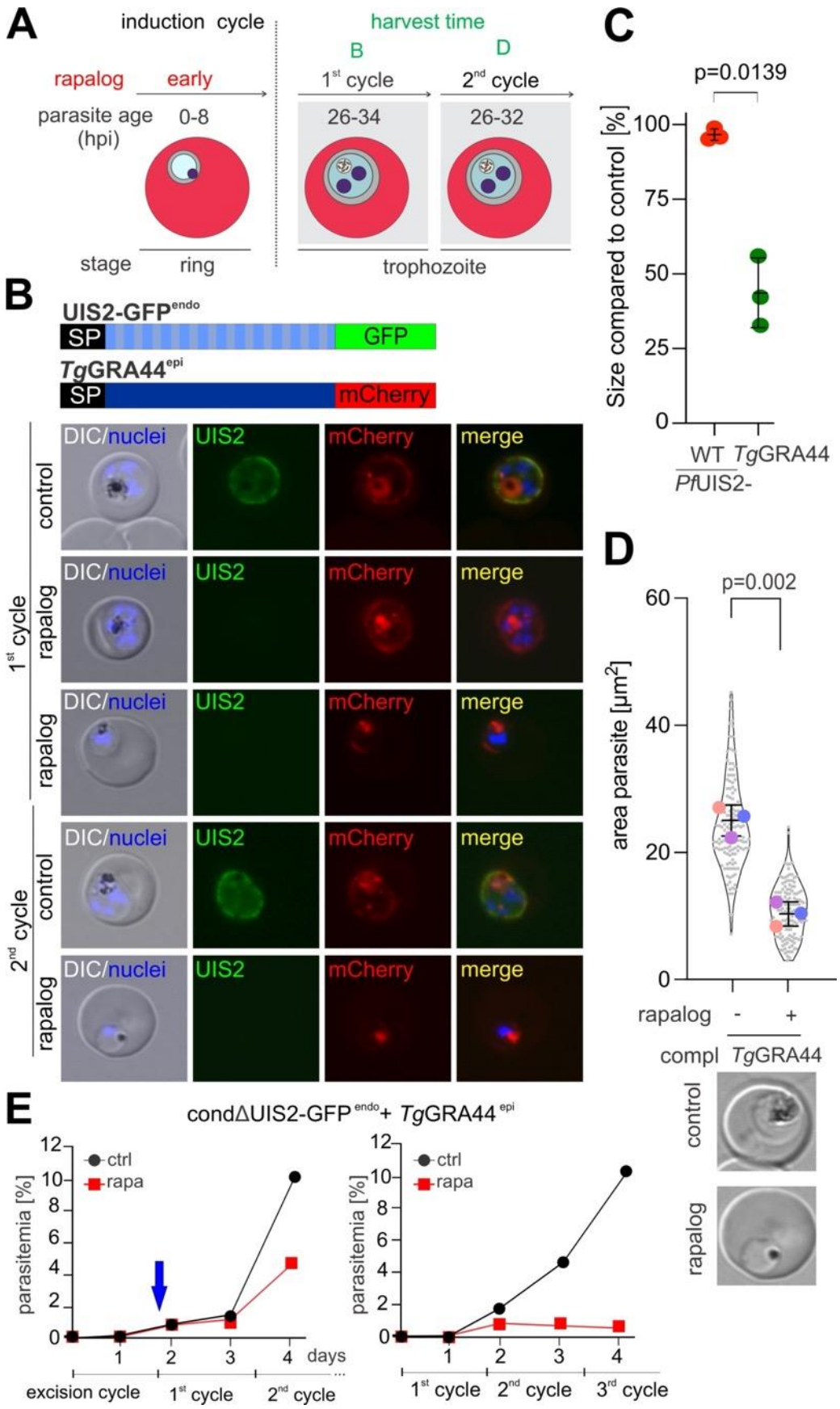
A
induction cycle
harvest time
B
D
rapalog
early
1st cycle
2nd cycle
parasite age (hpi)
0-8
26-34
26-32
stage
ring
trophozoite
B
UIS2-GFPendo
SP
GFP
TgGRA44epi
SP
mCherry
1st cycle
2nd cycle
control
rapalog
DIC/nuclei
UIS2
mCherry
merge
C
p=0.0139
Size compared to control [%]
100
75
50
25
0
WT
TgGRA44
PfUIS2-
D
p=0.002
area parasite [µm2]
60
40
20
0
rapalog
-
+
compl
TgGRA44
control
rapalog
E
condΔUIS2-GFPendo+ TgGRA44epi
parasitemia [%]
ctrl
rapa
days
excision cycle
1st cycle
2nd cycle
3rd cycle

Figure 30. TgGRA44 does not compensate for UIS2 loss. (A) Schematic representation of the experimental setup for the conditional knockout of UIS2-GFP expressing *Tg*GRA44 by inducing excision of the *uis2 gene* in 0 - 8 hpi ('early induction') ring stage parasites during the excision cycle. Parasites were harvested in time point B (1st cycle) and time point D (2nd cycle) at trophozoite stage. (B) Live cells microscope images of (+ rapalog) and control (without rapalog) condΔUIS2-GFP parasites expressing episomal *Tg*GRA44. Parasites were analysed at the 1st cycle (top panel) and 2nd cycle (bottom panel). Representative images of four independent experiments (+ rapa n = 34, - rapa n = 34 per experiment). DIC: differential interference contrast; nuclei were stained with Hoechst; the merge indicates overlay of blue, red and green channels. Size bar = 5µm. Measurement of area (μm^2) (C) and compared to the control (D) of condΔUIS2-GFP parasites (+ rapalog), expressing *Tg*GRA44. Parasites were harvested at point D (2nd cycle). Only parasites expressing the mCherry signal after excision of the endogenous *uis2* were measured and the parasite area was calculated based on the DIC images. Data from four independent experiments. Mean values of each independent experiment indicated by colored dots, with individual measurements by grey dots. Data presented according to SuperPlot guidelines (Lord *et al*, 2020). P values are indicated (unpaired two-tailed t-test); Error bars represent mean ± SD; DIC: differential interference contrast; Size bar = 5µm. (E) Flow cytometry growth curves of synchronous ring stage condΔUIS2-GFP parasites episomally expressing *Tg*GRA44 starting in excision cycle (left) or cycle 1 (right) on 5 consecutive days. Blue arrow indicates invasion into the first cycle and loss of *uis2*. One representative of n = 3 independent experiments (replicas are shown in Appendix 8).

The comparative analysis of growth on the fifth day of all generated complementation constructs, showed that complementation with UIS2-WT^{epi} restored parasitic growth to 99.4% ± 0.8%. In contrast, the UIS2-D542N^{epi} mutant parasites partially restored parasite growth to 54.5% ± 4.6% and UIS2-D591N^{epi} mutant parasites to 58.9% ± 3.2% after the removal of endogenous *uis2* (Figure 31). This result indicates that the single-point mutations in the UIS2 phosphatase domain reduces UIS2 function, suggesting a role of the phosphatase domain in the function of this protein (Figure 31). The complementation data collectively suggest that the observed UIS2 loss of function phenotype is specific to UIS2 and that activity of the phosphatase domain is important for UIS2 function.

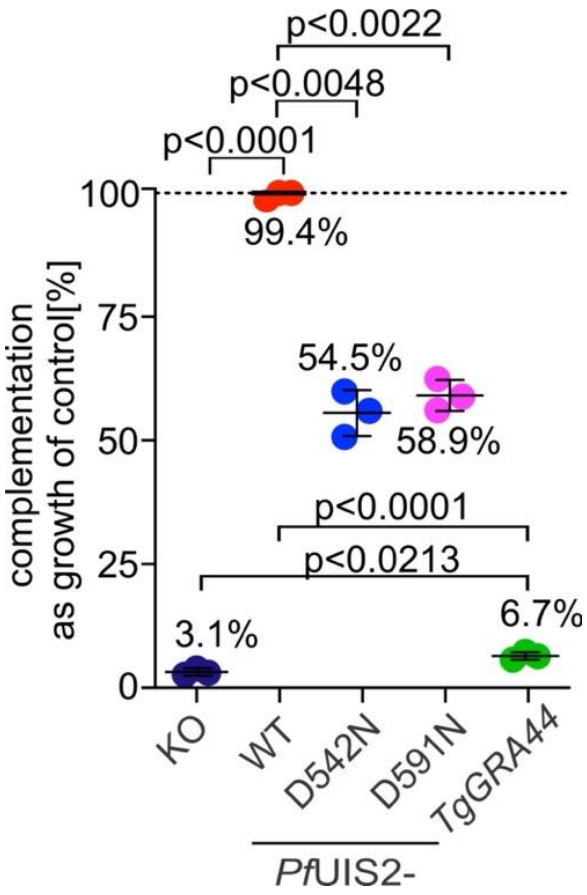

Figure 31. Complementation capacity of the UIS2 modified versions. The complementation capacity of each indicated construct was calculated relative to the control, which was set as 100% (top dotted black line). Each data point (colored dot) was obtained during the second cycle (harvest time C). Data from three independent experiments for complementation with UIS2-WT^{epi}, UIS2-D542N^{epi}, UIS2-D591N^{epi} and UIS2-D542N-D591N^{epi}, and four independent experiments for *Tg*GRA44 constructs. P values are indicated (Unpaired two-tailed t-test with Welch´s correction); Error bars represent mean ± SD; DIC: differential interference contrast; Size bar = 5µm.

3.9 DiQ-BioID with UIS2

In order to identify possible interactors and other proteins in proximity of UIS2, a DiQ-BioID with UIS2 was performed. DiQ-BioID is based on inducible heterodimerization which relies on the FKBP-FRB system, where the promiscuous biotin ligase BirA* (a mutated R118G version of *Escherichia coli* BirA* (Choi-Rhee et al., 2004)) is conditionally recruited to a target of interest to biotinylate proximal proteins (Birnbaum *et al*., 2020; Roux *et al*., 2012). The biotinylated proteins can be purified by streptavidin beads, followed by quantitative mass spectrometry using dimethyl labelling (Boersema *et al.,* 2019) to obtain the proteins enriched over the background by subtracting the control, where BirA* is not recruited to the target (Birnbaum *et al*.,

2020). For this study, this system was adapted to be carried out in the PV using BirA* with a signal peptide (SP-BirA*-FRB-mCherry) and UIS2 fused to 2xFKBP-GFP, a cell line obtained from Khosh-Naucke, 2018. The biotinylizer consists of a signal peptide of PF3D7_0830400 (Heiber *et al*., 2013), that mediates entry into the secretory pathway and is N-terminally fused to a BirA* domain, which is necessary for the biotinylation of proteins. Additionally, it includes an FRB domain that allows for the recruitment of the biotinylizer to the bait protein, which has the FKBP domain, UIS2-FKBP, fused to it, and an mCherry domain for the visual localization of the biotinylizer (Figure 32A).

To induce dimerization of FKBP and FRB domains, rapalog was added to the parasites which is expected to result in the recruitment of SP-BirA*-FRB-mCherry to UIS2-2xFKBP-GFP (Figure 32A). To assess the functionality of BirA* and its ability to biotinylate proteins at the expected site, the biotin was visualized using red fluorescent streptavidin in a streptavidin-immunofluorescence assay (IFA) after the addition of rapalog (Figure 32B). A parallel culture of parasites grown without rapalog served as a control. In this control group, IFA images confirmed the expression of UIS2-2xFKBP-GFP at the periphery of the parasite. A streptavidin signal was detected also in the parasite periphery, but no colocalization with the bait protein was observed (Figure 32B). Upon rapalog and biotin addition, a streptavidin signal was detected at the parasite periphery, co-localizing with the GFP signal of UIS2-2xFKBP-GFP, suggesting successful recruitment of BirA* to the target site (Figure 32B). The integrity of the UIS2-2xFKBP-GFP and SP-BirA*-FRB-mCherry - fusion proteins was evaluated through Western Blot analysis using anti-GFP and anti-RFP antibodies. The constructs were detected with the expected molecular weight of 210 and 70 kDa, respectively (Figure 32C). Next, protein biotinylation was further confirmed through streptavidin Western Blot analysis performed 24 hours after the addition of rapalog (Figure 32C). An additional band compared to the control, consistent in size with the predicted molecular weight of approximately 280 kDa, was detected in the extract of the rapalog-treated cells (Figure 32C). This observation suggests that the induction of dimerization with rapalog efficiently recruited the biotinylizer to UIS2 in the PV compartment.

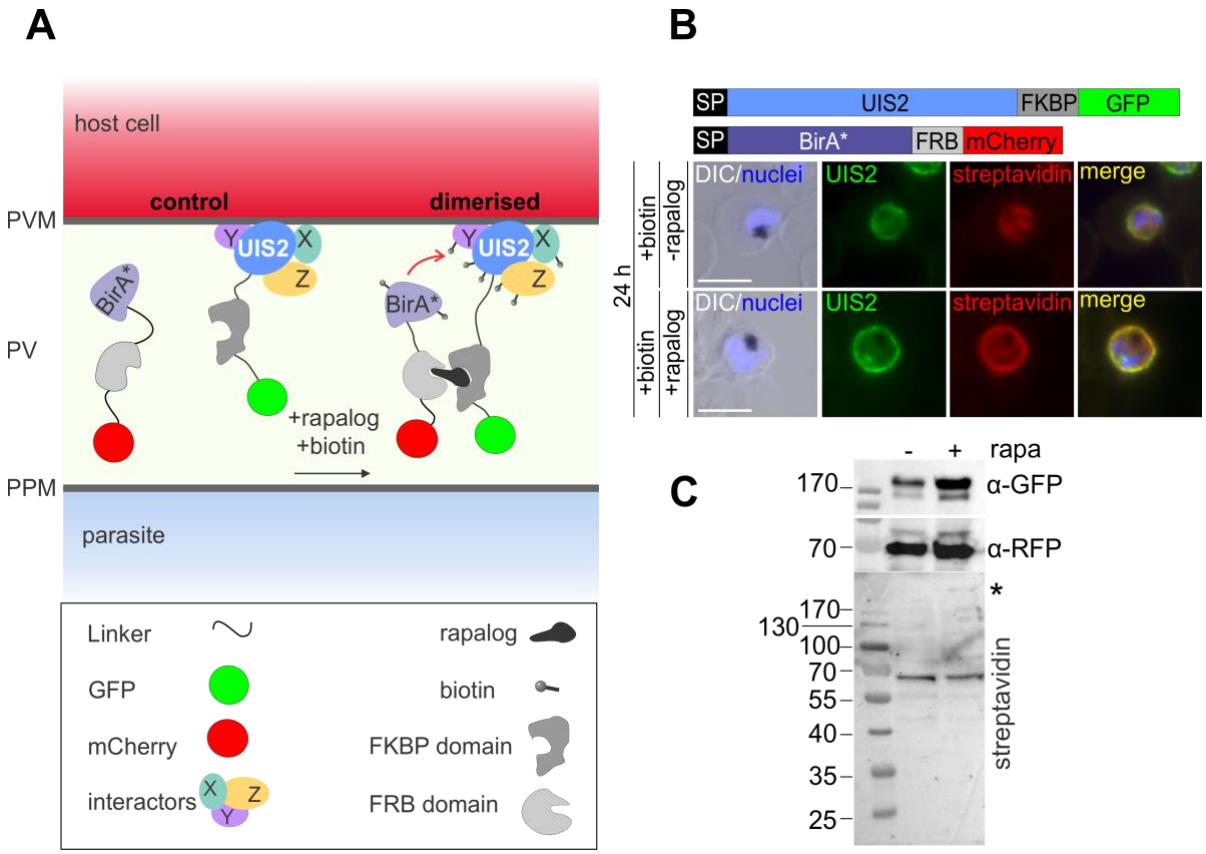

Figure 32. Inducible dimerization of SP-BirA*-FRB-mCherry with UIS2-2xFKBP-GFP. (A) Schematic illustration of DiQ-BioID with UIS2. Upon addition of rapalog, the biotin ligase BirA* (biotinylizer: BirA* fused with FRB-mCherry) is conditionally recruited to UIS2-2xFKBP-GFP and labelling of proteins in close proximity is initiated. (B) Immune fluorescence images of acetone fixed parasites 24 h after rapalog addition and controls without rapalog showing co-localization of biotinylated protein (detected using streptavidin-HRP) with UIS2 (detected using mouse anti-GFP). Images are representatives of 2 independent experiments with at least 15 images series per experiment. Merge indicates overlay of green and red channels; DIC: differential interference contrast; nuclei were stained with DAPI. Size bar: 5 μm. (C) Western blots of biotinylation experiment of SP-BirA*-FRB-mCherry + UIS2-2xFKBP-GFP cultivated 24 h in the presence (+) or absence (-) (control) of rapalog (rapa). Parasites were treated for 24 h with 50 μM biotin. Western blots were probed with Streptavidin-HRP to detect biotinylated proteins. The recruitment of the biotinylizer (SP-BirA*-FRB-mCherry) to UIS2-2xFKBP-GFP was evident from the additional band observed in the + rapalog sample with a molecular weight of 280 kDa consistent with the size of the UIS2 fusion protein (*). UIS2-FKBP-GFP was visualized with anti-GFP (from mouse), and SP-BirA*-FRB-mCherry with anti-red fluorescence protein (anti-RFP from rat). Mean of n = 2 independent experiments. Replicas of immunoblots are shown in Appendix 9.

In order to obtain a detailed analysis of possible UIS2 interactors, quantitative mass spectrometry of two independent experiments of asynchronous parasites were carried out in the laboratory of Dr. Richàrd Bàrtfai (Radboud Institute for Molecular Life Sciences in Nijmegen, Netherlands), resulting in a list of proteins enriched in the rapalog over the control sample. The results were plotted as log2-normalized ratio on the x- (experiment 1) and y- (experiment 2) axis and only proteins, in total 15 proteins, enriched average log2 > 1.0 are shown as labelled dots, all the other hist are shown as grey dots (Figure 33A).

Successful dimerization and hence recruitment of the BirA* ligase to UIS2 target was confirmed as UIS2 was the most significantly enriched protein over the control. In both experiments, the surface protein P113 (PF3D7_1420700) was the most enriched protein after UIS2 (Figure 33A,B). The other enriched proteins comprised PFK9 (6-phospho-1-fructokinase on chromosome 9), a protein identified in prior DiQ-BioID experiments (Birnbaum *et al*., 2020) and therefore a likely contaminant, as well as proteins without signal peptide or transmembrane domain which are unlikely to be in the PV (Figure 33B). This set includes the eukaryotic translation initiation factor 3 subunit A (EIF3A, PF3D7_1212700), a protein complex playing a crucial role in translation initiation and ribosomal recycling (Kaur *et al.*, 2020) that is essential for parasite development throughout the intraerythrocytic cycle of *P. falciparum* (Dobrescu *et al.*, 2023). EIF3A interacts in a protein complex with EIF2α (Jackson *et al.*, 2010), an initiation translational factor crucial for host infection, which was previously connected to the phosphatase UIS2 (role in translation regulation by dephosphorylating eIF2α-P) (Zhang *et al.*, 2016). However, it remains unclear how these proteins could come into contact in the PV compartment during blood stages in *P. falciparum* as it would be highly unusual (and none of the components harbor signal peptides) if the translation complex were located in the PV and not in the parasite cytosol.

Interestingly, no PTEX components were significantly enriched in this DiQ-BioID with UIS2 (HSP101, EXP2, PTEX150 (average log2 < 1.0) (Figure 33B)), indicating that despite its effect on export, UIS2 is likely not in direct contact with this complex. Three proteins, in addition to P113, exhibited an average log2 >1.0 in the UIS2 DiQ-BioID

and harbored a predicted signal peptide or transmembrane domain, essential features for proteins associated with the PV or PVM (Appendix 10). Those proteins were, a protein with an ubiquitin-like N-terminal region (PF3D7_0922100) and an RNA (uracil-5-) methyltransferase (PF3D7_1133800) found in positions 4 and 6 in experiment 1 and positions 13 and 14 in experiment 2, respectively (Appendix 11). Based on the average enrichment values (normalized log2 of 2 experiments), the candidates were found in enrichment positions 13 and 15 (Figure 33B). The third protein with a signal peptide was the *Plasmodium* exported protein PHIST (PF3D7_0401800) (Figure 33B, Appendix 11). Given the limited enrichment of the PHIST protein in experiment 2 and its likely export, it was here not further analysed. P113 was previously shown not to be needed for protein export (Bullen *et al.*, 2022), and this candidate was also not further evaluated. Therefore, an analysis was conducted on the two remaining candidates with signal peptide or transmembrane domain, PF3D7_0922100 and PF3D7_1133800. In order to validate these potential UIS2 interactors, their localization and function in protein export were analysed.

A

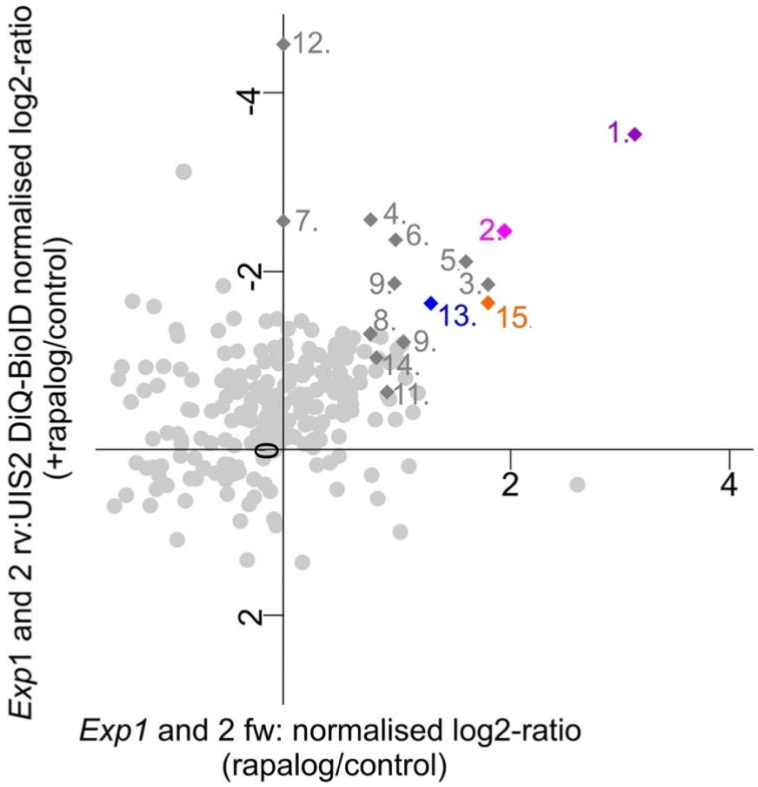

B

#	PlasmoDB ID	Name/description	Abbr	avg	TM	SP
1.	PF3D7_1464600	serine/threonine protein phosphtase	UIS2	3,07	-	+
2.	PF3D7_1420700	surface protein P113	P113	1,97	-	+
3.	PF3D7_0915400	ATP-dependent 6-phosphofructokinase	PFK9	1,69	-	-
4.	PF3D7_1212700	eukaryotic translation initiation factor 3A	EIF3A	1,41	-	-
5.	PF3D7_1407100	rRNA2-O-methyltransferase fibrillarin	NOP1	1,39	-	-
6.	PF3D7_1421200	40S ribosoma protein S25	RPS25	1,38	-	-
7.	PF3D7_1309100	60S ribosomal protein L24, putative	60S	1,33	-	-
8.	PF3D7_1118500	nucleolar protein 56, putative	NOP56	1,24	-	-
9.	PF3D7_0606700	coatomer alpha subunit, putative	coatomer-α	1,21	-	-
10.	PF3D7_1360900	RNA-binding protein, putative	RNA binding protein	1,19	-	-
11.	PF3D7_0401800	Plasmodium exported protein	PHISTb	1,09	-	+
12.	PF3D7_0727200	cysteine desulfurase	IscS	1,06	-	-
13.	PF3D7_0922100	ubiquitin-like protein, putative	ubiquitin like protein	1,04	+	-
14.	PF3D7_1453700	Hs90 co-chaperone p23	P23	1,03	-	-
15.	PF3D7_1133800	RNA(uracil-5-) methyltransferase	U5MTase	1,01	-	+

Figure 33. Scatter plot of UIS2-DIQ-BioID. (A) Full scatter plot of the averages of both DIQ-BioID experiments, showing proteins significantly enriched (log2 ratio) on rapalog (biotinyliser on target) compared with control (biotinyliser in the PV lumen). (B) Enriched proteins are numbered according to their enrichment score (all data is shown in Appendix 10). PlasmoDB identifiers and annotations are given. (Name/description; Abbr: abbreviation; Avg: average (normalized log2 of 2 experiments); TM: transmembrane domain, SP: signal peptide. Data from average of 2 experiments shown in A. The candidates in blue and orange were chosen for validation. Protein likely to be contaminants or without SP or TM are shown in grey (Independent scatter plot of each experiment are shown in Appendix 11).

3.9.1 Candidate PF3D7_1133800

PF3D7_1133800 (predicted molecular weight 101 kDa) is annotated as RNA (uracil-5) methyltransferase in PlasmoDB and contains a N-terminal signal peptide. For this candidate a conditional knock out was generated by truncating the gene and providing a floxed functional copy that can be excised using diCre in a similar approach used for uis2 (Figure 34A). The correct integration of the SLI-plasmid into the genome to generate the corresponding genomic modification was confirmed by PCR (Figure 34B). To analyse the effect of *PF3D7_1133800* deletion, the kinetics of protein loss was first assessed. For this, different analyses were conducted to test for gene and protein loss. For the former, to confirm that the cell line behaved as expected, the excision of the active *PF3D7_1133800* gene was demonstrated by PCR at 24 h and 48 h post addition of rapalog (Figure 34C). The bands observed demonstrate efficient excision of the functional copy of *PF3D7_1133800* gene, resulting in ∆PF3D7_1133800 parasites. The control cells maintained the original genomic locus (intact *PF3D7_1133800* locus) at both time points (Figure 34C). Taken together, these PCR results confirmed that complete excision of the functional *PF3D7_1133800* gene is achievable within a single asexual growth cycle.

Next, the protein levels of this candidate in ∆PF3D7_1133800 parasites was assessed by Western blot analysis at 48 h and 72 h post-addition of rapalog. Western blot analysis using α-HA (the epitope tag added to the functional PF3D7_1133800 copy), revealed that there was no band present in + rapalog samples (Figure 34D). This indicates the loss of PF3D7_1133800, with approximately 11% residual protein observed 48 h and approximately 7% residual protein observed 72 h after induction (Figure 34E). This was in comparison to two bands observed in the control, of which one band exhibited a migration consistent with the expected molecular weight of 101 kDa, while another band was detected at approximately 90 kDa (Figure 34D). As this band indicated a molecular weight below the full length UIS2 fusion protein, it may constitute an N-terminally processed version or a degradation product. The same immunoblot was re-probed with an anti-BIP antibody as a loading control (Figure 34D). Overall, these findings indicated efficient loss of PF3D7_1133800 in the 1st cycle after rapalog addition and validated this cell line to achieve a conditional knock out of *PF3D7_1133800.*

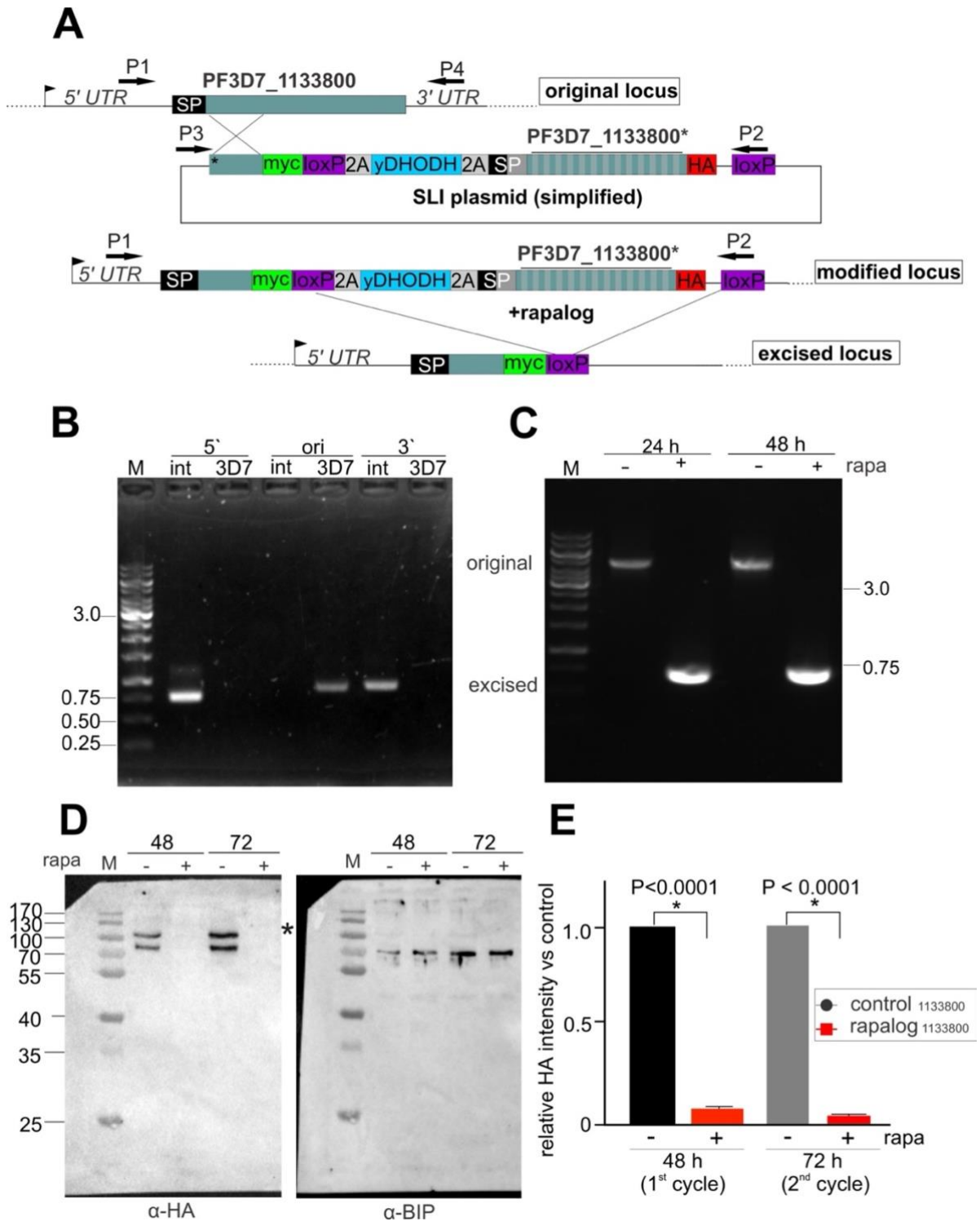

Figure 34. Candidate PF3D7_1133800. (A) Simplified schematic of the generation of the diCre-inducible condΔPF37_1133800 knockout cell line using SLI and subsequent excision upon the addition of rapalog (modified from Mesén-Ramírez *et al.*, 2019). Black arrows, native *PF3D7_1133800* promotor; light green box, entire gen and target region for homologous recombination; black/gray box, hybrid signal peptide comprising the first 22 aa of the PF3D7_0220200 protein (provided by Jan Stäcker, 2021) and the first 26 aa of the signal peptide of PF3D7_1333800; green/gray striped box, recodonized PF3D7_1133800; UTR, untranslated region; cond, conditional; HA, 3x human influenza

hemagglutinin; 2A, T2A skip peptide. Full condΔPF3D7_1133800 schematic is shown in Appendix 12. (B) Agarose gel showing PCR-products to assess correct integration of the SLI-plasmid into the genome to obtain the indicated cell line. For *Pf*3D7_1133800-HA^{endo}, primers (Appendix 1) were "1133800-Int-fw" + DHODH 42 rv" to demonstrate 5' integration (5' int, 751 bp) and "pARL55 fw" + "1133800-Int-rv" to demonstrate 3' integration (3' int, 896 bp). Primers "1133800-Int-fw" + "1133800-Int-rv" were used to show absence of unmodified original locus in the indicated cell line (ori int) and 3D7 gDNA was used as a control (ori 3D7, 860 bp). M, marker (GeneRuler^{TM} 1kb, Thermo Scientific); DNA fragment size standard is indicated in kbp. (C) Agarose gels showing PCR-products to test for excision of the floxed functional *PF3D7_1133800* in ΔPF3D7_1133800 knockout (+rapalog) and control (without rapalog) condΔPF3D7_1133800 parasites at 24 h and 48 h post-rapalog addition. Primers (Appendix 1) were P1/P2 as indicated in Figure 33A. (D) Western blot using anti-HA (from rat) confirmed loss of PF3D7_1133800 on the protein level 48 h and 72 h post-rapalog addition. The expected molecular weight of PF3D7_1133800-3xHA is 101 kDa. Anti-BIP (from rabbit) served as loading control. Molecular weight standard is indicated in kDa. One representative experiment of three biological replicas; full blots and replica in Appendix 13. (E) Quantification of PF3D7_1133800-3xHA levels based on densitometric analysis of anti-HA immunoblots at the indicated time points (mean of n = 3 independent experiments) (immunoblots used for quantification are shown in Appendix 13). HA signal was normalized to BIP. P value is indicated (unpaired two-tailed t-test). Error bars indicate standard deviation (SD).

3.9.1.1 Localization of PF3D7_1133800

Next, the localization of PF3D7_1133800-3xHA within the parasites was analyzed (Figure 35). The HA-tagged PF3D7_1133800 was detected in some cases as a prominent focus or in multiple foci within the parasite. This observation suggests a potential location in structures of the secretory pathway, nucleus or at the apicoplast (Figure 35). PF3D7_1133800-3xHA did not colocalize with EXP2, a resident PVM protein (Figure 35). This result suggests that this protein is not located in the PV but rather at a structure within the parasite cell.

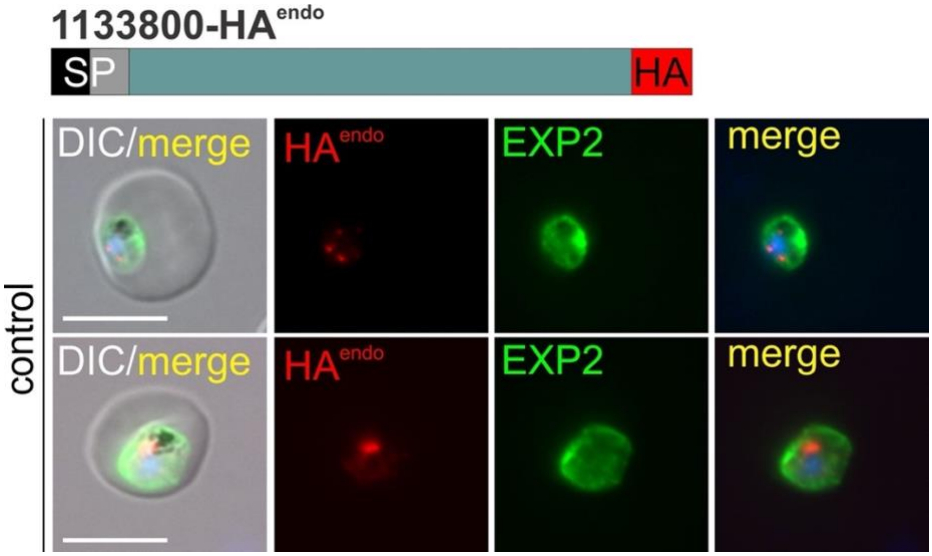

Figure 35. Localization of PF3D7_1133800-3xHA^{endo}. Immunofluorescence assay (IFA) of formaldehyde/glutaraldehyde fixed condΔPF3D7_1133800 parasites (control) at 1st cycle, showing localization of PF3D7_1133800-3xHA^{endo}, and location of EXP2 in trophozoite stages. Anti-HA (from rat) was used to detect PF3D7_1133800-3xHA^{endo} and anti-EXP2 (from mouse) was used to detect EXP2 (PVM). Representative images of three independent experiments with at least 25 image series per experiment. DIC: differential interference contrast. Nuclei were stained with Hoechst. Size bar = 5µm.

To more accurately determine the cellular location of PF3D7_1133800 using live cell imaging, an integration cell line resulting in a 2xFKBP-mNEON tagged PF3D7_1133800 was generated by Stephan Wichers-Misterek (Figure 36). The correct integration of the plasmid into the genome was confirmed by PCR (kindly performed by Stephan Wichers-Misterek, Figure 36A). Fluorescence microscopy with these parasites showed that PF3D7_1133800-mNEON was expressed in all asexual blood stages (Figure 36B), consistent with its transcriptional profile (Otto *et al.*, 2010). PF3D7_1133800-mNEON was detectable in a prominent focus in rings stages and in multiple foci in later stages (Figure 36B). The foci were in close proximity to the nucleus or in the nucleus. The location of this protein within the parasite indicates that it is unlikely to be associated with the same function as UIS2, given its completely different cellular location. Together with the failure to influence protein export after its ablation, these results indicate that this protein likely was a contaminant in the UIS2 DIQ-BioID.

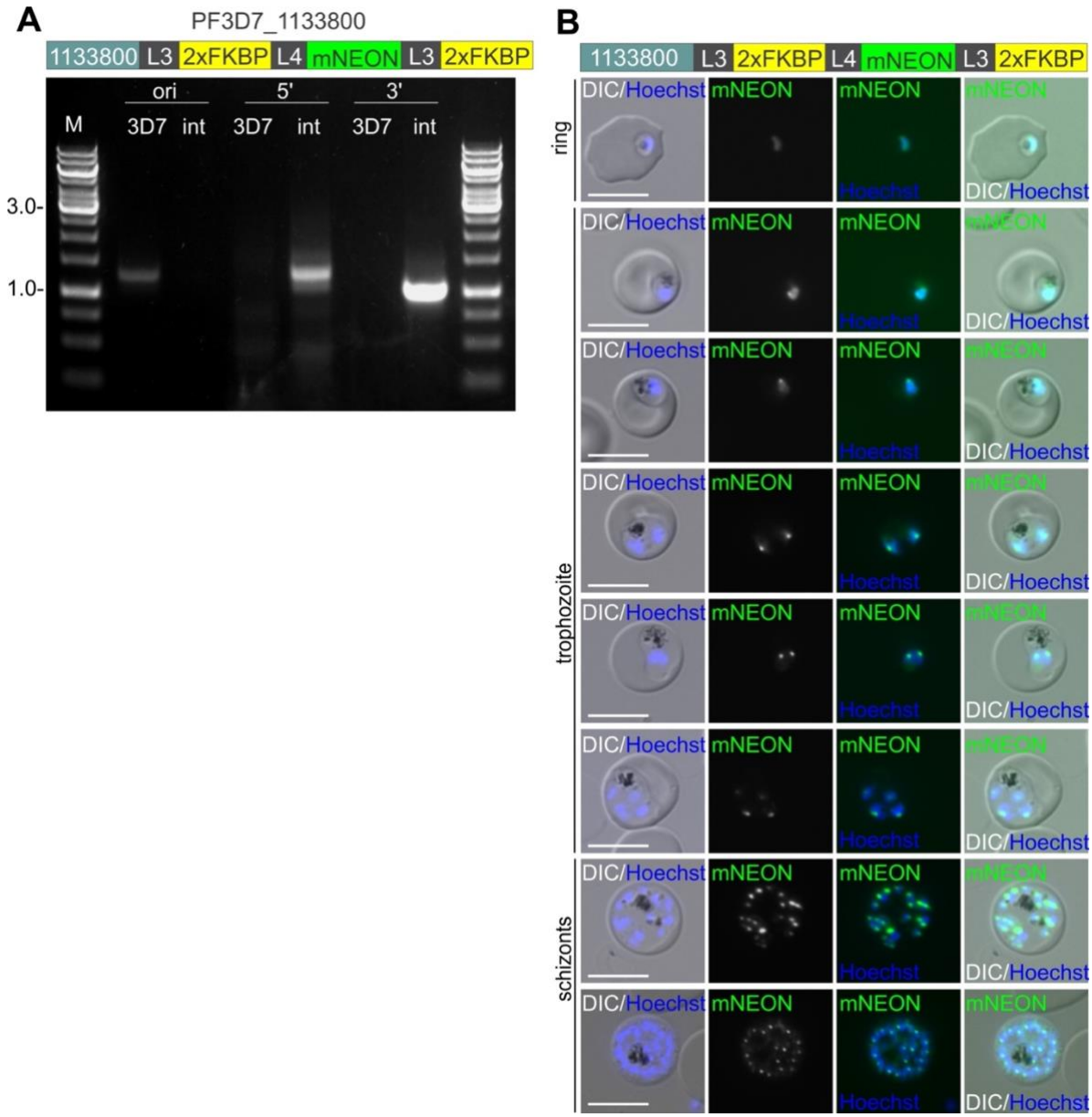

Figure 36. Localization of PF3D7_1133800 is not in the PV compartment. (A) Agarose gel showing PCR-products to assess correct integration of the plasmid into the genome to obtain the indicate cell line. For *PF*3D7_1133800-2xFKBP-mNEON-2xFKBP, primers (Appendix 1) were "1133800-mNEON-Int-fw" + FKBP 82 rv" to demonstrate 5' integration (5' int, 1362 bp) and "pARL55" + "1133800-mNEON-Int-rv" to demonstrate 3' integration (3' int, 1315 bp). Primers "1133800-mNEON-Int-fw" + "1133800-mNEON-int-rv" were used to show absence of unmodified original locus in the indicated cell line (ori int) and 3D7 gDNA was used as a control (ori 3D7, 1285 bp). M, marker (GeneRuler™ 1kb, Thermo Scientific); DNA fragment size standard is indicated in kbp. (B) Live cell microscopy images of *PF*3D7_1133800-2xFKBP-mNEON-2xFKBP of the intraerythrocytic stages indicated (from ring to schizont stage). Images are representative of two independent microscopy sessions with at least 30 images series each. DIC: differential interference contrast; nuclei were stained with Hoechst. Size bar = 5µm.

3.9.1.2 PF3D7_1133800-KO does not result in a defect in protein export

After demonstrating the effective excision of the functional *PF3D7_1133800*, absence of this gene in the 1st cycle post-rapalog addition and its localization within the parasite, the importance of this candidate for parasite growth was assessed. The growth of condΔPF3D7_1133800 parasites was monitored over five consecutive days, using the same culture split into one with rapalog and a control without rapalog (Figure 37B,C). The growth curves showed similar parasitemia until day 4 post-rapalog addition (Figure 37B). Tracking growth of ΔPF3D7_1133800 ring stage parasites (first cycle after induction) showed an impact on growth on day 2 and 3 (second cycle) (Figure 37C), indicating that the loss of *PF3D7_1133800* has a partial effect on parasite multiplication, underscoring the importance of this protein for parasite growth.

To investigate, whether the PF37_1133800 protein also has an effect on protein export, as observed in the previous results with UIS2 (section 3.4), different markers for exported proteins and a resident PVM protein were evaluated by IFAs (Figure 37D,E). The export of these markers was assessed in parasite treated under the early induction regime (0 - 8 hpi) (Figure 37A). Since the effect on parasite multiplication became evident in ΔPF3D7_1133800 after the ring stage of the first cycle, KAHRP and EXP2 were assessed at a later harvest time (termed B, 26 – 32 hpi), corresponding to the trophozoite stage of the first cycle (Figure 37A,D), while SBP1 was evaluated at the harvest time C (4 - 12 hpi, during the ring stage of the second cycle) (Figure 37A,E). In the control, SBP1 was correctly trafficked to the MCs, KAHRP to the erythrocyte membrane while EXP2 was located at the PVM (Figure 37D,E). After excision of the *PF3D7_1133800* in these parasites, those markers remained unaffected, indicating that protein export is not affected in ΔPF3D7_1133800 parasites (Figure 37D,E).

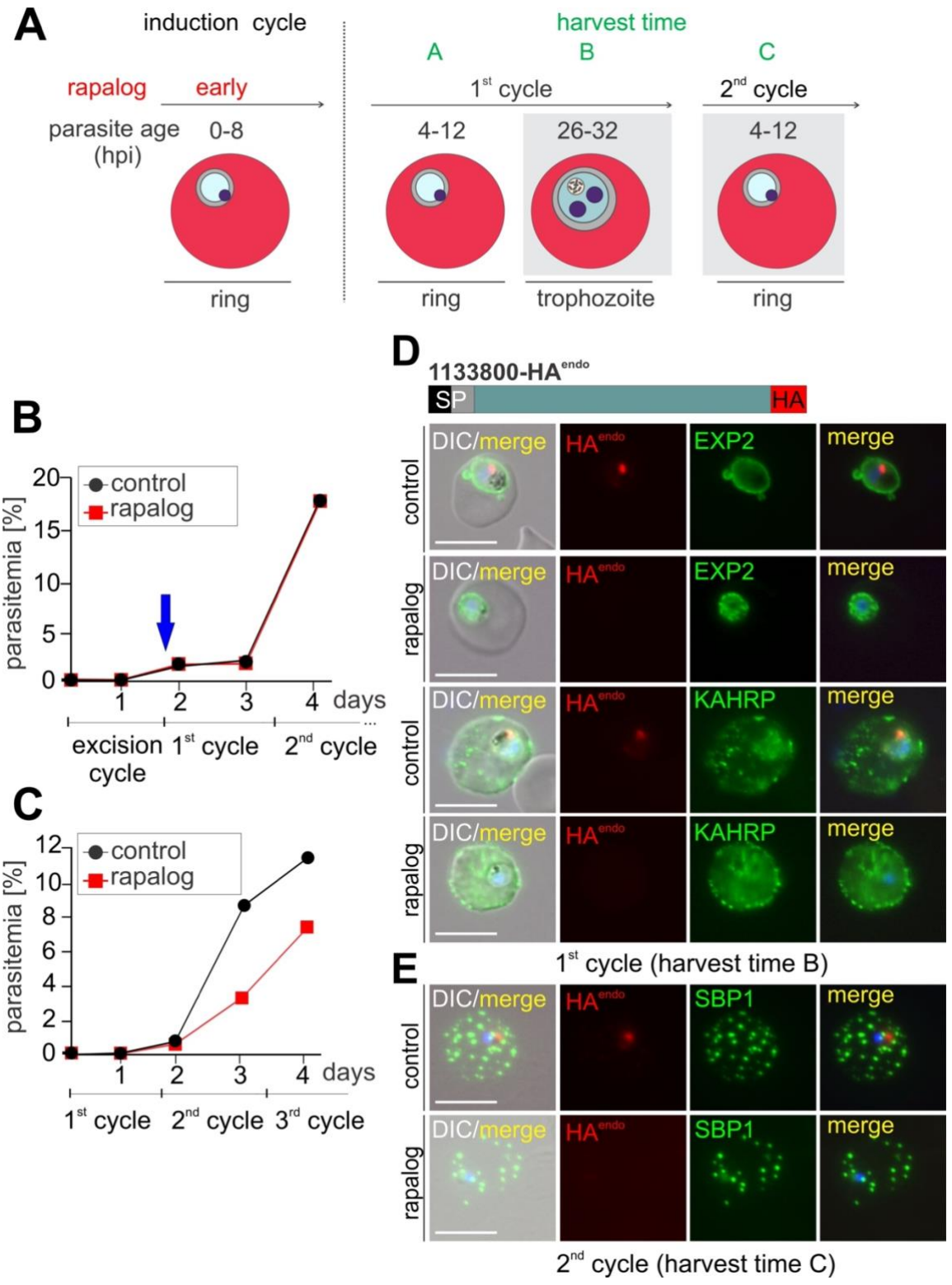

Figure 37. Conditional knock out of PF3D7_1133800 did not impact protein export. (A) Schematic representation of experimental setup for conditional knockout of PF3D7_1133800 by inducing excision of *PF3D7_1133800 gene* in 0 - 8 hpi ('early induction') ring stage parasites. Parasites were harvested at point B for the analysis of KAHRP and EXP2 and at point C for the analysis of SBP1. (B,C) Flow cytometry growth curves of synchronous ring stage condΔPF3D7_1133800 parasites starting either at the excision cycle (B) or cycle 1 (C) on 5 consecutive days. Blue arrow

indicates invasion into the first cycle and loss of PF3D7_1133800. One representative of n = 3 independent experiments (replicas are shown in Appendix 14). (D) Immunofluorescence assay (IFA) of formaldehyde/glutaraldehyde fixed ΔPF3D7_1133800 (+rapalog) and control (without rapalog) condΔPF3D7_1133800 parasites at 1st cycle, showing localization of PF3D7_1133800-3xHA^{endo}, and location of KAHRP and EXP2 in trophozoite stages. Anti-HA (from rat) was used to detect PF3D7_1133800-3xHA^{endo}, anti-KAHRP (from rabbit) was used to detected KAHRP (erythrocyte membrane) and anti-EXP2 (from mouse) was used to detect EXP2 (PVM). Representative images of three independent experiments with at least 25 image series per experiment and condition. (E) Microscopy images of IFAs using acetone-fixed cells of ΔPF3D7_1133800 parasites (+rapalog) and control (without rapalog) at the 2st cycle, showing localization of .PF3D7_1133800-3xHA^{endo} and location of SBP1 in ring stages. Anti-HA (from rat) was used to detect PF3D7_1133800-3xHA^{endo} and anti-SBP1C (from rabbit) to detected SBP1. Representative cells from one of three independent experiments with 25 image series per experiment and condition. DIC: differential interference contrast. Nuclei were stained with Hoechst. Size bar = 5µm.

3.9.2 Candidate PF3D7_0922100

Candidate PF3D7_0922100 (predicted molecular weight of 182 kDa), is annotated as a putative ubiquitin-like protein (due to an N-terminal ubiquitin-like region comprising amino acids 8-83, UniProt), and contains two transmembrane domains in close proximity at its center (amino acids 851 - 871 and 890 - 913 out of 1542 in total, PlasmoDB) (Figure 38A). For this candidate a conditional knock out was generated by truncating the gene and providing a floxed functional copy that can be excised using diCre in a similar approach used for *uis2* and *PF3D7_1133800*. The correct integration of the SLI-plasmid into the genome to generate the corresponding genomic modification was confirmed by PCR (Figure 38B). To analyse the effect of *PF3D7_0922100* deletion, the kinetics of protein loss was first assessed. For this, different analyses were conducted to test for gene and protein loss. For the former, to confirm the cell line behaved as expected the excision of the active PF3D7_*0922100* gene was investigated by PCR at 24 h and 48 h post addition of rapalog (Figure 38C). A faint band was observed at 24 h and no band was observed at 48 h after rapalog addition (note that the size of the PCR product after excision was not detected due to the small size of approximately 200 bp). This demonstrated efficient excision of the functional copy of *PF3D7_0922100,* resulting in ∆PF3D7_0922100 parasites. The control cells maintained the original genomic locus (intact *PF3D7_0922100* locus) at both time points (Figure 38C). Taken together,

these PCR results confirmed that complete excision of the functional *PF3D7_0922100* gene is achievable within a single asexual growth cycle.

Next, the protein levels of PF3D7_0922100 after induction of excision of the corresponding gene was assessed by Western blot 48 h and 72 h post-addition of rapalog. Western blot analysis using α-HA (the epitope tag added to the functional PF3D7_0922100 copy), revealed that there was no band present in + rapalog samples (Figure 38D), indicating loss of PF3D7_0922100 (approximately 7.5 % residual protein) 48 h and (approximately 4.1 % residual protein) 72 h after induction (Figure 38E). This was in comparison to the band observed in the control, which showed the expected molecular weight of 182 kDa (Figure 38D). The same immunoblot was re-probed with an anti-BIP antibody as a loading control (Figure 38D). Overall, these findings indicated successful loss of PF3D7_0922100 in the 1st cycle after rapalog addition and validated that this cell line can be used to achieve a conditional knock out of *PF3D7_0922100.*

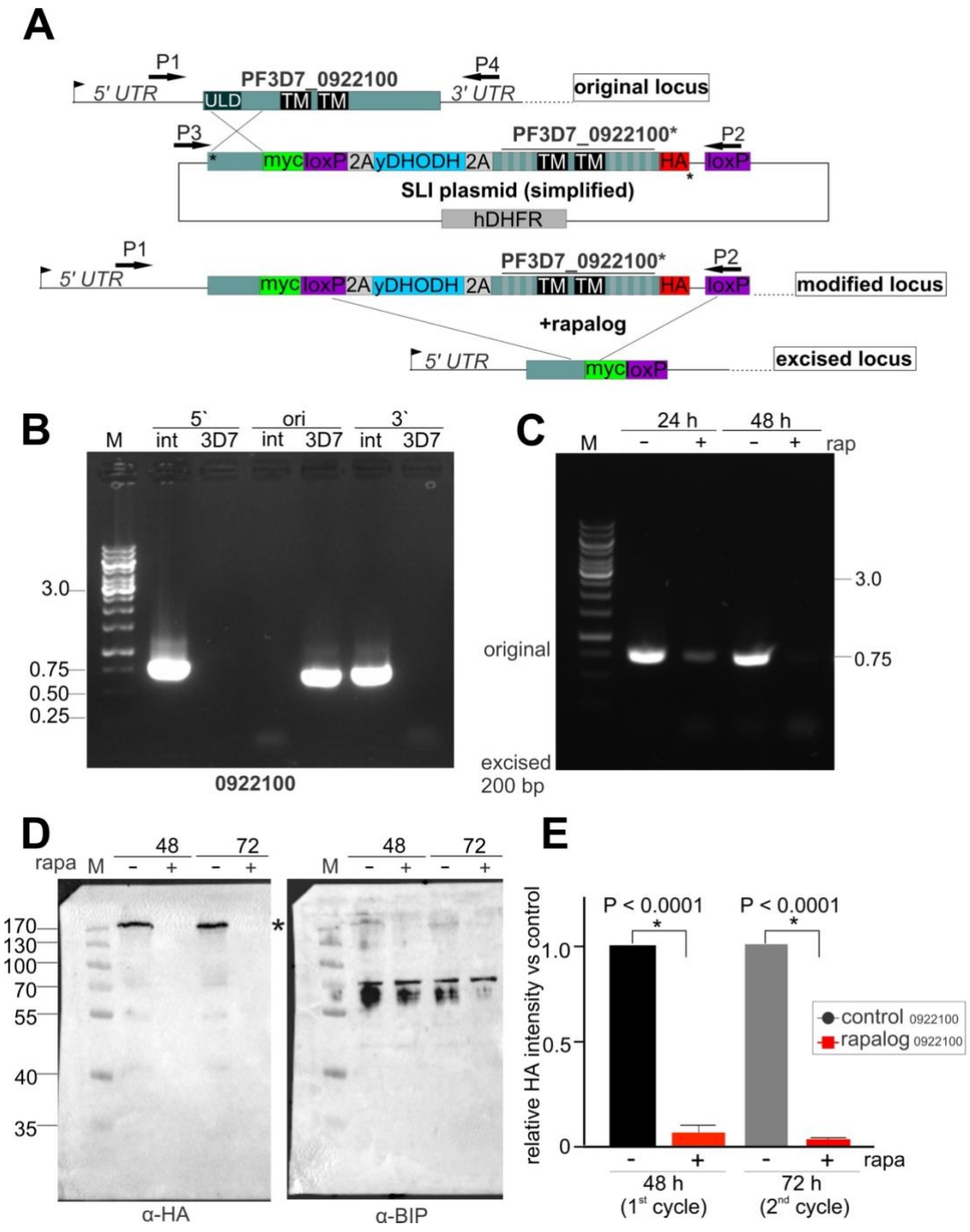

Figure 38. Candidate PF3D7_0922100 (A) Simplified schematic of the generation of the diCre-inducible condΔPF37_0922100 knockout cell line using SLI and subsequent excision upon the addition of rapalog (modified from Mesén-Ramírez *et al.*, 2019). Black arrows, native *PF3D7_0922100* promotor; dark green box, ubiquitin like domain; light green box, entire gene and target region for homologous recombination; green/gray striped box, recodonized PF3D7_0922100; UTR, untranslated region; cond, conditional; HA, 3x human influenza hemagglutinin; 2A, T2A skip peptide. Full condΔPF3D7_0922100 schematic is shown in Appendix 12. (B) Agarose gel showing PCR-products to assess correct integration of the SLI-plasmid into the genome to obtain the indicate cell line. For *Pf*3D7_09221000-HA^{endo}, primers (Appendix 1) were "0922100-Int-fw" + DHODH 42 rv" to demonstrate 5' integration (5' int, 751 bp) and "pARL55 fw" + "0922100-Int-rv" to demonstrate 3'

integration (3' int, 645 bp). Primers "0922100-Int-fw" + "0922100-Int-rv" were used to show absence of unmodified original locus in the indicated cell line (ori int) and 3D7 gDNA was used as a control (ori 3D7, 609 bp). M, marker (GeneRuler™ 1kb, Thermo Scientific); DNA fragment size standard is indicated in kbp. (C) Agarose gels showing PCR-products to test for excision of the floxed functional *PF3D7_0922100* in ΔPF3D7_0922100 knockout (+rapalog) and control (without rapalog) condΔPF3D7_0922100 parasites at 24 h and 48 h post-rapalog addition. Primers (Appendix 1) were P1/P2 as indicated in Figure 36A. (D) Western blot using anti-HA (from rat) confirmed loss of PF3D7_0922100 on the protein level 48 h and 72 h post-rapalog addition. The expected molecular weight of PF3D7_0922100-3xHA is 182 kDa. Anti-BIP (from rabbit) served as loading control. Molecular weight standard is indicated in kDa. One representative experiment of three biological replicas; full blots and replica in Appendix 13. (E) Quantification of PF3D7_0922100-3xHA levels based on densitometric analysis of anti-HA immunoblots at the indicated time points (mean of n = 3 independent experiments) (immunoblots used for quantification are shown in Appendix 13). HA signal was normalized to BIP. P value is indicated (unpaired two-tailed t-test). Error bars indicate standard deviation (SD).

3.9.2.1 Localization of PF3D7_0922100

Next, the localization of PF3D7_0922100-3xHA within the parasites was analyzed (Figure 39). The HA-tagged PF3D7_0922100 was detectable as foci in the parasite periphery at the trophozoite stage. Notable, there was an increase in the number of foci in the parasite periphery with increasing parasite age (Figure 39). Some foci also appeared to be present within the parasite; however, it cannot be excluded that these may be peripheral foci located on planes above or below the focal plane, giving the impression of internal localization. The localization of this protein in the parasite periphery was confirmed by the fact that it did colocalize with EXP2, a resident PVM protein (Figure 39). This result suggests that this protein is likely located at the PPM, PV or PVM which would in principle permit an interaction or vicinity with UIS2.

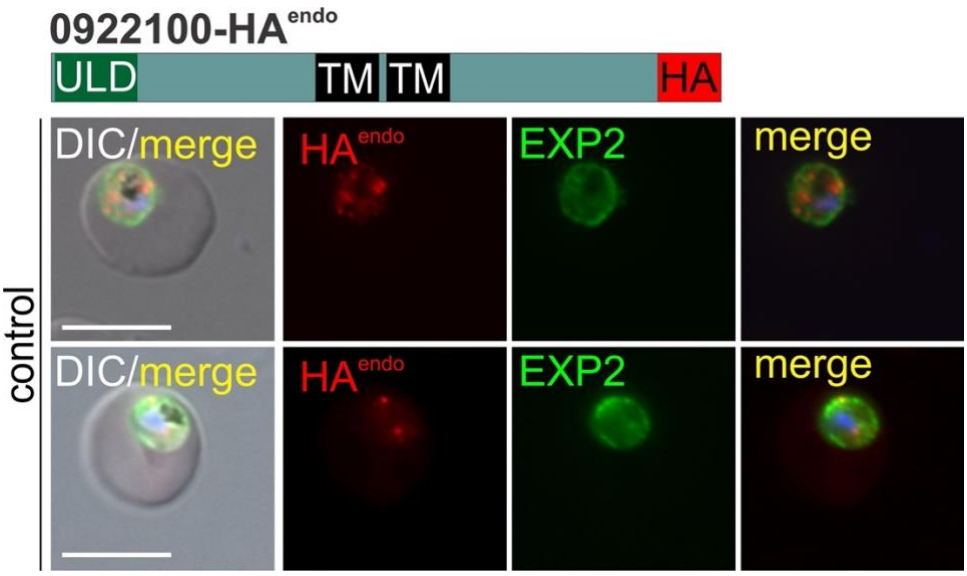

Figure 39. Localization of PF3D7_0922100-3xHA^{endo}. Immunofluorescence assay (IFA) of formaldehyde/glutaraldehyde fixed condΔPF3D7_0922100 parasites (control) at 1st cycle, showing localization of PF3D7_0922100-3xHA^{endo}, and location of EXP2 in trophozoite stages. Anti-HA (from rat) was used to detect PF3D7_0922100-3xHA^{endo} and anti-EXP2 (from mouse) was used to detect EXP2 (PVM). Representative images of three independent experiments with at least 25 image series per experiment. DIC: differential interference contrast. Nuclei were stained with Hoechst. Size bar = 5µm.

To further assess the cellular location of this candidate, an integration cell line resulting in a 2xFKBP-mNEON tagged PF3D7_0922100 was generated by Stephan Wichers-Misterek (Figure 40). The correct integration of the plasmid into the genome was confirmed by PCR (kindly performed by Stephan Wichers-Misterek, Figure 40A). Fluorescence microscopy with these parasites showed that PF3D7_0922100-mNEON was expressed in all asexual blood stages (Figure 40B), consistent with its transcriptional profile (Otto *et al.*, 2010). PF3D7_0922100-mNEON was discernible as prominent foci in the periphery of ring stages and young trophozoite parasites. In later stages, the number of foci increased although there frequently was one prominent focus (Figure 40B). The location of this protein does not exhibit a pattern similar to UIS2; however, it is consistent with a foci pattern often found at the periphery of the cell. These foci could potentially be situated at the PPM, within the PV, or on the PVM, which means they could, in principle, come into contact with UIS2.

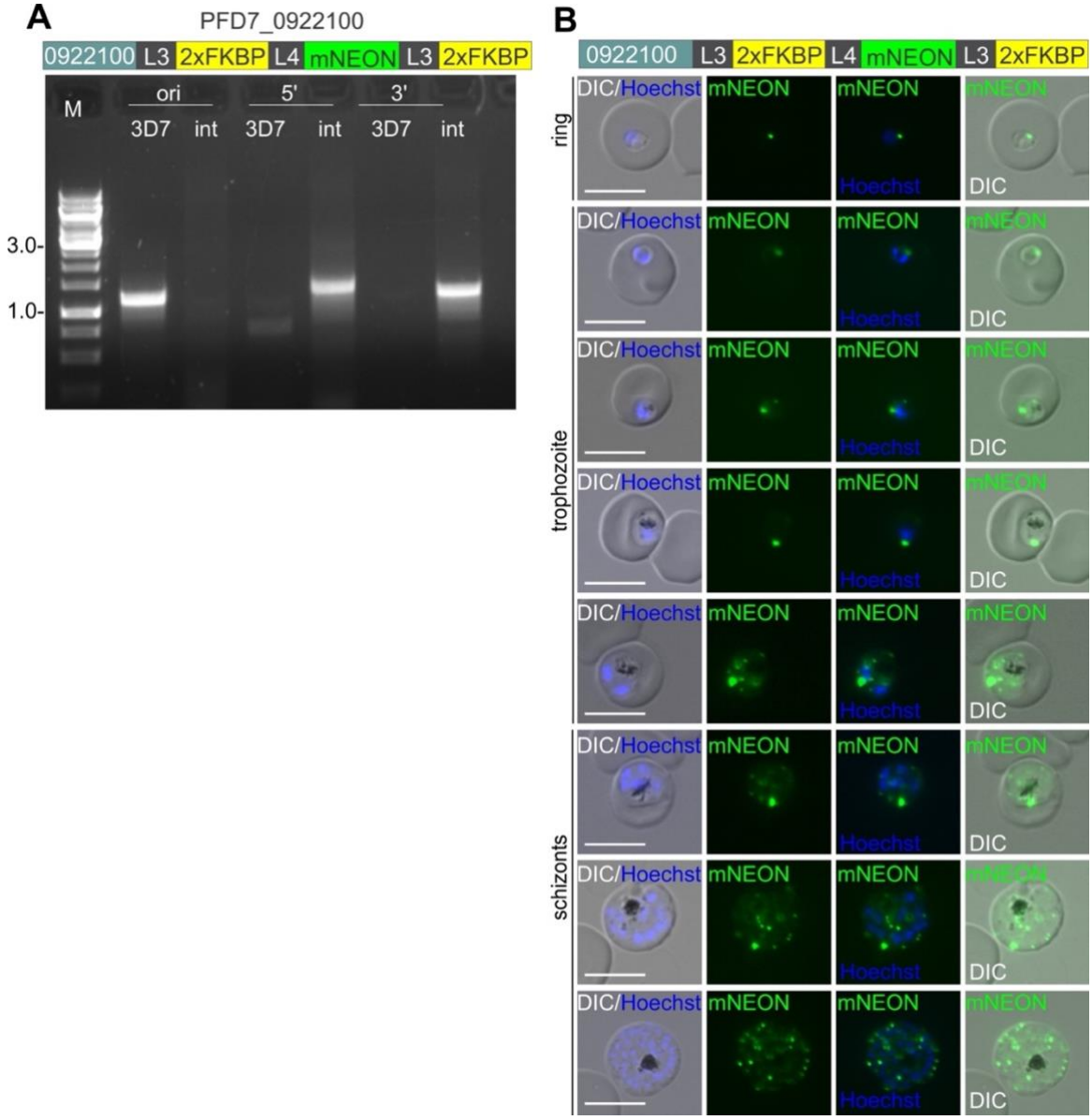

Figure 40. PF3D7_0922100 is located in foci frequently found in the periphery of the parasite. (A) Agarose gel showing PCR-products to assess correct integration of the plasmid into the genome to obtain the indicate cell line. For *PF*D7_0922100-2xFKBP-mNEON-2xFKBP, primers (Appendix 1) were "0922100-mNEON Int fw" + FKBP 82 rv" to demonstrate 5' integration (5' int, 1371 bp) and "pARL55" + "0922100-mNEON Int rv" to demonstrate 3' integration (3' int, 1262 bp). Primers "0922100-mNEON-Int-fw" + "0922100-mNEON-int-rv" were used to show absence of unmodified original locus in the indicated cell line (ori int) and 3D7 gDNA was used as a control (ori 3D7, 1230 bp). M, marker (GeneRuler^{TM} 1kb, Thermo Scientific); DNA fragment size standard is indicated in kbp. (B) Live cell microscopy images of *PF*3D7_0922100-2xFKBP-mNEON-2xFKBP of the intraerythrocytic stages indicated (from ring to schizont stage). Images are representative of two independent microscopy sessions with at least 30 images series each. DIC: differential interference contrast; nuclei were stained with Hoechst. Size bar = 5µm.

3.9.2.2 Validation of the localization of PF3D7_0922100

In order to validate the localization of PF3D7_0922100 at the periphery of the parasite, co-localization assays were conducted. For this an episomal plasmid expressing a wild-type (WT) copy of UIS2 (UIS2-WT-mCherry^{epi}) (Figure 41), previously generated in this study (section 3.8), and a plasmid expressing the Lyn-FRB^{epi}-mCherry at the PPM (Birnbaum *et al.,* 2017) (Figure 42) were employed, resulting in cell lines, PF3D7_0922100-2xFKBP-mNEON-2xFKBP^{endo} + UIS2-WT^{epi} and PF3D7_0922100-2xFKBP-mNEON-2xFKBP^{endo} + Lyn-FRB-mCherry^{epi}.

Fluorescence microscopy of live cells showed that in ring and trophozoite parasitesPF3D7_0922100-mNEON foci overlapped with the uniform distribution of UIS2 around the parasite, suggesting a localization in proximity of the PVM (Figure 41A). In schizonts, fainter PF3D7_0922100-mNEON foci were also found within the parasite (Figure 41A). Quantification of the live fluorescence images of ring, trophozoite and early schizont stage parasites revealed spatial associations of the protein PF3D7_0922100 with UIS2 (Figure 41B). This analysis showed that approximately 82% of PF3D7_0922100 foci overlapped with the UIS2 signal. Meanwhile, 15% showed PF3D7_0922100-mNEON foci were close to UIS2 (proximity to parasite peryphery but not overlapping), while 3% appeared to be located further away internally within the parasites and showed no overlap with the UIS2 signal (Figure 41B). This quantification suggests that PF3D7_0922100 and UIS2 can be in close proximity at the parasite periphery. This result was further confirmed by confocal microscopy (performed by Andrés Guillén-Samander), which showed that the foci of the mNEON-tagged PF3D7_0922100 were in close proximity to UIS2, suggesting a location at the PPM, PV, or PVM (Figure 41C). However, one limitation of confocal microscopy is that it shows structures within a single focal plane, potentially missing the full three-dimensional context of the sample.

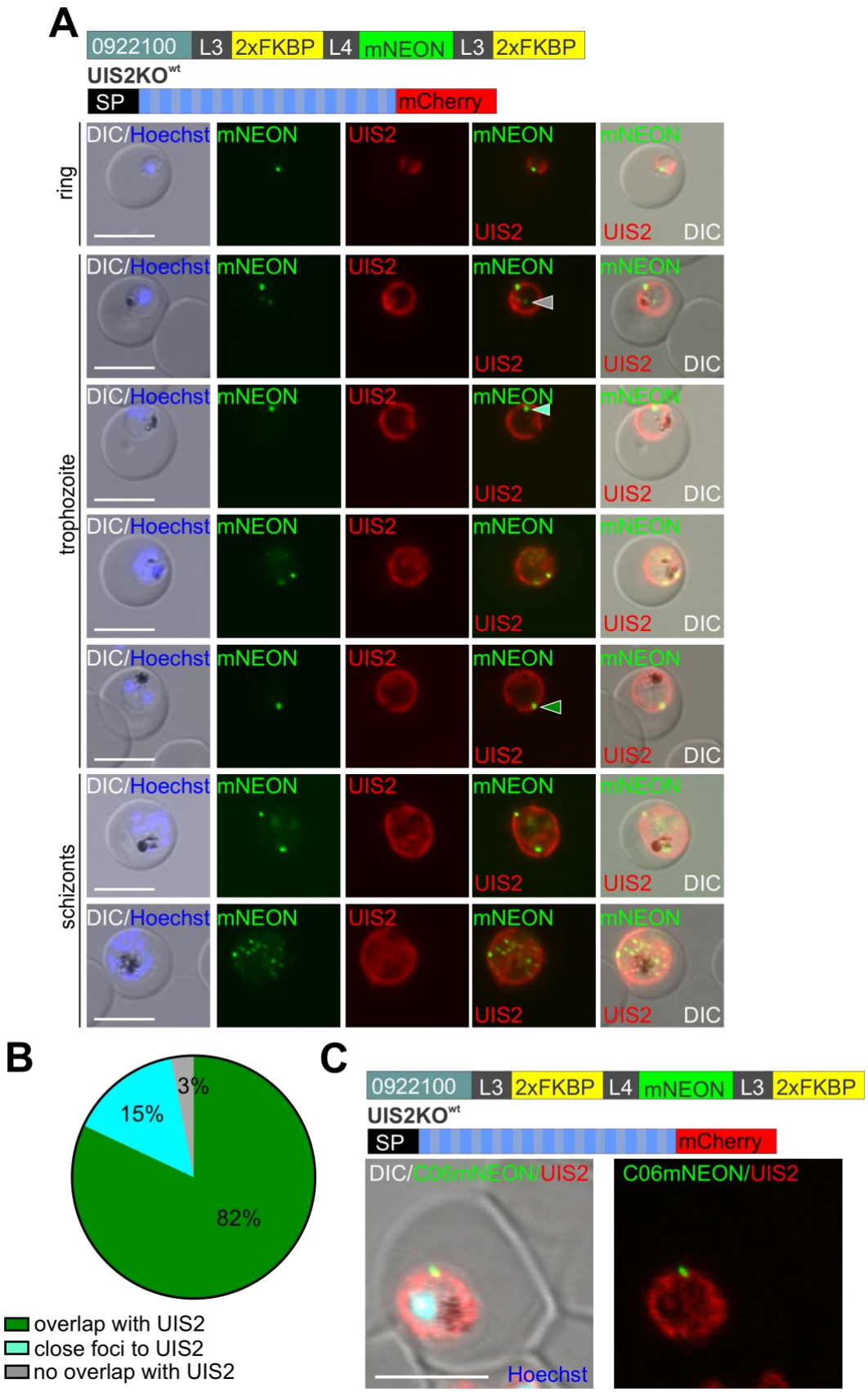

Figure 41. Localization of PF3D7_0922100 in the periphery of the parasite. (A) Live cell microscopy images of PF3D7_0922100-2xFKBP-mNEON-2xFKBP^{endo} parasites, co-expressing UIS2-WT^{epi}-mCherry. (B). Foci were categorized into 'overlap' (green arrow), 'foci close to UIS2^{epi} – signal' (Cyan arrow) and 'non overlap' (grey arrow). Three independent live microscopy sessions with

each n = 20 analysed parasites per experiment, as observed in Figure 40A. DIC: differential interference contrast; nuclei were stained with Hoechst. Size bar = 5µm. (C) Confocal images (single z-slice) of a young trophozoite of the cell line in A. Images are representative of three independent microscopy sessions with at least 10 images series. DIC: differential interference contrast; nuclei were stained with Hoechst. Size bar = 5µm.

Fluorescence microscopy of PF3D7_0922100-2xFKBP-mNEON-2xFKBP^{endo} parasites expressing Lyn-FRB-mCherry^{epi} further confirmed the localization of PF3D7_0922100 at the periphery of ring, trophozoite and early schizont stage parasites, as the PF3D7_0922100 foci were frequently in close proximity of the PPM marked by Lyn-FRB-mCherry^{epi} (Figure 42A). In the late schizont stage, the PF3D7_0922100-mNEON foci were also often found within the parasite, showing partial colocalization with the Lyn-FRB-mCherry^{epi} marked plasma membrane of forming merozoites (Figure 42B). Confocal microscopy confirmed the location of PF3D7_0922100-mNEON foci in the periphery of the parasite with the Lyn-FRB-mCherry^{epi} marked PPM of trophozoites (Figure 42C). Overall, these results suggest that the protein is likely located in the periphery of the parasite, where it potentially could get into contact with UIS2.

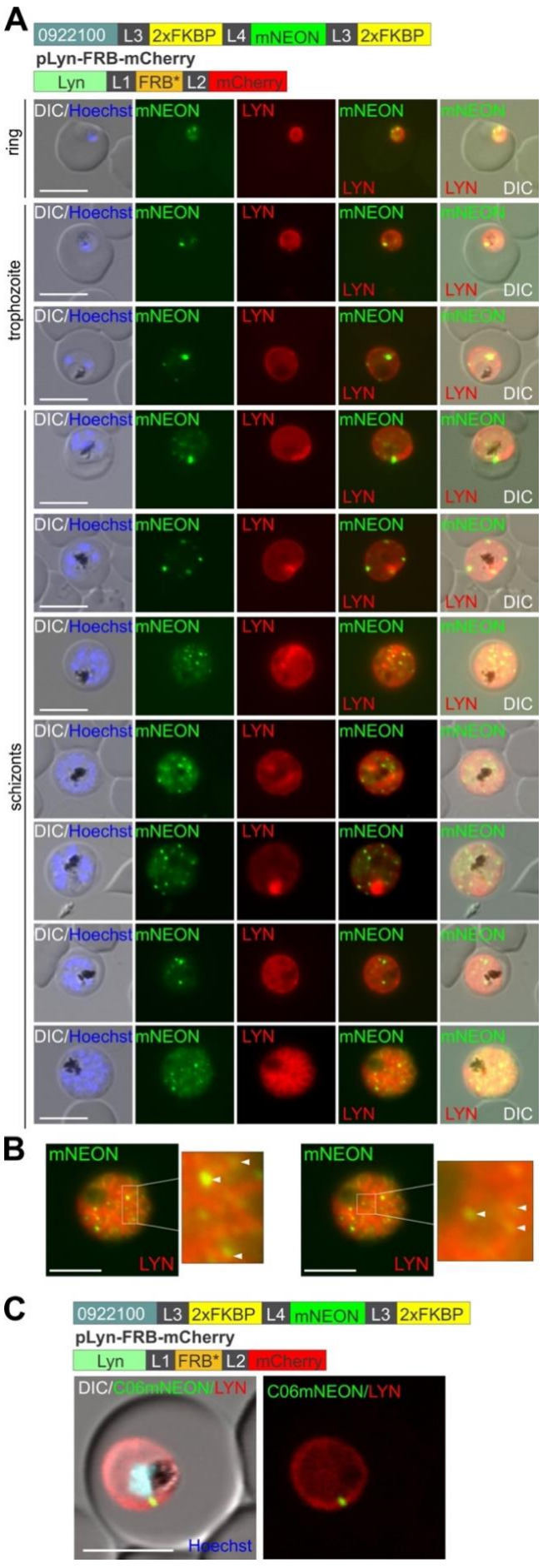
A
0922100 L3 2xFKBP L4 mNEON L3 2xFKBP
pLyn-FRB-mCherry
Lyn L1 FRB* L2 mCherry
ring
trophozoite
schizonts
DIC/Hoechst
mNEON
LYN
DIC
B
C
0922100 L3 2xFKBP L4 mNEON L3 2xFKBP
pLyn-FRB-mCherry
Lyn L1 FRB* L2 mCherry
DIC/C06mNEON/LYN
Hoechst
C06mNEON/LYN

Figure 42. Co-localization of PF3D7_0922100 with a PPM marker confirms location in the parasite periphery. (A) Live cell microscopy images of PF3D7_0922100-2xFKBP-mNEON-2xFKBP^{endo} parasites, co-expressing Lyn-FRB^{epi}-mCherry. Three independent live microscopy sessions with each n = 20 analysed parasites. DIC: differential interference contrast; nuclei were stained with Hoechst. Size bar = 5µm. (B) Higher magnifications of the boxed areas show PF3D7_0922100 foci (indicated by white arrows) in close proximity of the PVM marked by Lyn-FRB^{epi}-mCherry. Size bar = 5µm. (C) Confocal images (single slice) of a young to mid trophozoite stage parasite of the cell line in A. Images are representative of three independent microscopy sessions with at least 10 images series. DIC: differential interference contrast; nuclei were stained with Hoechst. Size bar = 5µm.

3.9.2.3 PF3D7_0922100-KO does not result in a defect in protein export

After demonstrating the effective excision of the functional *PF3D7_0922100,* absence of this protein in the 1st cycle post-rapalog addition and its localization in proximity to the parasite periphery, the importance of this candidate for parasite growth was assessed. The growth of cond∆PF3D7_0922100 parasites was monitored over five consecutive days, using the same culture split into one with rapalog and a control without rapalog (Figure 43B,C). The growth curves showed similar parasitemia until day 3 post-rapalog addition, but there was a reduced growth of the ∆PF3D7_0922100 parasites compared to the control on day 4 (Figure 43B). This discrepancy became more evident when tracking growth starting with ΔPF3D7_0922100 ring stage parasites, suggesting that this protein is important for parasite growth (Figure 43C).

To investigate, whether the PF37_0922100 needed for protein export, as observed in the previous results with UIS2 (section 3.4), different exported proteins and a resident PVM were evaluated by IFAs (Figure 43D,E). The export of these markers was assessed in parasite treated under the early induction regime (0 – 8 hpi) (Figure 43A). Since the effect on parasite multiplication became evident in ∆PF3D7_0922100 after ring stage of the first cycle, KAHRP and EXP2 were assessed at time point B (26 – 32 hpi), corresponding to the trophozoite stage of the first cycle (Figure 43A,D), while SBP1 was evaluated at time point C (4 - 12 hpi, the ring stage of the second cycle) (Figure 38A,C). In the control, SBP1 was correctly trafficked to the MCs, KAHRP to the erythrocyte membrane while EXP2 was located at the PVM (Figure

43A,E). After excision of the *PF3D7_0922100*, those markers remained unaffected, indicating that loss of PF3D7_0922100 did not impact protein export (Figure 43D,E).

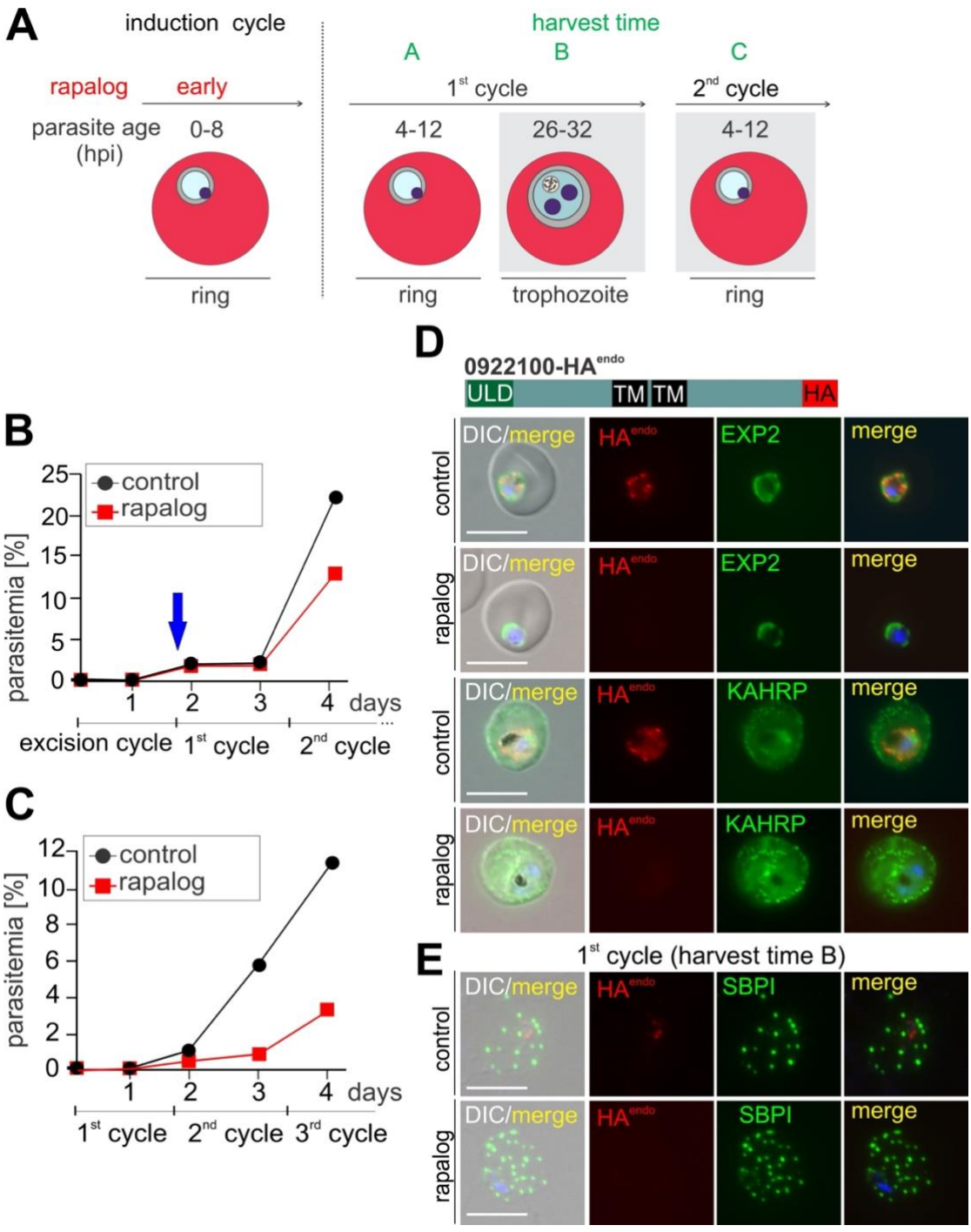

Figure 43. Conditional knock out of PF3D7_0922100 does not impact protein export. (A) Schematic representation of experimental setup for conditional knockout of PF3D7_0922100 by inducing excision of *PF3D7_0922100* in 0 - 8 hpi ('early induction') ring stage parasites. Parasites were harvested at point B for the analysis of KAHRP and EXP2 and at point C for the analysis of SBP1. UBL, N-terminal ubiquitin-like domain; TM, transmembrane domain. (B) Immunofluorescence assay (IFA) of formaldehyde/glutaraldehyde fixed ΔPF3D7_0922100 (+rapalog) and control (without

rapalog) condΔPF3D7_0922100 parasites at the 1st cycle, showing localization of PF3D7_0922100-3xHA^{endo}, and location of KAHRP and EXP2 in trophozoite stages. Anti-HA (from rat) was used to detect PF3D7_0922100-3xHA^{endo}, anti-KAHRP (from rabbit) was used to detected KAHRP (erythrocyte membrane) and anti-EXP2 (from mouse) was used to detect EXP2 (PVM). Representative images of three independent experiments with at least 25 image series per experiment and condition. (C) Microscopy images of IFAs using acetone-fixed cells of ΔPF3D7_0922100 parasites (+rapalog) and control (without rapalog) at the 2st cycle, showing localization of PF3D7_0922100-3xHA^{endo}, and location of SBP1 in ring stages. Anti-HA (from rat) was used to detect PF3D7_0922100-3xHA^{endo} and anti-SBP1C (from rabbit) to detected SBP1. Representative cells from one of three independent experiments with at least 25 image series per experiment and condition. DIC: differential interference contrast. Nuclei were stained with Hoechst. Size bar = 5µm. (D, E) Flow cytometry growth curves of synchronous ring stage condΔPF3D7_0922100 parasites starting either at the excision cycle (D) or cycle 1 (E) on 5 consecutive days. Blue arrow indicates invasion into the first cycle and loss of PF3D7_0922100. One representative of n = 3 independent experiments (replicas are shown in Appendix 14).

4 Discussion

4.1 Deletion of UIS2 affects protein export

Asexual blood stages of malaria parasites export proteins beyond the PVM, the membrane that separates the parasite from the host cell cytoplasm, a process mediated by the PTEX protein complex (de Konig-Ward *et al.*, 2009). These proteins fulfill diverse functions critical for either the virulence or the proliferation of the parasite (Maier *et al.*, 2008; Spillman *et al.*, 2015, de Koning-Ward *et al.*, 2016: Wahlgren *et al.*, 2017). The role of UIS2 in protein export of *P. falciparum* parasites was evaluated here through a series of experiments using episomal plasmids encoding trafficking markers analysed in the *uis2* cKO. Shifting the timing of *uis2* loss in the parasites was critical to confirm that the effect on protein export was specific to the loss of *uis2*, rather than resulting from the loss of viability in young rings. This was evident in the different levels of protein export observed in SBP1 and KAHRP between the control and *uis2* knockout parasites. The variation in the degree of export between individual cells could reflect heterogeneity in the induction time and then loss of *uis2*. These findings point to a direct role of UIS2 in protein export. A similar effect on protein export has also been observed by Beck *et al*, (2014) where the knockdown of the PTEX component HSP101 in *P. falciparum*, led to a significant block in the export of a wide range of PEXEL proteins (KAHRP, RESA) as well as PEXEL-negative exported proteins (PNEPs) such as REX1 and SBP1. Other studies have demonstrated that knockdown of the PTEX components HSP101 and PTEX150 in *P. berghei* (Elsworth *et al.*, 2014), and EXP2 in *P. falciparum* (Charnaud *et al.*, 2018; Garten *et al.*, 2018) led to a significant defect in protein export.

The expression of additional markers, such as the soluble PEXEL export reporter, GBP, the multipass plasma membrane protein FNT, and a soluble PV reporter, further clarified the role of UIS2. The loss of UIS2 did not affect the transmembrane protein FNT at the PPM, indicating that the specificity of UIS2 is for exported proteins rather than those proteins destined for the PPM. The export of the GBP reporter was notably affected, reinforcing the function of UIS2 in the export trafficking pathway. A particularly intriguing observation was the altered distribution of the soluble PV reporter (SP) in the parasite lacking UIS2. The confinement of the soluble reporter to

smaller peripheral regions might suggest that UIS2 deletion could affect the integrity or architecture of the PV, thereby influencing the correct distribution of proteins within it. Alternatively, it could affect a transport step necessary for the proper distribution of the soluble marker in the PV due to the lack of dephosphorylation of specific targets. By using various membrane protein markers in the PVM, including ETRAMP4, ETRAMP5, and EXP2, it was found that the loss of UIS2 resulted in an altered distribution of these proteins, characterized by their accumulation in a confined area of the PVM. This finding could indicate that UIS2 could influence the trafficking pathways of these markers through a dephosphorylation-dependent sorting step, which may be disrupted without UIS2 or impair the correct localization and alter the behavior of these proteins in the PVM. Also, it raises the possibility of a signaling cascade triggered by the lack of dephosphorylation of targets, which can influence their interaction with other proteins within the PV, which in turn could lead to altered distribution patterns of these membrane protein markers within the PVM.

4.2 Phenotype of ring stages lacking UIS2

In this study, the phenotype caused by the deletion of the *uis2* gene in *P. falciparum*, previously observed by Khosh-Naucke in 2018, was examined in more detail. Conditional *uis2* knockout cell lines were generated to characterize the function of the UIS2 protein during the asexual blood stage development of the parasite. The induction of knockout in the UIS2-3xHA knockout cell line resulted in an export phenotype. This led to an arrest in the early phase of the intraerythrocytic development cycle shortly after invasion, with cells appearing as rings with small diameters, often accompanied by a small translucent center (referred to as “phenotype rings”). This phenotype resulted in a severe growth defect. A similar phenotype was observed by Boonyalai *et al*, (2018) and Polino *et al*, (2020) following the conditional inactivation of *P. falciparum* Plasmepsin V (*Pf*PMV) which also leads to a protein export phenotype. Loss of *PfPMV* function resulted in parasites arresting in the ring stage immediately after invasion, indicating that this gene is essential for parasite growth. Additionally, it was noted that the parasites turned into pycnotic forms, resulting in a severe growth defect (Boonyalai *et al*., 2018; Polino *et al*., 2020). Treatment with the PMV inhibitor, WEHI-916 (Sleebs *et al.*, 2014) and WEHI-842 (Polino *et al.*, 2020) late in the erythrocytic cycle also resulted in an early-stage arrest

phenotype. This contrasts with the phenotype observed following the inactivation of the PTEX component HSP101 (Beck *et al*., 2014) and the knockdown of both HSP101 (Elsworth *et al*., 2014) and EXP2 (Garten *et al*., 2018; Charnaud *et al*., 2018; Pitman *et al*., 2024) and knockout of EXP2 (Mésen-Ramírez *et al*., 2019), which all also prevent protein export. These mutants, although also unable to export proteins like the PMV and UIS2 mutants, led to an arrest late in the ring stage-trophozoite transition (Beck *et al*., 2014; Elsworth *et al*., 2014; Sleebs *et al*., 2014; Charnaud *et al*., 2018). It is unclear why impairment of protein export shows these different phenotypes. However, the export phenotype observed after the loss of UIS2 resembles more that of PMV than that of the PTEX component, potentially indicating it acts before the translocation step at the PVM.

The closest export phenotype observed in this study was initially reported by Hill *et al*, (2016) and corroborated by Ressurreição *et al*, (2023) after the conditional inactivation of the PFA0210c protein, named parasitophorous vacuole PV6 (PV6). They observed that its phenotype became apparent during the ring stage immediately after invasion, and the phenotype observed is terminal rather than a delay in development, showing an expanded ring, often with a translucent center (Ressurreição *et al*., 2023). Despite PV6 being annotated as an exported PEXEL protein, the processing of PV6's PEXEL motif by the enzyme plasmepsin V (PMV) does not result in its export into the host cytosol; instead, it remains in the PV (Ressurreição *et al*., 2023). Similarly, UIS2 also contains a PEXEL motif, which is cleaved by PMV, despite UIS2 not being an exported protein (Fierro *et al*., 2023). Both proteins have an unusual PEXEL motif, with PV6 having a lysine and UIS2 having an aspartic acid at the fourth residue, which constitutes the extreme N-terminal residue following PEXEL cleavage. Typically, this position consists of an uncharged amino acid (Sargeant *et al*., 2006). These residues may prevent export into the host cell (Ressurreição *et al*., 2023; Fierro *et al*., 2023). The phenotype observed in the PV6 mutants and UIS2 mutants implies that both proteins can perform an essential function prior to the time at which protein translocation across the PVM is required. This also suggests that PMV may perform functions with non-exported PMV substrates in addition to preparing proteins for export.

4.3 Role of UIS2 in translation?

Furthermore, the arrest of parasites at early stages was observed by Zhang *et al*, (2016), who demonstrated that a knockout of *uis2* resulted in the developmental arrest of invaded sporozoites in liver stages in *P. berghei*, preventing their maturation into trophozoites and subsequent liver stage development. They postulated that UIS2 could be involved in the dephosphorylating of the eukaryotic initiation factor 2 alpha (eIF2α-P), which is present exclusively in its phosphorylated form in salivary gland sporozoites, where this eIF2α-P state leads to translational inhibition, culminating in the accumulation of stalled mRNAs into granules (Zhang *et al.*, 2016). To demonstrate the interaction between UIS2 and eIF2α-P, they conducted an *in vitro* pull-down assay, which provided evidence that UIS2's N-terminus binds stably to eIF2α-P but does not bind to the non-phosphorylated form of eIF2α. Additionally, co-immunoprecipitation experiments revealed that UIS2 from lysates of *P. berghei* blood-stage parasites also binds to recombinant GST-*Pf*eIF2α (Zhang *et al.*, 2016).

However, the localization of UIS2 observed by Khosh-Naucke, (2018) was associated with the luminal face of the parasitophorous vacuolar membrane (PVM) during the asexual blood stages (Khosh-Naucke *et al*., 2018). This suggests that UIS2 is unlikely to dephosphorylate cytosolic eIF2α-P as a physiological function, given the localization of the protein in a compartment without access to eIF2α-P. This finding was corroborated by Schnider *et al.*, 2018, who localized *Pb*UIS2 in association with the PVM in *P. berghei* liver stages, and by Fierro *et al.*, 2023, who also localized *Pf*UIS2 at the PV in *P. falciparum* blood stage parasites. Consequently, considering the localization of UIS2 at the PVM in both blood and liver stages, the proposed function of UIS2 in interacting with eIF2α-P *in vivo* seems improbable, but rather it indicates that there may be indispensable dephosphorylation events in the PV that are needed for parasite survival.

4.4 UIS2 phosphatase exhibits similarities and cross-species structural conservation with purple acid phosphatases

Previously it was not clear what class of phosphatase UIS2 belongs to. In this study, structural analysis of the UIS2 phosphatase domain revealed how it compares with other metallophsophoesterases and thus shed light on its catalytic mechanism. Zhang *et al.*, 2016, suggested that UIS2 is a protein phosphatase 2C (PP2C) due to its preference for Mn^{2+} over Mg^{2+} and that EDTA and Cd^{+2}, which are inhibitors of the PP2C/PPM family, inhibited its phosphatase activity. However, UIS2 notably lacks a canonical PP2C catalytic domain and the structure and sequence alignments of UIS2 to metallophosphoesterases (MPEs) showed similarity to the purple acid phosphatases (PAPs). The MPEs can be readily identified through the recognition and arrangement of five conserved residue blocks (DxG/GDxxY/ GNH(D/E)/VxxH/GHxH), with a conserved glycine residue in block I (DxG) typically exclusive to PAPs (Matange *et al*., 2015). PAPs commonly carry seven invariant amino acid residues distributed among these five blocks (**D**XG/G**D**XX**Y**/ G**N**H(D/E)/VXX**H**/G**H**X**H**; bold letters indicate metal-ligating residues), essential for coordinating the bimetallic nuclear center in the active site (Li *et al*., 2002). UIS2 contains these conserved motifs typical of PAPs and retains nearly all the invariant amino acid residues. However, it deviates from the canonical pattern in two aspects. Firstly, the tyrosine (Y) in block II (GDXX**Y**) is not located in the usual position due to the insertion of a unique sequence of 49 amino acids. Secondly, the substitution of an uncharged asparagine (N) with the negatively charged glutamic acid (E) which alters the charge of the amino acid in block III (G**N**H(D/E)).

To clarify the resemblance of UIS2 to this class of MEPs, structural comparisons of UIS2 phosphatase domain with the catalytic domains of the PAPs were performed. The AlphaFold Protein Structure Database, is a robust tool that provides a reliable approximation of three-dimensional (3D) protein structures with near-experimental accuracy for many proteins and that is based solely on its amino acid sequence for many proteins (Jumper *et al.,* 2021; Varadi *et al*., 2022). The AlphaFold-predicted structure of the phosphatase domain of UIS2 (AF-Q8IKJ1-F1) shows a high degree of structural conservation with human purple acid phosphatase, as well as with those from rat and pig PAPs, as evidenced by the low root-mean-square deviation (RMSD)

values. These RMSD values of less than 1.5 Å are strong evidence of structural similarity which underscore a near-atomic level match in the alignments. This indicates that despite these proteins deriving from different organisms and UIS2 possessing differences in two amino acids within the conserved motifs of these phosphatases, they share a common structural arrangement of the catalytic site. Therefore, it can be concluded that UIS2 shares a high similarity to the PAPs family.

PAPs have a unique active site containing two metal ions such as Mn (II), Zn (II), Fe (II), which are coordinated by amino acid residues, such as aspartate (D) and histidine (H). In this thesis it was found that UIS2 also contains the conserved metal-coordinating residues common to purple acids phosphatase, D542 and D591. Through structural comparisons this study identified conserved ligand-binding sites (LBs) of PAPs in UIS2. Mutation of these residues in the UIS2 phosphatase domain confirmed that these aspartate residues correspond to the conserved aspartate residues D20 and D49 in PAPs which were reported by Zhuo *et al*, (1994) to contribute both to metal ion binding and catalysis necessary for phosphatase activity in λ-phosphatase. This analysis further supports the classification of UIS2 within the PAPs family, as it has been observed in this study that UIS2 shares a similar composition of metal-ligating residues at the catalytic site with PAPs.

In a similar study the ligand-binding asparagine residues D50 and D12 were identified in human PAP (Sträter *et al.*, 2005), which are also in the structurally equivalent positions as D12 and D50 in lambda-phage phosphatase and D542 and D591 in UIS2. Furthermore, Sträter *et al*., 2005 showed that the structures of human, pig, and rat PAPs are very similar, which is consistent with their high level of sequence similarity. Other research has identified the locations of asparagine residues (D14, D52) in pig and rat phosphatase domains — equivalent to the mutated residues in the *Pf*UIS2, human, and lambda phosphatase domains — at the active site interacting with the binuclear metal ions. This research also confirmed that the ion-coordinating residues are invariant among PAPs (Schenk *et al.*, 2013). These observations allowed us to design phosphatase-mutated complementation constructs of UIS2 to analyse the significance of the phosphatase activity for the function of UIS2.

4.5 Single point mutations targeting the catalytic site only partially inactivate the phosphatase activity of UIS2

To better understand the role of UIS2 at the molecular level, particularly its association with the dephosphorylation of substrates, it was crucial to elucidate if the phosphatase domain in UIS2 is functional and determine whether it contributes to the activity of UIS2. To investigate the UIS2 phosphatase domain more closely, a complementation assay was conducted to assess the impact of catalytic site-residue mutations on UIS2 function. Episomal constructs expressing a wild-type copy or single-point mutations D542N and D591N – located in conserved domains I and II, respectively – as well as a double mutant (D542N-D591N) were expressed in the condΔUIS2-GFP integrant cell line. Subsequent fluorescence microscopy confirmed the episomal expression and the localization of the UIS2-WT^{epi}-mCherry construct in the periphery of the parasite, similar to the endogenously expressed UIS2-GFP fusion protein. This peripheral localization suggests proper targeting of the extra UIS2 copy used for the complementation assay. Flow cytometry analysis showed that after the excision of *uis2* gene, parasite growth was similar to the control, indicating that the episomal construct was able to fully complement the function of the endogenous UIS2. In contrast, the single-point mutants, UIS2-D542N^{epi} and UIS2-D591N^{epi}, while equally found in the periphery of the parasite, showed a delay in parasite development while the control grew at a typical rate, which was quantitatively assessed by flow cytometry. The observed growth delay was smaller than for the complete loss of UIS2, suggesting a partial complementation capability of the UIS2 mutants. It is conceivable that the observed developmental delays might have a greater impact on the timing of parasitemia measurement. In such scenario, differences in growth rates could become more pronounced as the control group progresses to subsequent developmental stages, while the knockout parasites lag behind. These results indicate that the single point mutations only partially inactivated the phosphatase activity of UIS2.

The double mutant UIS2-D542N-D591N^{epi} construct, with two residues mutated in the catalytic site of the UIS2 phosphatase domain, localized at the periphery of the parasite and colocalized with UIS2-GFP, similar to the single-mutation constructs. However, a decrease in the proportion of parasites expressing the mCherry signal from the UIS2-D542-D591N^{epi} construct was observed over time. This indicated

either poor expression of the complementation construct or that the double mutants phosphatase had a dominant negative effect on parasite growth. In a similar assay of complementation with a double mutant of UIS2 in *P. falciparum* containing (mutations in the residues D554N and D584N), Khosh-Naucke, (2018) observed a growth disadvantage and dominant negative effect due to the episomally expressed mutant construct. Structural analysis performed in the current study revealed that residue D584 is situated within the catalytic site of the phosphatase, while D554 is positioned in a random-coiled region outside the active site, rendering it unlikely to significantly contribute to the catalytic function of the phosphatase but possibly contributing to another function. In Khosh-Naucke, (2018) the effect on *uis2* knockout parasites that exclusively expressed the double mutant was profound, as there was no increase in parasitaemia observed in the corresponding growth assays, leading to the conclusion that the double mutant construct had no complementing capacity. In that work, it was noted that the parasites quickly adapted in an unknown way to the dominant negative effect, resulting in a cell line growing at typical rates that had lost the expression of the complementing construct, likely through strong selection based on the growth impairment. However, this scenario was not found to apply with the complementation constructs used in the present thesis.

One possible explanation for the poor expression of the double mutant episomal construct is that the plasmid copy number can vary between different cell lines which would lead to different expression levels. While copy number, promoter was the same in all episomal complementation constructs (*nmd3* promoter), and hence should not influence the outcome. The precise copy number of the plasmid of the different UIS2 complement constructs in the cells, was not determined in this study but it is unclear why it would have varied very much between cell lines as the constructs were based on the same backbone. Selection of parasites expressing the double mutant complementation construct relied on the presence of a DSM1 resistance marker expressed from the plasmid. Therefore, the DSM1 resistance (yDHODH) could be used to normalize the plasmid copy number, allowing for the quantification of the episomal double mutant construct at the protein level relative to the control cell line. Another possible explanation for the poor expression of this construct is that two mutations at the catalytic site have a detrimental effect on the enzymatic activity of the protein, potentially resulting in partial or complete loss of protein function. These

mutations could prevent the protein from functioning as an active phosphatase, thereby preventing it from effectively removing phosphate groups from substrate molecules. As a result, the parasite may struggle to express the double mutant episomal complementation construct at levels comparable to those of the wild-type construct. In conclusion, the exact reasons for the poor expression of the episomal construct and the potential dominant negative effect remain unclear.

The limited expression of the double mutant construct did not allow me to analyse its complementation capacity based on parasite growth. Instead, parasite size was used as an indirect measure of potential complementation activity. Upon evaluation, it was observed that parasites expressing the UIS2-D542N-D591N^{epi}-mCherry construct were approximately 30% smaller in area compared to those complemented with the wild-type UIS2. The less pronounced size reduction in the single mutant complementations compared to the double mutant supports the hypothesis that the reduced growth with the single-point mutations was the result of a partial loss of UIS2 phosphatase function. The more pronounced phenotype observed in the double-mutant construct likely indicates a significant disruption of the phosphatase activity of UIS2, which could compromise the ability of UIS2 to dephosphorylate substrates crucial for parasite growth and replication. It would be insightful to determine whether the function of UIS2 related to protein export is compromised in parasites harboring mutations within the domain and could reveal whether the phosphatase function of UIS2 influences protein export.

4.5.1 Lack of functional complementation by a potential UIS2 ortholog from *T. gondii*

In this study, UIS2 was found to be required for protein export, but it is known from previous studies that it is not part of the *Plasmodium* translocon of exported proteins (PTEX) complex (de Koning-Ward *et al*., 2009). Hence, the question arises how UIS2 contributes to protein export. In *T. gondii*, a related apicomplexan organism, a different system for protein export, a multi-protein translocon called the MYR complex, is used (Franco *et al*., 2016; Marino *et al*., 2018). Since UIS2 is not a part of the PTEX complex, its functional similarity to the *T. gondii* ortholog, GRA44, which also possesses characteristics typical of secreted proteins, an acid phosphatase domain, a predicted TEXEL motif, and is needed for protein export might indicate a

similar function. For this reason, GRA44 and its functional equivalence to UIS2 was investigated in this thesis.

Fierro *et al,* (2023) observed that processing UIS2's PEXEL motif is cleaved by the enzyme plasmepsin V (PMV) despite UIS2 not being an exported protein. Coffey *et al*, (2018) classified GRA44 as a substrate of the protease ASP5, which is secreted into the PV where it is remains, results that were corroborated by Blakely *et al*, (2020). Moreover, Cygan *et al*, 2020 showed that GRA44 is needed for the export of Toxoplasma effector proteins into the host cell and for effector-dependent host cell responses consistent with alter host cell, potentially indicating a role in the translocation of exported proteins for GRA44. This indicates that its acid phosphatase domain could be involved in the dephosphorylation of trafficked proteins or components of the translocon complex. This is noteworthy considering the absence of other PTEX components, such as HSP101 and PTEX150, *in T. gondii*. In this thesis, the episomally expressed *Tg*GRA44 in *P. falciparum* correctly localized to the periphery of the parasite. However, a significant proportion of the signal was also observed internalized within the food vacuole, suggesting that the episomally expressed protein might be internalised and degraded. However, as the food vacuole typically shows a high level of autofluorescence in the red emission spectrum, it is difficult to draw any firm conclusions from this observation. Carefully controlled quantifications of fluorescence levels compared to controls would be required for that purpose. Functional complementation was assessed by excising the endogenous *uis2* gene and monitoring parasite growth. The growth comparison between *Tg*GRA44-mCherry after the excision of *uis2* and the control parasites indicated a failure of the ΔUIS2 parasites to grow, while the control parasites continued to multiply. The failure to complement could be attributed to possibilities such as (i) improper protein folding, (ii) suboptimal protein expression levels, or (iii) differing functions of these proteins. In the first possibility, protein folding could directly impact protein stability and function. Proteins must fold into precise three-dimensional structures to function correctly, and even minor alterations in the folding process can lead to a loss of function. In the context of the present study, *Tg*GRA44 may not have achieved the necessary conformation to interact with the native *P. falciparum* cellular machinery. The second possibility, suboptimal protein expression levels could equally explain the lack of functional complementation observed. The detectable

presence of the *Tg*GRA44-mCherry signal within the food vacuole, along with the severe growth defect, suggests that the failure to complement may be more likely due to insufficient protein being in the PV. For instance, if *Tg*GRA44 is not expressed at levels comparable to the endogenous UIS2, there may not be enough of the protein to perform the essential functions carried out by UIS2. In *P. falciparum*, protein export may require a precise concentration of UIS2; deviations from this concentration could impair parasite growth and development. Interestingly, the size analysis of parasites after excision of the *uis2* gene, showed that parasites expressing *Tg*GRA44-mCherry showed an intermediate phenotype – they were larger than UIS2-D542N-D591N-double mutants but smaller than the UIS2-wild-type parasites. This observation raises a further reason for the failure to complement, suggesting that *Tg*GRA44 may partially restore UIS2 function or has a compensatory effect, although this is insufficient to fully substitute UIS2 function. These results might imply that *Tg*GRA44 can fulfill, albeit not all, functional roles of UIS2, suggesting that it may require organism-specific machinery to function in *P. falciparum.* Overall, further experiments are therefore required before completely discarding the capacity of *Tg*GRA44 to complement loss of at least some of the functions of UIS2. While it is evident with the results of this thesis that this construct does not complement, it cannot be categorically excluded that this is due to factors impacting protein folding or abundance and therefore the function of *Tg*GRA44 may still be somehow related to UIS2. Future studies could for instance observe protein export in the *Tg*GRA44-complemented parasites. However, based on the complementation assays in this thesis the most likely scenario is that there is limited functional conservation between the phosphatases of these two apicomplexan species.

Recent research has shown that the knockdown of GRA44 interferes with protein export and impacts parasite growth in *T. gondii* (Blakely *et al*., 2020). This result was also observed by Cygan *et al*, (2020), where the knockdown of GRA44 led to an impaired effector export phenotype, suggesting a failure to restore effector export to the host nucleus. It has been demonstrated that a knockdown of GRA44 impacted on the proper translocation of effector proteins (GRA16/24) across the PVM (Blakely *et al.*, 2020). It however is possible, that it also impacts the distribution of the EXP2 ortholog in *T. gondii,* GRA17/25, in the PVM which would result in a nutrient uptake phenotype. The aim would be to assess whether the deletion of *gra44* gene

expression correlates with alterations in the localization of PVM proteins, as observed with the disruption of the *uis2* gene on the localization and distribution of exported proteins in *P. falciparum*, as presented in the results of this thesis. Despite not observing a significant level of complementation, it is plausible that UIS2 and GRA44 share unifying features in PV organization and transport functions across divergent species.

4.6 DiQ-BioID with UIS2 identified two proteins important for parasite growth

DiQ-BioID was utilized to identify proteins in spatial proximity to UIS2. Successful dimerization was confirmed as UIS2 was the most significantly enriched protein over the control. Biotinylated proteins were enriched with streptavidin-coated beads and subsequent mass spectrometry analysis identified three potential UIS2 interaction candidates, considering the presence of a signal peptide or transmembrane domain, essential features for proteins associated with the PV or PVM. The surface protein *Pf*113 (PF3D7_1420700), located in the PV throughout the intraerythrocytic cycle (Bullen *et al*., 2022), was the second most enriched protein after UIS2. Bullen *et al*, (2022) demonstrated that a conditional knockdown of *Pf*113 did not impair parasite growth or protein export; therefore, it was not analysed in this thesis. However, its knockdown did lead to morphological changes in the PVM, suggesting that *Pf*113 might be involved in maintaining the architecture of the PVM (Bullen *et al.*, 2022). The precise function of *Pf*113 remains unclear; it has been implicated in various roles in previous studies, including as an invasion protein, an interactor of the reticulocyte-binding protein homologue 5 (RH5) (Campeotto *et al.*, 2020; Galaway *et al.*, 2017), a PV-resident protein in association with the PTEX complex and cargo proteins (Elsworth *et al.*, 2016, Miyazaki *et al.*, 2021) and an interactor of the exported protein-interacting complex, EPIC (Elsworth *et al.*, 2016; Batinovic *et al.*, 2017), which has been proposed to be involved in the trafficking of virulence factors to the surface of the infected erythrocyte (Batinovic *et al.*, 2017). However, the enrichment of the surface protein *Pf*113 in the DiQ-BioID with UIS2 suggests it may play a role closely related to UIS2, despite its established non-essentiality for protein export. It is possible that the phosphatase activity of UIS2 might regulate the function of *Pf*113 directly, by altering its phosphorylation state, or indirectly, by modulating the phosphorylation status of other proteins within the PV that interact with *Pf*113. An

interaction between UIS2 and *Pf*113 might be necessary for maintaining the integrity and architecture of the PV or PVM or serves as a connector protein between PPM-PVM and UIS2. In this thesis, IFAs and live cell images demonstrated that UIS2-knockout cells exhibit an altered distribution of PV markers, suggesting an impact on the PV architecture which would fit with the observation made with *Pf*113.However, given the dispensability of *Pf*113, these functions cannot be the reason for the growth relevant functions of UIS2. Further experiments are required to elucidate the effect of UIS2 loss on the integrity of the PV and to determine its interactions with *Pf*113. Such studies should include comparing the potential phosphorylation levels of *Pf*113 in both the presence and absence of UIS2.

Three proteins, in addition to *Pf*113 that were enriched in the UIS2 DiQ-BioID and possess a predicted signal peptide or transmembrane domain were PF3D7_0922100, PF3D7_1133800 and the *Plasmodium* exported protein, PHIST (PF3D7_0401800). The latter was not analysed in this thesis because it has been reported to be exported to the host erythrocyte in *P. falciparum*, associated with the plasma membrane or the spectrin cytoskeleton of the host erythrocyte (Tarr *et al.*, 2014). The other protein, PF3D7_1133800 annotated as an RNA (uracil-5) methyltransferase (U5MTase), was categorized in this study as a protein important for parasite growth and classified as a likely contaminant of the UIS2- DiQ-BioID. According to PlasmoGEM data derived from genome-scale transposon mutagenesis in *P. falciparum*, PF3D7_1133800 is non-mutable, which is consistent with the findings in this thesis indicating that it is an essential protein during the blood stage of the parasite. The ortholog of PF3D7_1133800 in *P. berghei* (PBANKA_0914600) has also been identified as essential for parasite growth (Zhang *et al.,* 2018b). The location of this protein within the parasite, as determined in this thesis, suggests that its potential location is either nuclear or in close proximity to it. One possibility, although not specifically tested in this thesis is that the IFA signal of PF3D7_1133800 corresponds to the apicoplast. RNA methyltransferases can influence the stability and processing of RNA within the apicoplast, change the location and binding affinity, or modulate the activity of enzymes, which can either enhance or inhibit their catalytic functions (Ralph *et al*., 2001; Foth & McFadden, 2003; McFadden & Yeh, 2017; Lucky *et al*., 2023). This may affect the integrity and function of the apicoplast, potentially impacting the efficiency and fidelity of the translation process, a crucial step for

apicoplast metabolic activities, such as synthesis of fatty acids. Recent research by Boucher *et al.*, 2018 has demonstrated that using a combination of BioID and a machine learning algorithm, specifically the PlastNN (apicoplast neural network), more precise identification of apicoplast-associated proteins in *P. falciparum* can be achieved. Although PF3D7_1133800 was not present in that BioID data, Boucher *et al.*, 2018 used the PlastNN algorithm with a new set of signal peptide-containing proteins not found in the BioID data to identify new apicoplast proteins. This analysis classified PF3D7_1133800 as a potential nuclear-encoded apicoplast protein (Boucher *et al.*, 2018). The location of PF3D7_1133800 in the apicoplast was further supported by Pramanik *et al.*, 2020, who used an *in silico* prediction of apicoplast-targeted proteins using the previously published algorithm ApicoAP (Cilingir *et al.*, 2012). Therefore, PF3D7_1133800 is likely a nuclear-encoded apicoplast protein and may be involved in one or several of the following biological functions: DNA replication and repair (Ralph *et al*., 2001; McFadden & Yeh, 2017), transcription (Fichera & Roos, 1997), translation (Ralph *et al*., 2001; Lucky *et al*., 2023), post-translational modifications (Foth & McFadden, 2003), cofactor synthesis (Waller *et al*., 1998), as well as various transport processes (Ralph *et al*., 2004). The lack of colocalization of PF3D7_1133800 with the PV-resident protein EXP2, together with its localization within the parasites and no impact of PF3D7_1133800 knockout on protein export, suggests that its identification in the UIS2 DiQ-BioID may have been due to non-specific binding rather than a direct functional connection with UIS2. PF3D7_1133800 could have been biotinylated during its transport to the apicoplast when passing through the endoplasmic reticulum (ER). Tonkin *et al*. (2006) proposed that nuclear-encoded apicoplast proteins are translocated into the apicoplast through a direct transport mechanism involving a two-part N-terminal signal sequence, where proteins are first directed into the ER, and then sorted directly to the apicoplast, without passing through the Golgi apparatus. Such a pathway would enable biotinylation of PF3D7_1133800 in the ER.

In this thesis, the other possible interaction candidate of UIS2, PF3D7_0922100, which is annotated as a putative ubiquitin-like protein, was found to be important for parasite growth. The observed overlap of PF3D7_0922100 foci with UIS2 at the parasite periphery provides the possibility for a close proximity or direct association between these two proteins. The close proximity raises the question whether

PF3D7_0922100 and UIS2 directly interact with each other and whether this interaction could be required for the integrity and functionality of the PV. Confocal microscopy further confirmed the peripheral location of PF3D7_0922100, supporting its association with PPM, PV, or PVM structures. Using a Lyn-FRB-mCherry-marked plasma membrane, it was possible to observe partial colocalization with the plasma membrane of forming merozoites suggesting a possible location at the PPM, as the PVM does not surround individual merozoites. In later stages, PF3D7_0922100 foci were found both at the parasite periphery and within the parasite, suggesting a possible stage-specific function with UIS2 or alternative roles for PF3D7_0922100 beyond the parasite periphery, although the results from late schizonts also raised the possibility that the internal foci were located at the plasma membrane of the forming merozoites. Upon observing that PF3D7_0922100 contains two transmembrane domains, there are several possibilities for the topology of this protein that may be revealed by such an assay: the C-terminus of PF3D7_0922100 could face the parasite cytosol while the N-terminus is oriented towards the host cell cytosol or vice versa, spanning both PPM and PVM. Alternatively, both N- and C-terminus either are facing the PV lumen or parasite cytosol if both transmembrane domains span the PPM. Finally, it is also possible that the protein is embedded in the PVM, again either both termini facing the PV lumen or the RBC cytosol. To clarify this hypothesis, a Western blot analysis on parasites that had been treated on detergents, streptolysin-O/saponin and trypsin/proteinase K treatment can be conducted. Additionally, self-complementing split fluorescent proteins (FPs), such as the split-GFP$_{1\text{-}10,11}$ approach (Cabantous *et al.*, 2005), could be employed, in which two fragments of the GFP tag are individually expressed. The two non-fluorescent fragments can self-assemble into a functional fluorescent protein only if they localize to the same compartment. Employing the FKBP-FRB heterodimerization system could also provide insights into the topology of this protein at the parasite periphery by facilitating controlled, topology dependent dimerization if the partner domain is available in the same compartment.

A recent study proposed a possible role for PF3D7_0922100 in the context of the Guided Entry of Tail-anchored (GET) pathway in *P. falciparum* (Kummar *et al*., 2021). The GET pathway has a homologous transmembrane domain recognition complex (TRC) pathway in mammals. The GET/TRC pathway is responsible for the insertion

of tail-anchored (TA) proteins—with a single transmembrane (TM) domain near their C-terminus—into the endoplasmic reticulum (ER) membrane (Stefanovic & Hedge, 2007; Schuldiner *et al*., 2008; Casson *et al*., 2016; Chio *et al*., 2017; Borgese *et al.*, 2019). Kummar and colleagues, 2021 used BioID to identify proteins that interact with *Pf*Get3 (component of the GET pathway). They found that PF3D7_0922100 was the top hit in their analysis. The UBL domain of PF3D7_0922100 was selected for the sequence alignment analysis, and they suggested that this protein is a potential homolog of the mammalian Bag6 complex—responsible for delivering TA substrates to the Get3 protein, facilitating their insertion into the ER membrane—which has upstream functions in the GET pathway and could contribute to understanding protein trafficking in *P. falciparum* parasites (Kummar *et al*., 2021). It is unclear how the location of PF3D7_0922100 in the parasite periphery can be reconciled with a role in the GET machinery which is an ER insertion complex. The locations of the PF3D7_1133800 and PF3D7_0922100 proteins are clearly different from that of UIS2 in the parasite periphery at the inner face of the PVM, indicating that these proteins are unlikely to function in the same process.

The aim of this study was to identify direct interaction candidates that are in close spatial proximity to UIS2 in the PV. However, the hit list of the BioID also included many likely which may have been detected due to their proximity to the UIS2 during the DiQ-BioID assay. A significant number of proteins found to be enriched could be attributed to non-specific labeling from the secretory pathway, considering that UIS2 and the biotinylated BirA* undergo trafficking through the endoplasmic reticulum (ER), Golgi apparatus, and vesicle forms, either in individual vesicles or interacting with each other in the same vesicle prior to localization within the PV. In the case of the addition of rapalog and biotin, the biotinylizer is recruited to the UIS2 bait also during trafficking to the PV. Consequently, false positive interaction candidates of the PV compartment may be biotinylated. However, many of the hits did not contain a signal peptide or transmembrane domain, raising questions how they could have come into contact with UIS2 within the ER.

One of the proteins classified as likely contaminants was the eukaryotic translation initiation factor 3 subunit A (EIF3A, PF3D7_1212700), which interacts with the initiation factor EIF2α (Jackson *et al*., 2010). EIF2α has been previously connected

to the phosphatase UIS2, in a function in translation regulation through dephosphorylation (Zhang *et al.*, 2016). Although EIF2α was present in the DiQ-BioID with UIS2, it was not significantly enriched (data not shown in this thesis, as with an average log2 < 1.0 it was too low in the list of detected proteins). The conclusion that this protein might be a contaminant was supported by recent research by Khosh-Naucke *et al*., 2018, which also demonstrated the presence of eIF2α in a proteome of PPM and PVM proteins where it was also categorized as a likely contaminant. These results suggest that eIF2α is a common contaminant in BioIDs. It is unclear how this protein could reach the PV compartment during the blood stages of *P. falciparum*. One possible scenario is that EIF2α could transiently interact with UIS2 during its translation, but in that case it is unclear why it is not enriched in the UIS2 sample and it would also mean that biotinylation would occur when the C-terminal domain is being synthesised. To unequivocally exclude that eIF2α might not have an unexpected location where it could come into contact with UIS2, it could be endogenously tagged and colocalized with UIS2.

4.6.1 UIS2 likely functions upstream of PTEX

PTEX components did not show a significant enrichment in the DiQ-BioID assay with UIS2. This finding suggests that despite the established role of UIS2 in protein export, it may not be in immediate physical contact with the PTEX complex. This observation is corroborated by the unpublished BioID data documented by Naranjo-Prado, 2022, which employed two constructs SBP1-GFP-mDHFR-BirA*, which gets stuck in PTEX, and REX2-GFP-mDHFR-BirA*, which gets stuck before entering into the PTEX, to probe the proteins in proximity of these transport-arrested exported proteins. The location of these proteins at their respective sites in the process of translocation depends on the addition of WR, which prevents the unfolding of the fused mDHFR domain (Mesén-Ramírez *et al.,* 2016). Mass spectrometry identifying the proteins biotinylated by the SBP1-GFP-mDHFR-BirA* construct indicated that UIS2 was not in direct contact with PTEX during translocation, while *Pf*113 was in close proximity. In contrast, mass spectrometry identifying the proteins biotinylated by the REX2-GFP-mDHFR-BirA* construct revealed that UIS2 was among the top enriched protein together with PTEX150, EXP2, ETRAMP5 and *Pf*113 (Naranjo-Prado, 2022). However, direct contact with PTEX cannot be completely dismissed, as previous findings by Khosh-Naucke in 2018 indicated that UIS2 is located on the

inner face of the PVM (Khosh-Naucke *et al*., 2018). Additionally, the top interaction candidate, *Pf*113, has previously been co-immunoprecipitated with the PTEX complex (Elsworth *et al.*, 2016). Moreover, the presence of UIS2 in immunoprecipitation assays (IPs) with EXP2 (Mésen-Ramírez *et al.*, 2016) and its proximity to EXP2 in BioID2 assays (Nessel *et al*., 2020) have been documented. Therefore, the lack of PTEX component enrichment in the DiQ-BioID assay with UIS2 can either be due to technical issues, or UIS2 may function immediately upstream of PTEX translocation.

4.7 Overall conclusions

Intracellular phosphatases are well-recognized for their roles in regulating cellular processes through dephosphorylation events. Interestingly, the secretion of phosphatases such as UIS2 indicates a potentially novel extracellular function, specifically within the PV, a compartment which is pivotal for the proliferation and survival of the parasite, although a role in the ER during transport cannot be fully excluded. The proximal relationship of UIS2 to the PVM is indicative of a specialized function—possibly the initiation of as-yet-undefined downstream signalling cascades that are integral to protein export, integrity of the PV or nutrient uptake (Figure 44). This thesis has demonstrated a role for UIS2 in the protein export process and that the phosphatase activity is important for UIS2. The mechanism how this occurs is unclear. Potential options are a direct action on components of the translocation machinery (PTEX) or dephosphorylation of substrates prior to their trafficking via PTEX (Figure 44). Furthermore, UIS2 could be involved in alterations of the architecture of the parasitophorous vacuole membrane (PVM) or in changes to the lipid/protein composition of the PVM, indirectly impacting the assembly of PTEX and other proteins at the PVM (Figure 50). Alternatively, impairment of the UIS2 function in protein export could compromise PVM integrity, which may be attributable to the dephosphorylation processes or other enzymatic activities of UIS2. Furthermore, UIS2 could also be critical for the distribution and operational integrity of EXP2 as a nutrient-permeable channel (NPC), which is essential for the diffusion of solute between the PV and erythrocyte cytosol because this protein has a dual function (Garten *et al*., 2018; Mesén-Ramírez *et al*., 2019; Mesén-Ramírez *et al*., 2021) (Figure 44). However, nutrient transport across the PVM was not specifically

analysed in this thesis. UIS2 could also modulate *Pf*113 phosphorylation or indirectly affect the phosphorylation of PV-associated proteins, interaction that could be important for PV or PVM integrity and architecture. As *Pf*113 mutants also show alterations to the PV compartment (Bullen *et al.*, 2022), this is a reasonable possibility. In conclusion, this work uncovered the parasite-specific nature and functions of UIS2, a secreted phosphatase which is essential for protein export.

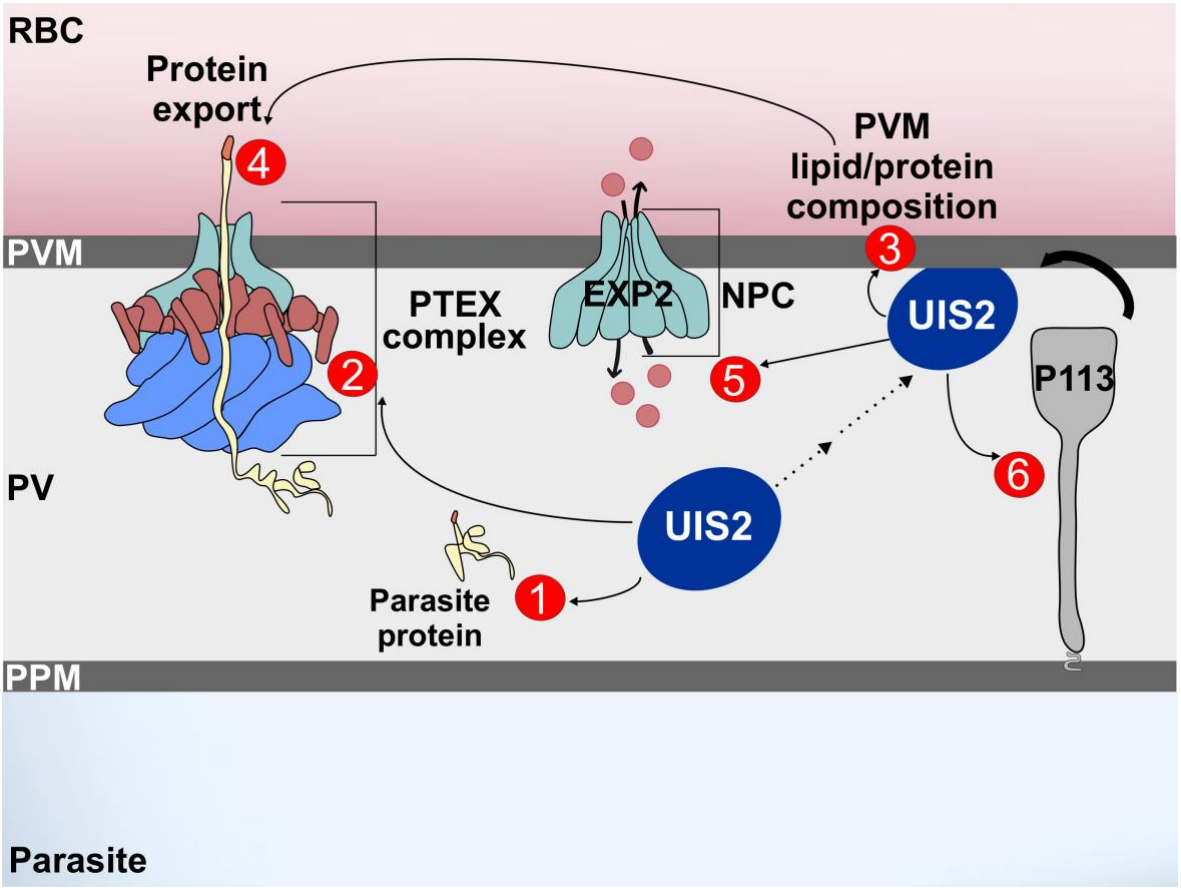

Figure 44. Speculations on possible roles of UIS2 in the PV of P. *falciparum* parasites. (1) UIS2 may catalyze the dephosphorylation of substrates before they pass through the Plasmodium Translocon of Exported Proteins (PTEX). (2) It might act directly on components of PTEX. (3) UIS2 could be essential for the dephosphorylation of substrates, influencing the PVM's structure or the lipid/protein composition. (4) These actions could indirectly modify the assembly of PTEX and, thereby, protein export. (5) UIS2 KO caused a misdistribution of EXP2, which besides negatively affecting protein export might also impair the nutrient-permeable channel function (NPC). (6) it could modulate the phosphorylation of *Pf*113. NPC: nutrient permeable channel; PVM, parasitophorous vacuole membrane; PV, parasitophorous

vacuole, PPM: Plasma parasite membrane; PTEX, Plasmodium Translocon of exported proteins.

4.8 Future research on the role of UIS2

The localization of UIS2 in a different compartment than phosphorylated eIF2α (eIF2α-P) raises the question which proteins might be the physiological targets of the UIS2 phosphatase activity. Localized at the PVM, UIS2 might for example dephosphorylate targets that trigger downstream signalling cascades that have not yet been identified. To gain a better understanding of the function of UIS2, a phosphoproteome analysis would be necessary to identify the differences in protein phosphorylation between parasites lacking UIS2 and the control cells.

The present study has demonstrated that UIS2 is essential for the export of both PEXEL-positive and negative proteins. It also leads to an altered distribution of PVM proteins (ETRAMPs, EXP2). Mesén-Ramírez *et al*, (2016) have shown that the mislocalization of EXP2 at the PVM does not necessarily lead to an export phenotype, whereas a knockout of EXP1 results in a nutrient transport phenotype. So, the distribution of EXP2 at the PVM might be important for nutrient pore activity but not PTEX function. This thesis suggested that UIS2 is essential for the proper distribution of EXP2 at the PVM, indicating that likely the absence of UIS2 may lead to an insufficient number or non-functional EXP2 pores at the PVM, which could impede nutrient acquisition and therefore induce parasite death. To investigate this, an assay using the import of a labeled glucose analogue, specifically 2-(N-(7-nitrobenz-2-oxa-1,3-diazol-4-yl) amino)-2-deoxyglucose (2-NBDG), as documented in prior studies (Low *et al.*, 2019; Mesén-Ramírez *et al.*, 2021; Ito *et al.*, 2023) or amino acids uptake, 5-aminolevulinic acid (ALA), resulting in accumulation of the phototoxic intermediate protoporphyrin IX (PPIX) (Sigala *et al*., 2015; Mesén-Ramírez *et al.*, 2021) can be performed in the conditional knock out of UIS2 cell line.

Given the localization of UIS2 at the PVM, its phosphatase likely is important in that compartment. In this thesis, it was observed that the organization of EXP2 at the PVM was affected in parasites lacking UIS2. Further experiments could investigate whether the observed effects are due to a membrane-insertion defect of EXP2 or a

defect in its solubility caused by the loss of UIS2. For this purpose, Urea in combination with Triton X-100, a common method for separating soluble proteins from membrane-associated proteins could be employed as previously used for PVM proteins in *P. falciparum* (Spielmann *et al*., 2006b). Spielmann and collaborators (2006) used this method to study the solubility properties of ETRAMP complex components. Alternatively, biochemical methods such as sodium carbonate (Na2CO3) extraction could be employed to assess EXP2 solubility and state in the PVM. This technique also distinguishes between integral and peripheral membrane proteins (Yadavalli *et al*., 2021; Robinson *et al*., 2022; Pitman *et al.,* 2024). Further experiments are also needed to elucidate whether the distribution and secretion of other PV/PVM proteins and components of the PTEX are affected by the loss of UIS2.

The integrity of the PVM in ΔUIS2 parasites could be further investigated by electron microscopy. This assessment could further investigate whether the disrupted protein export phenotype is directly attributable to the UIS2 deletion rather than to downstream alterations in the PVM architecture. Additionally, the expression of a soluble fluorescent marker, such as SP-mScarlet—which was generated in this thesis—within the PV, combined with confocal microscopy, could be employed to monitor its release into the host erythrocyte, serving as an indicator of compromised PVM integrity. Alternatively, to assess the leakage of PV proteins, biochemical approaches such as tetanolysin lysis (e.g.; Bhattacharjee *et al*., 2008; Grüring & Spielmann, 2012; Grüring *et al*., 2012; Schulze et al., 2015; Mesén-Ramírez *et al.,* 2019), Streptolysin O lysis (Ansorge *et al*., 1996; Jackson *et al*., 2007) or equinatoxin II lysis (Jackson *et al*., 2007) could be employed on SP-mScarlet expressing ΔUIS2 parasites. This would allow for the selective permeabilization of the RBC membranes without disrupting the PVM. Once the RBC membrane is permeabilized, the contents released can be analyzed for the presence of leaking PV proteins.

It has been observed that the absence of UIS2 inhibits protein export to the host cell and results in a phenotype characterized by ring stages with small diameters immediately after invasion. This is similar to the phenotype observed by Ressurreição *et al*. (2023) after the conditional inactivation of the parasitophorous vacuole protein PV6 and inhibition of Plasmepsin V (PMV). Since both UIS2 and PV6 proteins are cleaved by PMV, it is possible that UIS2 performs an essential function during

transport, perhaps in the ER during PEXEL processing. To investigate this, PEXEL cleavage of an exported reporter, GBP1-108-mScarlet—previously generated in this thesis—can be tested in the conditional knockout of UIS2 to determine if PEXEL processing of this protein is inhibited by the absence of UIS2. Western blot analysis will confirm the expected size of the exported reporter. The outcomes of these experiments could provide significant insights into the phosphatase function within the PV and understanding the role of UIS2 in *P. falciparum* parasites.

References

Abkarian, M., Massiera, G., Berry, L., Roques, M., Braun-Breton, C., 2011. A novel mechanism for egress of malarial parasites from red blood cells. https://doi.org/10.1182/blood-2010.

Absalon, S., Blomqvist, K., Rudlaff, R.M., Delano, T.J., Pollastri, M.P., Dvorin, J.D., 2018. Calcium-Dependent Protein Kinase 5 Is Required for Release of Egress-Specific Organelles in Plasmodium falciparum. https://doi.org/10.1128/mBio.

Aikawa, M., Huff, C.G., Sprinz, H., 1967. Fine structure of the asexual stages of Plasmodium elongatum. J Cell Biol 34, 229–249. https://doi.org/10.1083/jcb.34.1.229.

Aly, A.S.I., Vaughan, A.M., Kappe, S.H.I., 2009. Malaria parasite development in the mosquito and infection of the mammalian host. Annu Rev Microbiol 63, 195–221. https://doi.org/10.1146/annurev.micro.091208.073403.

Andersen, J.N., Mortensen, O.H., Peters, G.H., Drake, P.G., Iversen, L.F., Olsen, O.H., Jansen, P.G., Andersen, H.S., Tonks, N.K., Møller, N.P.H., 2001. Structural and Evolutionary Relationships among Protein Tyrosine Phosphatase Domains. Molecular and Cellular Biology 21, 7117–7136. https://doi.org/10.1128/mcb.21.21.7117-7136.2001.

Andreeva, A.V., Kutuzov, M.A., 2001. Letter to the Editor PPP Family of Protein Ser/Thr Phosphatases: Two Distinct Branches? Mol. Biol. Evol 18, 448–452.

Ansorge, I., Benting, J., Bhakdi, S., Lingelbach, K., 1996. Protein sorting in Plasmodium falciparum-infected red blood cells permeabilized with the pore-forming protein streptolysin O. Biochem J 315, 307–314.

Ansorge, I., Paprotka, K., Bhakdi, S., Lingelbach, K., 1997. Permeabilization of the erythrocyte membrane with streptolysin O allows access to the vacuolar membrane of Plasmodium falciparum and a molecular analysis of membrane topology. Mol Biochem Parasitol 84, 259–261. https://doi.org/10.1016/s0166-6851(96)02806-x.

Ashley, E.A., Dhorda, M., Fairhurst, R.M., Amaratunga, C., Lim, P., Suon, S., Sreng, S., Anderson, J.M., Mao, S., Sam, B., Sopha, C., Chuor, C.M., Nguon, C., Sovannaroth,

Baer, K., Klotz, C., Kappe, S.H.I., Schnieder, T., Frevert, U., 2007. Release of hepatic Plasmodium yoelii merozoites into the pulmonary microvasculature. PLoS Pathogens 3, 1651–1668. https://doi.org/10.1371/journal.ppat.0030171.

Bakkouri, M.E., Pow, A., Mulichak, A., Cheung, K.L.Y., Artz, J.D., Amani, M., Fell, S., Koning-Ward, T.F. de, Goodman, C.D., McFadden, G.I., Ortega, J., Hui, R., Houry, W.A., 2010. The Clp chaperones and proteases of the human malaria parasite Plasmodium falciparum. Journal of Molecular Biology 404, 456–477. https://doi.org/10.1016/j.jmb.2010.09.051.

Balikagala, B., Fukuda, N., Ikeda, M., Katuro, O.T., Tachibana, S.-I., Yamauchi, M., Opio, W., Emoto, S., Anywar, D.A., Kimura, E., Palacpac, N.M.Q., Odongo-Aginya, E.I., Ogwang, M., Horii, T., Mita, T., 2021. Evidence of Artemisinin-Resistant Malaria in Africa. New England Journal of Medicine 385, 1163–1171. https://doi.org/10.1056/nejmoa2101746.

Barford, D., Das, A.K., Egloff, M.P., 1998. The structure and mechanism of protein phosphatases: insights into catalysis and regulation. Annu Rev Biophys Biomol Struct 27, 133–164. https://doi.org/10.1146/annurev.biophys.27.1.133.

Barik, S., 1993. Expression and biochemical properties of a protein serine/threonine phosphatase encoded by bacteriophage lambda. Proc Natl Acad Sci U S A 90, 10633–10637.

Barton, G.J., Cohen, P.T.W., Barford, D., 1994. Conservation analysis and structure prediction of the protein serine/threonine phosphatases: Sequence similarity with diadenosine tetraphosphatase from Escherichia coli suggests homology to the protein phosphatases. European Journal of Biochemistry 220, 225–237. https://doi.org/10.1111/j.1432-1033.1994.tb18618.x.

Batinovic, S., McHugh, E., Chisholm, S.A., Matthews, K., Liu, B., Dumont, L., Charnaud, S.C., Schneider, M.P., Gilson, P.R., Koning-Ward, T.F.D., Dixon, M.W.A., Tilley, L., 2017. An exported protein-interacting complex involved in the trafficking of virulence determinants in Plasmodium-infected erythrocytes. Nature Communications 8. https://doi.org/10.1038/ncomms16044.

Baum, J., Richard, D., Healer, J., Rug, M., Krnajski, Z., Gilberger, T.W., Green, J.L., Holder, A.A., Cowman, A.F., 2006. A conserved molecular motor drives cell invasion and gliding motility across malaria life cycle stages and other apicomplexan parasites. Journal of Biological Chemistry 281, 5197–5208. https://doi.org/10.1074/jbc.M509807200.

Baumeister, S., Winterberg, M., Duranton, C., Huber, S.M., Lang, F., Kirk, K., Lingelbach, K., 2006. Evidence for the involvement of Plasmodium falciparum proteins in the formation of new permeability pathways in the erythrocyte membrane. Molecular Microbiology 60, 493–504. https://doi.org/10.1111/j.1365-2958.2006.05112.x.

Beck, J.R., Ho, C.-M., 2021. Transport mechanisms at the malaria parasite-host cell interface. PLoS Pathog 17, e1009394. https://doi.org/10.1371/journal.ppat.1009394.

Beck, J.R., Muralidharan, V., Oksman, A., Goldberg, D.E., 2014. PTEX component HSP101 mediates export of diverse malaria effectors into host erythrocytes. Nature 511, 592–595. https://doi.org/10.1038/nature13574.

Behrens, H.M., Spielmann, T., 2023. Identification of domains in Plasmodium falciparum proteins of unknown function using DALI search on Alphafold predictions. https://doi.org/10.1101/2023.06.05.543710.

Bergman, L.W., Kaiser, K., Fujioka, H., Coppens, I., Daly, T.M., Fox, S., Matuschewski, K., Nussenzweig, V., Kappe, S.H.I., 2003. Myosin A tail domain interacting protein

(MTIP) localizes to the inner membrane complex of Plasmodium sporozoites. J Cell Sci 116, 39–49. https://doi.org/10.1242/jcs.00194

Besteiro, S., Dubremetz, J.F., Lebrun, M., 2011. The moving junction of apicomplexan parasites: A key structure for invasion. Cellular Microbiology 13, 797–805. https://doi.org/10.1111/j.1462-5822.2011.01597.x.

Bhanot, P., Schauer, K., Coppens, I., Nussenzweig, V., 2005. A surface phospholipase is involved in the migration of Plasmodium sporozoites through cells. Journal of Biological Chemistry 280, 6752–6760. https://doi.org/10.1074/jbc.M411465200.

Bhattacharjee, S., Van Ooij, C., Balu, B., Adams, J.H., Haldar, K., 2008. Maurer's clefts of Plasmodium falciparum are secretory organelles that concentrate virulence protein reporters for delivery to the host erythrocyte. Blood 111, 2418–2426. https://doi.org/10.1182/blood-2007-09-115279.

Bhattacharyya, M.K., Hong, Z., Kongkasuriyachai, D., Kumar, N., 2002. Plasmodium falciparum protein phosphatase type 1 functionally complements a glc7 mutant in Saccharomyces cerevisiae. Int J Parasitol 32, 739–747. https://doi.org/10.1016/s0020-7519(02)00007-3.

Billker, O., Dechamps, S., Tewari, R., Wenig, G., Franke-Fayard, B., Brinkmann, V., 2004. Calcium and a calcium-dependent protein kinase regulate gamete formation and mosquito transmission in a malaria parasite. Cell 117, 503–514. https://doi.org/10.1016/s0092-8674(04)00449-0.

Billker, O., Lindo, V., Panico, M., Etienne, A.E., Paxton, T., Dell, A., Rogers, M., Sinden, R.E., Morris, H.R., 1998. Identification of xanthurenic acid as the putative inducer of malaria development in the mosquito. Nature 392, 289–292. https://doi.org/10.1038/32667.

Billker, O., Shaw, M.K., Margos, G., Sinden, R.E., 1997. The roles of temperature, pH and mosquito factors as triggers of male and female gametogenesis of Plasmodium berghei in vitro. Parasitology (1) 115. https://doi.org/10.1017/s0031182097008895.

Birnbaum, J., Flemming, S., Reichard, N., Soares, A.B., Mesén-Ramírez, P., Jonscher, E., Bergmann, B., Spielmann, T., 2017. A genetic system to study Plasmodium falciparum protein function. Nat Methods 14, 450–456. https://doi.org/10.1038/nmeth.4223

Birnbaum, J., Scharf, S., Schmidt, S., Jonscher, E., Hoeijmakers, W.A.M., Flemming, S., Toenhake, C.G., Schmitt, M., Sabitzki, R., Bergmann, B., Fröhlke, U., Mesén-Ramírez, P., Blancke Soares, A., Herrmann, H., Bártfai, R., Spielmann, T., 2020. A Kelch13-defined endocytosis pathway mediates artemisinin resistance in malaria parasites. Science 367, 51–59. https://doi.org/10.1126/science.aax4735.

Bitew, M.A., Gaete, P.S., Swale, C., Maru, P., Contreras, J.E., Saeij, J.P.J., 2023. GRA47 and GRA72 are Toxoplasma gondii pore-forming proteins that influence small molecule permeability of the parasitophorous vacuole. bioRxiv 2023.11.15.567216. https://doi.org/10.1101/2023.11.15.567216.

Blackman, M.J., Bannister, L.H., 2001. Apical organelles of Apicomplexa: biology and isolation by subcellular fractionation. Mol Biochem Parasitol 117, 11–25. https://doi.org/10.1016/s0166-6851(01)00328-0.

Blakely, W.J., Holmes, M.J., Arrizabalaga, G., 2020. The Secreted Acid Phosphatase Domain-Containing GRA44 from Toxoplasma gondii Is Required for c-Myc Induction in Infected Cells. mSphere 5, e00877-19. https://doi.org/10.1128/mSphere.00877-19.

Blisnick, T., Morales Betoulle, M.E., Barale, J.C., Uzureau, P., Berry, L., Desroses, S., Fujioka, H., Mattei, D., Braun Breton, C., 2000. Pfsbp1, a Maurer's cleft Plasmodium falciparum protein, is associated with the erythrocyte skeleton. Mol Biochem Parasitol 111, 107–121. https://doi.org/10.1016/s0166-6851(00)00301-7.

Blisnick, T., Vincensini, L., Fall, G., Braun-Breton, C., 2006. Protein phosphatase 1, a Plasmodium falciparum essential enzyme, is exported to the host cell and implicated in the release of infectious merozoites. Cellular Microbiology 8, 591–601. https://doi.org/10.1111/j.1462-5822.2005.00650.x.

Boddey, J.A., Cowman, A.F., 2013. Plasmodium nesting: Remaking the erythrocyte from the inside out. Annual Review of Microbiology 67, 243–269. https://doi.org/10.1146/annurev-micro-092412-155730.

Boddey, J.A., Hodder, A.N., Günther, S., Gilson, P.R., Patsiouras, H., Kapp, E.A., Pearce, J.A., Koning-Ward, T.F.D., Simpson, R.J., Crabb, B.S., Cowman, A.F., 2010. An aspartyl protease directs malaria effector proteins to the host cell. Nature 463, 627–631. https://doi.org/10.1038/nature08728.

Boddey, J.A., Moritz, R.L., Simpson, R.J., Cowman, A.F., 2009. Role of the Plasmodium export element in trafficking parasite proteins to the infected erythrocyte. Traffic 10, 285–299. https://doi.org/10.1111/j.1600-0854.2008.00864.x.

Boddey, J.A., O'Neill, M.T., Lopaticki, S., Carvalho, T.G., Hodder, A.N., Nebl, T., Wawra, S., West, P.V., Ebrahimzadeh, Z., Richard, D., Flemming, S., Spielmann, T., Przyborski, J., Babon, J.J., Cowman, A.F., 2016. Export of malaria proteins requires co-translational processing of the PEXEL motif independent of phosphatidylinositol-3-phosphate binding. Nature Communications 7. https://doi.org/10.1038/ncomms10470.

Bollen, M., Stalmans, W., 1992. The structure, role, and regulation of type 1 protein phosphatases. Critical Reviews in Biochemistry and Molecular Biology 27, 227–281. https://doi.org/10.3109/10409239209082564.

Boonyalai, N., Collins, C.R., Hackett, F., Withers-Martinez, C., Blackman, M.J., 2018. Essentiality of Plasmodium falciparum plasmepsin V. PLoS ONE 13. https://doi.org/10.1371/journal.pone.0207621.

Borgese, N., Coy-Vergara, J., Colombo, S.F., Schwappach, B., 2019. The Ways of Tails: the GET Pathway and more. Protein J 38, 289–305. https://doi.org/10.1007/s10930-019-09845-4.

Bosch, J., Paige, M.H., Vaidya, A.B., Bergman, L.W., Hol, W.G.J., 2012. Crystal structure of GAP50, the anchor of the invasion machinery in the inner membrane complex of Plasmodium falciparum. Journal of Structural Biology 178, 61–73. https://doi.org/10.1016/j.jsb.2012.02.009.

Boucher, M.J., Ghosh, S., Zhang, L., Lal, A., Jang, S.W., Ju, A., Zhang, S., Wang, X., Ralph, S.A., Zou, J., Elias, J.E., Yeh, E., 2018. Integrative proteomics and bioinformatic prediction enable a high-confidence apicoplast proteome in malaria parasites. PLoS Biology 16. https://doi.org/10.1371/journal.pbio.2005895.

Boyd, M.F., Stratman-Thomas, W.K., Kitchen, S.F., 1936. On the Duration of Infectiousness in Anophelines Harboring Plasmodium Falciparum. The American Journal of Tropical Medicine and Hygiene s1-16, 157–158. https://doi.org/10.4269/ajtmh.1936.s1-16.157.

Brian M. Cooke, A.F.C.& L.T.A.G.M., 2009. Malaria parasite proteins that remodel the host erythrocyte. nature reviews microbiology 7, 341–354.

Briquet, S., Marinach, C., Silvie, O., Vaquero, C., 2021. Preparing for Transmission: Gene Regulation in Plasmodium Sporozoites. Front Cell Infect Microbiol 10, 618430. https://doi.org/10.3389/fcimb.2020.618430.

Brown, G.V., Culvenor, J.G., Crewther, P.E., Bianco, A.E., Coppel, R.L., Saint, R.B., Stahl, H.D., Kemp, D.J., Anders, R.F., 1985. Localization of the ring-infected erythrocyte surface antigen (RESA) of Plasmodium falciparum in merozoites and ring-infected erythrocytes. J Exp Med 162, 774–779. https://doi.org/10.1084/jem.162.2.774.

Bullen, H.E., Charnaud, S.C., Kalanon, M., Riglar, D.T., Dekiwadia, C., Kangwanrangsan, N., Torii, M., Tsuboi, T., Baum, J., Ralph, S.A., Cowman, A.F., Koning-Ward, T.F.D., Crabb, B.S., Gilsona, P.R., 2012. Biosynthesis, localization, and macromolecular arrangement of the Plasmodium falciparum translocon of exported proteins (PTEX). Journal of Biological Chemistry 287, 7871–7884. https://doi.org/10.1074/jbc.M111.328591.

Bullen, H.E., Sanders, P.R., Dans, M.G., Jonsdottir, T.K., Riglar, D.T., Looker, O., Palmer, C.S., Kouskousis, B., Charnaud, S.C., Triglia, T., Gabriela, M., Schneider, M.P., Chan, J.A., Koning-Ward, T.F. de, Baum, J., Kazura, J.W., Beeson, J.G., Cowman, A.F., Gilson, P.R., Crabb, B.S., 2022. The Plasmodium falciparum parasitophorous vacuole protein P113 interacts with the parasite protein export machinery and maintains normal vacuole architecture. Molecular Microbiology 117, 1245–1262. https://doi.org/10.1111/mmi.14904.

Cabantous, S., Terwilliger, T.C., Waldo, G.S., 2005. Protein tagging and detection with engineered self-assembling fragments of green fluorescent protein. Nature Biotechnology 23, 102–107. https://doi.org/10.1038/nbt1044.

Cabrera, A., Herrmann, S., Warszta, D., Santos, J.M., Peter, A.T.J., Kono, M., Debrouver, S., Jacobs, T., Spielmann, T., Ungermann, C., Soldati-Favre, D., Gilberger, T.W., 2012. Dissection of minimal sequence requirements for rhoptry

membrane targeting in the malaria parasite. Traffic 13, 1335–1350. https://doi.org/10.1111/j.1600-0854.2012.01394.x.

Cai, J., Chen, S., Zhu, F., Lu, X., Liu, T., Xu, W., 2021. Whole-Killed Blood-Stage Vaccine: Is It Worthwhile to Further Develop It to Control Malaria? Front Microbiol 12, 670775. https://doi.org/10.3389/fmicb.2021.670775.

Campeotto, I., Galaway, F., Mehmood, S., Barfod, L.K., Quinkert, D., Kotraiah, V., Phares, T.W., Wright, K.E., Snijders, A.P., Draper, S.J., Higgins, M.K., Wright, G.J., 2020. The structure of the cysteine-rich domain of plasmodium falciparum p113 identifies the location of the rh5 binding site. mBio 11, 1–12. https://doi.org/10.1128/mBio.01566-20.

Carmo, O.M.S., Shami, G.J., Cox, D., Liu, B., Blanch, A.J., Tiash, S., Tilley, L., Dixon, M.W.A., 2022. Deletion of the Plasmodium falciparum exported protein PTP7 leads to Maurer's clefts vesiculation, host cell remodeling defects, and loss of surface presentation of EMP1. PLoS Pathogens 18. https://doi.org/10.1371/journal.ppat.1009882.

Carruthers, V.B., Tomley, F.M., 2008. Receptor-ligand interaction and invasion: Microneme proteins in apicomplexans. Subcell Biochem 47, 33–45.

Carter, R., Chen, D.H., 1976. Malaria transmission blocked by immunisation with gametes of the malaria parasite. Nature 263, 57–60. https://doi.org/10.1038/263057a0.

Carter, R., Mendis, K.N., Miller, L.H., Molineaux, L., Saul, A., 2000. Malaria transmission-blocking vaccines--how can their development be supported? Nat Med 6, 241–244. https://doi.org/10.1038/73062.

Casares, S., Brumeanu, T.-D., Richie, T.L., 2010. The RTS,S malaria vaccine. Vaccine 28, 4880–4894. https://doi.org/10.1016/j.vaccine.2010.05.033.

Casson, J., McKenna, M., High, S., 2016. On the road to nowhere: cross-talk between post-translational protein targeting and cytosolic quality control. Biochemical Society Transactions 44, 796–801. https://doi.org/10.1042/BST20160045.

Chang, H.H., Falick, A.M., Carlton, P.M., Sedat, J.W., DeRisi, J.L., Marletta, M.A., 2008. N-terminal processing of proteins exported by malaria parasites. Molecular and Biochemical Parasitology 160, 107–115. https://doi.org/10.1016/j.molbiopara.2008.04.011.

Charnaud, S.C., Kumarasingha, R., Bullen, H.E., Crabb, B.S., Gilson, P.R., 2018. Knockdown of the translocon protein EXP2 in Plasmodium falciparum reduces growth and protein export. PLoS ONE 13. https://doi.org/10.1371/journal.pone.0204785.

Chen, L., Lopaticki, S., Riglar, D.T., Dekiwadia, C., Uboldi, A.D., Tham, W.H., O'Neill, M.T., Richard, D., Baum, J., Ralph, S.A., Cowman, A.F., 2011. An egf-like protein forms a complex with pfrh5 and is required for invasion of human erythrocytes by

plasmodium falciparum. PLoS Pathogens 7. https://doi.org/10.1371/journal.ppat.1002199.

Chio, U.S., Cho, H., Shan, S.-O., 2017. Mechanisms of Tail-Anchored Membrane Protein Targeting and Insertion. https://doi.org/10.1146/annurev-cellbio-100616.

Chisholm, S.A., Kalanon, M., Nebl, T., Sanders, P.R., Matthews, K.M., Dickerman, B.K., Gilson, P.R., Koning-Ward, T.F. de, 2018. The malaria PTEX component PTEX88 interacts most closely with HSP101 at the host–parasite interface. FEBS Journal 285, 2037–2055. https://doi.org/10.1111/febs.14463.

Chitnis, C.E., Mukherjee, P., Mehta, S., Yazdani, S.S., Dhawan, S., Shakri, A.R., Bharadwaj, R., Gupta, P.K., Hans, D., Mazumdar, S., Singh, B., Kumar, S., Pandey, G., Parulekar, V., Imbault, N., Shivyogi, P., Godbole, G., Mohan, K., Leroy, O., Singh, K., Chauhan, V.S., 2015. Phase I clinical trial of a recombinant blood stage vaccine candidate for Plasmodium falciparum malaria based on MSP1 and EBA175. PLoS ONE 10. https://doi.org/10.1371/journal.pone.0117820.

Cilingir, G., Broschat, S.L., Lau, A.O.T., 2012. ApicoAP: The first computational model for identifying apicoplast-targeted proteins in multiple species of apicomplexa. PLoS ONE 7. https://doi.org/10.1371/journal.pone.0036598.

Clark, S.A., Ambrose, W.W., Anderson, T.R., Terrell, R.S., Toverud, S.U., 1989. Ultrastructural localization of tartrate-resistant, purple acid phosphatase in rat osteoclasts by histochemistry and immunocytochemistry. J Bone Miner Res 4, 399–405. https://doi.org/10.1002/jbmr.5650040315.

Coffey, C.J., Dagley, M.J., Seizova, L.F., Kapp, S.A., Infusini, E.A., Roos, G.S., Boddey, D.S., Webb, J.A., Tonkin, A.I., 2018. Aspartyl Protease 5 Matures Dense Granule Proteins That Reside at the Host-Parasite Interface in Toxoplasma gondii matures dense granule proteins that reside at the host-parasite interface in Toxoplasma gondii. mbio.asm.org 9, 1796–1814. https://doi.org/10.1128/mBio

Collins, C.R., Hackett, F., Strath, M., Penzo, M., Withers-Martinez, C., Baker, D.A., Blackman, M.J., 2013. Malaria Parasite cGMP-dependent Protein Kinase Regulates Blood Stage Merozoite Secretory Organelle Discharge and Egress. PLoS Pathogens 9. https://doi.org/10.1371/journal.ppat.1003344.

Collins, K.A., Brod, F., Snaith, R., Ulaszewska, M., Longley, R.J., Salman, A.M., Gilbert, S.C., Spencer, A.J., Franco, D., Ballou, W.R., Hill, A.V.S., 2021. Ultra-low dose immunization and multi-component vaccination strategies enhance protection against malaria in mice. Scientific Reports 11. https://doi.org/10.1038/s41598-021-90290-8.

Collins, K.A., Snaith, R., Cottingham, M.G., Gilbert, S.C., Hill, A.V.S., 2017. Enhancing protective immunity to malaria with a highly immunogenic virus-like particle vaccine. Scientific Reports 7. https://doi.org/10.1038/srep46621.

Cooke, B.M., Buckingham, D.W., Glenister, F.K., Fernandez, K.M., Bannister, L.H., Marti, M., Mohandas, N., Coppel, R.L., 2006. A Maurer's cleft-associated protein is essential for expression of the major malaria virulence antigen on the surface of

infected red blood cells. Journal of Cell Biology 172, 899–908. https://doi.org/10.1083/jcb.200509122.

Counihan, N.A., Chisholm, S.A., Bullen, H.E., Srivastava, A., Sanders, P.R., Jonsdottir, T.K., Weiss, G.E., Ghosh, S., Crabb, B.S., Creek, D.J., Gilson, P.R., Koning-Ward, T.F.D., 2017. Plasmodium falciparum parasites deploy RhopH2 into the host erythrocyte to obtain nutrients, grow and replicate. https://doi.org/10.7554/eLife.23217.001.

Cowman, A.F., Berry, D., Baum, J., 2012. The cellular and molecular basis for malaria parasite invasion of the human red blood cell. Journal of Cell Biology 198, 961–971. https://doi.org/10.1083/jcb.201206112.

Cowman, A.F., Healer, J., Marapana, D., Marsh, K., 2016. Malaria: Biology and Disease. Cell 167, 610–624. https://doi.org/10.1016/j.cell.2016.07.055.

Cowman, A.F., Tonkin, C.J., Tham, W.-H., Duraisingh, M.T., 2017. The Molecular Basis of Erythrocyte Invasion by Malaria Parasites. Cell Host Microbe 22, 232–245. https://doi.org/10.1016/j.chom.2017.07.003

Crabb, B.S., Cooke, B.M., Reeder, J.C., Waller, R.F., Caruana, S.R., Davern, K.M., Wickham, M.E., Brown, G.V., Coppel, R.L., Cowman, A.F., 1997. Targeted gene disruption shows that knobs enable malaria-infected red cells to cytoadhere under physiological shear stress. Cell 89, 287–296. https://doi.org/10.1016/s0092-8674(00)80207-x.

Crosnier, C., Bustamante, L.Y., Bartholdson, S.J., Bei, A.K., Theron, M., Uchikawa, M., Mboup, S., Ndir, O., Kwiatkowski, D.P., Duraisingh, M.T., Rayner, J.C., Wright, G.J., 2011. Basigin is a receptor essential for erythrocyte invasion by Plasmodium falciparum. Nature 480, 534–537. https://doi.org/10.1038/nature10606.

Cui, L., Fan, Q., Li, J., 2002. The malaria parasite Plasmodium falciparum encodes members of the Puf RNA-binding protein family with conserved RNA binding activity. Nucleic Acids Res 30, 4607–4617.

Culvenor, J.G., Day, K.P., Anders, R.F., 1991. Plasmodium falciparum ring-infected erythrocyte surface antigen is released from merozoite dense granules after erythrocyte invasion. Infect Immun 59, 1183–1187.

Currà, C., Pace, T., Franke-Fayard, B.M.D., Picci, L., Bertuccini, L., Ponzi, M., 2012. Erythrocyte Remodeling in Plasmodium berghei Infection: The Contribution of SEP Family Members. Traffic 13, 388–399. https://doi.org/10.1111/j.1600-0854.2011.01313.x.

Cygan, A.M., Beltran, P.M.J., Mendoza, A.G., Branon, T.C., Ting, A.Y., Carr, S.A., Boothroyd, J.C., Coyne, C.B., 2021. Proximity-Labeling Reveals Novel Host and Parasite Proteins at the Toxoplasma Parasitophorous Vacuole Membrane. https://doi.org/10.1128/mBio.

Cygan, A.M., Theisen, T.C., Mendoza, A.G., Marino, N.D., Panas, M.W., Boothroyd, J.C., 2020. Coimmunoprecipitation with MYR1 Identifies Three Additional Proteins

within the Toxoplasma gondii Parasitophorous Vacuole Required for Translocation of Dense Granule Effectors into Host Cells. mSphere 5. https://doi.org/10.1128/msphere.00858-19.

Das, A.K., Helps, N.R., Cohen, P.T., Barford, D., 1996. Crystal structure of the protein serine/threonine phosphatase 2C at 2.0 A resolution. EMBO J 15, 6798–6809.

Das, S., Lemgruber, L., Tay, C.L., Baum, J., Meissner, M., 2017. Multiple essential functions of Plasmodium falciparum actin-1 during malaria blood-stage development. BMC Biology 15. https://doi.org/10.1186/s12915-017-0406-2.

Francis, D. 1997. Hemoglobin Metabolism In The Malaria Parasite *Plasmodium falciparum*. Annual Review of Microbiology 97–123.

Davies, H., Belda, H., Broncel, M., Ye, X., Bisson, C., Introini, V., Dorin-Semblat, D., Semblat, J.P., Tibúrcio, M., Gamain, B., Kaforou, M., Treeck, M., 2020. An exported kinase family mediates species-specific erythrocyte remodelling and virulence in human malaria. Nature Microbiology 5, 848–863. https://doi.org/10.1038/s41564-020-0702-4.

Davis, T. M., Karunajeewa, H. A; Ilett, K. F. 2005. Artemisinin-based combination therapies for uncomplicated malaria. Med J Aust, 182, 181-5.

Davis, M.W., Jorgensen, E.M., 2022. ApE, A Plasmid Editor: A Freely Available DNA Manipulation and Visualization Program. Frontiers in Bioinformatics 2. https://doi.org/10.3389/fbinf.2022.818619.

de Koning-Ward, T.F., Dixon, M.W.A., Tilley, L., Gilson, P.R., 2016. Plasmodium species: master renovators of their host cells. Nat Rev Microbiol 14, 494–507. https://doi.org/10.1038/nrmicro.2016.79.

De Niz, M., Burda, P.-C., Kaiser, G., Del Portillo, H.A., Spielmann, T., Frischknecht, F., Heussler, V.T., 2017. Progress in imaging methods: insights gained into Plasmodium biology. Nat Rev Microbiol 15, 37–54. https://doi.org/10.1038/nrmicro.2016.158.

Dearnley, M.K., Yeoman, J.A., Hanssen, E., Kenny, S., Turnbull, L., Whitchurch, C.B., Tilley, L., Dixon, M.W.A., 2012. Origin, composition, organization and function of the inner membrane complex of Plasmodium falciparum gametocytes. Journal of Cell Science 125, 2053–2063. https://doi.org/10.1242/jcs.099002.

Desai, S.A., 2022. Epigenetics of malaria parasite nutrient uptake, but why? Trends in Parasitology 38, 618–628.

Desai, S.A., 2012. Ion and nutrient uptake by malaria parasite-infected erythrocytes. Cell Microbiol 14, 1003–1009. https://doi.org/10.1111/j.1462-5822.2012.01790.x.

Desai, S.A., Krogstad, D.J., McCleskey, E.W., 1993. A nutrient-permeable channel on the intraerythrocytic malaria parasite. Nature 362, 643–646. https://doi.org/10.1038/362643a0.

Dobrescu, I., Hammam, E., Dziekan, J.M., Claës, A., Halby, L., Preiser, P., Bozdech, Z., Arimondo, P.B., Scherf, A., Nardella, F., 2023. Plasmodium falciparum Eukaryotic Translation Initiation Factor 3 is Stabilized by Quinazoline-Quinoline Bisubstrate Inhibitors. ACS Infectious Diseases 9, 1257–1266. https://doi.org/10.1021/acsinfecdis.3c00127.

Dondorp, A.M., Nosten, F., Yi, P., Das, D., Phyo, A.P., Tarning, J., Lwin, K.M., Ariey, F., Hanpithakpong, W., Lee, S.J., Ringwald, P., Silamut, K., Imwong, M., Chotivanich, K., Lim, P., Herdman, T., An, S.S., Yeung, S., Singhasivanon, P., Day, N.P.J., Lindegardh, N., Socheat, D., White, N.J., 2009. Artemisinin Resistance in Plasmodium falciparum Malaria. New England Journal of Medicine 361, 455–467. https://doi.org/10.1056/nejmoa0808859.

Draper, S.J., Sack, B.K., King, C.R., Nielsen, C.M., Rayner, J.C., Higgins, M.K., Long, C.A., Seder, R.A., 2018. Malaria Vaccines: Recent Advances and New Horizons. Cell Host Microbe 24, 43–56. https://doi.org/10.1016/j.chom.2018.06.008.

Duffy, P.E., Patrick Gorres, J., 2020. Malaria vaccines since 2000: progress, priorities, products. npj Vaccines 5, 1–9. https://doi.org/10.1038/s41541-020-0196-3.

Dvorin, J.D., Goldberg, D.E., 2022. Annual Review of Microbiology Plasmodium Egress Across the Parasite Life Cycle. https://doi.org/10.1146/annurev-micro-041320.

Dvorin, J.D., Martyn, D.C., Patel, S.D., Grimley, J.S., Collins, C.R., Hopp, C.S., Bright, A.T., Westenberger, S., Winzeler, E., Blackman, M.J., Baker, D.A., Wandless, T.J., Duraisingh, M.T., 2010. A plant-like kinase in plasmodium falciparum regulates parasite egress from erythrocytes. Science 328, 910–912. https://doi.org/10.1126/science.1188191.

Eastman, R.T., Fidock, D.A., 2009. Artemisinin-based combination therapies: a vital tool in efforts to eliminate malaria. Nat Rev Microbiol 7, 864–874. https://doi.org/10.1038/nrmicro2239

Egan, T.J., 2008. Haemozoin formation. Molecular and Biochemical Parasitology 127–136.

Elaagip, A., Absalon, S., Florentin, A., 2022. Apicoplast Dynamics During Plasmodium Cell Cycle. Front Cell Infect Microbiol 12, 864819. https://doi.org/10.3389/fcimb.2022.864819.

Elmendorf, H.G., Haldar, K., 1994. Plasmodium falciparum exports the Golgi marker sphingomyelin synthase into a tubovesicular network in the cytoplasm of mature erythrocytes. J Cell Biol 124, 449–462. https://doi.org/10.1083/jcb.124.4.449.

Elsworth, B., Matthews, K., Nie, C.Q., Kalanon, M., Charnaud, S.C., Sanders, P.R., Chisholm, S.A., Counihan, N.A., Shaw, P.J., Pino, P., Chan, J.A., Azevedo, M.F., Rogerson, S.J., Beeson, J.G., Crabb, B.S., Gilson, P.R., Koning-Ward, T.F.D., 2014. PTEX is an essential nexus for protein export in malaria parasites. Nature 511, 587–591. https://doi.org/10.1038/nature13555.

Elsworth, B., Sanders, P.R., Nebl, T., Batinovic, S., Kalanon, M., Nie, C.Q., Charnaud, S.C., Bullen, H.E., Ward, T.F. de K., Tilley, L., Crabb, B.S., Gilson, P.R., 2016. Proteomic analysis reveals novel proteins associated with the Plasmodium protein exporter PTEX and a loss of complex stability upon truncation of the core PTEX component, PTEX150. Cellular Microbiology 18, 1551–1569. https://doi.org/10.1111/cmi.12596.

Epstein, J.E., Paolino, K.M., Richie, T.L., Sedegah, M., Singer, A., Ruben, A.J., Chakravarty, S., Stafford, A., Ruck, R.C., Eappen, A.G., Li, T., Billingsley, P.F., Manoj, A., Silva, J.C., Moser, K., Nielsen, R., Tosh, D., Cicatelli, S., Ganeshan, H., Case, J., Padilla, D., Davidson, S., Garver, L., Saverino, E., Murshedkar, T., Gunasekera, A., Twomey, P.S., Reyes, S., Moon, J.E., James, E.R., Natasha, K.C., Li, M., Abot, E., Belmonte, A., Hauns, K., Belmonte, M., Huang, J., Vasquez, C., Remich, S., Carrington, M., Abebe, Y., Tillman, A., Hickey, B., Regules, J., Villasante, E., Sim, B.K.L., Hoffman, S.L., 2017. Protection against Plasmodium falciparum malaria by PfSPZ Vaccine. JCI Insight 2. https://doi.org/10.1172/jci.insight.89154.

Ferreira, J.L., Heincke, D., Wichers, J.S., Liffner, B., Wilson, D.W., Gilberger, T.-W., 2020. The Dynamic Roles of the Inner Membrane Complex in the Multiple Stages of the Malaria Parasite. Front Cell Infect Microbiol 10, 611801. https://doi.org/10.3389/fcimb.2020.611801.

Fichera, M.E., Roos, D.S., 1997. A plastid organelle as a drug target in apicomplexan parasites. Nature 390, 407–409. https://doi.org/10.1038/37132.

Fierro, M.A., Muheljic, A., Sha, J., Wohlschlegel, J.A., Beck, J.R., 2023. PEXEL is a proteolytic maturation site for both exported and non-exported Plasmodium proteins. bioRxiv 2023.07.12.548774. https://doi.org/10.1101/2023.07.12.548774.

Fischer, K., Marti, T., Rick, B., Johnson, D., Benting, J., Baumeister, S., Helmbrecht, C., Lanzer, M., Lingelbach, K., 1998. Characterization and cloning of the gene encoding the vacuolar membrane protein EXP-2 from Plasmodium falciparum. Mol Biochem Parasitol 92, 47–57. https://doi.org/10.1016/s0166-6851(97)00224-7.

Foth, B.J., McFadden, G.I., 2003. The apicoplast: a plastid in Plasmodium falciparum and other Apicomplexan parasites. Int Rev Cytol 224, 57–110. https://doi.org/10.1016/s0074-7696(05)24003-2.

Francia, M.E., Striepen, B., 2014. Cell division in apicomplexan parasites. Nat Rev Microbiol 12, 125–136. https://doi.org/10.1038/nrmicro3184.

Frénal, K., Polonais, V., Marq, J.B., Stratmann, R., Limenitakis, J., Soldati-Favre, D., 2010. Functional dissection of the apicomplexan glideosome molecular architecture. Cell Host and Microbe 8, 343–357. https://doi.org/10.1016/j.chom.2010.09.002.

Fréville, A., Gnangnon, B., Khelifa, A.S., Gissot, M., Khalife, J., Pierrot, C., 2022. Deciphering the Role of Protein Phosphatases in Apicomplexa: The Future of Innovative Therapeutics? Microorganisms 10, 585. https://doi.org/10.3390/microorganisms10030585.

Frischknecht, F., Matuschewski, K., 2017. Plasmodium sporozoite biology. Cold Spring Harbor Perspectives in Medicine 7. https://doi.org/10.1101/cshperspect.a025478.

Gabaldón, T., 2010. Peroxisome diversity and evolution. Philosophical Transactions of the Royal Society B: Biological Sciences 365, 765. https://doi.org/10.1098/rstb.2009.0240.

Galaway, F., Drought, L.G., Fala, M., Cross, N., Kemp, A.C., Rayner, J.C., Wright, G.J., 2017. P113 is a merozoite surface protein that binds the N terminus of Plasmodium falciparum RH5. Nature Communications 8. https://doi.org/10.1038/ncomms14333.

Gallego, M., Virshup, D.M., 2005. Protein serine/threonine phosphatases: life, death, and sleeping. Curr Opin Cell Biol 17, 197–202. https://doi.org/10.1016/j.ceb.2005.01.002.

Gardner, M.J., Hall, N., Fung, E., White, O., Berriman, M., Hyman, R.W., Carlton, J.M., Pain, A., Nelson, K.E., Bowman, S., Paulsen, I.T., James, K., Eisen, J.A., Rutherford, K., Salzberg, S.L., Craig, A., Kyes, S., Chan, M.S., Nene, V., Shallom, S.J., Suh, B., Peterson, J., Angiuoli, S., Pertea, M., Allen, J., Selengut, J., Haft, D., Mather, M.W., Vaidya, A.B., Martin, D.M.A., Fairlamb, A.H., Fraunholz, M.J., Roos, D.S., Ralph, S.A., McFadden, G.I., Cummings, L.M., Subramanian, G.M., Mungall, C., Venter, J.C., Carucci, D.J., Hoffman, S.L., Davis, R.W., Fraser, C.M., Barrell, B., 2002. Genome sequence of the human malaria parasite Plasmodium falciparum. Nature 419, 498–511. https://doi.org/10.1038/nature01097.

Garrido-Cardenas, J.A., González-Cerón, L., Manzano-Agugliaro, F., Mesa-Valle, C., 2019. Plasmodium genomics: an approach for learning about and ending human malaria. Parasitology Research 118, 1–27. https://doi.org/10.1007/s00436-018-6127-9.

Garten, M., Beck, J.R., Roth, R., Tenkova-Heuser, T., Heuser, J., Istvan, E.S., Bleck, C.K.E., Goldberg, D.E., Zimmerberg, J., 2020. Contacting domains segregate a lipid transporter from a solute transporter in the malarial host–parasite interface. Nature Communications 11. https://doi.org/10.1038/s41467-020-17506-9.

Garten, M., Nasamu, A.S., Niles, J.C., Zimmerberg, J., Goldberg, D.E., Beck, J.R., 2018. EXP2 is a nutrient-permeable channel in the vacuolar membrane of Plasmodium and is essential for protein export via PTEX. Nat Microbiol 3, 1090–1098. https://doi.org/10.1038/s41564-018-0222-7.

Gaskins, E., Gilk, S., DeVore, N., Mann, T., Ward, G., Beckers, C., 2004. Identification of the membrane receptor of a class XIV myosin in Toxoplasma gondii. Journal of Cell Biology 165, 383–393. https://doi.org/10.1083/jcb.200311137.

Geiger, M., Brown, C., Wichers, J.S., Strauss, J., Lill, A., Thuenauer, R., Liffner, B., Wilcke, L., Lemcke, S., Heincke, D., Pazicky, S., Bachmann, A., Löw, C., Wilson, D.W., Filarsky, M., Burda, P.C., Zhang, K., Junop, M., Gilberger, T.W., 2020. Structural Insights Into PfARO and Characterization of its Interaction With PfAIP. Journal of Molecular Biology 432, 878–896. https://doi.org/10.1016/j.jmb.2019.12.024.

Gibson, D.G., Young, L., Chuang, R.Y., Venter, J.C., Hutchison, C.A., Smith, H.O., 2009. Enzymatic assembly of DNA molecules up to several hundred kilobases. Nature Methods 6, 343–345. https://doi.org/10.1038/nmeth.1318.

Ginsburg, H., Krugliak, M., Eidelman, O., Cabantchik, Z.I., 1983. New permeability pathways induced in membranes of Plasmodium falciparum infected erythrocytes. Mol Biochem Parasitol 8, 177–190. https://doi.org/10.1016/0166-6851(83)90008-7.

Gold, D.A., Kaplan, A.D., Lis, A., Bett, G.C.L., Rosowski, E.E., Cirelli, K.M., Bougdour, A., Sidik, S.M., Beck, J.R., Lourido, S., Egea, P.F., Bradley, P.J., Hakimi, M.A., Rasmusson, R.L., Saeij, J.P.J., 2015. The Toxoplasma dense granule proteins GRA17 and GRA23 mediate the movement of small molecules between the host and the parasitophorous vacuole. Cell Host and Microbe 17, 642–652. https://doi.org/10.1016/j.chom.2015.04.003.

Goldberg, D.E., Zimmerberg, J., 2020. Hardly Vacuous: The Parasitophorous Vacuolar Membrane of Malaria Parasites. Trends Parasitol 36, 138–146. https://doi.org/10.1016/j.pt.2019.11.006.

Greenwood, B.M., Fidock, D.A., Kyle, D.E., Kappe, S.H.I., Alonso, P.L., Collins, F.H., Duffy, P.E., 2008. Malaria: progress, perils, and prospects for eradication. J Clin Invest 118, 1266–1276. https://doi.org/10.1172/JCI33996

Grüring, C., Heiber, A., Kruse, F., Flemming, S., Franci, G., Colombo, S.F., Fasana, E., Schoeler, H., Borgese, N., Stunnenberg, H.G., Przyborski, J.M., Gilberger, T.W., Spielmann, T., 2012. Uncovering common principles in protein export of malaria parasites. Cell Host and Microbe 12, 717–729. https://doi.org/10.1016/j.chom.2012.09.010

Grüring, C., Heiber, A., Kruse, F., Ungefehr, J., Gilberger, T.W., Spielmann, T., 2011. Development and host cell modifications of Plasmodium falciparum blood stages in four dimensions. Nature Communications 2. https://doi.org/10.1038/ncomms1169

Grüring, C., Spielmann, T., 2012. Imaging of live malaria blood stage parasites, in: Methods in Enzymology. Academic Press Inc., pp. 81–92. https://doi.org/10.1016/B978-0-12-391856-7.00029-9

Gubbels, M.-J., Coppens, I., Zarringhalam, K., Duraisingh, M.T., Engelberg, K., 2021. The Modular Circuitry of Apicomplexan Cell Division Plasticity. Front Cell Infect Microbiol 11, 670049. https://doi.org/10.3389/fcimb.2021.670049.

Guddat, L.W., McAlpine, A.S., Hume, D., Hamilton, S., de Jersey, J., Martin, J.L., 1999. Crystal structure of mammalian purple acid phosphatase. Structure 7, 757–767. https://doi.org/10.1016/s0969-2126(99)80100-2

Gupta, A., Balabaskaran-Nina, P., Nguitragool, W., Saggu, G.S., Schureck, M.A., Desai, S.A., 2018. CLAG3 self-associates in malaria parasites and quantitatively determines nutrient uptake channels at the host Membrane. mBio 9. https://doi.org/10.1128/mBio.02293-17.

Haldar, K., 1998. Intracellular trafficking in Plasmodium-infected erythrocytes. Curr Opin Microbiol 1, 466–471. https://doi.org/10.1016/s1369-5274(98)80067-2.

Hale, V.L., Watermeyer, J.M., Hackett, F., Vizcay-Barrena, G., Ooij, C.V., Thomas, J.A., Spink, M.C., Harkiolaki, M., Duke, E., Fleck, R.A., Blackman, M.J., Saibil, H.R., 2017. Parasitophorous vacuole poration precedes its rupture and rapid host erythrocyte cytoskeleton collapse in Plasmodium falciparum egress. Proceedings of the National Academy of Sciences of the United States of America 114, 3439–3444. https://doi.org/10.1073/pnas.1619441114.

Hallée, S., Thériault, C., Gagnon, D., Kehrer, J., Frischknecht, F., Mair, G.R., Richard, D., 2018. Identification of a Golgi apparatus protein complex important for the asexual erythrocytic cycle of the malaria parasite Plasmodium falciparum. Cellular Microbiology 20. https://doi.org/10.1111/cmi.12843.

Hanboonkunupakarn, B., Pluijm, R.W.V.D., Hoglund, R., Pukrittayakamee, S., Winterberg, M., Mukaka, M., Waithira, N., Chotivanich, K., Singhasivanon, P., White, N.J., Dondorp, A.M., Tarning, J., Jittamala, P., 2019. Sequential open-label study of the safety, tolerability, and pharmacokinetic interactions between dihydroartemisinin-piperaquine and mefloquine in healthy Thai adults. Antimicrobial Agents and Chemotherapy 63. https://doi.org/10.1128/AAC.00060-19.

Hanboonkunupakarn, B., Tarning, J., Pukrittayakamee, S., Chotivanich, K., 2022. Artemisinin resistance and malaria elimination: Where are we now? Front Pharmacol 13, 876282. https://doi.org/10.3389/fphar.2022.876282.

Hanssen, E., Carlton, P., Deed, S., Klonis, N., Sedat, J., DeRisi, J., Tilley, L., 2010. Whole cell imaging reveals novel modular features of the exomembrane system of the malaria parasite, Plasmodium falciparum. International Journal for Parasitology 40, 123–134. https://doi.org/10.1016/j.ijpara.2009.09.004.

Hanssen, E., Dekiwadia, C., Riglar, D.T., Rug, M., Lemgruber, L., Cowman, A.F., Cyrklaff, M., Kudryashev, M., Frischknecht, F., Baum, J., Ralph, S.A., 2013. Electron tomography of Plasmodium falciparum merozoites reveals core cellular events that underpin erythrocyte invasion. Cellular Microbiology 15, 1457–1472. https://doi.org/10.1111/cmi.12132.

Hanssen, E., Goldie, K.N., Tilley, L., 2010. Ultrastructure of the asexual blood stages of Plasmodium falciparum. Methods Cell Biol 96, 93–116. https://doi.org/10.1016/S0091-679X(10)96005-6.

Harding, C.R., Meissner, M., 2014. The inner membrane complex through development of Toxoplasma gondii and Plasmodium. Cell Microbiol 16, 632–641. https://doi.org/10.1111/cmi.12285.

Hawthorne, P.L., Trenholme, K.R., Skinner-Adams, T.S., Spielmann, T., Fischer, K., Dixon, M.W.A., Ortega, M.R., Anderson, K.L., Kemp, D.J., Gardiner, D.L., 2004. A novel Plasmodium falciparum ring stage protein, REX, is located in Maurer's clefts. Molecular and Biochemical Parasitology 136, 181–189. https://doi.org/10.1016/j.molbiopara.2004.03.013.

Healer, J., Thompson, J.K., Mackwell, K.L., Browne, C.D., Seager, B.A., Ngo, A., Lowes, K.N., Silk, S.E., Pulido, D., King, L.D.W., Christen, J.M., Noe, A.R., Kotraiah, V., Masendycz, P.J., Rajagopalan, R., Lucas, L., Stanford, M.M., Soisson, L., Diggs, C., Miller, R., Youll, S., Wycherley, K., Draper, S.J., Cowman, A.F., 2022. RH5.1-CyRPA-Ripr antigen combination vaccine shows little improvement over RH5.1 in a preclinical setting. Frontiers in Cellular and Infection Microbiology 12. https://doi.org/10.3389/fcimb.2022.1049065.

Heiber, A., Kruse, F., Pick, C., Grüring, C., Flemming, S., Oberli, A., Schoeler, H., Retzlaff, S., Mesén-Ramírez, P., Hiss, J.A., Kadekoppala, M., Hecht, L., Holder, A.A., Gilberger, T.W., Spielmann, T., 2013. Identification of New PNEPs Indicates a Substantial Non-PEXEL Exportome and Underpins Common Features in Plasmodium falciparum Protein Export. PLoS Pathogens 9. https://doi.org/10.1371/journal.ppat.1003546.

Hill, R.J., Ringel, A., Knuepfer, E., Moon, R.W., Blackman, M.J., Ooij, C.V., 2016. Regulation and essentiality of the star-related lipid transfer (START) domain-containing phospholipid transfer protein pfa0210c in malaria parasites. Journal of Biological Chemistry 291, 24280–24292. https://doi.org/10.1074/jbc.M116.740506.

Hiller, N.L., Bhattacharjee, S., van Ooij, C., Liolios, K., Harrison, T., Lopez-Estraño, C., Haldar, K., 2004. A host-targeting signal in virulence proteins reveals a secretome in malarial infection. Science 306, 1934–1937. https://doi.org/10.1126/science.1102737.

Ho, C.M., Beck, J.R., Lai, M., Cui, Y., Goldberg, D.E., Egea, P.F., Zhou, Z.H., 2018. Malaria parasite translocon structure and mechanism of effector export. Nature 561, 70–75. https://doi.org/10.1038/s41586-018-0469-4.

Hoffman, S.L., Billingsley, P.F., James, E., Richman, A., Loyevsky, M., Li, T., Chakravarty, S., Gunasekera, A., Chattopadhyay, R., Li, M., Stafford, R., Ahumada, A., Epstein, J.E., Sedegah, M., Reyes, S., Richie, T.L., Lyke, K.E., Edelman, R., Laurens, M.B., Plowe, C.V., Sim, B.K.L., 2010. Development of a metabolically active, non-replicating sporozoite vaccine to prevent Plasmodium falciparum malaria. Hum Vaccin 6, 97–106. https://doi.org/10.4161/hv.6.1.10396.

Holder, A.A., 1994. Proteins on the surface of the malaria parasite and cell invasion. Parasitology 5–18.

Hu, G., Cabrera, A., Kono, M., Mok, S., Chaal, B.K., Haase, S., Engelberg, K., Cheemadan, S., Spielmann, T., Preiser, P.R., Gilberger, T.W., Bozdech, Z., 2010. Transcriptional profiling of growth perturbations of the human malaria parasite Plasmodium falciparum. Nature Biotechnology 28, 91–98. https://doi.org/10.1038/nbt.1597.

Huang, K.Y., Lee, T.Y., Kao, H.J., Ma, C.T., Lee, C.C., Lin, T.H., Chang, W.C., Huang, H.D., 2019. DbPTM in 2019: Exploring disease association and cross-Talk of post-Translational modifications. Nucleic Acids Research 47, D298–D308. https://doi.org/10.1093/nar/gky1074.

Hubbard, S.R., 2004. Juxtamembrane autoinhibition in receptor tyrosine kinases. Nat Rev Mol Cell Biol 5, 464–471. https://doi.org/10.1038/nrm1399

Hunter, T., 1995. Protein kinases and phosphatases: the yin and yang of protein phosphorylation and signaling. Cell 80, 225–236. https://doi.org/10.1016/0092-8674(95)90405-0

Huse, M., Kuriyan, J., 2002. The conformational plasticity of protein kinases. Cell 109, 275–282. https://doi.org/10.1016/s0092-8674(02)00741-9

Inoue, H., Nojima, H., Okayama, H., 1990. High efficiency transformation of Escherichia coli with plasmids. Gene 96, 23–28. https://doi.org/10.1016/0378-1119(90)90336-p.

Iriko, H., Ishino, T., Otsuki, H., Ito, D., Tachibana, M., Torii, M., Tsuboi, T., 2018. Plasmodium falciparum Exported Protein 1 is localized to dense granules in merozoites. Parasitology International 67, 637–639. https://doi.org/10.1016/j.parint.2018.06.001.

Ito, D., Kondo, Y., Takashima, E., Iriko, H., Thongkukiatkul, A., Torii, M., Otsuki, H., 2023. Roles of the RON3 C-terminal fragment in erythrocyte invasion and blood-stage parasite proliferation in Plasmodium falciparum. Frontiers in Cellular and Infection Microbiology 13. https://doi.org/10.3389/fcimb.2023.1197126

Ito, D., Schureck, M.A., Desai, S.A. 2017. An essential dual-function complex mediates erythrocyte invasion and channel-mediated nutrient uptake in malaria parasites. https://doi.org/10.7554/eLife.23485.001.

Jackson, K.E., Spielmann, T., Hanssen, E., Adisa, A., Separovic, F., Dixon, M.W.A., Trenholme, K.R., Hawthorne, P.L., Gardiner, D.L., Gilberger, T., Tilley, L., 2007. Selective permeabilization of the host cell membrane of Plasmodium falciparum-infected red blood cells with streptolysin O and equinatoxin II. Biochem J 403, 167–175. https://doi.org/10.1042/BJ20061725.

Jackson, R.J., Hellen, C.U.T., Pestova, T.V., 2010. The mechanism of eukaryotic translation initiation and principles of its regulation. Nat Rev Mol Cell Biol 11, 113–127. https://doi.org/10.1038/nrm2838.

Janouškovec, J., Horák, A., Oborník, M., Lukeš, J., Keeling, P.J., 2010. A common red algal origin of the apicomplexan, dinoflagellate, and heterokont plastids. Proceedings of the National Academy of Sciences of the United States of America 107, 10949–10954. https://doi.org/10.1073/pnas.1003335107.

Jin, J., Pawson, T., 2012. Modular evolution of phosphorylation-based signalling systems. Philos Trans R Soc Lond B Biol Sci 367, 2540–2555. https://doi.org/10.1098/rstb.2012.0106.

Jones, M.L., Kitson, E.L., Rayner, J.C., 2006. Plasmodium falciparum erythrocyte invasion: A conserved myosin associated complex. Molecular and Biochemical Parasitology 147, 74–84. https://doi.org/10.1016/j.molbiopara.2006.01.009

Jongo, S.A., Church, L.W.P., Mtoro, A.T., Schindler, T., Chakravarty, S., Ruben, A.J., Swanson, P.A., Kassim, K.R., Mpina, M., Tumbo, A.M., Milando, F.A., Qassim, M., Juma, O.A., Bakari, B.M., Simon, B., James, E.R., Abebe, Y., Natasha, K.C., Saverino, E., Fink, M., Cosi, G., Gondwe, L., Studer, F., Styers, D., Seder, R.A., Schindler, T., Billingsley, P.F., Daubenberger, C., Sim, B.K.L., Tanner, M., Richie, T.L., Abdulla, S., Hoffman, S.L., 2020. Increase of dose associated with decrease in protection against controlled human malaria infection by PfSPZ vaccine in Tanzanian Adults. Clinical Infectious Diseases 71, 2849–2857. https://doi.org/10.1093/cid/ciz1152.

Jonsdottir, T.K., Gabriela, M., Crabb, B.S., F de Koning-Ward, T., Gilson, P.R., 2021. Defining the Essential Exportome of the Malaria Parasite. Trends Parasitol 37, 664–675. https://doi.org/10.1016/j.pt.2021.04.009.

Jumper, J., Evans, R., Pritzel, A., Green, T., Figurnov, M., Ronneberger, O., Tunyasuvunakool, K., Bates, R., Žídek, A., Potapenko, A., Bridgland, A., Meyer, C., Kohl, S.A.A., Ballard, A.J., Cowie, A., Romera-Paredes, B., Nikolov, S., Jain, R., Adler, J., Back, T., Petersen, S., Reiman, D., Clancy, E., Zielinski, M., Steinegger, M., Pacholska, M., Berghammer, T., Bodenstein, S., Silver, D., Vinyals, O., Senior, A.W., Kavukcuoglu, K., Kohli, P., Hassabis, D., 2021. Highly accurate protein structure prediction with AlphaFold. Nature 596, 583–589. https://doi.org/10.1038/s41586-021-03819-2

Kaiser, K., Matuschewski, K., Camargo, N., Ross, J., Kappe, S.H.I., 2004. Differential transcriptome profiling identifies Plasmodium genes encoding pre-erythrocytic stage-specific proteins. Molecular Microbiology 1221–1232. https://doi.org/10.1046/j.1365-2958.2004.03909.x.

Kaneko, O., Lim, B.Y.S.Y., Iriko, H., Ling, I.T., Otsuki, H., Grainger, M., Tsuboi, T., Adams, J.H., Mattei, D., Holder, A.A., Torii, M., 2005. Apical expression of three RhopH1/Clag proteins as components of the Plasmodium falciparum RhopH complex. Molecular and Biochemical Parasitology 143, 20–28. https://doi.org/10.1016/j.molbiopara.2005.05.003.

Kara, U.A., Stenzel, D.J., Ingram, L.T., Bushell, G.R., Lopez, J.A., Kidson, C., 1988. Inhibitory monoclonal antibody against a (myristylated) small-molecular-weight antigen from Plasmodium falciparum associated with the parasitophorous vacuole membrane. Infect Immun 56, 903–909. https://doi.org/10.1128/iai.56.4.903-909.1988.

Kaur, C., Kumar, M., Patankar, S., 2020. Messenger RNAs with large numbers of upstream open reading frames are translated via leaky scanning and reinitiation in the asexual stages of Plasmodium falciparum. Parasitology 147, 1100–1113. https://doi.org/10.1017/S0031182020000840.

Kaushansky, A., Douglass, A.N., Arang, N., Vigdorovich, V., Dambrauskas, N., Kain, H.S., Austin, L.S., Sather, D.N., Kappe, S.H.I., 2015. Malaria parasites target the hepatocyte receptor EphA2 for successful host infection. Science 350, 1089–1092. https://doi.org/10.1126/science.aad3318.

Khosh-Naucke, M., Becker, J., Mesén-Ramírez, P., Kiani, P., Birnbaum, J., Fröhlke, U., Jonscher, E., Schlüter, H., Spielmann, T., 2018. Identification of novel parasitophorous vacuole proteins in P. falciparum parasites using BioID. International Journal of Medical Microbiology 308, 13–24. https://doi.org/10.1016/j.ijmm.2017.07.007.

Khosh-Naucke. 2018. Identification of novel parasitophorous vacuole proteins in P. falciparum parasites using BioID. University of Hamburg.

Kilian, N., Dittmer, M., Cyrklaff, M., Ouermi, D., Bisseye, C., Simpore, J., Frischknecht, F., Sanchez, C.P., Lanzer, M., 2013. Haemoglobin s and c affect the motion of maurer's clefts in plasmodium falciparum-infected erythrocytes. Cellular Microbiology 15, 1111–1126. https://doi.org/10.1111/cmi.12102

Kimmel, J., Kehrer, J., Frischknecht, F., Spielmann, T., 2022. Proximity-dependent biotinylation approaches to study apicomplexan biology. Mol Microbiol 117, 553–568. https://doi.org/10.1111/mmi.14815.

Kimmel, J., Schmitt, M., Sinner, A., Jansen, P.W.T.C., Mainye, S., Ramón-Zamorano, G., Toenhake, C.G., Wichers-Misterek, J.S., Cronshagen, J., Sabitzki, R., Mesén-Ramírez, P., Behrens, H.M., Bártfai, R., Spielmann, T., 2023. Gene-by-gene screen of the unknown proteins encoded on Plasmodium falciparum chromosome 3. Cell Syst 14, 9-23.e7. https://doi.org/10.1016/j.cels.2022.12.001.

Kirk, K., Saliba, K.J., 2007. Targeting nutrient uptake mechanisms in *Plasmodium*. Curr Drug Targets 8, 75–88. https://doi.org/10.2174/138945007779315560.

Kirk, K., Lehane, A.M., 2014. Membrane transport in the malaria parasite and its host erythrocyte. Biochem J 457, 1–18. https://doi.org/10.1042/BJ20131007.

Klee, C.B., Ren, H., Wang, X., 1998. Regulation of the calmodulin-stimulated protein phosphatase, calcineurin. J Biol Chem 273, 13367–13370. https://doi.org/10.1074/jbc.273.22.13367.

Kloprogge, F., McGready, R., Phyo, A.P., Rijken, M.J., Hanpithakpon, W., Than, H.H., Hlaing, N., Zin, N.T., Day, N.P.J., White, N.J., Nosten, F., Tarning, J., 2015. Opposite malaria and pregnancy effect on oral bioavailability of artesunate - A population pharmacokinetic evaluation. British Journal of Clinical Pharmacology 80, 642–653. https://doi.org/10.1111/bcp.12660.

Knuepfer, E., Rug, M., Klonis, N., Tilley, L., Cowman, A.F., 2005. Trafficking of the major virulence factor to the surface of transfected P falciparum-infected erythrocytes. Blood 105, 4078–4087. https://doi.org/10.1182/blood-2004-12-4666.

Koch, M., Baum, J., 2016. The mechanics of malaria parasite invasion of the human erythrocyte – towards a reassessment of the host cell contribution. Cell Microbiol 18, 319–329. https://doi.org/10.1111/cmi.12557.

Köhler, S., Delwiche, C.F., Denny, P.W., Tilney, L.G., Webster, P., Wilson, R.J.M., Palmer, J.D., Roos, D.S., 1997. A plastid of probable green algal origin in

Apicomplexan parasites. Science 275, 1485–1489. https://doi.org/10.1126/science.275.5305.1485.

Kojin, B.B., Adelman, Z.N., 2019. The sporozoite's journey through the mosquito: A critical examination of host and parasite factors required for salivary gland invasion. Frontiers in Ecology and Evolution 7. https://doi.org/10.3389/fevo.2019.00284.

Koning-Ward, T.F.D., Gilson, P.R., Boddey, J.A., Rug, M., Smith, B.J., Papenfuss, A.T., Sanders, P.R., Lundie, R.J., Maier, A.G., Cowman, A.F., Crabb, B.S., 2009. A newly discovered protein export machine in malaria parasites. Nature 459, 945–949. https://doi.org/10.1038/nature08104.

Kono, M., Herrmann, S., Loughran, N.B., Cabrera, A., Engelberg, K., Lehmann, C., Sinha, D., Prinz, B., Ruch, U., Heussler, V., Spielmann, T., Parkinson, J., Gilberger, T.W., 2012. Evolution and architecture of the inner membrane complex in asexual and sexual stages of the malaria parasite. Molecular Biology and Evolution 29, 2113–2132. https://doi.org/10.1093/molbev/mss081.

Koussis, K., Withers-Martinez, C., Yeoh, S., Child, M., Hackett, F., Knuepfer, E., Juliano, L., Woehlbier, U., Bujard, H., Blackman, M.J., 2009. A multifunctional serine protease primes the malaria parasite for red blood cell invasion. EMBO Journal 28, 725–735. https://doi.org/10.1038/emboj.2009.22.

Krebs, E.G., 1983. Historical perspectives on protein phosphorylation and a classification system for protein kinases. Philos Trans R Soc Lond B Biol Sci 302, 3–11. https://doi.org/10.1098/rstb.1983.0033

Kumar, T., Maitra, S., Rahman, A., Bhattacharjee, S., 2022. A conserved guided entry of tail-anchored pathway is involved in the trafficking of a subset of membrane proteins in Plasmodium falciparum. PLoS Pathogens 17. https://doi.org/10.1371/journal.ppat.1009595.

Kurtovic, L., Atre, T., Feng, G., Wines, B.D., Chan, J.A., Boyle, M.J., Drew, D.R., Hogarth, P.M., Fowkes, F.J.I., Bergmann-Leitner, E.S., Beeson, J.G., 2021. Multifunctional Antibodies Are Induced by the RTS,S Malaria Vaccine and Associated with Protection in a Phase 1/2a Trial, in: Journal of Infectious Diseases. Oxford University Press, pp. 1128–1138. https://doi.org/10.1093/infdis/jiaa144

Kutuzov, M.A., Andreeva, A.V., 2008. Protein Ser/Thr phosphatases of parasitic protozoa. Mol Biochem Parasitol 161, 81–90. https://doi.org/10.1016/j.molbiopara.2008.06.008.

Kutuzov, M.A., Andreeva, A.V., 2002. Protein Ser/Thr phosphatases with kelch-like repeat domains. Cell Signal 14, 745–750. https://doi.org/10.1016/s0898-6568(02)00018-9.

Langreth, S.G., Jensen, J.B., Reese, R.T., Trager, W., 1978. Fine structure of human malaria in vitro. J Protozool 25, 443–452. https://doi.org/10.1111/j.1550-7408.1978.tb04167.x.

Lambros, C., & Vanderberg, J. P. 1979. Synchronization of Plasmodium falciparum erythrocytic stages in culture. *J Parasitol*, *65*(3), 418-420. https://www.ncbi.nlm.nih.gov/pubmed/383936.

Lanzer, M., Wickert, H., Krohne, G., Vincensini, L., Braun Breton, C., 2006. Maurer's clefts: a novel multi-functional organelle in the cytoplasm of Plasmodium falciparum-infected erythrocytes. Int J Parasitol 36, 23–36. https://doi.org/10.1016/j.ijpara.2005.10.001.

Lauer, S., VanWye, J., Harrison, T., McManus, H., Samuel, B.U., Hiller, N.L., Mohandas, N., Haldar, K., 2000. Vacuolar uptake of host components, and a role for cholesterol and sphingomyelin in malarial infection. EMBO J 19, 3556–3564. https://doi.org/10.1093/emboj/19.14.3556.

Lauer, S.A., Rathod, P.K., Ghori, N., Haldar, K., 1997. A membrane network for nutrient import in red cells infected with the malaria parasite. Science 276, 1122–1125. https://doi.org/10.1126/science.276.5315.1122.

Le Roch, K.G., Zhou, Y., Blair, P.L., Grainger, M., Moch, J.K., Haynes, J.D., De La Vega, P., Holder, A.A., Batalov, S., Carucci, D.J., Winzeler, E.A., 2003. Discovery of gene function by expression profiling of the malaria parasite life cycle. Science 301, 1503–1508. https://doi.org/10.1126/science.1087025

Leech, J.H., Barnwell, J.W., Aikawa, M., Miller, L.H., Howard, R.J., 1984. Plasmodium falciparum malaria: association of knobs on the surface of infected erythrocytes with a histidine-rich protein and the erythrocyte skeleton. J Cell Biol 98, 1256–1264. https://doi.org/10.1083/jcb.98.4.1256

Li, D., Zhu, H., Liu, K., Liu, X., Leggewie, G., Udvardi, M., Wang, D., 2002. Purple acid phosphatases of Arabidopsis thaliana. Comparative analysis and differential regulation by phosphate deprivation. Journal of Biological Chemistry 277, 27772–27781. https://doi.org/10.1074/jbc.M204183200.

Li, J.L., Baker, D.A., 1998. A putative protein serine/threonine phosphatase from Plasmodium falciparum contains a large N-terminal extension and five unique inserts in the catalytic domain. Mol Biochem Parasitol 95, 287–295. https://doi.org/10.1016/s0166-6851(98)00106-6.

Liffner, B., Frölich, S., Heinemann, G.K., Liu, B., Ralph, S.A., Dixon, M.W.A., Gilberger, T.W., Wilson, D.W., 2020. PfCERLI1 is a conserved rhoptry associated protein essential for Plasmodium falciparum merozoite invasion of erythrocytes. Nature Communications 11. https://doi.org/10.1038/s41467-020-15127-w

Lingelbach, K., Joiner, K.A., 1998. The parasitophorous vacuole membrane surrounding Plasmodium and Toxoplasma: an unusual compartment in infected cells. J Cell Sci 111 (Pt 11), 1467–1475. https://doi.org/10.1242/jcs.111.11.1467

Lord, S.J., Velle, K.B., Mullins, R.D., Fritz-Laylin, L.K., 2020. SuperPlots: Communicating reproducibility and variability in cell biology. J Cell Biol 219, e202001064. https://doi.org/10.1083/jcb.202001064.

Mackellar, D.C., Vaughan, A.M., Aly, A.S.I., Deleon, S., Kappe, S.H.I., 2011. A systematic analysis of the early transcribed membrane protein family throughout the life cycle of Plasmodium yoelii. Cellular Microbiology 13, 1755–1767. https://doi.org/10.1111/j.1462-5822.2011.01656.x.

Maier, A.G., Rug, M., O'neill, M.T., Beeson, J.G., Marti, M., Reeder, J., Cowman, A.F., 2007. Skeleton-binding protein 1 functions at the parasitophorous vacuole membrane to traffic PfEMP1 to the Plasmodium falciparum-infected erythrocyte surface 109, 1289–1297. https://doi.org/10.1182/blood-2006.

Maier, A.G., Rug, M., O'Neill, M.T., Brown, M., Chakravorty, S., Szestak, T., Chesson, J., Wu, Y., Hughes, K., Coppel, R.L., Newbold, C., Beeson, J.G., Craig, A., Crabb, B.S., Cowman, A.F., 2008. Exported Proteins Required for Virulence and Rigidity of Plasmodium falciparum-Infected Human Erythrocytes. Cell 134, 48–61. https://doi.org/10.1016/j.cell.2008.04.051.

Manning, G., Whyte, D.B., Martinez, R., Hunter, T., Sudarsanam, S., 2002. The protein kinase complement of the human genome. Science 298, 1912–1934. https://doi.org/10.1126/science.1075762.

Marapana, D.S., Dagley, L.F., Sandow, J.J., Nebl, T., Triglia, T., Pasternak, M., Dickerman, B.K., Crabb, B.S., Gilson, P.R., Webb, A.I., Boddey, J.A., Cowman, A.F., 2018. Plasmepsin V cleaves malaria effector proteins in a distinct endoplasmic reticulum translocation interactome for export to the erythrocyte. Nature Microbiology 3, 1010–1022. https://doi.org/10.1038/s41564-018-0219-2.

Marchetti, R.V., Lehane, A.M., Shafik, S.H., Winterberg, M., Martin, R.E., Kirk, K., 2015. A lactate and formate transporter in the intraerythrocytic malaria parasite, Plasmodium falciparum. Nature Communications 6. https://doi.org/10.1038/ncomms7721.

Marin-Mogollon, C., van de Vegte-Bolmer, M., van Gemert, G.-J., van Pul, F.J.A., Ramesar, J., Othman, A.S., Kroeze, H., Miao, J., Cui, L., Williamson, K.C., Sauerwein, R.W., Janse, C.J., Khan, S.M., 2018. The Plasmodium falciparum male gametocyte protein P230p, a paralog of P230, is vital for ookinete formation and mosquito transmission. Sci Rep 8, 14902. https://doi.org/10.1038/s41598-018-33236-x

Marreiros, I.M., Marques, S., Parreira, A., Mastrodomenico, V., Mounce, B.C., Harris, C.T., Kafsack, B.F., Billker, O., Zuzarte-Luís, V., Mota, M.M., 2023. A non-canonical sensing pathway mediates Plasmodium adaptation to amino acid deficiency. Communications Biology 6. https://doi.org/10.1038/s42003-023-04566-y

Marti, M., Baum, J., Rug, M., Tilley, L., Cowman, A.F., 2005. Signal-mediated export of proteins from the malaria parasite to the host erythrocyte. J Cell Biol 171, 587–592. https://doi.org/10.1083/jcb.200508051.

Marti, M., Good, R.T., Rug, M., Knuepfer, E., Cowman, A.F., 2004. Targeting malaria virulence and remodeling proteins to the host erythrocyte. Science 306, 1930–1933. https://doi.org/10.1126/science.1102452.

Marti, M., Spielmann, T., 2013. Protein export in malaria parasites: many membranes to cross. Curr Opin Microbiol 16, 445–451. https://doi.org/10.1016/j.mib.2013.04.010.

Matthews, K., Kalanon, M., Chisholm, S.A., Sturm, A., Goodman, C.D., Dixon, M.W.A., Sanders, P.R., Nebl, T., Fraser, F., Haase, S., Mcfadden, G.I., Gilson, P.R., Crabb, B.S., Koning-Ward, T.F.D., 2013. The Plasmodium translocon of exported proteins (PTEX) component thioredoxin-2 is important for maintaining normal blood-stage growth. Molecular Microbiology 89, 1167–1186. https://doi.org/10.1111/mmi.12334.

Matthews, K.M., Pitman, E.L., de Koning-Ward, T.F., 2019. Illuminating how malaria parasites export proteins into host erythrocytes. Cell Microbiol 21, e13009. https://doi.org/10.1111/cmi.13009.

Matuschewski, K., Nunes, A.C., Nussenzweig, V., Ménard, R., 2002a. Plasmodium sporozoite invasion into insect and mammalian cells is directed by the same dual binding system. EMBO J 21, 1597–1606. https://doi.org/10.1093/emboj/21.7.1597.

Matuschewski, K., Ross, J., Brown, S.M., Kaiser, K., Nussenzweig, V., Kappe, S.H.I., 2002b. Infectivity-associated changes in the transcriptional repertoire of the malaria parasite sporozoite stage. Journal of Biological Chemistry 277, 41948–41953. https://doi.org/10.1074/jbc.M207315200.

Matz, J.M., Beck, J.R., Blackman, M.J., 2020. The parasitophorous vacuole of the blood-stage malaria parasite. Nat Rev Microbiol 18, 379–391. https://doi.org/10.1038/s41579-019-0321-3

Matz, J.M., Matuschewski, K., 2018. An in silico down-scaling approach uncovers novel constituents of the Plasmodium-containing vacuole. Scientific Reports 8. https://doi.org/10.1038/s41598-018-32471-6

McFadden, G.I., Yeh, E., 2017. The apicoplast: now you see it, now you don't. Int J Parasitol 47, 137–144. https://doi.org/10.1016/j.ijpara.2016.08.005.

McHugh, E., Batinovic, S., Hanssen, E., Mcmillan, P.J., Kenny, S., Griffin, M.D.W., Crawford, S., Trenholme, K.R., Gardiner, D.L., Dixon, M.W.A., Tilley, L., 2015. A repeat sequence domain of the ring-exported protein-1 of Plasmodium falciparum controls export machinery architecture and virulence protein trafficking. Molecular Microbiology 98, 1101–1114. https://doi.org/10.1111/mmi.13201.

Meng, T.C., Lin, M.F., 1998. Tyrosine phosphorylation of c-ErbB-2 is regulated by the cellular form of prostatic acid phosphatase in human prostate cancer cells. J Biol Chem 273, 22096–22104. https://doi.org/10.1074/jbc.273.34.22096.

Mesén-Ramírez, P., Bergmann, B., Elhabiri, M., Zhu, L., Thien, H. von, Castro-Peña, C., Gilberger, T.W., Davioud-Charvet, E., Bozdech, Z., Bachmann, A., Spielmann, T., 2021. The parasitophorous vacuole nutrient channel is critical for drug access in malaria parasites and modulates the artemisinin resistance fitness cost. Cell Host and Microbe 29, 1774-1787.e9. https://doi.org/10.1016/j.chom.2021.11.002.

Mesén-Ramírez, P., Bergmann, B., Tran, T.T., Garten, M., Stäcker, J., Naranjo-Prado, I., Höhn, K., Zimmerberg, J., Spielmann, T., 2019. EXP1 is critical for nutrient uptake

across the parasitophorous vacuole membrane of malaria parasites. PLoS Biology 17. https://doi.org/10.1371/journal.pbio.3000473.

Mesén-Ramírez, P., Reinsch, F., Soares, A.B., Bergmann, B., Ullrich, A.K., Tenzer, S., Spielmann, T., 2016. Stable Translocation Intermediates Jam Global Protein Export in Plasmodium falciparum Parasites and Link the PTEX Component EXP2 with Translocation Activity. PLoS Pathogens 12. https://doi.org/10.1371/journal.ppat.1005618.

Monerri, N.C.S.D., Flynn, H.R., Campos, M.G., Hackett, F., Koussis, K., Withers-Martinez, C., Skehel, J.M., Blackman, M.J., 2011. Global identification of multiple substrates for Plasmodium falciparum SUB1, an essential malarial processing protease. Infection and Immunity 79, 1086–1097. https://doi.org/10.1128/IAI.00902-10.

Moorhead, G.B.G., De Wever, V., Templeton, G., Kerk, D., 2009. Evolution of protein phosphatases in plants and animals. Biochem J 417, 401–409. https://doi.org/10.1042/BJ20081986.

Moris, P., Jongert, E., van der Most, R.G., 2018. Characterization of T-cell immune responses in clinical trials of the candidate RTS,S malaria vaccine. Hum Vaccin Immunother 14, 17–27. https://doi.org/10.1080/21645515.2017.1381809.

Morita, M., Nagaoka, H., Ntege, E.H., Kanoi, B.N., Ito, D., Nakata, T., Lee, J.W., Tokunaga, K., Iimura, T., Torii, M., Tsuboi, T., Takashima, E., 2018. PV1, a novel Plasmodium falciparum merozoite dense granule protein, interacts with exported protein in infected erythrocytes. Scientific Reports 8. https://doi.org/10.1038/s41598-018-22026-0.

Morrissette, N.S., Sibley, L.D., 2002. Cytoskeleton of Apicomplexan Parasites. Microbiology and Molecular Biology Reviews 66, 21–38. https://doi.org/10.1128/mmbr.66.1.21-38.2002.

Mota, M.M., Hafalla, J.C.R., Rodriguez, A., 2002. Migration through host cells activates Plasmodium sporozoites for infection. Nat Med 8, 1318–1322. https://doi.org/10.1038/nm785.

Mueller, A.-K., Camargo, N., Kaiser, K., Andorfer, C., Frevert, U., Matuschewski, K., Kappe, S.H.I., 2005. Plasmodium liver stage developmental arrest by depletion of a protein at the parasite-host interface. Proc Natl Acad Sci U S A 102, 3022–3027. https://doi.org/10.1073/pnas.0408442102.

Müller 0, 2011a. Malaria in Africa: Challenges for Control and Elimination in the 21 st Century.

Mundwiler-Pachlatko, E., Beck, H.-P., 2013. Maurer's clefts, the enigma of Plasmodium falciparum. Proc Natl Acad Sci U S A 110, 19987–19994. https://doi.org/10.1073/pnas.1309247110

Ndwiga, L., Osoti, V., Ochwedo, K.O., Wamae, K., Bejon, P., Rayner, J.C., Githinji, G., Ochola-Oyier, L.I., 2021. The Plasmodium falciparum Rh5 invasion protein complex

reveals an excess of rare variant mutations. Malaria Journal 20. https://doi.org/10.1186/s12936-021-03815-x.

Naranjo Prado, I. 2020. Quest for factors involved in the extraction of transmembrane proteins from the PPM to the PVM and the effect of jamming PTEX on PfEMP1 export in Plasmodium falciparum. University of Hamburg.

Nessel, T., Beck, J.M., Rayatpisheh, S., Jami-Alahmadi, Y., Wohlschlegel, J.A., Goldberg, D.E., Beck, J.R., 2020. EXP1 is required for organisation of EXP2 in the intraerythrocytic malaria parasite vacuole. Cellular Microbiology 22. https://doi.org/10.1111/cmi.13168

Nguitragool, W., Bokhari, A.A.B., Pillai, A.D., Rayavara, K., Sharma, P., Turpin, B., Aravind, L., Desai, S.A., 2011. Malaria parasite clag3 genes determine channel-mediated nutrient uptake by infected red blood cells. Cell 145, 665–677. https://doi.org/10.1016/j.cell.2011.05.002

Nussenzweig, V.N.R., 1984. Development of sporozoite vaccines. Philos Trans R Soc Lond B Biol Sci . 307, 117–128.

Nyboer, B., Heiss, K., Mueller, A.-K., Ingmundson, A., 2018. The Plasmodium liver-stage parasitophorous vacuole: A front-line of communication between parasite and host. Int J Med Microbiol 308, 107–117. https://doi.org/10.1016/j.ijmm.2017.09.008

O'Donnell, R.A., Saul, A., Cowman, A.F., Crabb, B.S., 2000. Functional conservation of the malaria vaccine antigen MSP-119across distantly related Plasmodium species. Nat Med 6, 91–95. https://doi.org/10.1038/71595

Ooij, C.V., Withers-Martinez, C., Ringel, A., Cockcroft, S., Haldar, K., Blackman, M.J., 2013. Identification of a plasmodium falciparum phospholipid transfer protein. Journal of Biological Chemistry 288, 31971–31983. https://doi.org/10.1074/jbc.M113.474189

Otto, T.D., Böhme, U., Jackson, A.P., Hunt, M., Franke-Fayard, B., Hoeijmakers, W.A.M., Religa, A.A., Robertson, L., Sanders, M., Ogun, S.A., Cunningham, D., Erhart, A., Billker, O., Khan, S.M., Stunnenberg, H.G., Langhorne, J., Holder, A.A., Waters, A.P., Newbold, C.I., Pain, A., Berriman, M., Janse, C.J., 2014. A comprehensive evaluation of rodent malaria parasite genomes and gene expression. BMC Medicine 12. https://doi.org/10.1186/s12915-014-0086-0.

Otto, T.D., Wilinski, D., Assefa, S., Keane, T.M., Sarry, L.R., Böhme, U., Lemieux, J., Barrell, B., Pain, A., Berriman, M., Newbold, C., Llinás, M., 2010. New insights into the blood-stage transcriptome of Plasmodium falciparum using RNA-Seq. Molecular Microbiology 76, 12–24. https://doi.org/10.1111/j.1365-2958.2009.07026.x.

Pachlatko, E., Rusch, S., Müller, A., Hemphill, A., Tilley, L., Hanssen, E., Beck, H.P., 2010. MAHRP2, an exported protein of Plasmodium falciparum, is an essential component of Maurer's cleft tethers. Molecular Microbiology 77, 1136–1152. https://doi.org/10.1111/j.1365-2958.2010.07278.x

Pandey, R., Mohmmed, A., Pierrot, C., Khalife, J., Malhotra, P., Gupta, D., 2014. Genome wide in silico analysis of Plasmodium falciparum phosphatome. BMC Genomics 15. https://doi.org/10.1186/1471-2164-15-1024.

Patel, A., Perrin, A.J., Flynn, H.R., Bisson, C., Withers-Martinez, C., Treeck, M., Flueck, C., Nicastro, G., Martin, S.R., Ramos, A., Gilberger, T.W., Snijders, A.P., Blackman, M.J., Baker, D.A., 2019. Cyclic AMP signalling controls key components of malaria parasite host cell invasion machinery. PLoS Biology 17. https://doi.org/10.1371/journal.pbio.3000264

Patzewitz, E.M., Guttery, D.S., Poulin, B., Ramakrishnan, C., Ferguson, D.J.P., Wall, R.J., Brady, D., Holder, A.A., Szöodoubleacuter, B., Tewari, R., 2013. An Ancient Protein Phosphatase, SHLP1, Is Critical to Microneme Development in Plasmodium Ookinetes and Parasite Transmission. Cell Reports 3, 622–629. https://doi.org/10.1016/j.celrep.2013.01.032

Paul, A.S., Miliu, A., Paulo, J.A., Goldberg, J.M., Bonilla, A.M., Berry, L., Seveno, M., Braun-Breton, C., Kosber, A.L., Elsworth, B., Arriola, J.S.N., Lebrun, M., Gygi, S.P., Lamarque, M.H., Duraisingh, M.T., 2020. Co-option of Plasmodium falciparum PP1 for egress from host erythrocytes. Nature Communications 11. https://doi.org/10.1038/s41467-020-17306-1.

Paul, A.S., Saha, S., Engelberg, K., Jiang, R.H.Y., Coleman, B.I., Kosber, A.L., Chen, C.T., Ganter, M., Espy, N., Gilberger, T.W., Gubbels, M.J., Duraisingh, M.T., 2015. Parasite calcineurin regulates host cell recognition and attachment by apicomplexans. Cell Host and Microbe 18, 49–60. https://doi.org/10.1016/j.chom.2015.06.003.

Payne, R.O., Milne, K.H., Elias, S.C., Edwards, N.J., Douglas, A.D., Brown… Dutta, S., Draper, S.J., 2016. Demonstration of the blood-stage plasmodium falciparum controlled human malaria infection model to assess efficacy of the p. falciparum apical membrane antigen 1 Vaccine, FMP2.1/AS01. Journal of Infectious Diseases 213, 1743–1751. https://doi.org/10.1093/infdis/jiw039.

Payne, R.O., Silk, S.E., Elias, S.C., Miura, K., Diouf, A., Galaway, F., Graaf, H.D… Lawrie, A.M., Draper, S.J., 2017. Human vaccination against RH5 induces neutralizing antimalarial antibodies that inhibit RH5 invasion complex interactions. JCI Insight 2. https://doi.org/10.1172/jci.insight.96381.

Pazicky, S., Dhamotharan, K., Kaszuba, K., Mertens, H.D.T., Gilberger, T., Svergun, D., Kosinski, J., Weininger, U., Löw, C., 2020. Structural role of essential light chains in the apicomplexan glideosome. Communications Biology 3. https://doi.org/10.1038/s42003-020-01283-8.

Pei, X., Guo, X., Coppel, R., Bhattacharjee, S., Haldar, K., Gratzer, W., Mohandas, N., An, X., 2007. The ring-infected erythrocyte surface antigen (RESA) of Plasmodium falciparum stabilizes spectrin tetramers and suppresses further invasion. Blood 110, 1036–1042. https://doi.org/10.1182/blood-2007-02-076919

Peng, M., Cascio, D., Egea, P.F., 2015. Crystal structure and solution characterization of the thioredoxin-2 from Plasmodium falciparum, a constituent of an essential

parasitic protein export complex. Biochemical and Biophysical Research Communications 456, 403–409. https://doi.org/10.1016/j.bbrc.2014.11.096.

Philip, N., Vaikkinen, H.J., Tetley, L., Waters, A.P., 2012. A Unique Kelch Domain Phosphatase in Plasmodium Regulates Ookinete Morphology, Motility and Invasion. PLoS ONE 7. https://doi.org/10.1371/journal.pone.0044617.

Philip, N., Waters, A.P., 2015. Conditional degradation of plasmodium calcineurin reveals functions in parasite colonization of both host and vector. Cell Host and Microbe 18, 122–131. https://doi.org/10.1016/j.chom.2015.05.018

Pinzon-Ortiz, C., Friedman, J., Esko, J., Sinnis, P., 2001. The Binding of the Circumsporozoite Protein to Cell Surface Heparan Sulfate Proteoglycans is Required for Plasmodium Sporozoite Attachment to Target Cells. Journal of Biological Chemistry 276, 26784–26791. https://doi.org/10.1074/jbc.M104038200.

Pitman, E.L., Counihan, N.A., Modak, J.K., Chowdury, M., Gilson, P.R., Webb, C.T., Koning-Ward, T.F. de, 2024. Dissecting EXP2 sequence requirements for protein export in malaria parasites. Frontiers in Cellular and Infection Microbiology 13. https://doi.org/10.3389/fcimb.2023.1332146.

Polino, A.J., Nasamu, A.S., Niles, J.C., Goldberg, D.E., 2020. Assessment of Biological Role and Insight into Druggability of the Plasmodium falciparum Protease Plasmepsin v. ACS Infectious Diseases 6, 738–746. https://doi.org/10.1021/acsinfecdis.9b00460.

Pramanik, S., Thaker, M., Perumal, A.G., Ekambaram, R., Poondla, N., Schmidt, M., Kim, P.S., Kutzner, A., Heese, K., 2020. Proteomic Atomics Reveals a Distinctive Uracil-5-Methyltransferase. Molecular Informatics 39. https://doi.org/10.1002/minf.201900135.

Prudêncio, M., Rodriguez, A., Mota, M.M., 2006. The silent path to thousands of merozoites: the Plasmodium liver stage. Nat Rev Microbiol 4, 849–856. https://doi.org/10.1038/nrmicro1529.

Rajendran, E., Hapuarachchi, S.V., Miller, C.M., Fairweather, S.J., Cai, Y., Smith, N.C., Cockburn, I.A., Broër, S., Kirk, K., Dooren, G.G.V., 2017. Cationic amino acid transporters play key roles in the survival and transmission of apicomplexan parasites. Nature Communications 8. https://doi.org/10.1038/ncomms14455.

Ralph, S.A., D'Ombrain, M.C., McFadden, G.I., 2001. The apicoplast as an antimalarial drug target. Drug Resistance Updates 4, 145–151. https://doi.org/10.1054/drup.2001.0205.

Ralph, S.A., van Dooren, G.G., Waller, R.F., Crawford, M.J., Fraunholz, M.J., Foth, B.J., Tonkin, C.J., Roos, D.S., McFadden, G.I., 2004. Metabolic maps and functions of the Plasmodium falciparum apicoplast. Nat Rev Microbiol 2, 203–216. https://doi.org/10.1038/nrmicro843.

Ramaprasad, A., Burda, P.-C., Koussis, K., Thomas, J.A., Pietsch, E., Calvani, E., Howell, S.A., Snijders, A.P., Gilberger, T.-W., Blackman, M.J. 2023. A malaria

parasite phospholipase facilitates efficient asexual blood stage. https://doi.org/10.1101/2023.03.13.532312.

Richie, T.L., Billingsley, P.F., Sim, B.K.L., James, E.R., Chakravarty, S., Epstein, J.E., Lyke, K.E., Mordmüller, B., Alonso, P., Duffy, P.E., Doumbo, O.K., Sauerwein, R.W., Tanner, M., Abdulla, S., Kremsner, P.G., Seder, R.A., Hoffman, S.L., 2015. Progress with Plasmodium falciparum sporozoite (PfSPZ)-based malaria vaccines. Vaccine 33, 7452–7461. https://doi.org/10.1016/j.vaccine.2015.09.096.

Riglar, D.T., Richard, D., Wilson, D.W., Boyle, M.J., Dekiwadia, C., Turnbull, L., Angrisano, F., Marapana, D.S., Rogers, K.L., Whitchurch, C.B., Beeson, J.G., Cowman, A.F., Ralph, S.A., Baum, J., 2011. Super-resolution dissection of coordinated events during malaria parasite invasion of the human erythrocyte. Cell Host and Microbe 9, 9–20. https://doi.org/10.1016/j.chom.2010.12.003

Robinson, D.R.L., Hock, D.H., Muellner-Wong, L., Kugapreethan, R., Reljic, B., Surgenor, E.E., Rodrigues, C.H.M., Caruana, N.J., Stroud, D.A., 2022. Applying Sodium Carbonate Extraction Mass Spectrometry to Investigate Defects in the Mitochondrial Respiratory Chain. Frontiers in Cell and Developmental Biology 10. https://doi.org/10.3389/fcell.2022.786268

Roy, A., Yang, J., Zhang, Y., 2012. COFACTOR: An accurate comparative algorithm for structure-based protein function annotation. Nucleic Acids Research 40. https://doi.org/10.1093/nar/gks372.

RTS,S Clinical Trials Partnership, 2015. Efficacy and safety of RTS,S/AS01 malaria vaccine with or without a booster dose in infants and children in Africa: final results of a phase 3, individually randomised, controlled trial. Lancet 386, 31–45. https://doi.org/10.1016/S0140-6736(15)60721-8.

Ruecker, A., Shea, M., Hackett, F., Suarez, C., Hirst, E.M.A., Milutinovic, K., Withers-Martinez, C., Blackman, M.J., 2012. Proteolytic activation of the essential parasitophorous vacuole cysteine protease SERA6 accompanies malaria parasite egress from its host erythrocyte. Journal of Biological Chemistry 287, 37949–37963. https://doi.org/10.1074/jbc.M112.400820.

Rug, M., Cyrklaff, M., Mikkonen, A., Lemgruber, L., Kuelzer, S., Sanchez, C.P., Thompson, J., Hanssen, E., O'neill, M., Langer, C., Lanzer, M., Frischknecht, F., Maier, A.G., Cowman, A.F., 2014. Export of virulence proteins by malaria-infected erythrocytes involves remodeling of host actin cytoskeleton. https://doi.org/10.1182/blood-2014-06.

Rusnak, F., Mertz, P., 2000. Calcineurin: form and function. Physiol Rev 80, 1483–1521. https://doi.org/10.1152/physrev.2000.80.4.1483.

Russo, I., Babbitt, S., Muralidharan, V., Butler, T., Oksman, A., Goldberg, D.E., 2010. Plasmepsin v licenses Plasmodium proteins for export into the host erythrocyte. Nature 463, 632–636. https://doi.org/10.1038/nature08726.

Sagara, I., Dicko, A., Ellis, R.D., Fay, M.P., Diawara, S.I., Assadou, M.H., Sissoko, M.S., Kone, M., Diallo, A.I., Saye, R., Guindo, M.A., Kante, O., Niambele, M.B., Miura, K.,

Mullen, G.E.D., Pierce, M., Martin, L.B., Dolo, A., Diallo, D.A., Doumbo, O.K., Miller, L.H., Saul, A., 2009. A randomized controlled phase 2 trial of the blood stage AMA1-C1/Alhydrogel malaria vaccine in children in Mali. Vaccine 27, 3090–3098. https://doi.org/10.1016/j.vaccine.2009.03.014.

Sala, K.A., Angrisano, F., Da, D.F., Taylor, I.J., Churcher, T.S., Blagborough, A.M., 2018. Immunization with Transgenic Rodent Malaria Parasites Expressing Pfs25 Induces Potent Transmission-Blocking Activity. Scientific Reports 8. https://doi.org/10.1038/s41598-017-18831-8.

Salamanca, D.R., Gómez, M., Camargo, A., Cuy-Chaparro, L., Molina-Franky, J., Reyes, C., Patarroyo, M.A., Patarroyo, M.E., 2019. Plasmodium falciparum Blood Stage Antimalarial Vaccines: An Analysis of Ongoing Clinical Trials and New Perspectives Related to Synthetic Vaccines. Front Microbiol 10, 2712. https://doi.org/10.3389/fmicb.2019.02712.

Sanders, P.R., Gilson, P.R., Cantin, G.T., Greenbaum, D.C., Nebl, T., Carucci, D.J., McConville, M.J., Schofield, L., Hodder, A.N., Yates, J.R., Crabb, B.S., 2005. Distinct protein classes including novel merozoite surface antigens in raft-like membranes of Plasmodium falciparum. Journal of Biological Chemistry 280, 40169–40176. https://doi.org/10.1074/jbc.M509631200.

Sargeant, T.J., Marti, M., Caler, E., Carlton, J.M., Simpson, K., Speed, T.P., Cowman, A.F., 2006. Lineage-specific expansion of proteins exported to erythrocytes in malaria parasites. Genome Biol 7, R12. https://doi.org/10.1186/gb-2006-7-2-r12.

Scally, S.W., Triglia, T., Evelyn, C., Seager, B.A., Pasternak, M., Lim, P.S., Healer, J., Geoghegan, N.D., Adair, A., Tham, W.H., Dagley, L.F., Rogers, K.L., Cowman, A.F., 2022. PCRCR complex is essential for invasion of human erythrocytes by Plasmodium falciparum. Nature Microbiology 7, 2039–2053. https://doi.org/10.1038/s41564-022-01261-2

Schenk, G., Mitić, N., Hanson, G., Comba, P., 2013. Purple acid phosphatase: A journey into the function and mechanism of a colorful enzyme. Coordination Chemistry Reviews 257, 473–482. https://doi.org/10.1016/j.ccr.2012.03.020.

Schindelin, J., Arganda-Carreras, I., Frise, E., Kaynig, V., Longair, M., Pietzsch, T., Preibisch, S., Rueden, C., Saalfeld, S., Schmid, B., Tinevez, J.-Y., White, D.J., Hartenstein, V., Eliceiri, K., Tomancak, P., Cardona, A., 2012. Fiji - an Open Source platform for biological image analysis. Nat Methods 9, 10.1038/nmeth.2019. https://doi.org/10.1038/nmeth.2019.

Schlüter, A., Fourcade, S., Ripp, R., Mandel, J.L., Poch, O., Pujol, A., 2006. The evolutionary origin of peroxisomes: An ER-peroxisome connection. Molecular Biology and Evolution 23, 838–845. https://doi.org/10.1093/molbev/msj103.

Schnider, C.B., Bausch-Fluck, D., Brühlmann, F., Heussler, V.T., Burda, P.-C., 2018. BioID Reveals Novel Proteins of the Plasmodium Parasitophorous Vacuole Membrane. https://doi.org/10.1128/mSphere.

Schuldiner, M., Metz, J., Schmid, V., Denic, V., Rakwalska, M., Schmitt, H.D., Schwappach, B., Weissman, J.S., 2008. The GET Complex Mediates Insertion of Tail-Anchored Proteins into the ER Membrane. Cell 134, 634–645. https://doi.org/10.1016/j.cell.2008.06.025.

Schulze, J., Kwiatkowski, M., Borner, J., Schlüter, H., Bruchhaus, I., Burmester, T., Spielmann, T., Pick, C., 2015. The Plasmodium falciparum exportome contains non-canonical PEXEL/HT proteins. Molecular Microbiology 97, 301–314. https://doi.org/10.1111/mmi.13024.

Schureck, M.A., Darling, J.E., Merk, A., Shao, J., Daggupati, G., Srinivasan, P., Olinares, P.D.B., Rout, M.P., Chait, B.T., Wollenberg, K., Subramaniam, S., Desai, S.A., 2021. Malaria parasites use a soluble Rhoph complex for erythrocyte invasion and an integral form for nutrient uptake. eLife 10, 1–24. https://doi.org/10.7554/ELIFE.65282.

Seder, R.A., Chang, L.J., Enama, M.E., Zephir, K.L., Sarwar, U.N., Gordon, I.J., Holman, L.S.A., James, E.R., Billingsley, P.F., Gunasekera, A., Richman, A., Chakravarty, S., Manoj, A., Velmurugan, S., Li, M.L., Ruben, A.J., Li, T., Eappen, A.G., Stafford, R.E., Plummer, S.H., Hendel, C.S., Novik, L., Costner, P.J.M., Mendoza, F.H., Saunders, J.G., Nason, M.C., Richardson, J.H., Murphy, J., Davidson, S.A., Richie, T.L., Sedegah, M., Sutamihardja, A., Fahle, G.A., Lyke, K.E., Laurens, M.B., Roederer, M., Tewari, K., Epstein, J.E., Sim, B.K.L., Ledgerwood, J.E., Graham, B.S., Hoffman, S.L., 2013. Protection against malaria by intravenous immunization with a nonreplicating sporozoite vaccine. Science 341, 1359–1365. https://doi.org/10.1126/science.1241800.

Seifried, A., Schultz, J., Gohla, A., 2013. Human HAD phosphatases: structure, mechanism, and roles in health and disease. FEBS J 280, 549–571. https://doi.org/10.1111/j.1742-4658.2012.08633.x.

Sharma, Ashwani, Sharma, Arvind, Dixit, S., Sharma, Amit, 2011. Structural insights into thioredoxin-2: A component of malaria parasite protein secretion machinery. Scientific Reports 1. https://doi.org/10.1038/srep00179.

Sherling, E.S., Knuepfer, E., Brzostowski, J.A., Miller, L.H., Blackman, M.J., Ooij, C.V., 2017. The Plasmodium falciparum rhoptry protein RhopH3 plays essential roles in host cell invasion and nutrient uptake. https://doi.org/10.7554/eLife.23239.001.

Sherling, E.S., van Ooij, C., 2016. Host cell remodeling by pathogens: the exomembrane system in Plasmodium-infected erythrocytes. FEMS Microbiol Rev 40, 701–721. https://doi.org/10.1093/femsre/fuw016.

Sherman, I.W., 1998. Malaria: Parasite Biology, Pathogenesis, and Protection. American Society for Microbiology.

Shi, Y., 2009. Serine/threonine phosphatases: mechanism through structure. Cell 139, 468–484. https://doi.org/10.1016/j.cell.2009.10.006.

Sievers, F., Wilm, A., Dineen, D., Gibson, T.J., Karplus, K., Li, W., Lopez, R., McWilliam, H., Remmert, M., Söding, J., Thompson, J.D., Higgins, D.G., 2011. Fast, scalable

generation of high-quality protein multiple sequence alignments using Clustal Omega. Molecular Systems Biology 7. https://doi.org/10.1038/msb.2011.75

Sigala, P.A., Crowley, J.R., Henderson, J.P., Goldberg, D.E., 2015. Deconvoluting heme biosynthesis to target blood-stage malaria parasites. eLife 4. https://doi.org/10.7554/eLife.09143.001

Simmons, D., Woollett, G., Bergin-Cartwright, M., Kay, D., Scaife, J., 1987. A malaria protein exported into a new compartment within the host erythrocyte. EMBO J 6, 485–491.

Skamnaki, V.T., Owen, D.J., Noble, M.E.M., Lowe, E.D., Lowe, G., Oikonomakos, N.G., Johnson, L.N., 1999. Catalytic mechanism of phosphorylase kinase probed by mutational studies. Biochemistry 38, 14718–14730. https://doi.org/10.1021/bi991454f

Sleebs, B.E., Lopaticki, S., Marapana, D.S., O'Neill, M.T., Rajasekaran, P., Gazdik, M., Günther, S., Whitehead, L.W., Lowes, K.N., Barfod, L., Hviid, L., Shaw, P.J., Hodder, A.N., Smith, B.J., Cowman, A.F., Boddey, J.A., 2014. Inhibition of Plasmepsin V Activity Demonstrates Its Essential Role in Protein Export, PfEMP1 Display, and Survival of Malaria Parasites. PLoS Biology 12, 1–16. https://doi.org/10.1371/journal.pbio.1001897.

Soldati-Favre, D., 2008. Molecular dissection of host cell invasion by the Apicomplexans: The glideosome, in: Parasite. PRINCEPS Editions, pp. 197–205. https://doi.org/10.1051/parasite/2008153197

Spielmann, T., Fergusen, D.J.P., Beck, H.-P., 2003. etramps, a new Plasmodium falciparum gene family coding for developmentally regulated and highly charged membrane proteins located at the parasite-host cell interface. Mol Biol Cell 14, 1529–1544. https://doi.org/10.1091/mbc.e02-04-0240.

Spielmann, T., Gardiner, D.L., Beck, H.P., Trenholme, K.R., Kemp, D.J., 2006a. Organization of ETRAMPs and EXP-1 at the parasite-host cell interface of malaria parasites. Molecular Microbiology 59, 779–794. https://doi.org/10.1111/j.1365-2958.2005.04983.x.

Spielmann, T., Hawthorne, P.L., Dixon, M.W.A., Hannemann, M., Klotz, K., Kemp, D.J., Klonis, N., Tilley, L., Trenholme, K.R., Gardiner, D.L., 2006b. A cluster of ring stage-specific genes linked to a locus implicated in cytoadherence in Plasmodium falciparum codes for PEXEL-negative and PEXEL-positive proteins exported into the host cell. Mol Biol Cell 17, 3613–3624. https://doi.org/10.1091/mbc.e06-04-0291.

Spielmann, T., Gilberger, T.-W., 2010. Protein export in malaria parasites: do multiple export motifs add up to multiple export pathways? Trends Parasitol 26, 6–10. https://doi.org/10.1016/j.pt.2009.10.001.

Spielmann, T., Hawthorne, P.L., Dixon, M.W.A., Hannemann, M., Klotz, K., Kemp, D.J., Klonis, N., Tilley, L., Trenholme, K.R., Gardiner, D.L., 2006b. A Cluster of Ring Stage-specific Genes Linked to a Locus Implicated in Cytoadherence in Plasmodium

falciparum Codes for PEXEL-negative and PEXEL-positive Proteins Exported into the Host Cell Mol Biology of the Cell 17, 3613–3624. https://doi.org/10.1091/mbc.E06

Spielmann, T., Montagna, G.N., Hecht, L., Matuschewski, K., 2012. Molecular make-up of the Plasmodium parasitophorous vacuolar membrane. Int J Med Microbiol 302, 179–186. https://doi.org/10.1016/j.ijmm.2012.07.011.

Spillman, N.J., Beck, J.R., Goldberg, D.E., 2015. Protein export into malaria parasite-infected erythrocytes: mechanisms and functional consequences. Annu Rev Biochem 84, 813–841. https://doi.org/10.1146/annurev-biochem-060614-034157

Spycher, C., Klonis, N., Spielmann, T., Kump, E., Steiger, S., Tilley, L., Beck, H.P., 2003. MAHRP-1, a novel Plasmodium falciparum histidine-rich protein, binds ferriprotoporphyrin IX and localizes to the Maurer's clefts. Journal of Biological Chemistry 278, 35373–35383. https://doi.org/10.1074/jbc.M305851200

Spycher, C., Rug, M., Klonis, N., Ferguson, D.J.P., Cowman, A.F., Beck, H.-P., Tilley, L., 2006. Genesis of and Trafficking to the Maurer's Clefts of Plasmodium falciparum -Infected Erythrocytes. Molecular and Cellular Biology 26, 4074–4085. https://doi.org/10.1128/mcb.00095-06

Srinivasan, P., Beatty, W.L., Diouf, A., Herrera, R., Ambroggio, X., Moch, J.K., Tyler, J.S., Narum, D.L., Pierce, S.K., Boothroyd, J.C., Haynese, J.D., Millera, L.H., 2011. Binding of Plasmodium merozoite proteins RON2 and AMA1 triggers commitment to invasion. Proceedings of the National Academy of Sciences of the United States of America 108, 13275–13280. https://doi.org/10.1073/pnas.1110303108.

Srinivasan, P., Yasgar, A., Luci, D.K., Beatty, W.L., Hu, X., Andersen, J., Narum, D.L., Moch, J.K., Sun, H., Haynes, J.D., Maloney, D.J., Jadhav, A., Simeonov, A., Miller, L.H., 2013. Disrupting malaria parasite AMA1-RON2 interaction with a small molecule prevents erythrocyte invasion. Nature Communications 4. https://doi.org/10.1038/ncomms3261.

Stefanovic, S., Hegde, R.S., 2007. Identification of a Targeting Factor for Posttranslational Membrane Protein Insertion into the ER. Cell 128, 1147–1159. https://doi.org/10.1016/j.cell.2007.01.036.

Sträter, N., Jasper, B., Scholte, M., Krebs, B., Duff, A.P., Langley, D.B., Han, R., Averill, B.A., Freeman, H.C., Guss, J.M., 2005. Crystal structures of recombinant human purple acid phosphatase with and without an inhibitory conformation of the repression loop. Journal of Molecular Biology 351, 233–246. https://doi.org/10.1016/j.jmb.2005.04.014.

Striepen, B., Crawford, M.J., Shaw, M.K., Tilney, L.G., Seeber, F., Roos, D.S., 2000. The Plastid of Toxoplasma gondii Is Divided by Association with the Centrosomes. J Cell Biol 151, 1423–1434.

Struck, N.S., Dias, S. de S., Langer, C., Marti, M., Pearce, J.A., Cowman, A.F., Gilberger, T.W., 2005. Re-defining the Golgi complex in Plasmodium falciparum using the novel Golgi marker PfGRASP. Journal of Cell Science 118, 5603–5613. https://doi.org/10.1242/jcs.02673.

Sturm, A., Amino, R., van de Sand, C., Regen, T., Retzlaff, S., Rennenberg, A., Krueger, A., Pollok, J.-M., Menard, R., Heussler, V.T., 2006. Manipulation of host hepatocytes by the malaria parasite for delivery into liver sinusoids. Science 313, 1287–1290. https://doi.org/10.1126/science.1129720.

Suarez, C., Lentini, G., Ramaswamy, R., Maynadier, M., Aquilini, E., Berry-Sterkers, L., Cipriano, M., Chen, A.L., Bradley, P., Striepen, B., Boulanger, M.J., Lebrun, M., 2019. A lipid-binding protein mediates rhoptry discharge and invasion in Plasmodium falciparum and Toxoplasma gondii parasites. Nature Communications 10. https://doi.org/10.1038/s41467-019-11979-z

Swift, R.P., Rajaram, K., Liu, H.B., Prigge, S.T., 2021. Dephospho-CoA kinase, a nuclear-encoded apicoplast protein, remains active and essential after Plasmodium falciparum apicoplast disruption. The EMBO Journal 40. https://doi.org/10.15252/embj.2020107247

Takano, R., Kozuka-Hata, H., Kondoh, D., Bochimoto, H., Oyama, M., Kato, K., 2019. A High-Resolution Map of SBP1 Interactomes in Plasmodium falciparum-infected Erythrocytes. iScience 19, 703–714. https://doi.org/10.1016/j.isci.2019.07.035

Tamez, P.A., Bhattacharjee, S., Ooij, C.V., Hiller, N.L., Llinás, M., Balu, B., Adams, J.H., Haldar, K., 2008. An erythrocyte vesicle protein exported by the malaria parasite promotes tubovesicular lipid import from the host cell surface. PLoS Pathogens 4. https://doi.org/10.1371/journal.ppat.1000118

Tarning, J., Kloprogge, F., Piola, P., Dhorda, M., Muwanga, S., Turyakira, E., Nuengchamnong, N., Nosten, F., Day, N.P., White, N.J., Guerin, P.J., Lindegardh, N., 2012. Population pharmacokinetics of Artemether and dihydroartemisinin in pregnant women with uncomplicated Plasmodium falciparum malaria in Uganda. Malar J 11, 293. https://doi.org/10.1186/1475-2875-11-293

Tarr, S.J., Moon, R.W., Hardege, I., Osborne, A.R., 2014. A conserved domain targets exported PHISTb family proteins to the periphery of Plasmodium infected erythrocytes. Molecular and Biochemical Parasitology 196, 29–40. https://doi.org/10.1016/j.molbiopara.2014.07.011

Taylor, H.M., McRobert, L., Grainger, M., Sicard, A., Dluzewski, A.R., Hopp, C.S., Holder, A.A., Baker, D.A., 2010. The malaria parasite cyclic GMP-dependent protein kinase plays a central role in blood-stage schizogony. Eukaryotic Cell 9, 37–45. https://doi.org/10.1128/EC.00186-09.

Tham, W.-H., Healer, J., Cowman, A.F., 2012. Erythrocyte and reticulocyte binding-like proteins of Plasmodium falciparum. Trends Parasitol 28, 23–30. https://doi.org/10.1016/j.pt.2011.10.002

Thomas, J.A., Tan, M.S.Y., Bisson, C., Borg, A., Umrekar, T.R., Hackett, F., Hale, V.L., Vizcay-Barrena, G., Fleck, R.A., Snijders, A.P., Saibil, H.R., Blackman, M.J., 2018. A protease cascade regulates release of the human malaria parasite Plasmodium falciparum from host red blood cells. Nature Microbiology 3, 447–455. https://doi.org/10.1038/s41564-018-0111-0.

Tonkin, C.J., Dooren, G.G.V., Spurck, T.P., Struck, N.S., Good, R.T., Handman, E., Cowman, A.F., McFadden, G.I., 2004. Localization of organellar proteins in Plasmodium falciparum using a novel set of transfection vectors and a new immunofluorescence fixation method. Molecular and Biochemical Parasitology 137, 13–21. https://doi.org/10.1016/j.molbiopara.2004.05.009.

Tonkin, C.J., Struck, N.S., Mullin, K.A., Stimmler, L.M., McFadden, G.I., 2006. Evidence for Golgi-independent transport from the early secretory pathway to the plastid in malaria parasites. Molecular Microbiology 61, 614–630. https://doi.org/10.1111/j.1365-2958.2006.05244.x.

Tonkin, M.L., Beck, J.R., Bradley, P.J., Boulanger, M.J., 2014. The inner membrane complex sub-compartment proteins critical for replication of the apicomplexan parasite Toxoplasma gondii adopt a pleckstrin homology fold. Journal of Biological Chemistry 289, 13962–13973. https://doi.org/10.1074/jbc.M114.548891.

Tonkin, M.L., Roques, M., Lamarque, M.H., Pugnière, M., Douguet, D., Crawford, J., Lebrun, M., Boulanger, M.J., 2011. Host cell invasion by apicomplexan parasites: Insights from the co-structure of AMA1 with a RON2 peptide. Science 333, 463–467. https://doi.org/10.1126/science.1204988.

Trager, W., Jensen, J.B., 2005. Human malaria parasites in continuous culture. Journal of Parasitology 91, 484–486. https://doi.org/10.1645/0022-3395(2005)091[0484:HMPICC]2.0.CO;2.

Trelka, D.P., Schneider, T.G., Reeder, J.C., Taraschi, T.F., 2000. Evidence for vesicle-mediated trafficking of parasite proteins to the host cell cytosol and erythrocyte surface membrane in Plasmodium falciparum infected erythrocytes. Mol Biochem Parasitol 106, 131–145. https://doi.org/10.1016/s0166-6851(99)00207-8.

Triglia, T., Thompson, J., Caruana, S.R., Delorenzi, M., Speed, T., Cowman, A.F., 2001. Identification of proteins from Plasmodium falciparum that are homologous to reticulocyte binding proteins in Plasmodium vivax. Infection and Immunity 69, 1084–1092. https://doi.org/10.1128/IAI.69.2.1084-1092.2001.

Uwimana, A., Legrand, E., Stokes, B.H., Ndikumana, J.L.M., Warsame, M., Umulisa, N., Ngamije, D., Munyaneza, T., Mazarati, J.B., Munguti, K., Campagne, P., Criscuolo, A., Ariey, F., Murindahabi, M., Ringwald, P., Fidock, D.A., Mbituyumuremyi, A., Menard, D., 2020. Emergence and clonal expansion of in vitro artemisinin-resistant Plasmodium falciparum kelch13 R561H mutant parasites in Rwanda. Nature Medicine 26, 1602–1608. https://doi.org/10.1038/s41591-020-1005-2.

van Dijk, M.R., Janse, C.J., Thompson, J., Waters, A.P., Braks, J.A., Dodemont, H.J., Stunnenberg, H.G., van Gemert, G.J., Sauerwein, R.W., Eling, W., 2001. A central role for P48/45 in malaria parasite male gamete fertility. Cell 104, 153–164. https://doi.org/10.1016/s0092-8674(01)00199-4.

Vander Jagt, D.L., Hunsaker, L.A., Campos, N.M., 1986. Characterization of a hemoglobin-degrading, low molecular weight protease from Plasmodium falciparum. Mol Biochem Parasitol 18, 389–400. https://doi.org/10.1016/0166-6851(86)90095-2.

Varadi, M., Anyango, S., Deshpande, M., Nair, S., Natassia, C., Yordanova, G., Yuan, D., Stroe, O., Wood, G., Laydon, A., Zídek, A., Green, T., Tunyasuvunakool, K., Petersen, S., Jumper, J., Clancy, E., Green, R., Vora, A., Lutfi, M., Figurnov, M., Cowie, A., Hobbs, N., Kohli, P., Kleywegt, G., Birney, E., Hassabis, D., Velankar, S., 2022. AlphaFold Protein Structure Database: Massively expanding the structural coverage of protein-sequence space with high-accuracy models. Nucleic Acids Research 50, D439–D444.

Van Dooren, G.G, Marti, M., Tonkin, C.J., Stimmler, L.M., Cowman, A.F., McFadden, G.I., 2005. Development of the endoplasmic reticulum, mitochondrion and apicoplast during the asexual life cycle of Plasmodium falciparum. Molecular Microbiology 57, 405–419. https://doi.org/10.1111/j.1365-2958.2005.04699.x.

Van Dooren, B.S.G.G. van, 2013. The algal past and parasite present of the apicoplast. Epub 6, 271–289.

Verhoef, J.M.J., Meissner, M., Kooij, T.W.A., 2021. Organelle Dynamics in Apicomplexan Parasites. mBio 12, e0140921. https://doi.org/10.1128/mBio.01409-21

Villiers, T.J.E.K.A. de, 2021. Heme Detoxification in the Malaria Parasite: A Target for Antimalarial Drug Development. Acc. Chem. Res. 11, 2649–2659.

Vincensini, L., Fall, G., Berry, L., Blisnick, T., Breton, C.B., 2008. The RhopH complex is transferred to the host cell cytoplasm following red blood cell invasion by Plasmodium falciparum. Molecular and Biochemical Parasitology 160, 81–89. https://doi.org/10.1016/j.molbiopara.2008.04.002.

Vincensini, L., Richert, S., Blisnick, T., Dorsselaer, A.V., Leize-Wagner, E., Rabilloud, T., Breton, C.B., 2005. Proteomic analysis identifies novel proteins of the Maurer's clefts, a secretory compartment delivering Plasmodium falciparum proteins to the surface of its host cell. Molecular and Cellular Proteomics 4, 582–593. https://doi.org/10.1074/mcp.M400176-MCP200.

Vincent, J.B., Averill, B.A., 1990. An enzyme with a double identity: purple acid phosphatase and tartrate-resistant acid phosphatase. FASEB J 4, 3009–3014. https://doi.org/10.1096/fasebj.4.12.2394317.

Voegtli, W.C., White, D.J., Reiter, N.J., Rusnak, F., Rosenzweig, A.C., 2000. Structure of the bacteriophage λ Ser/Thr protein phosphatase with sulfate ion bound in two coordination modes. Biochemistry 39, 15365–15374. https://doi.org/10.1021/bi0021030.

Volz, J.C., Yap, A., Sisquella, X., Thompson, J.K., Lim, N.T.Y., Whitehead, L.W., Chen, L., Lampe, M., Tham, W.H., Wilson, D., Nebl, T., Marapana, D., Triglia, T., Wong, W., Rogers, K.L., Cowman, A.F., 2016. Essential Role of the PfRh5/PfRipr/CyRPA Complex during Plasmodium falciparum Invasion of Erythrocytes. Cell Host and Microbe 20, 60–71. https://doi.org/10.1016/j.chom.2016.06.004

Wahlgren, M., Goel, S., Akhouri, R.R., 2017. Variant surface antigens of Plasmodium falciparum and their roles in severe malaria. Nat Rev Microbiol 15, 479–491. https://doi.org/10.1038/nrmicro.2017.47

Waller, R.F., Keeling, P.J., Donald, R.G.K., Striepen, B., Handman, E., Lang-Unnasch, N., Cowman, A.F., Besra, G.S., Roos, D.S., McFadden, G.I., 1998. Nuclear-encoded proteins target to the plastid in Toxoplasma gondii and Plasmodium falciparum. Proc Natl Acad Sci U S A 95, 12352–12357.

Waller, R.F., Reed, M.B., Cowman, A.F., McFadden, G.I., 2000. Protein trafficking to the plastid of Plasmodium falciparum is via the secretory pathway. EMBO J 19, 1794–1802. https://doi.org/10.1093/emboj/19.8.1794

Walliker, D., Quakyi, I.A., Wellems, T.E., McCutchan, T.F., Szarfman, A., London, W.T., Corcoran, L.M., Burkot, T.R., Carter, R., 1987. Genetic analysis of the human malaria parasite Plasmodium falciparum. Science 236, 1661–1666. https://doi.org/10.1126/science.3299700

Warmka, J., Hanneman, J., Lee, J., Amin, D., Ota, I., 2001. Ptc1, a Type 2C Ser/Thr Phosphatase, Inactivates the HOG Pathway by Dephosphorylating the Mitogen-Activated Protein Kinase Hog1. Molecular and Cellular Biology 21, 51–60. https://doi.org/10.1128/mcb.21.1.51-60.2001

Waterhouse, A., Bertoni, M., Bienert, S., Studer, G., Tauriello, G., Gumienny, R., Heer, F.T., Beer, T.A.P.D., Rempfer, C., Bordoli, L., Lepore, R., Schwede, T., 2018. SWISS-MODEL: Homology modelling of protein structures and complexes. Nucleic Acids Research 46, W296–W303. https://doi.org/10.1093/nar/gky427

Weiss, G.E., Crabb, B.S., Gilson, P.R., 2016. Overlaying Molecular and Temporal Aspects of Malaria Parasite Invasion. Trends Parasitol 32, 284–295. https://doi.org/10.1016/j.pt.2015.12.007.

Weiss, G.E., Gilson, P.R., Taechalertpaisarn, T., Tham, W.H., Jong, N.W.M. de, Harvey, K.L., Fowkes, F.J.I., Barlow, P.N., Rayner, J.C., Wright, G.J., Cowman, A.F., Crabb, B.S., 2015. Revealing the Sequence and Resulting Cellular Morphology of Receptor-Ligand Interactions during Plasmodium falciparum Invasion of Erythrocytes. PLoS Pathogens 11. https://doi.org/10.1371/journal.ppat.1004670.

Wharton, R.P., Sonoda, J., Lee, T., Patterson, M., Murata, Y., 1998. The Pumilio RNA-binding domain is also a translational regulator. Mol Cell 1, 863–872. https://doi.org/10.1016/s1097-2765(00)80085-4

White, N.J., Pukrittayakamee, S., Hien, T.T., Faiz, M.A., Mokuolu, O.A., Dondorp, A.M., 2014. Malaria. Lancet 383, 723–735. https://doi.org/10.1016/S0140-6736(13)60024-0.

World malaria report 2021. Geneva, World Health Organization. Licence: CC BY-NC-SA 3.0 IGO.

World malaria report 2022. Geneva, World Health Organization. Licence: CC BY-NC-SA 3.0 IGO.

Wickert, H., Göttler, W., Krohne, G., Lanzer, M., 2004. Maurer's cleft organization in the cytoplasm of plasmodium falciparum-infected erythrocytes: new insights from three-dimensional reconstruction of serial ultrathin sections. Eur J Cell Biol 83, 567–582. https://doi.org/10.1078/0171-9335-00432.

Wickham, M.E., Rug, M., Ralph, S.A., Klonis, N., McFadden, G.I., Tilley, L., Cowman, A.F., 2001. Trafficking and assembly of the cytoadherence complex in Plasmodium falciparum-infected human erythrocytes. EMBO J 20, 5636–5649. https://doi.org/10.1093/emboj/20.20.5636.

Wong, W., Huang, R., Menant, S., Hong, C., Sandow, J.J., Birkinshaw, R.W., Healer, J., Hodder, A.N., Kanjee, U., Tonkin, C.J., Heckmann, D., Soroka, V., Søgaard, T.M.M., Jørgensen, T., Duraisingh, M.T., Czabotar, P.E., Jongh, W.A. de, Tham, W.H., Webb, A.I., Yu, Z., Cowman, A.F., 2019. Structure of Plasmodium falciparum Rh5–CyRPA–Ripr invasion complex. Nature 565, 118–121. https://doi.org/10.1038/s41586-018-0779-6.

Wu, B., Rambow, J., Bock, S., Holm-Bertelsen, J., Wiechert, M., Soares, A.B., Spielmann, T., Beitz, E., 2015. Identity of a Plasmodium lactate/H+ symporter structurally unrelated to human transporters. Nature Communications 6. https://doi.org/10.1038/ncomms7284.

Yadavalli, R., Peterson, J.W., Drazba, J.A., Sam-Yellowe, T.Y., 2021. Trafficking and association of plasmodium falciparum mc-2tm with the maurer's clefts. Pathogens 10. https://doi.org/10.3390/pathogens10040431.

Yang, C., Arrizabalaga, G., 2017. The serine/threonine phosphatases of apicomplexan parasites. Molecular Microbiology 106, 1–21. https://doi.org/10.1111/mmi.13715.

Yeh, E., DeRisi, J.L., 2011. Chemical rescue of malaria parasites lacking an apicoplast defines organelle function in blood-stage plasmodium falciparum. PLoS Biology 9. https://doi.org/10.1371/journal.pbio.1001138.

Yeoh, S., O'Donnell, R.A., Koussis, K., Dluzewski, A.R., Ansell, K.H., Osborne, S.A., Hackett, F., Withers-Martinez, C., Mitchell, G.H., Bannister, L.H., Bryans, J.S., Kettleborough, C.A., Blackman, M.J., 2007. Subcellular Discharge of a Serine Protease Mediates Release of Invasive Malaria Parasites from Host Erythrocytes. Cell 131, 1072–1083. https://doi.org/10.1016/j.cell.2007.10.049.

Yeoman, J.A., Hanssen, E., Maier, A.G., Klonis, N., Maco, B., Baum, J., Turnbull, L., Whitchurch, C.B., Dixon, M.W.A., Tilley, L., 2011. Tracking glideosome-associated protein 50 reveals the development and organization of the inner membrane complex of Plasmodium falciparum. Eukaryotic Cell 10, 556–564. https://doi.org/10.1128/EC.00244-10.

Žárský, V., Tachezy, J., 2015. Evolutionary loss of peroxisomes - not limited to parasites. Biology Direct 10. https://doi.org/10.1186/s13062-015-0101-6

Zhang, C., Freddolino, P.L., Zhang, Y., 2017. COFACTOR: Improved protein function prediction by combining structure, sequence and protein-protein interaction information. Nucleic Acids Research 45, W291–W299. https://doi.org/10.1093/nar/gkx366.

Zhang, M., Fennell, C., Ranford-Cartwright, L., Sakthivel, R., Gueirard, P., Meister, S., Caspi, A., Doerig, C., Nussenzweig, R.S., Tuteja, R., Sullivan, W.J., Roos, D.S., Fontoura, B.M.A., Ménard, R., Winzeler, E.A., Nussenzweig, V., 2010. The Plasmodium eukaryotic initiation factor-2α kinase IK2 controls the latency of sporozoites in the mosquito salivary glands. Journal of Experimental Medicine 207, 1465–1474. https://doi.org/10.1084/jem.20091975.

Zhang, M., Mishra, S., Sakthivel, R., Fontoura, B.M.A., Nussenzweig, V., 2016. UIS2: A Unique Phosphatase Required for the Development of Plasmodium Liver Stages. PLoS Pathogens 12. https://doi.org/10.1371/journal.ppat.1005370.

Zhang, M., Wang, C., Otto, T.D., Oberstaller, J., Liao, X., Adapa, S.R., Udenze, K., Bronner, I.F., Casandra, D., Mayho, M., Brown, J., Li, S., Swanson, J., Rayner, J.C., Jiang, R.H.Y., Adams, J.H., 2018. Uncovering the essential genes of the human malaria parasite Plasmodium falciparum by saturation mutagenesis. Science 360. https://doi.org/10.1126/science.aap7847.

Zhang, Q., Wang, C., Tian, J., Li, K., Shou, H., 2011. Identification of rice purple acid phosphatases related to posphate starvation signalling. Plant Biology 13, 7–15. https://doi.org/10.1111/j.1438-8677.2010.00346.x.

Zhang, Z.-Y., 2002. Protein Tyrosine Phosphatases: Structure and Function, Substrate Specificity, and Inhibitor Development. Annual Review of Pharmacology and Toxicology 42, 209–234. https://doi.org/10.1146/annurev.pharmtox.42.083001.144616.

4.9 Appendix

Appendix 1 Oligonucleotides used in this study

Primer name	Sequence (5'-3')
1464600-Int-fw	5´-GTCTACCGAGGAAAGTGAAATAGC
1464600-Int-rv	5´-CAATTCATCAAAAATATCATACG
1464600_1436-1461_fw	5´-GAACGAGTACGTTGTTGGAAAGA
1464600_1436-1461_rv	5´-CTTCTTTCCAACAACGTACCGT
1464600_2888-2912_fw	5´-CGACAACAGCTCAATGGGTCGTG
1464600_2888-2912-rv	5´-CCACGACCCATTAGCTTGTC
1464600_186-209_fw	5´-GACTACCTTGACGACAAGGGAAG
1464600_1112-1234_fw	5´-CGTAGGATACGTACGTGAGAAC
1464600_2668-2690_fw	5´-CAGACTGGATATTCGTAGTAGG
1464600-GFP-Int-fw	5´-GTCTACCGAGGAAAGTGAAATAGC
1464600-GFP-Int-rv	5´-CAATTCATCAAAAATATCATACG
1464600+L4+GFP-fw	5´-GTTTAAACCGTATTAGTCGTCCCG GGGGTACCGCTAGAGGTGCTGCTGCTGG
1464600+L4+GFP-rv	5´-GCATGGATGAGCTCTACAAAGTCGACAT AACTTCGTATAGCATACATTATACGA
nmd3-SBPI+L4+GFP-fw	5´-TATATATATATATATTTATAAACTAGTAT GTGTAGCGCAGCACGAGCATTTGATTTTTTTA CCGATTTAG
nmd3-SBPI+L4+GFP-rv	5´-CAAAAACAGTTGCTAGAGAAACCacgcgt GCTAGAGGTGCTGCTGCTGGTGCTGGAGGTGC AGGTAGA
crt-KAHRP-mScarlet-DMSI-fw	5´-catataactcgaccccgggatCTCGAGAT GAAAAGTTTTAAGAACAAAAATA
crt-KAHRP-mScarlet-DMSI-rv	5´-GAAGAAAAGAGGATGCTGTGGTCCTAGG ATGGTGAGTAAGGGTGAGGCAG
crt-*GBP* $^{1-108}$-fw	5´-catataactcgaccccgggatCTCGAGA TGCCACCAAATAATTCCAAATA
crt-*GBP* $^{1-108}$-rv	5´-gcaggagcaatattaagtagaCCTAGGAT GGTGAGTAAGGGTGAGGCAG

Crt-*FNT-fw*	5´catataactcgaccccgggatCTCGAGATG CCACCAAATAATTCCAAATA
Crt-*FNT-L-rv*	5´-GTTTATCTATAGAATTACGAAATTCAGGA TCTGGTAGTGGATCAGGTTCTG
Crt-*FNT-mScarlet-rv*	5´-TCAGGTTCTGGAAGTGGTTCTGGAAGTCC TAGGATGGTGAGTAAGGGTGAGGCAG
crt-SP -mScarlet-fw	5´-catataactcgaccccgggatCTCGAGAT GGTATATCGCTTATTTATTATTT
crt-SP -mScarlet-rv	5´-TCCTCCTGATAGTACTGTTGGTGCACCTA GGATGGTGAGTAAGGGTGAGGCAG
PF3D7_1133800 HR-fw	5´-tatagaatactcgcggccgcTAATGTAAT AAGAAAGGGTTTCATTTTTGT
PF3D7_1133800 HR-rv	5´-GATAGAAAATAAACGTTTTTGTTTAAAC GAGCAGAAGTTAATATCAGAAG
PF3D7_1133800 recodonized-fw1	5´-ACTTCTTATTTACATATTCTTCCTTTGCA ACAAAAAGGGATTCCACTTCTGCCATCGTATA A TACTTCGTAAGCGTACATTCAGT
T2A-SP^{hybrid}- PF3D7_1133800-fw2	5´-AGGTTCTTTGTTGACTTGTGGTGATGTT GAAGAAAATCCAGGTCCAgctagcAAAATGTT TATATACTACTTCGTATACTACCTTGCTTTAC TTCTTATTTACATATTCTT
PF3D7_1133800-3xHA-rv1	5´-AGTCGCGTAGTCCGGCACGTCGTACGGG TACATCGTAGCGTAATCTGGAACATCGTAT GGGTACATGGTcccgggAGCTTTCTTAACTAT GTTAGTTATG
PF3D7_1133800-3xHA (last 49 bp) -LoxP (first 17 bp)-rv2	5´-atgctatacgaagttataggcctTTAAGC ATAATCTGGAACATCATATGGATACATAGTC GCGTAGTCCGGC
PF3D7_0922100 HR-fw	5´-gtgacactatagaatactcgcggccgcTA AGCCGAAGAAAGGAATACAAT
PF3D7_0922100 HR-rv	5´-CTCTTCTGATATTAACTTCTGCTCGTTT AAACTTGATAATCTCATATGCGTAAAATA
T2A (last 54 bp)+ PF3D7_0922100 recodonized (first 30bp)-fw	5´-GGTGAAGGTAGAGGTTCTTTGTTGACTT GTGGTGATGTTGAAGAAAATCCAGGTCCAgct agcAAAATGGCAGAGGAGCGTAACACTATTAA AATT
PF3D7_0922100 recod. (last 39bp)+ 3xHA(first 54bp)-rv1	5´-CACGTCGTACGGGTACATCGTAGCGTAAT CTGGAACATCGTATGGGTACATGGTcccgggA TTATCTTTGTTCTGCTCCATCTCCTCG
PF3D7_0922100-3xHA (last 64bp)-LoxP (first 17 bp)-rv2	5´-gtatgctatacgaagttataggcctTT AAGCATAATCTGGAACATCATATGGATACATA GTCGCGTAGTCCGGCACGTCGTACGGGTACAT CGTAGCG
1133800-Int-fw	5´-GAATGAGTACATATCTCTTTGTTTATTA TTTAGC

1133800-Int-rv	5´-ATTATTGTTGTTGTTGTTGTTATTATC
0922100-Int-fw	5´-CATATATATTTATATATATATAACATTATTACATACG
0922100-Int-rv	5´GGTTTATATTAACTTGACTCATTATATCATTTAATAATGAGC
WT complementation nmd3+UIS2 fw1	5´GTATATCATTTTAAAGATAACTCGAGATGAACATTCTTAACTTATTCATTTGC
WT complementation nmd3+UIS2 rv1	5´-CCTTAATCACTGCCTCACCCTTACTCACCATCCTAGGACGACTAATACGGTTTAAACTGTCC
WR complementattion intern segment 1 rv	5´-GCGTTGTTCATTTTTATTGAGTTGTCGTTAAGGTTCTCTTTCTCGTTGTTCTCGTTCTGTGCC
WT complementattion internt segment 2 fw	5´-CGACAACTCAATAAAAATGAACAACGCAAAGGGAACTTCATCAAAGATAAACGACC
Complementation D542N fw1	5´-CGTATATCATTTTAAAGATAACTCGAGATGAACATTCTTAACTTATTCATTTGC
Complementation D542N fw2	5´-AACATAGGTCAGGGATTCGAGGAGGAGAAGAACTTCGATGTAC
Complementation D542N rv1	5´-CCTCCTCGAATCCCTGACCTATGTTACCAAGCATCATTATCTTAAGT
Complementation D542N rv2	5´GCCTCACCCTTACTCACCATCCTAGGACGACTAATACGGTTTAAACTGTCC
Complementation D591N fw1	5´-CGTATATCATTTTAAAGATAACTCGAGATGAACATTCTTAACTTATTCATTTGC
Complementation D591N fw2	5´-AACAACATTCCAAACGACGGATCATATAACTTCATAGG
Complementation D591N rv1	5´-GATCCGTCGTTTGGAATGTTGTTTCCAAGGTTTATTACG
Complementation D542N+D591N fw1	5´-CGTATATCATTTTAAAGATAACTCGAGATGAACATTCTTAACTTATTCATTTGC
Complementation D542N+D591N rv1	5´-GTTGACTTAAGCTCGTTGAATCCCATGAAATTGTATATGTTTTGTACATCGAAGTTCTTCTCCTCCTCGAATCCCTGACCTATGTTACCAAGCATCATTATC
Complementation D542N+D591N r2	5´-*GATCCGTCGTTTGGAATGTTGTTTCCAA*

	GGTTTATTACGAAGTCAGCGTTGTTCTCAAGG TGCCACTTCTTCATTGACTGTACTGTTGACTT AAGCTCGTTGAATCCC
Complementation D542N+D591N rv3	5´-GGACAGTTTAAACCGTATTAGTCGTCCT AGGATGGTGAGTAAGGGTGAGGC
TgGRA44_exon1_NMD3_frw	5´-CGTATATCATTTTAAAGATAACTCGAGA TGGAAAGACGTACACGTCCGGATGTGTCG
TgGRA44_exon1_rev	5´-CAAAACGGTGGTACGACATATTCGTCAA GGATGCCAAACTGGACATCCCGTGGCTAATG
TgGRA44_exon2_frw	5´-CAAAACGGTGGTACGACATATTCGTCAAG GATGCCAAACTGGACATCCCGTGGCTAATG
TgGRA44_exon2_rev	5´-GCGGTCCATCATCGACTGCATATTGTT CGCGATAGGATTGCCTACGAAGAGATTCCACG
TgGRA44_exon3_frw	5´-CGTGGAATCTCTTCGTAGGCAATCCTA TCGCGAACAATATGCAGTCGATGATGGACCGC
TgGRA44_exon3_Sca_rev	5´-CACTGCCTCACCCTTACTCACCATCCTA GGTCATTCCGTTGCGTCAGTCGAGTCTTCCC
TgGRA44-NheI-fw	5´-CCGCAGAAGAAGGCAGATCTGGAGAA ACGGCTAGCTGCACTGAAGGACCAGGCGGAAC AGGAAGCGC
TgGRA44-AvrII-rv	5´-CCTTAATCACTGCCTCACCCTTACTC ACCATCCTAGGTTCCGTTGCGTCAGTCGAGTC TTCCC
1133800-mNG 5´HR-fw	5´-GGGgcggccgctaaGTTGTTCAAGAAA TGAAGAC
1133800-mNG 5´HR-rv	5´-GGGcctaggTGCCTTTTTGACAATATTTG
0922100-mNG 5´HR-fw	5´-GGGgcggccgctaaGTAAATGATGACTTT GTAAATG
0922100-mNG 5´HR-rv	5´-GGGcctaggGTTGTCCTTATTTTGTTCCA TTTC
1133800-mNG-Int-fw	5´-CGTATTATCTAAATCCAATAG
1133800-mNG-Int-rv	5´-CATATTTATAAACATTTAAATATGTACA AC
0922100-mNG-Int-fw	5´-GCATCAAATAAATTAAACG
0922100-mNG-Int-rv	5´-CTATGTCCATGTTTAAATGC
DHODH 865 fw	5´-GTCAAGATTTTTGAACGTATCG
DHODH 875 fw	5´-AAAAGACATAATGGAAGCTAAGG

DHODH 42 rv	5´-GATGCATTCATAAATGGGTTTTC
DHODH 76 rv	5´-CTAATTCTTGTGTAGTCATGC
GFP 85 rv	5´-ACCTTCACCCTCTCCACTGAC
GFP 272 rv	5´-CCTTCGGGCATGGCACTC
GFP 633 fw	5´-gccctttcgaaagatccc
FKBP 253 fw	5´-TCACCAGATTATGCATACGGTG
FKBP 276fw	5´-CAGGCCATCCTGGCATCATC
FKBP 39 rv	5´-TTGACCTCTTTTTGGAAATGTACG
FKBP 82 rv	5´-CTTTCCATCTTCAAGCATTCCAG
FRB 251 fw	5´-gaatgtcaaggacctcctccaagc
pArl 55 fw	5´-GGAATTGTGAGCGGATAACAATTTCAC ACAGG
pARLminus rv	5´-CAGTTATAAATACAATCAATTGG
Crt fw	5´-CCGTTAATAATAAATACACGCAGTC
Crt 131 fw	5´-cacatatatgacataaatattttaaaa tcg
3xHA rv	5´-AGCATAATCTGGAACATCATATG
mCherry 620 fw	5´-ctcccacaacgaggactacacc
mCherry 88 rv	5´-GGCCGTTCACGGAGCCCTCC
mScarlet 38 rv	5´-CCCTCCATGTGCACCTTAAAACGC
Neo 40 rv	5´-CGAATAGCCTCTCCACCCAAG
LoxP FW	5´-CTTCGTATAGCATACATTATACGAAG
Nmd3 fw	5´-AGAAACCGTTGATTAAATAATAC

Appendix 2

Full schematic representation of the SLI strategy to obtain a cell line for DiCre-based conditional KO of uis2-HA (Top image) or uis2-GFP (bottom image).

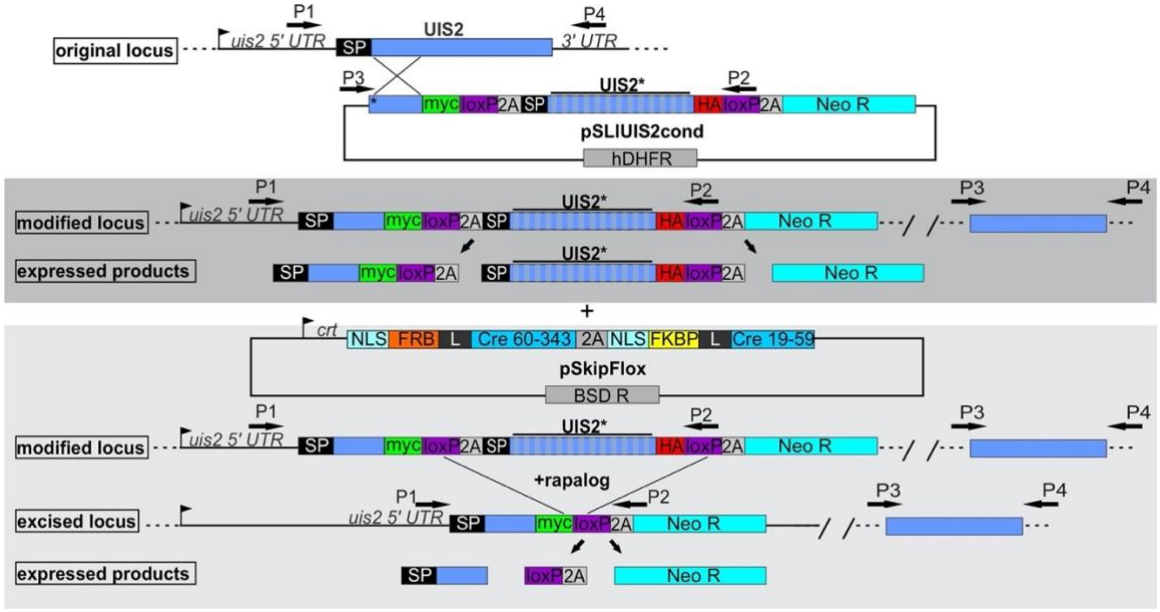

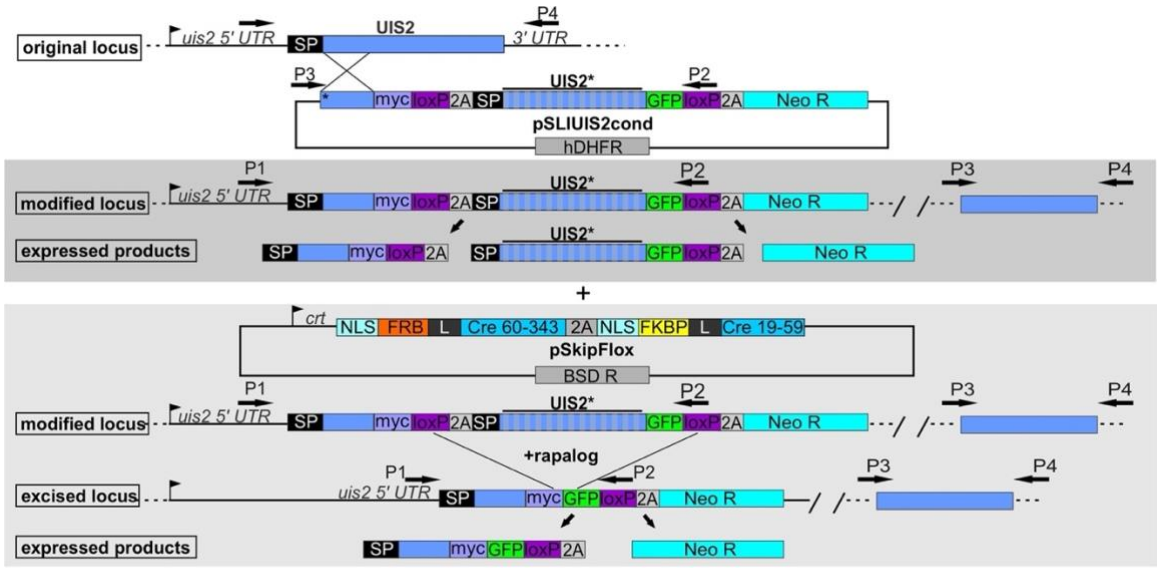

Appendix 3

Immunoblots used for quantification of the abundance of conditional KO of uis2.

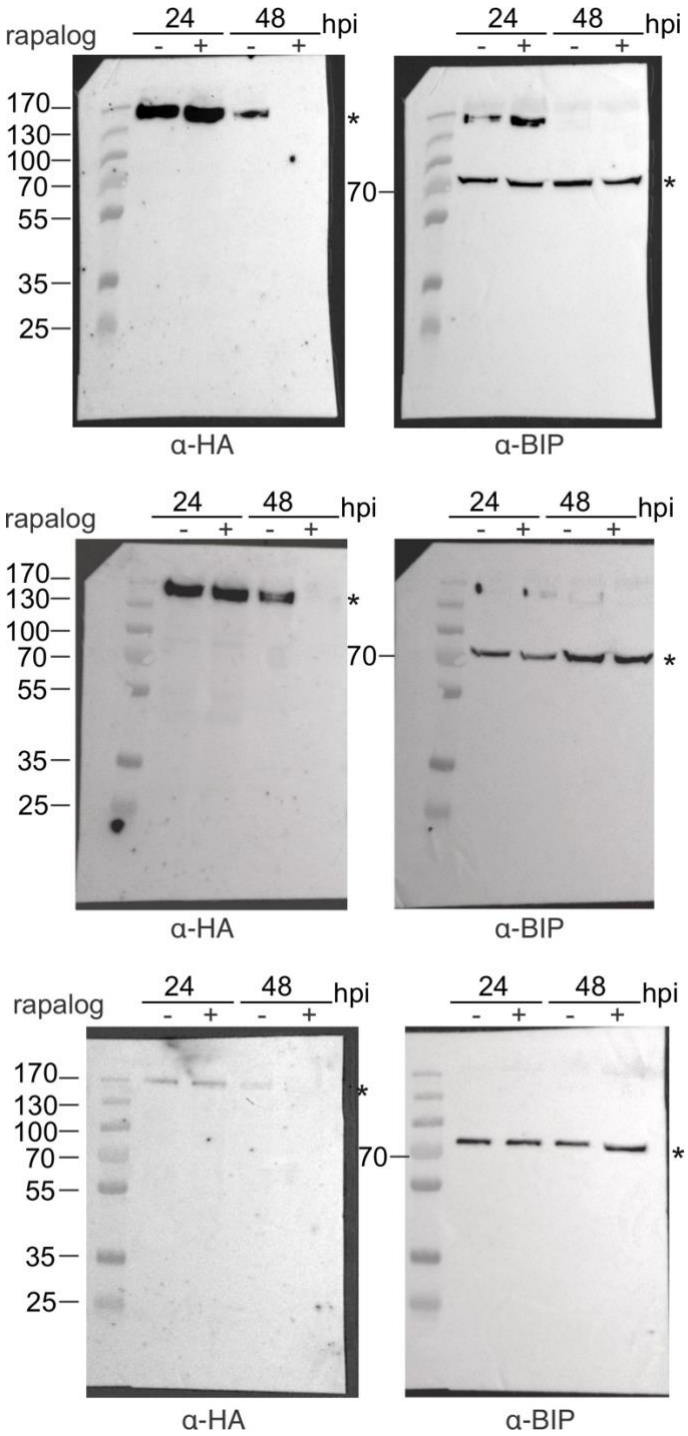

Appendix 4

Replicas of growth curve of condΔUIS2 -HA in presence (rapa) or absence (ctrl) of rapalog

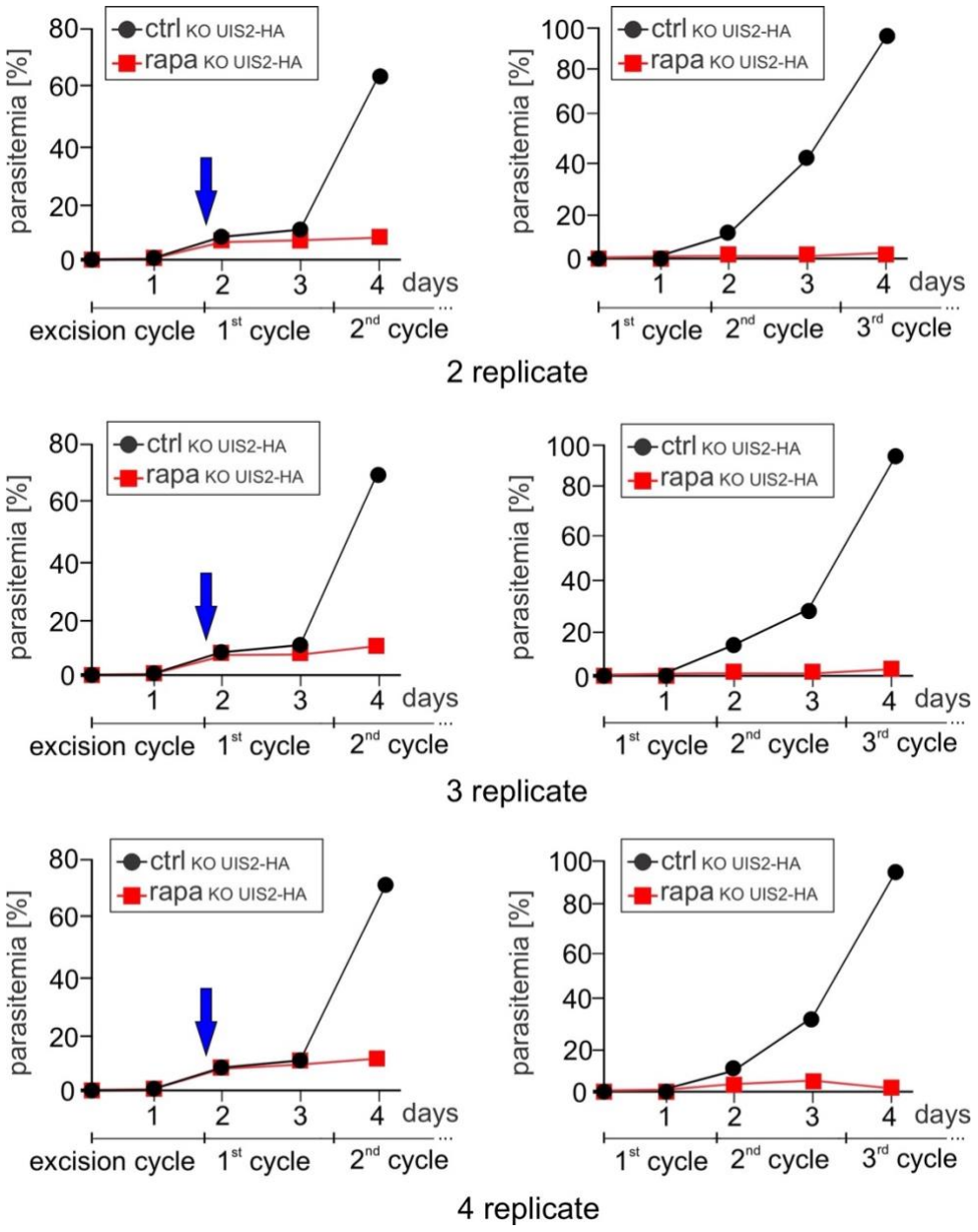

Appendix 5

Replicas of growth curve of condΔUIS2-GFP in presence (rapa) or absence (ctrl) of rapalog.

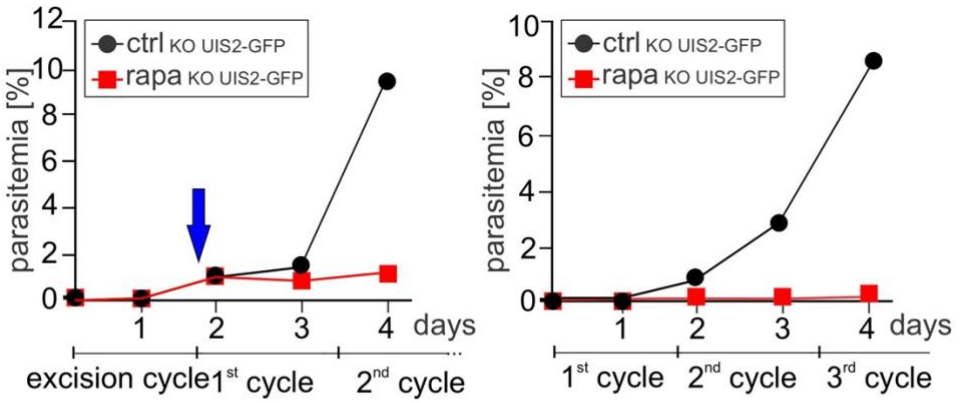

2 replicate

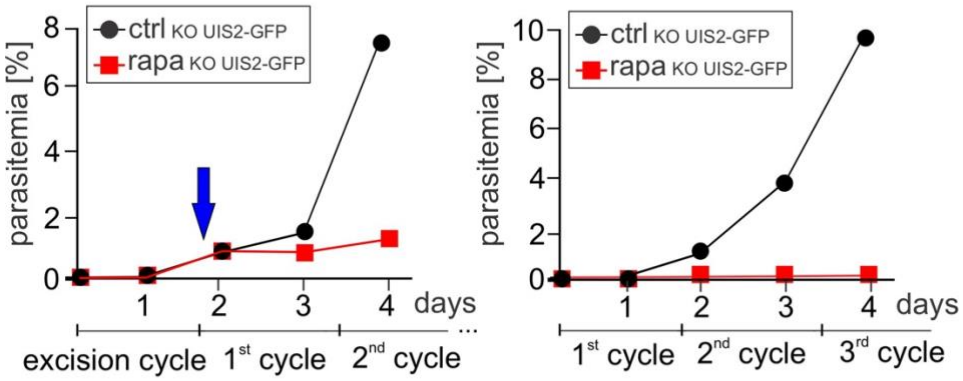

3 replicate

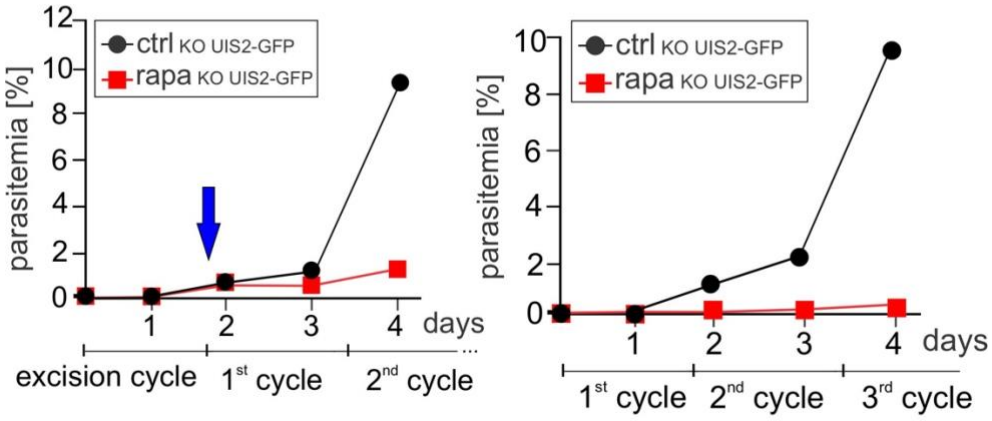

4 replicate

Appendix 6

Replicas of growth curve of condΔUIS2-GFP episomally expressing UIS2-WT^{epi} in presence (rapa) or absence (ctrl) of rapalog.

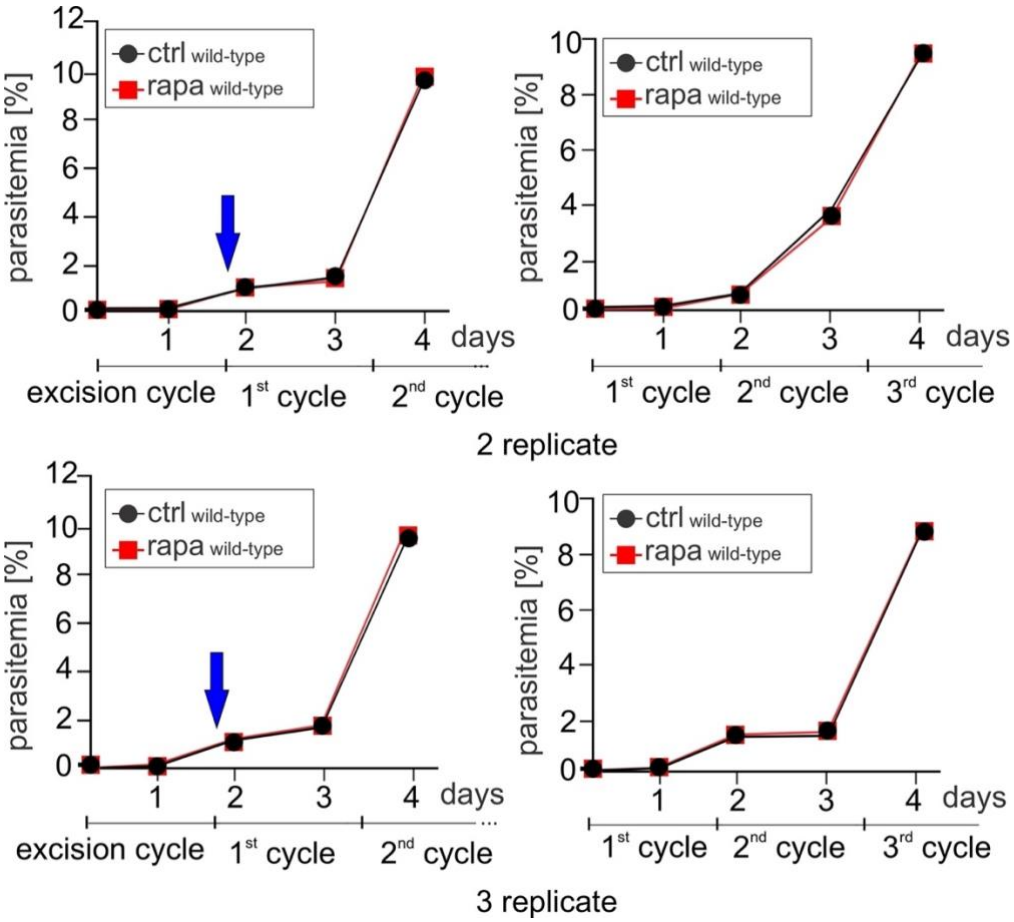

Appendix 7

Replicas of growth curve of condΔUIS2-GFP episomally expressing UIS2-D542N^{epi} or UIS2-D591N^{epi} in presence (rapa) or absence (ctrl) of rapalog.

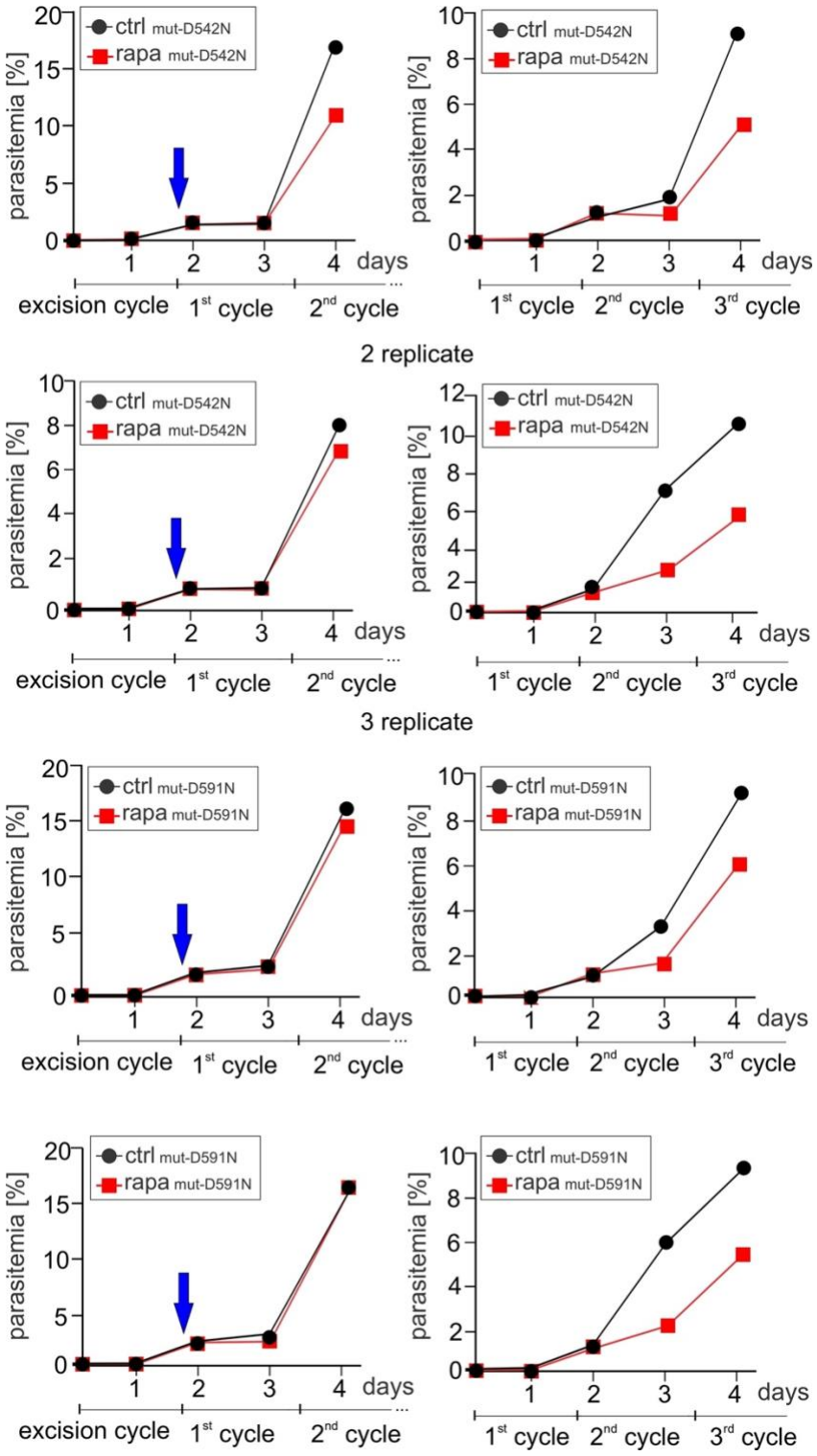

Appendix 8

Replicas of growth curve of condΔUIS2-GFP episomally expressing *Tg*UIS2 in presence (rapa) or absence (ctrl) of rapalog

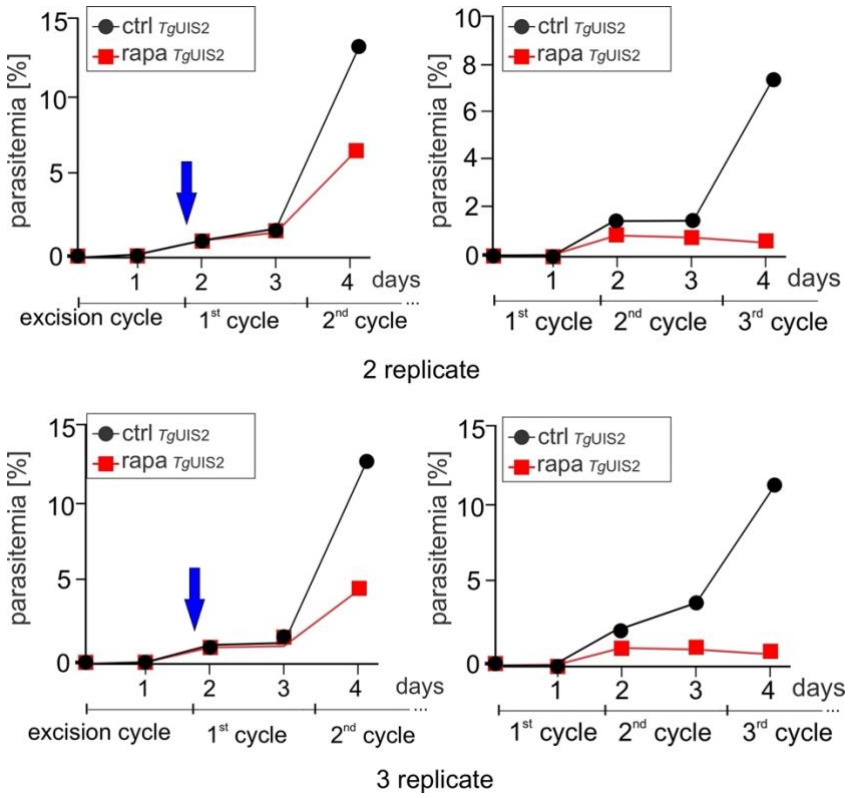

Appendix 9

Replicas of Immunoblots of DIQ-BioID with UIS2

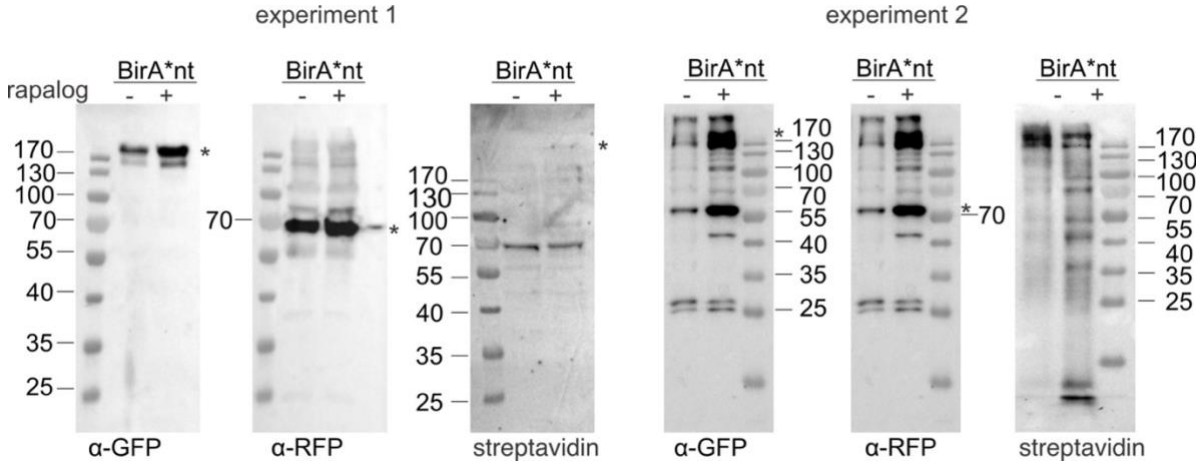

Appendix 10

Raw data of UIS2-DIQ-BioID experiments. Enriched proteins are represented in colour, with orange indicating enrichment in Experiment 1 and yellow for Experiment 2.

Majority protein IDs	Protein name	Ratio H/L normalized UIS2_for1	Ratio H/L normalized UIS2_rev1	Ratio H/L normalized UIS2_for2	Ratio H/L normalized UIS2_rev2	Peptides
PF3D7_1464600	serine/threonine protein phosphatase UIS2, putative	**2,91006**	**3,39608**	**3,00506**	**3,00451**	**62**
PF3D7_1420700	surface protein P113	1,98196	2,3913	1,39709	2,11597	13
PF3D7_0727200	cysteine desulfurase IscS	0	4,26235	0	0	6
PF3D7_1407100	rRNA 2-O-methyltransferase fibrillarin, putative	1,60426	2,12042	0	1,87287	8
PF3D7_0915400	ATP-dependent 6-phosphofructokinase	1,81348	1,85308	1,10923	1,99948	57
PF3D7_1421200	40S ribosomal protein S25	0,992261	2,40415	0	2,13555	5
PF3D7_1133800	RNA (uracil-5-)methyltransferase, putative	1,77058	1,6137	0,244765	0,440459	13
PF3D7_1212700	eukaryotic translation initiation factor 3 subunit A, putative	0,823912	2,55199	0,954047	1,3499	30
PF3D7_0922100	ubiquitin-like protein, putative	1,31777	1,62322	-0,597933	1,84337	27
PF3D7_1360900	RNA-binding protein, putative	1,04432	1,81614	0,911807	1,00816	9
PF3D7_1330800	RNA-binding protein, putative	0	2,75867	0	0,793482	8
PF3D7_1444800	fructose-bisphosphate aldolase	0	2,59719	-0,687358	0,21098	13
PF3D7_0719600	60S ribosomal protein L11a, putative	0	2,40882	-2,16897	1,86119	3
PF3D7_1016400	serine/threonine protein kinase, FIKK family	0	2,37385	-0,904035	0,942668	8
PF3D7_1309100	60S ribosomal protein L24, putative	0	2,31638	-0,865911	3,88189	5
PF3D7_0829200	prohibitin 1, putative	0	2,3128	0,00647761	0	3
PF3D7_1302800	40S ribosomal protein S7, putative	-0,805283	3,07936	0,604166	0,640456	6
PF3D7_0708100	DNA-directed RNA polymerases I, II, and III subunit RPABC5, putative	0	2,24557	0	0	2
PF3D7_0606700	coatomer alpha subunit, putative	1,06247	1,16085	0,820322	1,82266	25
PF3D7_0831700	heat shock protein 70	2,62181	-0,416083	0,510557	0,0971469	12
PF3D7_1130200	60S ribosomal protein P0	1,01771	1,09878	0,53097	0,490699	16
PF3D7_1118500	nucleolar protein 56, putative	0,87523	1,23909	0,520447	2,33825	15
PF3D7_1109900	60S ribosomal protein L36	0,8292	1,26219	0,249991	0,618096	3
PF3D7_0424600	Plasmodium exported protein (PHISTb)	1,05672	0,937547	0	0,586948	8
PF3D7_0716800	eukaryotic translation initiation factor 3 subunit I, putative	1,028	0,936414	0,505383	1,08522	14
PF3D7_1024800	exported protein 3	0,95977	0,949895	0,480472	0,736677	21
PF3D7_1134200	conserved Plasmodium protein, unknown function	0	1,88795	0,479334	1,47505	7
PF3D7_0907400	ATP-dependent protease ATPase subunit ClpY	0	1,88401	0	0	3
PF3D7_1417500	H/ACA ribonucleoprotein complex subunit 4, putative	1,09167	0,783291	0	1,10172	8
PF3D7_1004400	RNA-binding protein, putative	0,645609	1,22631	0,368824	1,41943	25
PF3D7_1105300	conserved Plasmodium protein, unknown function	0	1,86802	0	0	4
PF3D7_1403900	serine/threonine protein phosphatase CPPED1, putative	0	1,86365	0	0	4
PF3D7_1453700	HSP90 co-chaperone p23	0,856149	0,993379	1,81869	0,462734	5
PF3D7_0217800	40S ribosomal protein S26	0,556699	1,28093	0,545771	1,41485	3
PF3D7_1124900	60S ribosomal protein L35, putative	0	1,83084	0	2,01304	3
PF3D7_1027300	peroxiredoxin	0	1,82271	0,348799	1,01127	5
PF3D7_1006200	DNA/RNA-binding protein Alba 3	1,20345	0,612924	1,04103	1,1406	10
PF3D7_1108400	casein kinase 2, alpha subunit	0,738811	1,07257	0,713784	1,00512	10
PF3D7_0709700	prodrug activation and resistance esterase	0	1,79621	0,318809	-0,0652966	4
PF3D7_1010100	PI31 domain-containing protein, putative	0	1,77631	0	0,378307	6
PF3D7_0309600	60S acidic ribosomal protein P2	0	1,75307	0	0,827615	6
PF3D7_1027800	60S ribosomal protein L3	0,611645	1,10989	0,553459	1,12652	15
PF3D7_1103100	60S acidic ribosomal protein P1, putative	0	1,70675	-0,218078	1,18259	5
PF3D7_0624000	hexokinase	0,838427	0,854283	-0,198245	-0,0586628	12

PF3D7_0422500	pre-mRNA-splicing helicase BRR2, putative	0	1,68747	-0,274076	0,267028	29
PF3D7_1353900	proteasome subunit alpha type-7, putative	0	1,68399	0	0	6
PF3D7_1364800	DNA-directed RNA polymerases I, II, and III subunit RPABC1, putative	0	1,67927	-0,968887	0	5
PF3D7_1239700	ATP-dependent zinc metalloprotease FTSH 1	0,496718	1,14886	0,708849	0,275926	10
PF3D7_0931100	nucleolar protein Nop52, putative	0	1,64386	0	0	4
PF3D7_1242700	40S ribosomal protein S17, putative	0,209391	1,41569	0,308244	1,07421	9
PF3D7_1246800	signal recognition particle receptor subunit beta, putative	0	1,61905	0	0,254702	4
PF3D7_0322900	40S ribosomal protein S3A, putative	0,288063	1,31391	0,50782	0,945193	17
PF3D7_1330600	elongation factor Tu, putative	0,484808	1,10203	0,500394	0,104418	4
PF3D7_0517300	serine/arginine-rich splicing factor 1	0,580821	1,00113	0,938248	1,53864	14
PF3D7_0729100		0	1,56986	-0,751708	0,816596	42
PF3D7_0823800	DnaJ protein, putative	1,15497	0,397372	0,638769	0,362659	21
PF3D7_0517000	60S ribosomal protein L12, putative	0,703632	0,840733	0,885418	1,0122	6
PF3D7_0532400	lysine-rich membrane-associated PHISTb protein	0,935158	0,581022	1,05596	0,982876	13
PF3D7_0217500	calcium-dependent protein kinase 1	0	1,51461	0	0	13
PF3D7_0401800	Plasmodium exported protein (PHISTb), unknown function	0,955238	0,552876	0,846313	2,03724	14
PF3D7_0819900	U6 snRNA-associated Sm-like protein LSm3, putative	0	1,49891	0	0,912727	3
PF3D7_1460700	60S ribosomal protein L27	0	1,49842	0,356933	1,47806	5
PF3D7_0919000	nucleosome assembly protein	0,00963388	1,48253	0,777451	0,793357	10
PF3D7_0415500	nuclear cap-binding protein subunit 2, putative	0,482848	0,98017	0,501923	0,729746	9
PF3D7_0517700	eukaryotic translation initiation factor 3 subunit B, putative	0,703366	0,731374	0,483055	0,986388	39
PF3D7_1308200	carbamoyl phosphate synthetase	0,473423	0,955396	0,521252	0,84931	65
PF3D7_1367100	U1 small nuclear ribonucleoprotein 70 kDa homolog, putative	0	1,42186	0	0	4
PF3D7_1011800	PRE-binding protein	0,0761487	1,32539	0,742265	0,639917	31
PF3D7_1464700	ATP synthase (C/AC39) subunit, putative	0	1,39977	0	0	3
PF3D7_0106300	calcium-transporting ATPase	0	1,39161	0	0	13
PF3D7_1347500	DNA/RNA-binding protein Alba 4	0,350384	1,03251	0,796515	0,775466	11
PF3D7_1203700	nucleosome assembly protein	0,53655	0,843681	0,724388	1,2537	10
PF3D7_1426000		0,271426	1,10752	0,450485	1,59497	5
PF3D7_0217100	ATP synthase subunit alpha, mitochondrial	0	1,35864	-0,0875647	0	3
PF3D7_1129100	parasitophorous vacuolar protein 1	0,420509	0,937215	0,288654	0,167944	15
PF3D7_1134000	heat shock protein 70	-0,465162	1,82261	0,0927488	-0,0415233	28
PF3D7_1445100	histidine--tRNA ligase, putative	0	1,35627	0	0	11
PF3D7_0617200	BFR1 domain-containing protein, putative	-0,0942486	1,45032	0,145612	0,589138	7
PF3D7_1441200	60S ribosomal protein L1, putative	0,424385	0,922183	0,704252	0,886246	7
PF3D7_1206200	eukaryotic translation initiation factor 3 subunit C, putative	0,637471	0,689357	0,24732	0,413538	24
PF3D7_0609000	nucleoporin NUP637, putative	1,01028	0,315415	0,192194	0,0781219	62
PF3D7_1224300	polyadenylate-binding protein 1, putative	0,58246	0,729483	0,55562	1,08109	33
PF3D7_0624400	conserved protein, unknown function	0	1,3105	0	1,06879	4
PF3D7_1414300	60S ribosomal protein L10, putative	0,525367	0,783961	0,484808	0	7
PF3D7_1424400		0	1,28602	1,31278	1,16654	8
PF3D7_0824400	nucleoside transporter 2	0	1,26649	0	0	8
PF3D7_0801800	mannose-6-phosphate isomerase, putative	0	1,25977	0	0,278846	12
PF3D7_0413600	26S protease regulatory subunit 6B, putative	0,0561673	1,16586	0,333195	0,432708	17
PF3D7_0507100	60S ribosomal protein L4	0,403486	0,817155	0,456491	1,20148	14
PF3D7_1034900	methionine--tRNA ligase	0,375735	0,839596	0,0229004	-1,12254	11
PF3D7_1331800		0,62499	0,586319	0,548141	0,62391	5
PF3D7_0905400	high molecular weight rhoptry protein 3	0,240253	0,958757	-0,160734	0,137235	16
PF3D7_0605100	KH domain-containing protein, putative	0,520146	0,677726	0,0526941	1,25718	15
PF3D7_1429800	coatomer subunit beta, putative	0	1,18666	0,33674	0,429187	15
PF3D7_1412500	actin II	0	1,18161	0	0,575271	10
PF3D7_1119000	acyl-CoA-binding protein, putative	1,15827	0	0,692338	0,564478	6

PF3D7_1241800	ATP-dependent RNA helicase DBP9, putative	0	1,15136	1,00863	0	4
PF3D7_0813400	conserved protein, unknown function	1,15043	0	0	0	9
PF3D7_1338100	26S proteasome regulatory subunit RPN3, putative	0	1,15005	-0,46341	0,224048	6
PF3D7_1201000	Plasmodium exported protein (PHISTb), unknown function	0,833011	0,316977	0,59579	1,15512	8
PF3D7_0916700	RNA-binding protein musashi, putative	0,461738	0,678672	0,632547	1,02371	7
PF3D7_0802000	glutamate dehydrogenase, putative	0	1,12812	-0,231498	0,230567	20
PF3D7_1447000	40S ribosomal protein S5	0,0762854	1,04904	0,108892	1,28332	12
PF3D7_0726500	ubiquitin carboxyl-terminal hydrolase, putative	0	1,11785	0	1,87901	42
PF3D7_0814000	60S ribosomal protein L13-2, putative	0,245982	0,869016	0,546956	0,898538	8
PF3D7_1211400	heat shock protein DNAJ homologue Pfj4	0,563744	0,54654	0,436801	0,331736	9
PF3D7_1439300	Sad1/UNC domain-containing protein, putative	0	1,10948	-1,29074	0	5
PF3D7_0703500	erythrocyte membrane-associated antigen	0,486354	0,62171	0,226262	0,504428	74
PF3D7_0520000	40S ribosomal protein S9, putative	0,39835	0,704395	0,964436	0,952155	10
PF3D7_1468900	zinc finger protein, putative	0	1,09724	0	0	9
PF3D7_1464900	ATP-dependent zinc metalloprotease FTSH, putative	0	1,09274	0	0,358398	11
PF3D7_0813300	NPL domain-containing protein, putative	0	1,08779	-0,263646	1,94186	5
PF3D7_0815600	eukaryotic translation initiation factor 3 subunit G, putative	-0,373738	1,45403	0,223175	1,29106	14
PF3D7_1346300	DNA/RNA-binding protein Alba 2	-0,030855	1,1102	0,992406	0,754918	5
PF3D7_1219600	phospholipid-transporting ATPase 2	0	1,07476	0	-0,401958	7
PF3D7_0831400	Plasmodium exported protein, unknown function	0	1,07148	0	2,72271	4
PF3D7_0814200	DNA/RNA-binding protein Alba 1	0,611078	0,458564	1,00813	1,20025	11
PF3D7_1211900	non-SERCA-type Ca2+ -transporting P-ATPase	0	1,06597	0	0	14
PF3D7_1357700	U3 small nucleolar RNA-associated protein 21, putative	0	1,05421	0	0	12
PF3D7_1211700	DNA replication licensing factor MCM5, putative	0	1,04722	0,260628	0	13
PF3D7_1226900	parasitophorous vacuolar protein 2	0	1,04531	0,794437	0,96432	3
PF3D7_0604500	GYF domain-containing protein, putative	0,621431	0,413826	0,336283	0,281386	80
PF3D7_0618300	60S ribosomal protein L27a, putative	0	1,03466	0,929791	0,95674	8
PF3D7_0312800		0	1,03401	0	0	3
PF3D7_1338200	60S ribosomal protein L6, putative	0,20964	0,811093	0,626019	0,740432	8
PF3D7_1236100	clustered-asparagine-rich protein	0	1,01981	0	0,591962	10
PF3D7_0406200	parasitophorous vacuole membrane protein S16	0	1,01298	0,667029	0,630282	2

Appendix 11

Full scatters plots of UIS2-DiQ-BioID experiments showing proteins significantly enriched in experiment 1 and 2.

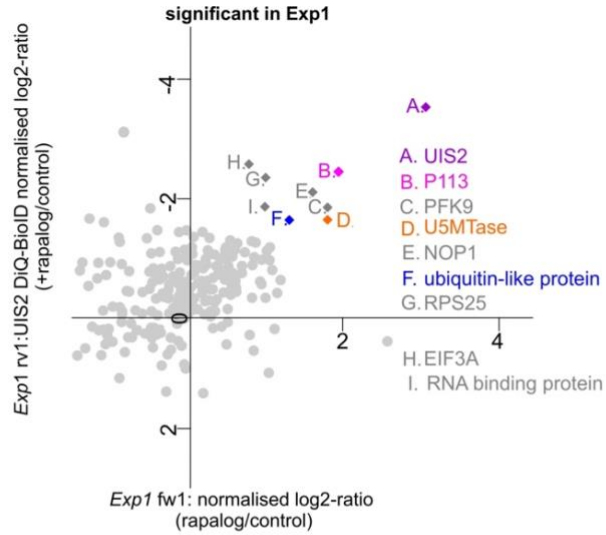

	PlasmoDB ID	name/description
A.	PF3D7_1464600	serine/threonine protein phosphtase,UIS2
B.	PF3D7_1420700	surface protein P113
C.	PF3D7_0915400	ATP-dependent 6-phosphofructokinase,PFK9
D.	PF3D7_1133800	RNA(uracil-5-) methyltransferase, putative
E.	PF3D7_1407100	rRNA2-O-methyltransferase fibrillarin, putative,NOP1
F.	PF3D7_0922100	ubiquitin-like protein, putative
G.	PF3D7_1421200	40S ribosome protein S25,RPS25
H.	PF3D7_1212700	eukaryotic translation initiation factor 3A, putative,EIF3A
I.	PF3D7_1360900	RNA-binding protein, putative

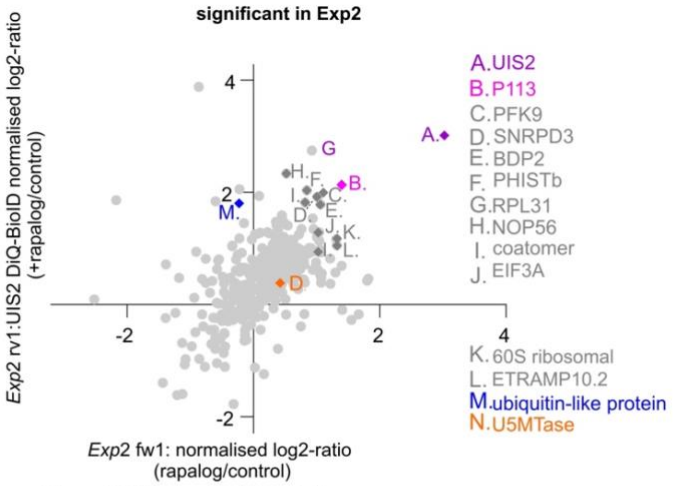

	PlasmoDB ID	name/description
A.	PF3D7_1464600	serine/threonine protein phosphtase UIS2
B.	PF3D7_1420700	surface protein P113
C.	PF3D7_0915400	ATP-dependent 6-phosphofructokinase,PFK9
D.	PF3D7_0503800	small nuclear ribonucleoprotein Sm D3, putative,SNRPD3
E.	PF3D7_1212900	bromodomain protein 2, putative,BDP2
F.	PF3D7_0401800	Plasmodium exported protein (PHISTb),unknown function
G.	PF3D7_0503800	60S ribosomal protein L31,RPL31
H.	PF3D7_1118500	nucleolar protein 56, putative NOP56
I.	PF3D7_0606700	coatomer alpha subunit, putative
J.	PF3D7_1212700	eukaryotic translation initiation factor 3A, putative,EIF3A
K.	PF3D7_1424400	60S ribosomal protein L7-3, putative
L.	PF3D7_1033200	early transcribed membrane protein 10.2,ETRAMP10.2
M.	PF3D7_0922100	ubiquitin-like protein, putative
N.	PF3D7_1133800	RNA(uracil-5-) methyltransferase, putative

Appendix 12

Full schematic representation of the SLI strategy to obtain a cell line for DiCre-based conditional KO of PF3D7_1133800-HA (Top image) and PF3D7_0922100 (bottom image).

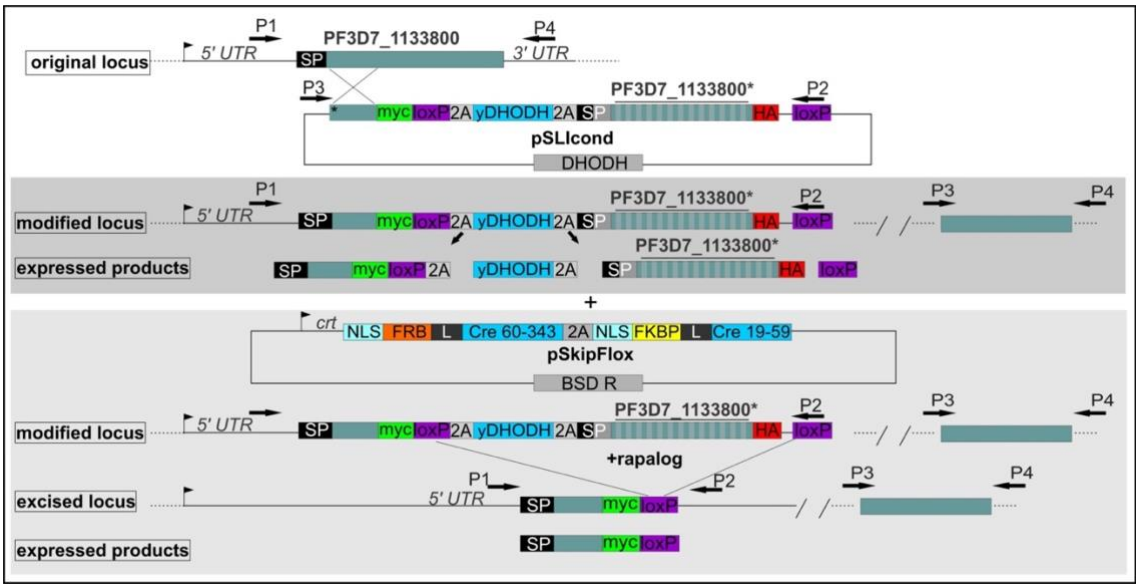

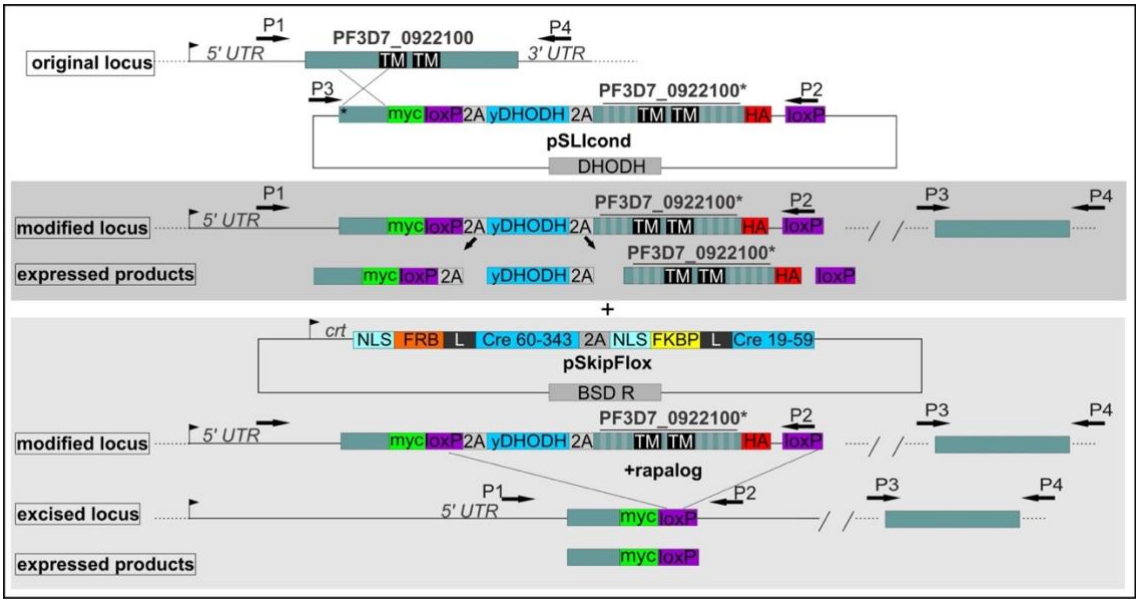

Appendix 13

Immunoblots used for quantification of the abundance of conditional KO of PF3D7_1133800 and PF3D7_0922100.

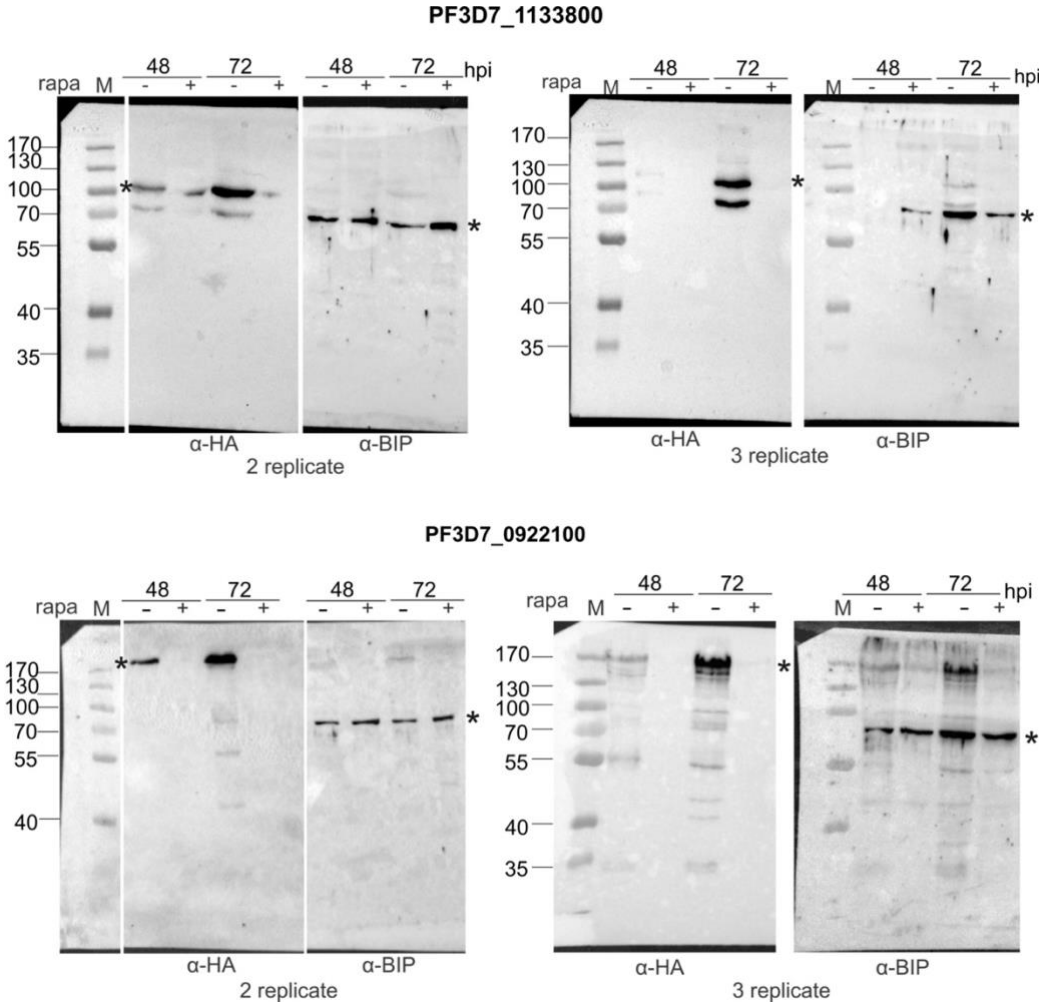

Appendix 14

Replicas of growth curve of condΔPF3D7_1133800 and condΔ0922100 in presence (rapa) or absence (ctrl) of rapalog.

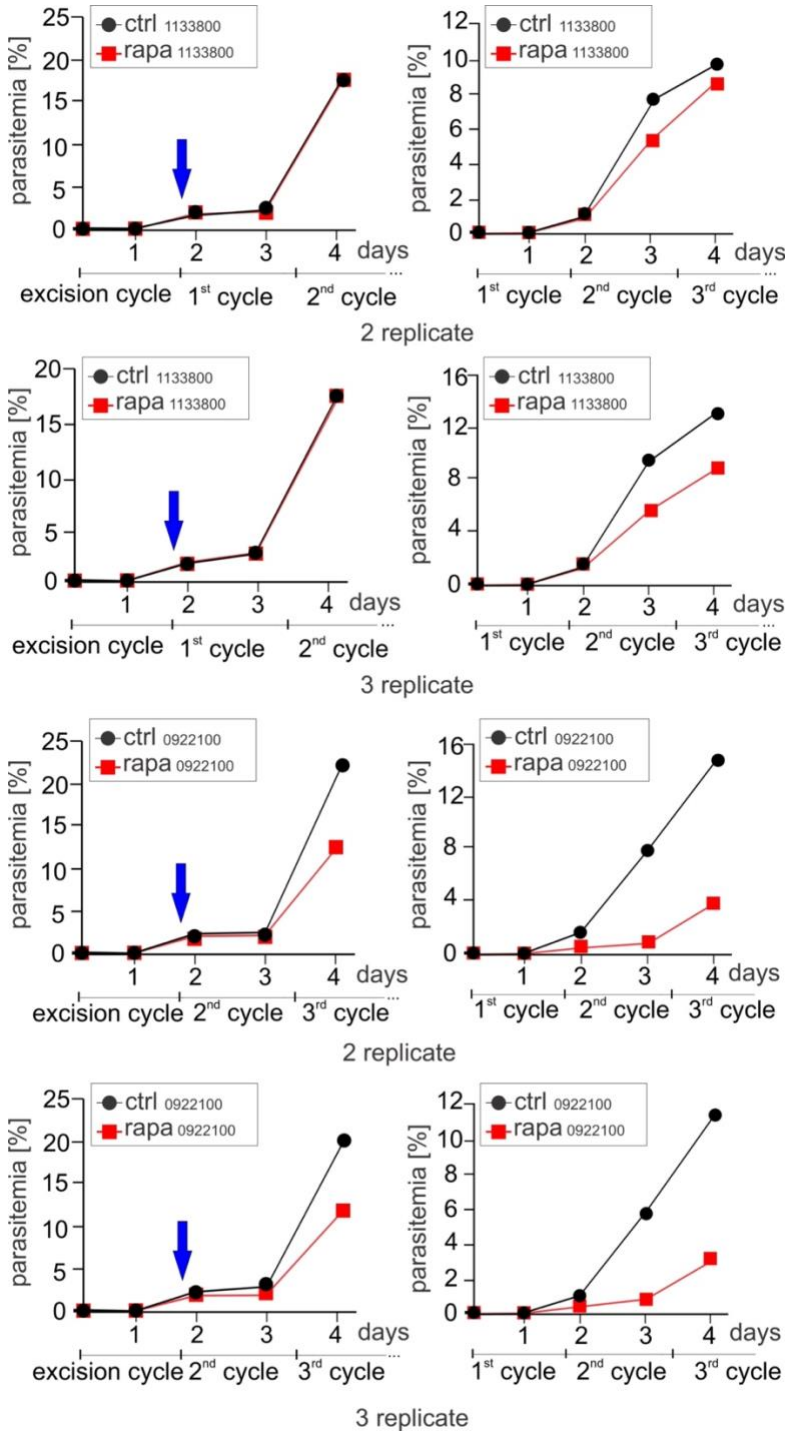

List of publications

Mesén-Ramírez, P., Bergmann, B., Elhabiri, M., Zhu, L., Thien, H. von, **Castro-Peña, C**., Gilberger, T.W., Davioud-Charvet, E., Bozdech, Z., Bachmann, A., Spielmann, T., 2021. The parasitophorous vacuole nutrient channel is critical for drug access in malaria parasites and modulates the artemisinin resistance fitness cost. Cell Host and Microbe 29, 1774-1787.e9. https://doi.org/10.1016/j.chom.2021.11.002.

Schmidt, S., Wichers-Misterek, J.S., Behrens, H.M., Birnbaum, J., Henshall, I.G., Dröge, J., Jonscher, E., Flemming, S., **Castro-Peña, C.,** Mesén-Ramírez, P., Spielmann, T., 2023. The Kelch13 compartment contains highly divergent vesicle trafficking proteins in malaria parasites. PLoS Pathog 19, e1011814. https://doi.org/10.1371/journal.ppat.1011814.